UNIVERSITY OF LONDON THESIS

Degree PhD Year 2006 Name of Author RAMPAUL
Ashti

The Photocatalytic and Cytotoxic Effects Of Titanium Dioxide Particles Used In Sunscreens

A thesis presented to the University of London in partial fulfilment of the requirements for the Degree of Doctor of Philosophy

Ashti Rampaul

University College London

Christopher Ingold Laboratories

20 Gordon Street

London WC1H 0AJ

ProQuest LLC
789 East Eisenhower Parkway
P.O. Box 1346
Ann Arbor, MI 48106-1346

I Ashti Rampaul, confirm that the work presented in this thesis is my own. Where information has been derived from other sources, I confirm that this has been indicated in the thesis,

For Mum, Dad

and Pravin

Table of Contents

Acknowledgements

Professor Ivan Parkin made this project possible. Thank you for being such an approachable and supportive supervisor. A great post graduate experience depends a lot on the mentor and Ivan fulfilled that part better than anyone else could possible do. Dr. Louise Cramer became my secondary supervisor during my second year. Thank you for helping me to take this project to the next level. I have never studied Biology before but your passion and drive was infectious and I soon learnt tons whilst in the LMCB.

Thank you to Dr. Damien Murphy and Emma Richardson at the Electron Paramagnetic Centre in Cardiff University for assisting me with the free radical measurements. Trips to Cardiff involved hard work but were always fun!

Thank you to Dr. Abil Aliv and Mr. David Butler for help with Solid State NMR analysis; Mr. Kevin Reeves for Scanning Electron Microscopy; Dr. Dorothy Farrell for Transmission Electron Microscopy, Mr. Robert Palgrave for XPS and Dr. Christopher Blackman for teaching me to use just about every other machine in the lab. Also, thank you Chris for useful discussions (not only the ones about food).

Working can sometimes be tedious but being around like-minded and fun people can make it less so. I have to thank Karen, Tayamika and Tom for making my stay in the LMCB one that I will always treasure. Thanks to Dina (I will miss our Nandos outings), Jalpa, Jesus, Russel, Saima, and everyone in the lab for any help they may have given me during the last few years.

A special thanks goes to Rob who motivated and kept me focussed, especially during the lengthy writing-up stage. Your wit and intelligence always kept me entertained especially when I needed it. Last but not least, thanks to my family for being so supportive during my whole time at university. This thesis is dedicated to you.

Abstract

Titanium dioxide nanoparticles are used in sunscreens to reflect UV radiation from the skin. However, titanium dioxide as anatase and rutile crystal forms is a well-known photocatalyst. The nanoparticles are surface coated with inert inorganic oxides such as silica and alumina or organics such as organosilanes or silicone polymers and more recently, have been doped with manganese oxide. These modifications to the titanium dioxide particles are purported to prevent the production of harmful reactive oxygen species. A range of sunscreens was tested with crystal form and modification type identified via XRD, Raman Spectroscopy, XPS and SSNMR. The particle modification and crystal form determined whether the particles were inert or rapidly degraded methylene blue dye, and killed or protected cultured human epithelium cells. Novel solid state Electron Paramagnetic Resonance analysis showed that the greatest amount of superoxide anions was formed during UVA irradiation of the mixed anatase and rutile crystal forms coated with an organosilane. These particles also degraded methylene blue at a similar rate to Degussa P25, a standard uncoated titanium dioxide powder and produced an increase in UVA induced apoptosis of human keratinocytes. Double Stranded Breaks were observed extensively in cells exposed to UVA irradiated mixed anatase and rutile titanium dioxide with organosilane. A new apoptotic-like cell death mechanism may have been recognised during the UVA irradiation of animal and human cells in the presence of titanium dioxide. This research concludes that mixed anatase and rutile crystal forms of titanium dioxide coated with organosilane or dimethicone may not be safe to use in sunscreen lotions. A less harmful alternative for sunscreen formulations is the manganese doped rutile particles or the alumina coated rutile powders, both of which exhibited a protective effect on cultured epithelial cells.

List of Figures

List of Tables

List of Abbreviations

BCC	Basal Cell Carcinoma
BET	Braunaur Emmet Teller
CP	Cross Polarisation
CMM	Cutaneous Malignant Melanoma
DMEM	Dulbecco's Modified Eagle Medium
DNA	Deoxyribonucleic Acid
DSB	Double Stranded Break
e^-	Photogenerated electron
EMEM	Minimum Essential Medium
EPR	Electron Paramagnetic Resonance
FBS	Fetal Bovine Serum
FTIR	Fourier Transform Infra-Red
g	g-factor
h^+	Photogenerated hole
HaCaT	Human keratinocyte
MAS	Magic Angle Spinning
MDCK-I	Madin-Darby Canine Kidney
NMSC	Non-Melanoma Skin Cancer
NMR	Nuclear Magnetic Resonance
ppm	parts per million
PtK2	Potorous tridactylis Kidney
ROS	Reactive Oxygen Species
SB	Side Band
SCC	Squamous Cell Carcinoma
SEM	Scanning Electron Microscopy
SPF	Sun Protection Factor
SSNMR	Solid State Nuclear Magnetic Resonance
TEM	Transmission Electron Microscopy
TiO_2	Titanium Dioxide
Tx	Triton-X 100
XPS	X-Ray Photoelectron Spectroscopy
XRD	X-Ray Diffraction
UV	Ultra-violet
ZnO	Zinc Oxide
Z-VAD-FMK	Benzyloxycarbonyl-valyl-ananyl-aspartic acid (O-methyl)-fluoro-methylketone

Chapter 1 – Introduction

This thesis concerns the photocatalytic and cytotoxic properties of coated titanium dioxide and zinc oxide powders, which are used in sunscreens. Titanium dioxide or titania is paradoxically both safe and harmful. In the absence of ultraviolet light (UV), titanium dioxide is generally considered inert and is commonly found in toothpastes and foods as a colour additive[1]. However, in the presence of UV light ($\leq$ 420 nm for titanium dioxide as rutile, which is in the UVA portion of sunlight), titanium dioxide becomes activated, producing photogenerated electron and hole pairs that can react with adsorbed species such as O_2 or H_2O on the titania surface to produce free radicals[2]. Both titanium dioxide and zinc oxide are well known photocatalysts but titania has a higher oxidising power than the latter[3]. This makes it one of the most widely used and most versatile photocatalysts used today especially in creating a cleaner environment. Its uses range from water and air purification, decontamination and removal of organic compounds by self-cleaning glass and antibacterial coatings that sterilise and purify[2,3,4].

There has been a dramatic increase in the usage of sunscreens for the past three decades, during which time skin cancer has become the fastest growing worldwide cancer[5,6]. Over the years, several of the organic chemicals that are active ingredients used in these lotions have been found to have serious side effects. An example is Para-aminobenzoic Acid (PABA), which was one of the first organic UVB absorbers to be used in sunscreens. In the presence of sunlight, this chemical can generate free radicals, which can ultimately damage DNA[7] and as a consequence was voluntarily withdrawn from use by some sunscreen manufacturers. Other UV blocking organics in sunscreens such as 2-phenylbenzimidazole-5-sulfonic acid[8] (PBSA), avobenzone[9] and benzophenones[10] are

not photostable, breaking down into useless or more toxic compounds. This is the reason why sunscreen lotions need to be reapplied every hour in order to be effective.

Titanium dioxide was first incorporated into sunscreens in 1952 and is even more widely used today due to the development of microfine particles that appear transparent on the skin[11]. In order to prevent reactive oxygenated free radicals from being created, the titanium dioxide particle used in sunscreens is often coated with an inert material. Dunford[12] studied micronized titanium dioxide samples from over-the-counter sunscreens and found that all the samples catalysed the photo-oxidation of a phenol and caused oxidative damage to DNA.

Skin cancer has become the most common type of cancer and is continuously on the rise, accounting for half of new cancer cases in the western population[13]. In Australia, by the age of 75, 2 out of 3 people will have been treated for some form of skin cancer and in the United States of America; approximately 1,000,000 cases are diagnosed annually[14]. In the UK[5], over 100,000 cases of skin cancer were diagnosed in 2005. These are worrying statistics and the reasons for this rise are not known completely although they may be attributed to several causes such as lifestyle changes, insufficient application of sunscreen and environmental factors. In the current times, it is considered fashionable to have a tan, which can lead to over-exposure to the sun and use of tanning salons, which use large doses of high energy wavelengths of light that can damage skin. Another contribution may be due to the reduction of the protective ozone layer that would allow more dangerous, shorter wavelengths of light to penetrate the earth's atmosphere[15].

These changes have pressed the need for more efficient protection against the sun's harmful rays, hence the creation of sunscreens, which contain a wide variety of chemicals. The reactivities, structural chemistry and potential interactions of these chemicals have to be fully researched before formulating a sunscreen, especially as some of them are harmful free radical initiators and photocatalytic agents.

1.1 ULTRA-VIOLET RADIATION

Sunlight is composed of visible light (400-700 nm) and other wavelengths that are invisible to the human eye such as UV light (100-400 nm). UV radiation is thought to be a complete carcinogen i.e. it initiates the malignant process and promotes its growth[16]. Even though ultraviolet light comprises less than 5% of the incident sunlight at the Earth's surface[11], it has been evident from epidemiological, animal and biological studies that the most common cause of all three types of skin cancer is exposure to this radiation[17,18]. There are three classifications of UV radiation:

UVA (further subdivided into *UVA I* or far UVA (340-400 nm) and *UVA II* or near UVA (320 – 340 nm))

UVA rays constitute 90-95% of the sun's ultraviolet light reaching the Earth's surface. Although not as energetic as UVB rays, due to its longer wavelength, UVA rays penetrate deeper into the skin, through glass windows and some clothing materials. It is also the primary inducer of the tanning response in humans and contributes to photoaging, immunosuppression and skin cancer[18].

UVB (280 –320 nm)

These rays are at shorter wavelengths but higher in energy than UVA and are 1000 times more effective at causing sunburn. UVB rays are partially absorbed by the ozone layer however 5-10% of this radiation available from the sun reaches the Earth's surface. UVB in moderation has a positive effect as it is active in the synthesis of

vitamin D on the skin's surface, which in turn aids the absorption of calcium and other minerals[19]. However, this radiation is also thought to be the main cause of sunburn, skin aging and skin cancer. It is the most erythemogenic i.e. causing erythema or skin redness, solar radiation reaching the Earth and has been shown to be a skin carcinogen in animal studies[17]. Studies on the effects of UV light on skin cells have shown that UVB directly causes mutations in the DNA of genes[20].

UVC (100 – 280 nm)

This radiation has the shortest wavelengths and hence is the most energetic and dangerous. Fortunately, these rays are stopped from reaching the Earth by the ozone layer and molecular oxygen in the stratosphere[21]. There are however some artificial light sources such as tanning salons, mercury arcs or welding arcs which emit a small amount of UVC and should be avoided[11].

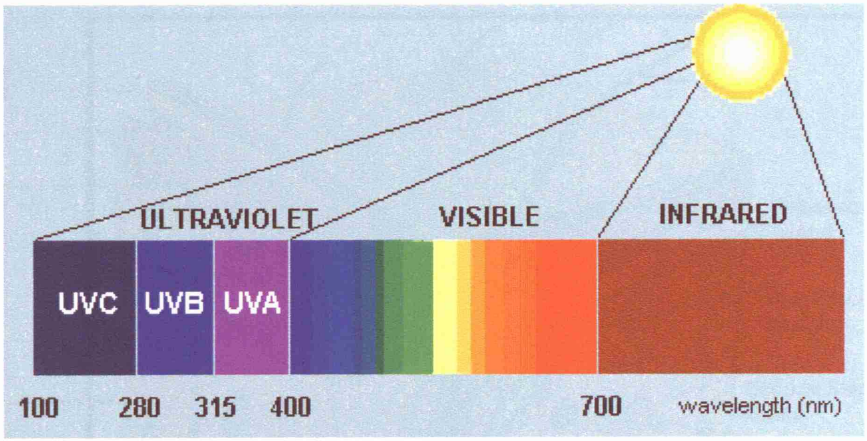

Figure 1.1: Schematic diagram of the Solar Spectrum[22]

1.2 SKIN

Humans are protected from UV rays by their skin, which is composed of three main layers: epidermis, dermis and hypodermis[23]. The epidermis is the topmost and thinnest of the three, consisting of at least four cell types (keratinocytes, melanocytes, Merkel cells and Langerhans cells) and five layers: *stratum corneum* or horny layer; *stratum lucidum* or transparent layer; *stratum granulosum* or granular cell layer; *stratum spinosum* or prickle cell layer and *stratum germinativum* or basal layer. The basal and prickle layers are the active areas of cell renewal, whereas the others are the upper area where cells are constantly changing from living cells with a nucleus to dead horny flat cells with no nucleus[23]. These dead cells are constantly shed from the surface. The melanocytes are the cells that donate melanin pigment to the keratinocytes. It is this pigment which gives the skin its colour and is the skin's natural protection from UV radiation. The hypodermis or subcutaneous layer is an area for formation and storage of fat.

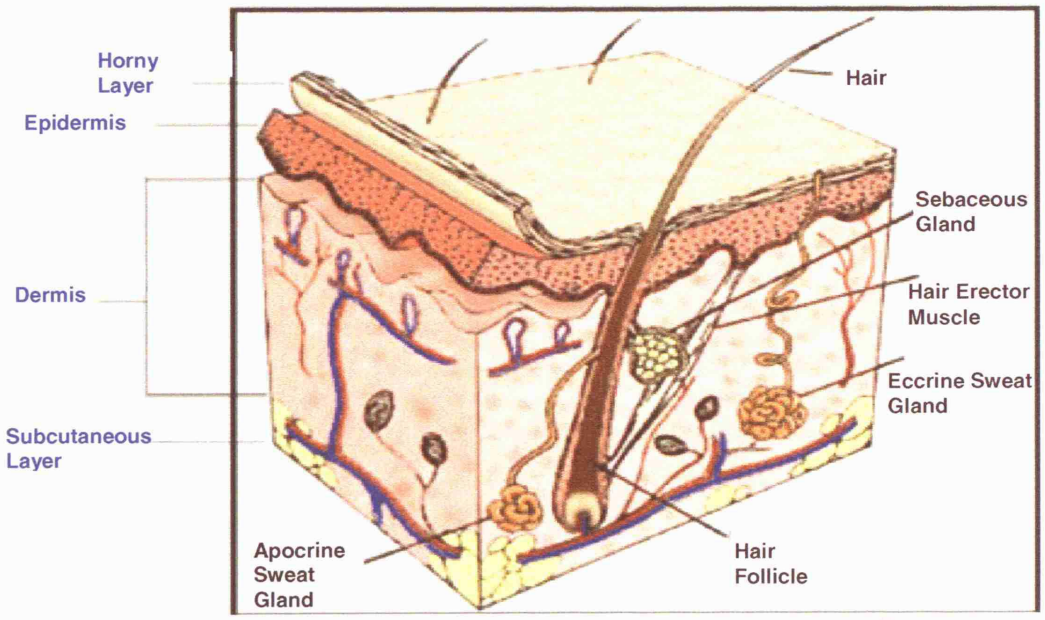

Figure 1.2: Three dimensional representation of skin[23]

Beneath the epidermis lies the dermis, which is the supportive layer for the epidermis. It consists mainly of two types of protein fibre: collagen which forms the main constituent of the dermis and elastin which makes up a small proportion of the bulk. Hair follicles and sweat glands originate in the dermis and open onto the surface of the epidermis[24]. Nerve endings, blood and lymph vessels also pass through the dermis. Radiation with wavelengths longer than 350 nm (UVA) penetrates into the living dermis where the prolonged exposure damages the collagen and elastic fibres leading to premature aging, wrinkling and skin cancer.

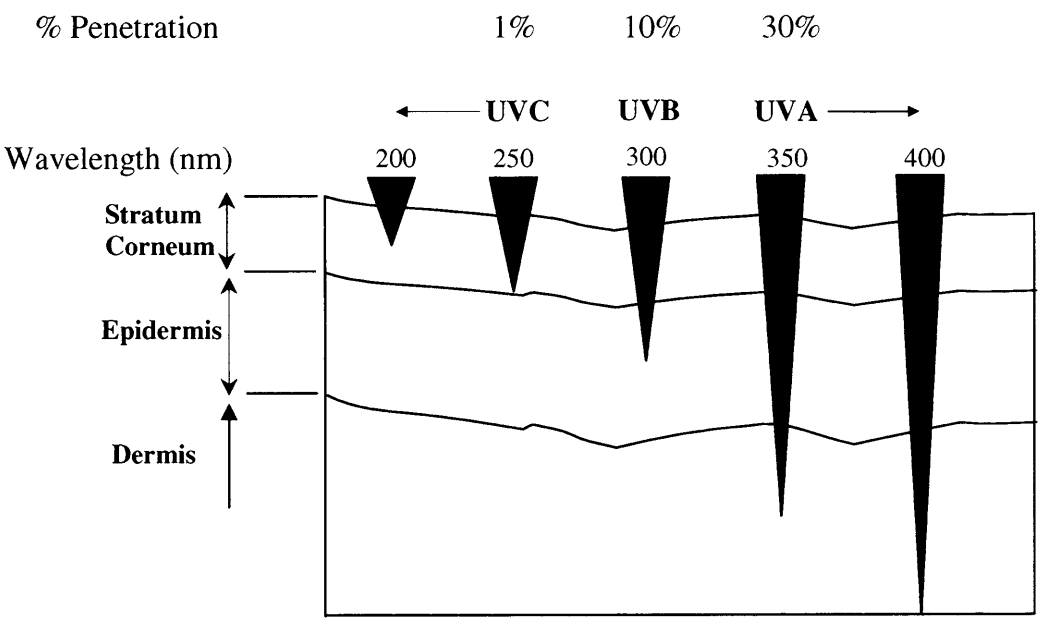

Figure 1.3: Schematic representation of the penetration depth of ultra-violet radiation through the skin[25]

1.2.1 Skin Cancer and Ultraviolet Radiation

Sunburn represents the visible damage caused by UV rays, however the unseen damage done to the keratinocytes is that which leads to cancer. DNA is made up of four bases: adenine (A), thymine (T), guanine (G) and cytosine (C), which are always paired up the same way with A and T paired, and C and G paired. UVB and UVC directly damages DNA by breaking the chemical bond that joins the cytosine and guanine bases and creates a new bond between two cytosine bases[26].

This mutation of the keratinocyte's genetic code leads to permanent damage of the DNA and is known as a thymine dimmer[26]. Thymine dimmers are caused only by UVB light. Genes contain the information for cells to make proteins and if a gene is mutated, then there will be an error in the making of that protein. If that particular protein is being overproduced and involved in controlling cell division, it can lead to cancer. There is one gene in particular which is often damaged by UVB radiation and this is the p53 tumour suppressor gene. As its name implies, it is involved in suppressing cell division. More than 90% of certain types of skin cancer show mutated p53 genes that are of the thymine type, linking UVB as the cause[26]. When these cancerous cells leave the epidermis and spread to other organs in the body, they then multiply rapidly causing organ failure and consequently, death.

Ultraviolet radiation (UVA and UVB) can also indirectly cause cancer by producing reactive oxygen species (ROS) that can lead to chromosomal damage. ROS have high chemical reactivity and can damage lipids, proteins and DNA resulting in cell death[19].

Tumours such as warts, moles (or nevi), seborrhetic keratosis, keratoacanthoma and premalignant actinic keratosis are benign (does not invade and destroy the surrounding tissue). These tumours are not fatal and sometimes regress over time[27]. Tumours that are malignant means that they grow rapidly and are metastatic i.e. spreads to other parts of the body via the lymph system or through the blood. Malignant disorders include basal cell carcinoma, squamous cell carcinoma and malignant melanoma[26].

1.2.2 Types of Skin Cancer

1.2.2.1 Basal Cell Carcinoma (BCC)

This is the most frequent type of skin cancer with yearly incidences in the US, UK and Europe at approximately 900 000, 50 000 and 300 000 people respectively[14]. The estimated lifetime risk of BCC in the white European population is 33-39% in men and 23-28% in women. BCCs come from changed cells of the innermost (basal) layer deep in the epidermis. This slow growing cancer rarely metastasises (5 out of every 10 000 cases) and can occur on any sun-exposed or sunburnt area but is most evident on the face and neck[28].

1.2.2.2 Squamous Cell Carcinoma (SCC)

Incidence rates of SCC have also steadily risen over the past 30 years. The number of annual cases in USA is 105 per 100 000 with 2 500 people dying from SCC each year[14]. SCCs are altered, flattened (squamous) cells in the outer layers of the epidermis. Squamous is a term that indicates a surface which is scaly in nature. This cancer often occurs in sun-exposed or sunburnt areas such as the head and neck, forearms, back of

the hands, upper part of the torso and lower legs where both the skin and mucous membranes can be affected[29].

BCCs and SCCs are known as Non Melanoma Skin Cancer (NMSC). The incidence of NMSC follows a pattern of increased risk with cumulative ultraviolet radiation exposure. These cancers can be removed with simple surgeries if detected early as they grow quite slowly. However, if neglected these type of tumours can invade larger parts of the skin and may cause greater health concerns.

1.2.2.3 Cutaneous Malignant Melanoma (CMM)

Melanoma is the least common but most serious form of skin cancer and it is more likely to progress rapidly than NMSC[17]. In the US, it has been currently approximated that an individual's lifetime risk of having malignant melanoma is 1 in 75 however; this is estimated to increase to 1 in 50 by 2010. The incidence of melanoma is increasing faster than the incidence of cancer at any other leading site for men and is only second to lung cancer in women[13]. During the last 40 years, melanoma has tripled in the white American population with approximately 51 400 people developing the deadly disease in 2001. In the UK, melanomas are not as prevalent with 7000 cases reported annually. Many of the patients are older adults however, unlike other types of cancer, a large number of cases also occur in young adults.

The main risk factor involved with the cause of melanomas is exposure to the sun or more precisely, the ultraviolet portion of sunlight. The exact wavelength of light responsible for the induction of CMM in humans is still unknown. A study on cross hybrids of the fish model (*Xiphophorous*) showed that the action spectrum for the

induction of melanoma was active at 365, 405 and 436 nm[17]. This suggests that wavelengths which are not directly absorbed by DNA maybe responsible for malignant melanomas. The authors concluded that in natural sunlight, 90-95% of melanomas are caused by wavelengths of light > 320 nm i.e. UVA and the visible spectrum.

CMM originates in the pigment producing cells, melanocytes and is extremely invasive and metastatic. CMM are changed melanocytes that sit in among the basal cells in the epidermis or top layer of the skin and can occur anywhere on the body. It is estimated that 50-70% of malignant melanomas start spontaneously whilst the remainder begin from pre-existing moles[30]. In men, it is most common on the trunk and in women, it is usually found on the back of the legs. This type of cancer does not show increased risk with cumulative UVR exposure like NMSC but rather it is the history of severe sunburn especially during an early age that can increase the risk of CMM[30]. If melanoma is found in its early stages, it can be cured however if detected late, can kill due to the compromised vital functions of organs such as the brain, liver or lung. At present, there is no effective chemotherapy for extensive malignant melanoma.

1.3 EPIDEMIOLOGICAL EVIDENCE

Many researchers and dermatologists have already dismissed the idea that there could be an association between the components of sunscreens and melanoma[31,32,33], despite the fact that an equal number of the epidemiological studies have found contradictory results[34,35,36]. So far, there has been no direct evidence for sunscreen use reducing the risk for malignant melanoma. Other suggestions have been made that may account for

the observed relationship between sunscreen use and melanoma. These include host and behavioural factors such as sun-sensitivity and increased recreational sun exposure by patients who use sunscreen. The main disadvantage of epidemiological types of studies is that they are all exposed to bias especially in memory recall and some important details such as the Sun Protection Factor or SPF of the sunscreens used is unknown. Many of these case control studies used hospital registries rather than population derived databases, which is considered selection bias, as dermatological patients are not representative of the general population.

1.3.1 Other Epidemiological Evidence

Autier et al[37] reported a significant association between the duration of sun exposure and SPF of the sunscreen used (SPF 30 vs. 10). The researchers concluded that the use of sunscreens with high SPF seemed to increase the duration of sun exposure time. They therefore proposed using nevi (mole) counts to predict both melanoma and non-melanoma skin cancer risks. They found contradictory results. Autier et al[38] reported that children using sunscreens had higher nevus count. A randomised controlled trial by Gallagher *et al*[39] showed that the number of nevi decreased in children regularly using sunscreens.

1.3.2 Randomised Trials

The ideal study to confirm that sunscreen use can prevent melanoma in humans is the randomised controlled trial. A sunscreen trial would entail randomising many thousands of individuals early in life and follow them for a long period, ensuring there

is a measurable difference in sunscreen usage between the subjects in the intervention and the control groups. However, a randomised trial of the efficacy of sunscreen use versus non-sunscreen use would create an ethical dilemma.

There have been no randomised trials conducted which address the efficacy of sunscreens in the prevention of melanoma. There are other problems in a sunscreen trial such as the rarity of melanoma even amongst high incidence populations, the long induction period and the unknown relevant time of sun exposure.

There is no conclusive evidence for the association of sunscreen use and protection against melanoma. This is expected as the induction period for melanoma is two decades or more and high SPF sunscreens have only become popular in the 1980s and broad-spectrum sunscreens (i.e. sunscreens which protect against both UVA and UVB) in even less time. The ability of epidemiological methods to determine sunscreen effects is also severely hindered by the difficulty in controlling for confounding factors.

It seems that in order to prove the effectiveness of sunscreens via epidemiological studies, these researchers will have to wait for a couple of decades when a considerable number of people would have been using broad-spectrum suncreams. Hence, more scientific methods must be proposed in order to determine if there is a link between melanoma and sunscreen use.

1.4 SUNSCREENS

Sunscreens were first commercialised in the 1920s in America and later in the 1930s in Europe[40]. Its primary goal was the prevention of sunburn in human skin. These lotions, creams, sprays or gels provide a mechanism for protection against the damaging effects of solar radiation with many of the active ingredients absorbing, reflecting or scattering the wavelengths of light in the 290–400 nm region.

Suncare products are regulated differently around the world: in Europe, Japan and South Africa, they are considered cosmetics whereas in Australia, New Zealand and USA, they are classed as Over The Counter drugs (OTC). Their efficacy is measured by the Sunburn Protection Factor or SPF, which is a universal indicator of the product's effectiveness against one specific parameter, sunburn or erythema[11].

$$\text{SPF} = \frac{\text{Time for protected skin to reach erythema}}{\text{Time for unprotected skin to reach erythema}}$$

As sunburn is mainly caused by UVB, the SPF value only gives the consumer an idea of the amount of protection that the sunscreen has against UVB radiation. There is yet no standard indicator for a sunscreen's proficiency against UVA radiation because it was only within the last decade that researchers[18] realised that the UVA portion of sunlight was possibly detrimental to human health.

Sunscreens are also being marketed as methods for preventing skin cancer, however there are no conclusive studies that show a decrease in the incidence of skin cancer in sunscreen users. Researchers[41] at the Queensland Institute for Medical Research in

Brisbane, Australia carried out a study following 1,383 adults for 5 years and in September 1999 reported that sunscreen use reduces the risk of developing squamous cell carcinoma by 40% but did not reduce the risk of developing melanoma or basal cell carcinoma. The International Agency for Research on Cancer (IRAC) acknowledges this study by saying in their report that there is 'inadequate evidence in humans for a cancer preventative effect of topical use of sunscreen formulations against cutaneous malignant melanoma and basal cell carcinoma[40].

It has been reported from both laboratory and epidemiological studies that sunscreens may not block the initiation or promotion of melanoma formation and also that the action spectrum for the formation of erythema (sunburn) is different to that of melanoma. The action spectrum for SCC, based on the rodent model is similar to the action spectrum for sunburn in humans i.e. UVB[42,43]. The action spectrum for melanoma is unknown, but as previously mentioned, UVA is thought to play a significant role as it has been observed in animal experiments[44,45]

Most sunscreens today contain one or both types of the following compounds:

1) *Chemical Agents* - organic chemical compounds that absorb the UV light.

2) *Physical Agents* - opaque materials that reflect and scatter light (inorganic oxides).

1.4.1 Organic Sunscreens

Chemical agents are further divided into UVA and UVB absorbers as there are no available broad spectrum organics which can protect against the whole ultraviolet spectrum (λ 290 – 400 nm). Most organic sunscreens are aromatic compounds conjugated with a carbonyl group with an electron-releasing amine or methoxy group situated in the *ortho-* or *para-* position. These alternating single and double bonds, act as filters by absorbing the high-energy UV rays causing the electronic structure to move up to a higher energy state. Most of the energy is then dissipated and converted to lower energy wave radiation (>380 nm), which is re-emitted harmlessly as heat[46]. However, some UV absorbers have the ability to induce chemical photosensitization, leading to structural changes such as producing non-absorbing isomers. This could cause allergic reactions and would also make the UV filters ineffective[47]. These chemical changes could also generate reactive oxygen species e.g. hydroxyl radicals and singlet oxygen. Such radicals can be extremely harmful, having the potential to react with all the components of skin causing mutations and apoptosis or cell suicide.

Many of the organic ingredients used in the past and some still used in current sunscreens have two main problems: contact irritation/allergy and photochemical instability. PABA or para-aminobenzoic acid and its derivatives are compounds which are known to cause such problems, but they also exhibit more serious side-effects. Knowland[7] showed that these organics break down in the presence of sunlight and can produce DNA strand breaks. Other UVB filters which have been proven to be similarly hazardous are 2-phenylbenzimidazole-5-sulfonic acid (PBSA) and 2-phenylbenzimidazole (PBI)[48]. Of the UVA absorbers, benzophenone is a powerful free

radical initiator and in a recent study, has been found to penetrate the body as it was discovered in urine samples[10]. Earlier research by Maibach[49], warned that up to 35% of sunscreen applied topically can pass through the skin and into the bloodstream. Avobenzone (butyl-methyloxydibenzolmethane) is another UVA absorber that is easily absorbed through the epidermis and in the present of sunlight, photodegrades, becoming ineffective within one hour[9]. Despite this, it is still used in 90% of sunscreen formulations worldwide.

Physical Sunscreens

The main types of physical blockers are titanium dioxide and zinc oxide. Inorganic sunscreens can reflect, scatter and absorb solar radiation because they are mainly semiconductors which have small bandgaps and high refractive indices. Other examples of physical sunscreen components are iron oxides, barium sulfate, magnesium oxide and talcum powder[11]. Powders of TiO_2 and ZnO appear white when exposed to sunlight because these materials do not absorb visible light. The particles instead reflect the incident visible light with minimal absorption. At 360 nm, 90% of the UV attenuation by titanium dioxide is by scattering[11]. This whitening effect of physical sunscreens has made them cosmetically unacceptable even though they provide a broader spectrum of protection against UV exposure.

Thus to overcome this problem, the pigment industry has developed micronized or ultra-fine powders which are 'transparent' when applied onto skin. They are cosmetically more acceptable and are now widely used in the sunscreen industry. This change in the optical properties of the powders is obtained only by reducing their mean particle size whereas the chemical structure of the base material remains the same.

Smaller crystals are generally poorer light scatterers than larger crystals since the scattering efficiency is proportional to d^6 in a relation known as Raleigh's scattering law[50]. Hence, the powders appear less white. Raleigh scattering is the scattering of light by particles much smaller than the wavelength of light. The intensity of light *I*, scattered by a single particle from a beam of light with intensity I_0 and wavelength, λ is given by the relation[51]:

$$I = I_0 \frac{(1 + \cos^2\theta)}{2R^2} \left(\frac{2\pi}{\lambda}\right)^4 \left(\frac{n^2-1}{n^2+2}\right)^2 \left(\frac{d}{2}\right)^6$$

where *R* is the distance to the particle; θ is the scattering angle; *n* is the refractive index of the particle and *d* is the diameter of the particle.

These microfine powders were first introduced to replace the organic UV filters but were found to have a synergistic effect when properly formulated in conjunction with these UV absorbing chemicals.

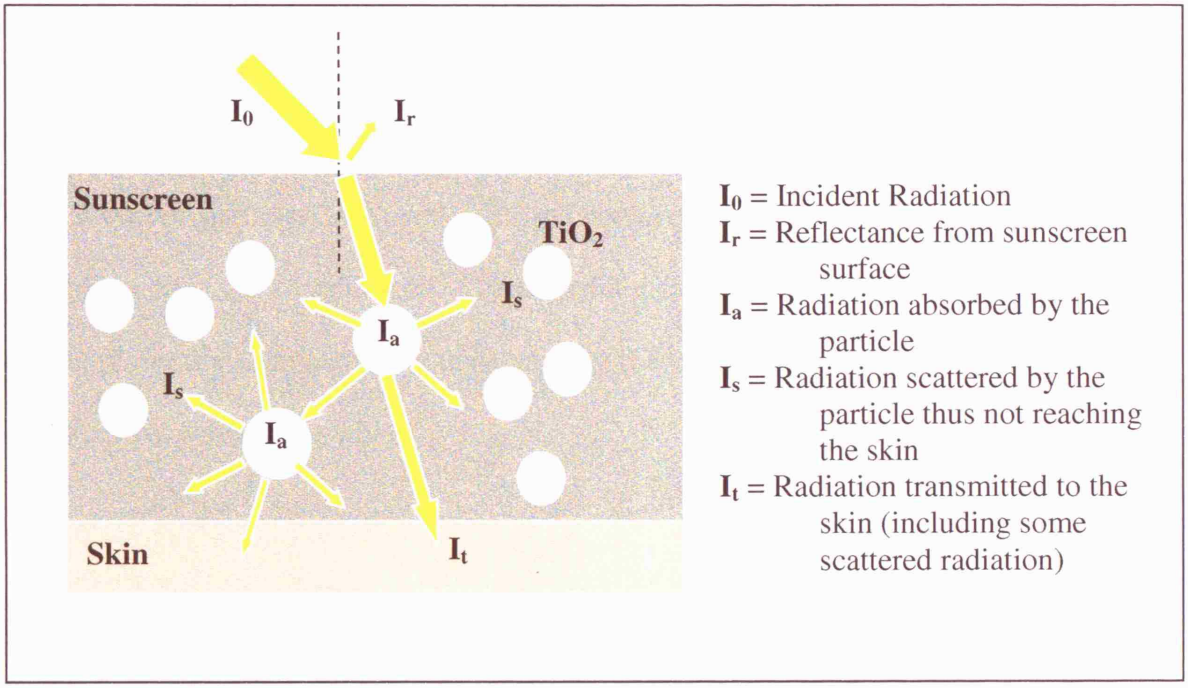

Figure 1.4: Schematic of attenuation process by physical sunscreens on skin[11]

Micronized is a term currently used to describe particle sizes anywhere from 4 nm to several microns but is most commonly used to describe a definite particle size which is distinguishable from the pigmentary grades which have an average diameter of 250 nm[11]. The extent of UV protection offered by the inorganic components of sunscreens depends upon the size of these particles, with smaller particles providing more UVB and less UVA protection. This is because a smaller particle shifts the absorption edge of the substance to the blue region i.e. to higher energies.

Micronized zinc oxide of particle size 40-100 nm is transparent on the skin compared to the larger particles (200-400 nm) that produce an opaque colour. Micronized titanium dioxide (20-100 nm compared with 250-300 nm for the non-micronized forms) attenuates UVB and UVA II (320-340 nm) however it is less effective than ZnO in attenuating UVA I (> 340 nm)[11]. Hence, TiO_2 is mainly a UVB absorber but a UVA

scatterer. Due to its higher refractive index in visible light, TiO_2 (2.6) appears whiter than ZnO (1.9). Therefore, the micronized form of titanium dioxide has to be smaller in size than ZnO in order to obtain the same amount of transparency. Optimal dispersion of micronized particles in a sunscreen is necessary as they can form agglomerates, which increases the particle size. The material then reverts to its original pigmentary optical properties, losing efficacy in attenuating the UV and increasing interaction in the visible thereby appearing white.

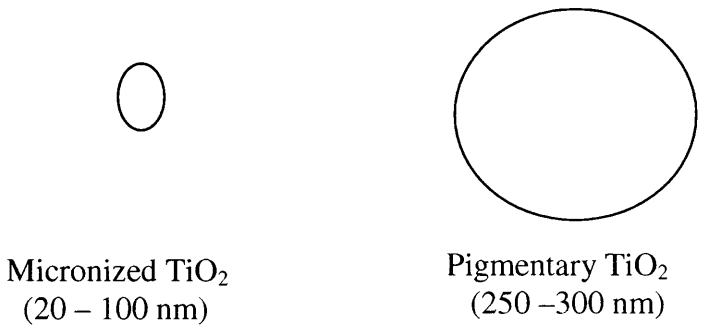

Figure 1.5: Relative sizes[11] of UV attenuating and pigmentary grades of titanium dioxide.

Fine powders have a tendency to agglomerate and several surface methods have been developed to prevent agglomeration, in particular, surface coatings. Surface coating allows the inorganic particles such as titanium dioxide and zinc oxide to co-exist in a more stable suspension.

1.4.2.1 Surface Coatings

Surface treatments of titanium dioxide or zinc oxide can be with inorganic oxides (silica, alumina, zirconium, tin and zinc), silicones, or organic fatty acids and organosilanes. The coatings can be physically precipitated or chemically adsorbed onto the particle. Physical coatings sit on the surface and are held together by electrostatic

forces, lyphobic interaction or hydrogen bonding, depending on the surface chemistry of the material. However, the adsorbate can easily be displaced by another molecule, which has a stronger affinity for the particle surface, or by severe thermal and mechanical agitation[11].

Chemically grafted coatings are more resilient and can only be removed by chemical means and extreme mechanical agitation. Another type of treatment is encapsulation where the particle is completely surrounded by a matrix such as waxes and synthetic or natural macromolecules. Encapsulation is carried out to protect the underlying material (if it is toxic or hazardous) from its surrounding or vice versa. This method however can change the performance characteristics of the material[11]. These surface treatments have another priority, which, for some of the inorganic substances such as titanium dioxide, is the most important of all: it can supposedly hide unwanted properties of the particle such as photocatalytic activity.

1.4.2.2 Doping

Incorporating a particular ion into the titanium dioxide lattice can either enhance or reduce the photo-generation of free radicals. These ions are usually transition metals and depending upon their position in the titanium dioxide lattice, they can act as recombination centres or charge separators. As recombination centres, the lifetime of the charge carriers and therefore photocatalytic efficiency are decreased and for charge separators there is an enhanced photocatalytic efficiency due to increased lifetimes of the e^-/h^+ pairs. Manganese ions have recently been doped into rutile lattices[52] in order to prohibit the generation of reactive oxygen species (Figure 1.6) and therefore can be

used as a UV scatterer in sunscreens but without the harmful side effects of free radical damage.

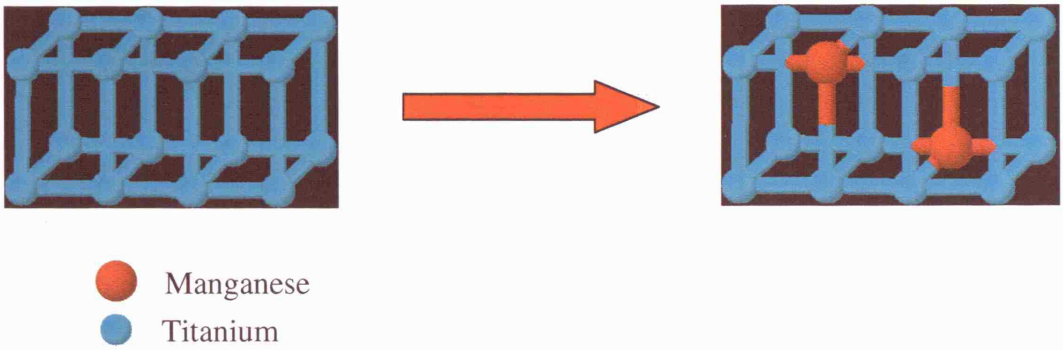

Figure 1.6: Diagrammatic representation of doping showing integrated manganese ions in a titanium dioxide lattice.

In order to inhibit free radical production, the transition metal ion would have to lie in the middle of the band-gap where the charges would remain localised to the dopant ion[53]. If the ion was to lie close to the valence or conduction band, then the charges could be thermally promoted to the energy bands and produce free radicals via surface redox reactions (Figure1.7).

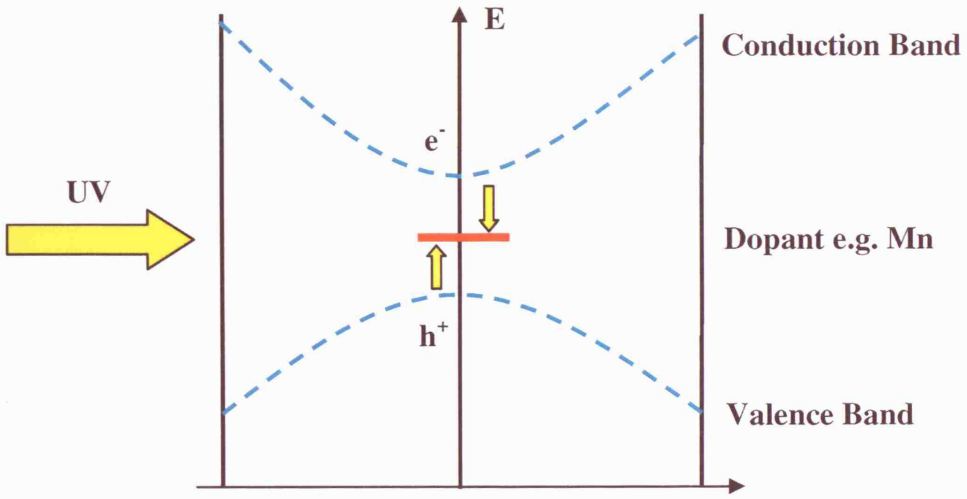

Figure 1.7: Schematic band structure of dopant ion in relation to the conduction and valence energy bands.

1.5 TITANIUM DIOXIDE

1.5.1. Photocatalytic Activity of Titanium Dioxide

Titanium dioxide exists in three major forms: anatase, rutile and brookite, the latter being quite rare. The band-gaps for rutile and anatase are 3.06 eV and 3.23 eV, which correspond to UV wavelengths of 405 nm and 385 nm, respectively[54]. When the titanium dioxide semiconductor is irradiated by UV light with energy greater than or equal to its band-gap, an electron is excited from the valence band into the conduction band, leaving a positively charged 'hole' in the valence band[54]. Photons of less than 405 nm i.e. ultra band gap energy are found to activate rutile titanium dioxide and cause this electron transference thus resulting in an electron-hole pair. Both the photogenerated hole and electron migrate to the surface of the semiconductor, where they recombine and lose the input energy as heat or they participate in redox reactions with adsorbed species. Titanium dioxide acts as a photosensitiser, where the valence

band holes are powerful oxidants and the conduction band electrons are good reductants. In order to achieve high productivity, the electron transfer must be fast and recombination of the photoexcited e^- - h^+ pairs must be reduced[55].

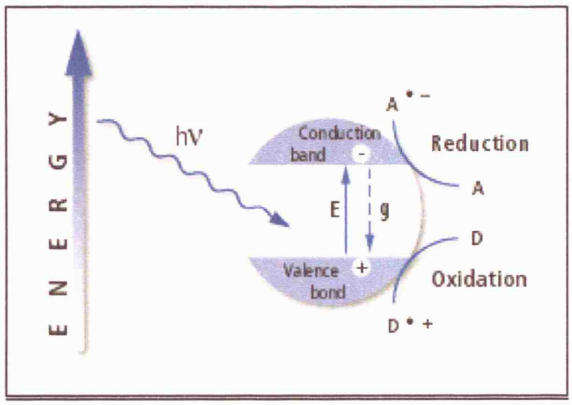

Figure 1.8: Simplified diagram showing the processes when TiO_2 particle receives bandgap illumination[56]

The following reactions indicate the processes that can occur during UV irradiation of titanium dioxide.

- Photogenerated electron and hole produced upon excitation of titanium dioxide with UV light.

$$TiO_2 + h\nu \rightarrow e^- + h^+ \quad (1)$$

- The charge carriers recombine and generate thermal energy.

$$e^- + h^+ \rightarrow heat \quad (2)$$

- A photogenerated electron can be trapped onto a surface site.

$$e^- \rightarrow e^-_{surf} \quad (3)$$

- Adsorbed oxygen is reduced to the superoxide anion by a trapped electron.

$$O_2 + e^-_{surf} \rightarrow O_2^{\bullet -} \quad (4)$$

- A photogenerated hole is trapped on the surface or subsurface of the lattice.

$$h^+ \rightarrow h_{sub\text{-}surf} \quad (5)$$

- A hole can oxidise any adsorbed species, **S**.

$$h^+ + S \rightarrow {}^{\bullet}S^+ \quad (6)$$

- A surface hydroxide anion reacts with a hole to produce a surface hydroxyl radical.

$$h^+ + Ti-OH^-_{surf} \rightarrow Ti-{}^{\bullet}OH_{surf} \quad (7)$$

- The hydroxyl radical oxidises the adsorbed molecule, **S**.

$$Ti-{}^{\bullet}OH_{surf} + S + H_2O \rightarrow Ti-OH^-_{surf} + {}^{\bullet}S-OH + H^+ \quad (8)$$

- The trapped electron reduces the hydroxyl radical to a surface hydroxide anion.

$$e^-_{surf} + Ti-{}^{\bullet}OH_{surf} \rightarrow Ti-OH^-_{surf} + heat \quad (9)$$

In reactions (6) and (8), **S** is an adsorbed molecule in air-saturated aqueous environment which can undergo oxidation reactions. The use of inorganic coatings on the titanium dioxide particle relies on the inhibition of reactions (3), (5) or (7) and/or the enhancement of reactions (2) and (9)[57].

Researchers have proven that firstly powders and then thin films of anatase titanium dioxide will photodegrade a wide range of organic and inorganic chemicals in air and water, leading to applications such as water disinfection; waste treatment and air purification[3,58,59]. Other uses have included the elimination of micro-organisms such as bacteria, viruses, cancer cells and the reduction of trace heavy metals in industrial waste streams[60,61,62,63].

Therefore, in order to prevent photodegradation of its environment, titanium dioxide is coated with inorganic materials. However, research by Picatonotto *et al*[57] showed that although TiO_2 particles coated with alumina, Al_2O_3, reduced the degradation rate of phenol, it was totally ineffective against preventing the destruction of salicylic acid.

Unlike the organic chemical agents, the inorganic compounds such as titanium dioxide and zinc oxide have extremely low solubilities in the sunscreen vehicle and are said to remain as a layer on top of the skin, rather than be absorbed.

1.5.2 Penetration of Titanium Dioxide into the Skin

There have been many studies on whether the microfine particles penetrate into the skin or remain as a totally separate layer on top of the skin. Tan *et al*[64] researched the percutaneous absorption of microfine titanium dioxide on subjects who had daily application of a sunscreen containing 8% micronized TiO_2 for several weeks. The tape stripping method was used to remove the stratum corneum (horny layer), which is 15-20 μm thick and controls absorption[65]. Inductive plasma spectroscopy determined the titanium concentration in the epidermis and dermis and found that the concentration of TiO_2 was higher in the dermis of subjects than in the controls.

Other researchers[66,67] who have also studied penetration depths of ultra-fine titanium dioxide on human skin have found that the particles stay on the uppermost surface of the stratum corneum and could not be detected in deeper stratum corneum layers, epidermis and dermis. However, both of these studies failed to take into account possible penetration through the hair follicles, sebaceous glands and sweat glands.

Lademann *et al*[68] investigated the penetration of micronized titanium dioxide particles inside and outside of the hair follicles, using the tape stripping method, histology, X-ray fluorescence and laser scanning microscopy. They found the majority of microparticles to be located on the corneocytes, in the upper part of the stratum corneum and the pilosebaceous orifices, with this number obviously decreasing with increasing depth of the stratum corneum. Some titanium dioxide microparticles were still detected in single hair follicles, including their deeper parts.

Penetration through the stratum corneum is dependent upon molecular size. The average width of the intercellular space is approximately 100 nm. The aqueous gap between the lamellar bilayers that occupy the intercellular space measures only 0.5-1.0 nm. However, these gaps can enlarge when filled with topically applied materials, allowing penetration of 10-50 nm particles of materials such as micronized titanium dioxide[64].

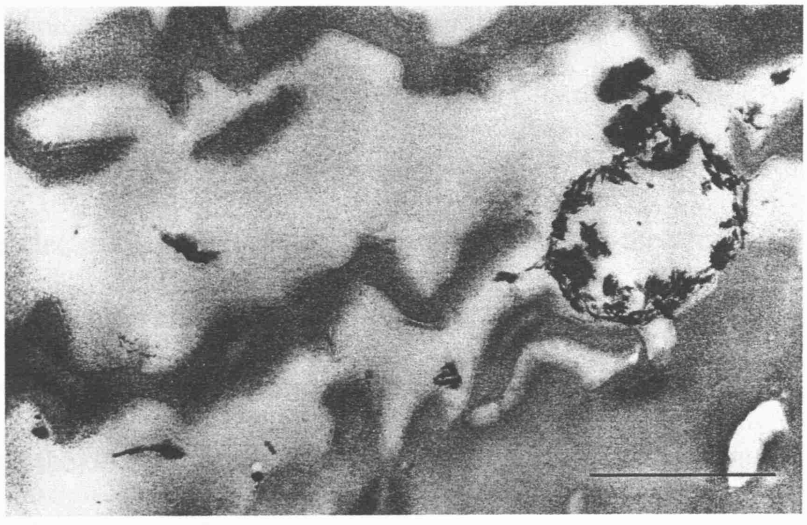

Figure 1.9: TEM showing a titanium dioxide micronized particle penetrated into the widened intercellular spaces of the horny layer of the skin[69]. (scale bar = 1 μm)

Van der Molen *et al*[69] looked at the influence of different morphologies of titanium dioxide particles (platelet and spherical) on the integrity of the stratum corneum barrier (intercellular lipids and desmosomes) under UVB irradiation (280-320 nm). They found that application of the platelet titanium dioxide onto human skin for 60 minutes of UVB irradiation, severely affected the intracellular spaces of the stratum corneum with the lipid layers transformed from smooth planes to rough, irregular structures. In addition, desmosomes were not detected, indicating they may have been destroyed. Hence, these particles managed to penetrate into the deeper layers of the epidermis and seriously damage cells. A more recent study has shown titanium dioxide particles have the ability to penetrate through the stratum corneum and into the living stratum granulosum via intercellular space[70].

1.5.3 Rutile vs. Anatase

The preferred form of titanium dioxide used in sunscreens is rutile because it generally has a lower photocatalytic activity than anatase[2]. This could possibly be explained by the Ti – O – Ti interatomic distances in the crystal lattice of rutile, which are much shorter than in anatase thus giving rise to stronger bonds[71]. Due to the smaller bandgap of rutile, the electron-hole recombination rate is faster and the amounts of hydroxides and reactants attached to the surface are much less than in anatase. In some cases, rutile has been found to be more photocatalytically active than anatase[72,73,74]. Mills *et al*[55] suggested that the difference in photoactivity could be due to the manufacturing process which determines the surface area and porosity of the powders rather than the crystalline phase itself.

Despite the well-known photocatalytic activity properties of the anatase and rutile crystal forms, titanium dioxide is still used in sunscreens.

1.5.4 Nanoparticular Size

Nanometer sized inorganic particles such as those used in sunscreens have different physical and chemical properties compared to their bulk materials. Their photocatalytic activity is enhanced not only by the increased surface area but also because of the change in surface properties such as surface defects. Research by Anpo *et al*[75], investigated the photocatalytic hydrogenation of $CH_3C{\equiv}CH$ with H_2O on rutile- and anatase-type titanium dioxide catalysts having various particle sizes. They found that the quantum yields for this reaction significantly increased with decreasing particle size. Particles 40 nm in diameter were three times more active than those 120 nm in diameter.

1.6 FREE RADICALS

As seen previously in the photocatalytic reactions of titanium dioxide (Section 1.5.1), various free radicals are formed upon irradiation with ultra-violet light. Studies have shown hydroxyl radicals[76,77] superoxide anion radicals or protonated perhydroxyl radicals and singlet oxygen[78,79] produced via UV irradiation of titanium dioxide. However, it is still uncertain as to which radicals are exactly generated and under what conditions. More research and better experimental design is needed in this area.

Free radicals are extremely reactive species, containing one or more unpaired electrons. The hydroxyl radical is a particularly strong oxidising species that can react with any

biological molecule. Singlet oxygen ($^1O_2$) is an electronically excited form of molecular oxygen ($^3O_2$) and has a relatively long half-life compared to $^{\bullet}OH$. It is thought to be able to diffuse appreciable distances before reacting with and damaging lipids, amino acids and DNA[19].

Studies[80] with amino acids and nucleic acids have shown that irradiation of titanium dioxide with UVA light catalyses the degradation of these molecules. Dunford researched micronized titanium dioxide samples extracted from over-the-counter sunscreens and found that all the samples catalysed the photo-oxidation of a phenol[12]. They also found that the hydroxyl radicals produced by titanium dioxide under simulated sunlight irradiation inflicted direct DNA strand breaks in vitro and in cultured human fibroblasts. The damage was however suppressed by DMSO and mannitol, suggesting that the hazardous $^{\bullet}OH$ radicals were involved.

1.7 RESEARCH AIMS

Previous research has shown titanium dioxide, under irradiation by sunlight, produces reactive oxygen species which can cause lipid peroxidation and chronic cutaneous damage[80]. Despite this, titanium dioxide is still used in a number of cosmetic products including sunscreens. This is probably because the hazardous effects of titanium dioxide are thought to be inhibited by the modifications (coating and doping) used on the inorganic particles. What is currently unknown is what crystal form of titanium dioxide along with the type of coating/modification is used in commercial sunscreens and whether it is damaging or protecting to cells. This research addresses this problem and found that not all forms/modifications of titanium dioxide are protective and 50% of

the tested titanium dioxide samples isolated from sunscreens damaged human and animal cell lines.

The next section, Chapter 2 describes the experimental chemical methods, materials and techniques used for the characterisation and photocatalytic testing of the different powders. Chapter 3 details the analysis results from the various techniques (SEM, TEM, XRD, XPS, SSNMR, BET surface area) used to characterise the physical properties such as particle size, crystal form and specific coatings/doping ions of the titanium dioxide powders. Chapter 4 entails the novel method of determining the free radical species formed during irradiation of the modified titanium dioxide particles via solid state Electron Paramagnetic Resonance. The photocatalytic efficiencies of the different powders were tested by the photodegradation of methylene blue dye and are detailed in Chapter 5. Chapter 6 describes the biological experimentation including cell culture and gives background information on the biological techniques used in these experiments. Chapter 7 sets out to prove whether these UVA irradiated titanium dioxide particles are protective or damaging to cells by using an apoptosis assay and a DNA damage assay. Chapter 8 gives the conclusions and overview of this work correlating both the chemical and biological studies.

Chapter 2 – Chemical Experimental

This chapter describes the materials, methods and different techniques used to characterise the titanium dioxide and zinc oxide powders together with their coatings. The photocatalytic degradation of methylene blue dye was used to determine the photocatalytic abilities of the inorganic powders and is also detailed in this chapter.

2.1 MATERIALS

Two types of powders were used in these experiments. The first type of samples was obtained directly from suppliers who provide the sunscreen manufacturers with the titanium dioxide powders. These types of powders shall be referred to as 'pure' as they are unadulterated and were not subjected (unless specified) to a solvent wash procedure. The second type of powder was solvent extracted from store-bought sunscreen bottles. The titanium dioxide and zinc oxide powders tested in this work are all used in sunscreens (except for Degussa P25). Due to legal reasons, the names of the sunscreens could not be revealed therefore a codification was used for the different powders.

Pure Titanium Dioxide powders:

Degussa P25 (Degussa) **S1**; **S3**; **S10**; **S12**

***Commercial (store-bought) Sunscreens with Titanium dioxide*:**

S2; **S4**; **S5**; **S6**; **S7**; **S8**; **S9**; **S11**

Table 2.0: Summary of Titanium Dioxide powders with codes used in the following chapters.

Sample	Crystal Form	Possible coating	Future Code of Identification
S1	85% Anatase 15% Rutile	None (known)	A&R+no coat
S2	90% Anatase 10% Rutile	Organosilane/ Silicone Polymer	A&R+Si coat
S3	85% Anatase 15% Rutile	Organosilane/ Silicone Polymer (known)	A&R+Si coat
S4	85% Anatase 15% Rutile	Silicone Polymer	A&R+Si coat
S5	75% Anatase 25% Rutile	Organosilane/ Silicone Polymer	A&R+Si coat
S6	100% Rutile	Silica Aluminium Oxide	R+Al+Si coat
S7	100% Rutile	Silicone polymer Aluminium Oxide	R+Al+Si coat
S8	100% Rutile	Silica Aluminium Oxide	R+Al+Si coat
S9	100% Rutile	Aluminium Hydroxide	R+Al coat
S10	100% Rutile	Aluminium Oxide (known)	R+Al coat
S11	100% Rutile	Aluminium Hydroxide	R+Al coat
S12	100% Rutile	Manganese oxide (known)	R+Mn doped

The known coatings are from manufacturer's data sheet.

Table 2.1: Summary of zinc oxide and mixed titanium dioxide/zinc oxide powders with codes used in the following chapters.

Sample	Crystal Form	Possible Coating	Future Code of Identification
a	Zincite & Rutile	None	Zn&R+ no coat
b	Zincite & Rutile	Aluminium Oxide	Zn&R + Al coat
c	Zincite & Rutile	Aluminium Oxide	Zn&R + Al coat
d	Zincite	None (known)	Zn + no coat
e	Zincite	Dimethicone (known)	Zn + Si coat
f	Zincite	Dimethicone (known)	Zn + Si coat

The known coatings are from manufacturer's data sheet.

***Pure Zinc Oxide powders*:**

Samples -**d**, -**f.**

***Commercial Sunscreens with mixed Titanium dioxide/Zinc Oxide powders*:**

Samples -**a**, -**b**, -**c**.

Commercial Sunscreens with ZnO powders:

Sample -**e**.

Chemicals: Acetone (Anal Grade); Chloroform; Hexane; Isopropanol; Methylene blue (98% purity) (Aldrich)

2.2 SAMPLE PREPARATION: EXTRACTION AND PURIFICATION

The inorganic powders had to be separated from the sunscreen emulsions for analysis. This was done using a washing procedure.

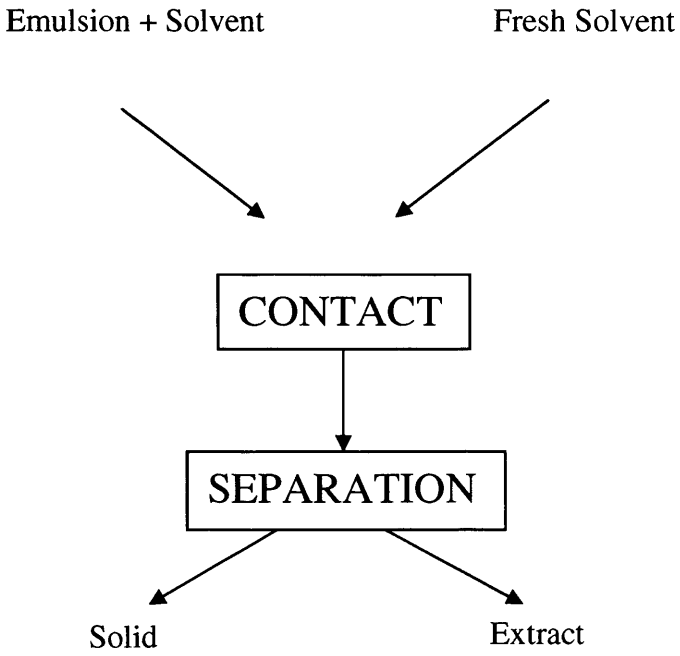

Scheme 2.1: Washing procedure used to retrieve titanium dioxide powders from sunscreen emulsions.

The appropriate solvent was added to 30 cm^3 of the sunscreen emulsion in a 50 cm^3 centrifuge tube. The tube was shaken vigorously by hand then sonicated for 15 minutes. The mixture was centrifuged at 3000 rpm for 5 minutes to separate the two layers (solid titania at the bottom). The distinct top layer was then decanted and discarded. This procedure was repeated until no further visible changes were noticed.

A range of solvents was used from polar to non-polar varieties. Acetone was used because of its miscibility with water and it usually removed the majority of the initial volume.

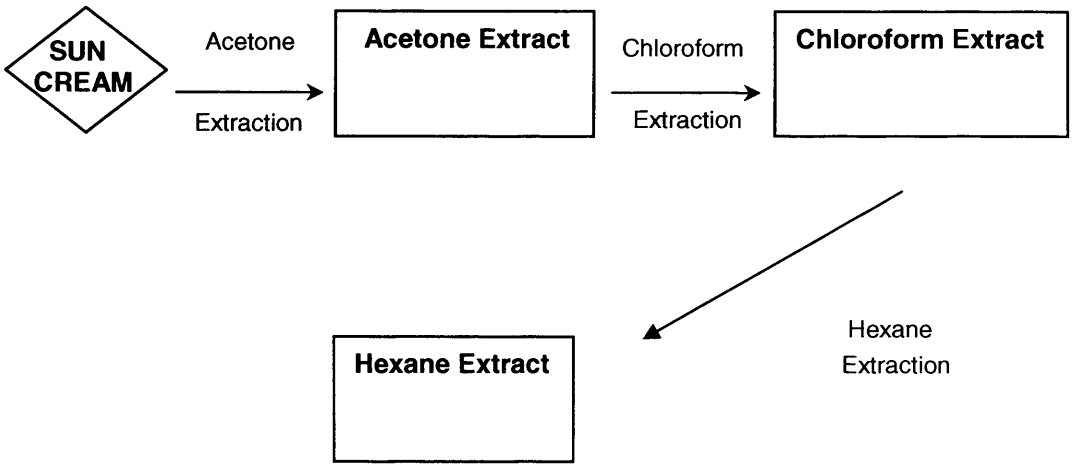

Scheme 2.2: Solvents used in extraction procedure.

Chloroform was used next to remove most of the organic compounds and finally n-hexane, a non-polar solvent, was used in the final step.

The majority of the organic compounds found in sunscreens are cyclic and conjugated indicating that they would fluoresce under UVC light. This property was used to determine the end point of the extraction process for that particular solvent. A drop of the decanted top layer was placed onto a TLC plate and observed under a 254 nm lamp to determine whether there were any cyclic carbon compounds remaining in the powder.

After the final wash step, the remaining slurry was left to dry overnight. The dried mass was ground up using a mortar and pestle. The powder was transferred into a Schlenk tube attached to a Schlenk line and vacuum pump, so that the majority of the remaining solvents would be removed overnight at RT *in vacuo*. The powders would now be ready for analysis and experimentation.

2.3 METHODS

2.3.1 Characterisation of the Inorganic Powders

2.3.1.1 Scanning Electron Microscopy (SEM)

SEM images of the powders were taken with a Jeol Field Emission Gun Scanning Electron Microscope JSM 6301-F. The samples were mounted onto aluminium stubs with carbon sticky paper and sputtered with gold to increase conductivity.

2.3.1.2 Transmission Electron Microscopy (TEM)

Images of the nanoparticles were taken using a Transmission Electron Microscope Philips 200 instrument. The powders were suspended in propan-2-ol, sonicated for 30 minutes to break up agglomerates and added to copper grids for imaging.

2.3.1.3 X-Ray Photoelectron Spectroscopy (XPS)

The instrument VG ESCALAB 220i XL imaging XPS spectrometer was used to determine the amount and elemental composition of the coating substance on the particles.

2.3.1.4 X-Ray Diffraction Spectroscopy (XRD)

The crystal phase composition of the samples was determined using a Siemens D5000 X-ray diffractometer with a monochromated Cu Kα1 radiation source (λ = 1.5406) in the reflection mode over the range $20° < 2\theta < 70°$. The CMPR Graphical Manual Powder Indexing and Powder Diffraction program was used to determine the lattice parameters of each titanium dioxide crystal[81].

2.3.1.5 Raman Spectroscopy

A Renishaw Raman System 1000 using a helium-neon laser of wavelength 632.8 nm was used to identify crystal forms in the powders. The Raman system was calibrated against the emission lines of neon.

2.3.1.6 Solid State Nuclear Magnetic Resonance (SSNMR)

All NMR experiments were carried out on MSL300 (Bruker) with 7.05 T wide-bore magnet, suitable for both high resolution and wideline solid-state NMR experiments. High-resolution solid-state ^{13}C, ^{29}Si and ^{27}Al were recorded at 75.5, 59.6 and 78.2 MHz respectively using a standard 7 mm double-resonance Magic Angle Spinning (MAS) probe (Bruker) for the first two nuclei and a 4 mm one for the latter. Parchments rolled into a cylindrical shape were fitted with zirconia rotors of 7 mm diameter and spun at MAS frequencies in the range 5 kHz with stability better than ± 3 Hz. High-resolution solid-state spectra were recorded using cross polarisation.

2.3.1.7 Specific Surface Area Measurements

Three samples, **S5**, **S6** and **S9** were sent to Leeds Particle Characterisation Laboratories to undergo surface area measurements via BET nitrogen adsorption/desorption.

2.3.2 PHOTOCATALYTIC DECOLOURISATION AND DEGRADATION OF METHYLENE BLUE

A catalyst loading of 1 g/dm^3 of 1x10^{-4} M methylene blue in distilled water and titanium dioxide were used in these experiments. The suspension was stirred overnight in the dark in order to ensure that the adsorption equilibrium was obtained between the solid and the liquid. 10 cm^3 of suspension was transferred to a 6 cm diameter petridish to be irradiated under air-equilibrated conditions whilst stirring vigorously in order to maintain the powder dispersion. The control was a dish containing 10 cm^3 methylene blue but no titanium dioxide powder. The irradiation was carried out using an 8W BLB light (maximum emission at λ_m = 365 nm) with an irradiance of 35 W/m^2 at a distance of 5.5 cm from the surface of the reaction mixture. 3 ml aliquots were taken after 15 minute time intervals, centrifuged at 3400 rpm for 5 minutes to remove the solid, and the left over solution was analysed using a Helios single beam UV-Vis spectrophotometer. Both solid and liquid were returned to the reaction dish to be irradiated. This method was used to measure the variation in methylene blue concentration in each degraded sample at 660 nm, the absorption maximum for the dye. The decrease in absorption over time was then related to photocatalytic ability of that particular powder. The dye concentration measured from the control served as the initial concentration C_0 for the calculation of $C(t)/C_0$.

Chapter 3 – Analytical/Characterisation Results

The purpose of this chapter is to identify the different physical properties of the titanium dioxide and zinc oxide powders and their coatings. The physical characteristics of the inorganic materials such as crystal form, shape, size and composition are of major importance in deciphering their behaviour in chemical interactions. Firstly, images of the powders were taken using Scanning Electron Microscopy (SEM) to determine the average size and morphologies of the particles. Transmission Electron Microscopy (TEM), which has an enhanced resolution compared to SEM, gave a better understanding of the nanometer sized particles. X-ray diffraction (XRD) was used to determine the particular crystal forms present in the samples and gave additional information on the crystallite size of the particles and possible titanium dioxide solid solutions. As titanium dioxide is known to be a strong Raman scatterer, Raman spectroscopy was used to determine the crystal forms present in the powders. As the powders were not all crystalline, Solid State Nuclear Magnetic Resonance (SSNMR) gave vital structural information on the amorphous components of the coating materials. Investigations of coated materials are a difficult task because of the low coating concentrations. The typical concentration of surface modifiers/coatings ranges from 0.1-5% wt. The low concentrations involved required certain analytical instrumentations such as X-Ray Photoelectron Spectroscopy (XPS), which is a surface sensitive technique. As surface area is an important property of a catalytic powder, nitrogen BET (Braunaur Emmet Teller) measurements were carried out on a few samples. All the analytical results were collected and combined to form an understanding of the chemical and physical composition of these powders.

3.1 SCANNING ELECTRON MICROSCOPY

SEM images were taken to determine the average size and morphology of the nanoparticles. Most of the titanium dioxide powders (Figure 3.1) showed distinct shapes and sizes. Many of the samples, both pure and extracted (**S2**, **S3**, **S5**, **S10**, **S12**) had particles which appeared to be spherical in shape, possessing diameters within a 12 – 45 nm range except for **S12**, which contained the largest particle size (60 – 100 nm) of the spherical samples tested (Figure 3.1 Cii). The images of **S9** and **S11** showed that these particles were cylindrical in shape rather than spherical (Figure 3.2 G, H). The morphologies of **S6** and **S7** (Figure 3.2 D, E) were difficult to elucidate, as the SEM images did not reveal any individual particles but they did show the powders to be more agglomerated than the other samples. **S11** and **S2** were slightly similar to **S6** and **S7** as they contained large aggregates, however, distinct particles could be easily recognised and their diameters calculated.

3.1.1 SEM Images of Pure Titanium Dioxide Powders

(A) **S3**

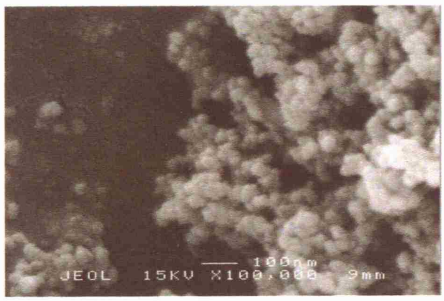

(B) **S10**

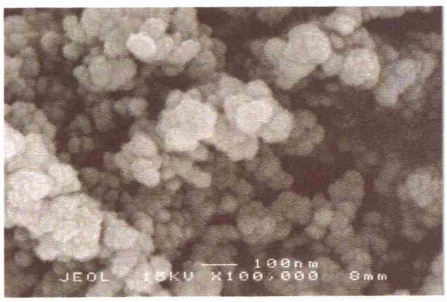

(C) (i) **S12**

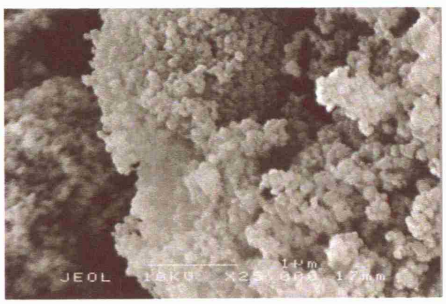

(C)(ii) **S12**

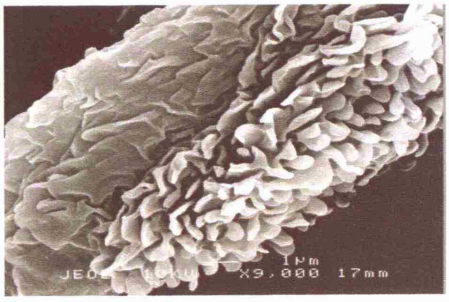

Figure 3.1: Scanning Electron Microscopy images of the pure titanium dioxide powders **S3**, **S10** and **S12**.

3.1.2 SEM Images of Extracted Titanium Dioxide Powders

(A) **S2**

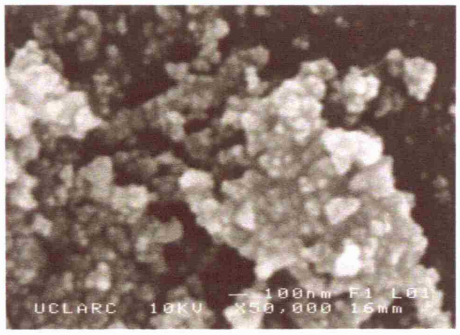

(B) **S4**

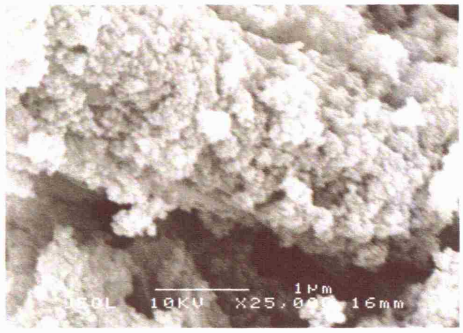

(C) **S5**

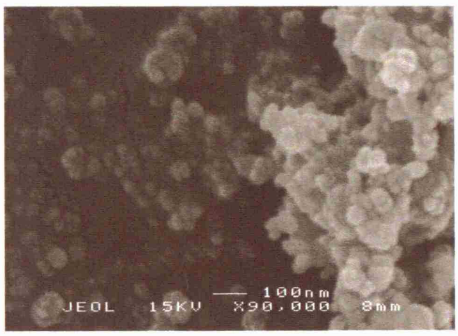

(D) **S6**

(E) **S7**

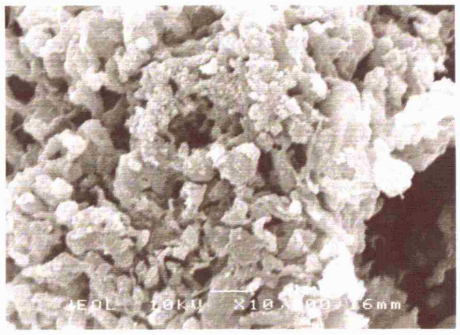

(F) **S8**

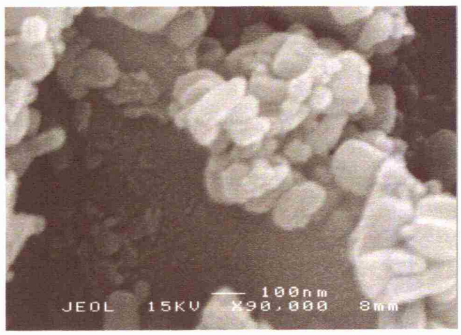

(G) (i) **S9**

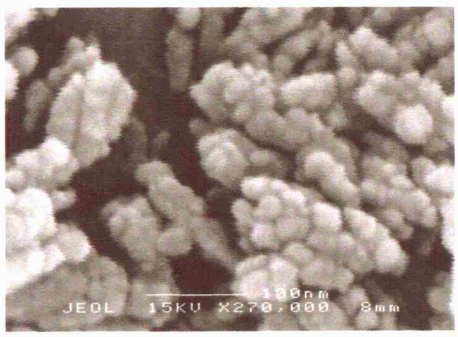

(H) **S11**

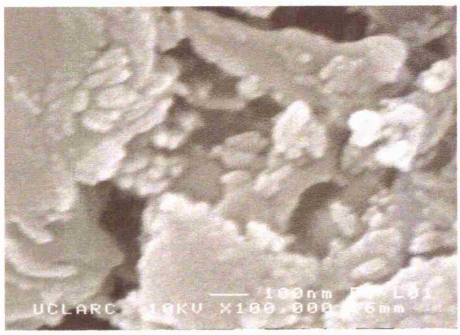

Figure 3.2: Scanning Electron Microscopy images of extracted titanium dioxide powders.

Table 3.0: Shape and particle size of pure and extracted titanium dioxide samples from Scanning Electron Microscopy.

Sample	Shape	Size/nm
Pure **S3** **S10** **S12** *Extracted* **S2** **S4** **S5** **S6** **S7** **S8** **S9** **S11**	Agglomerated Florets	12 - 100

3.1.3 SEM Images of Zinc Oxide Powders

(A) Sample-**d**

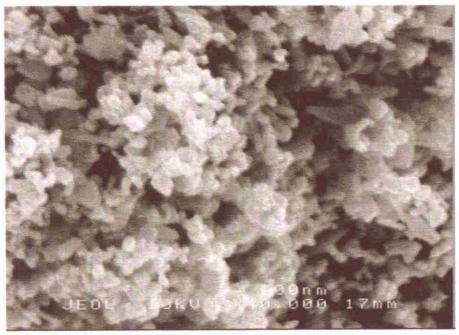

(B) Sample-**f**

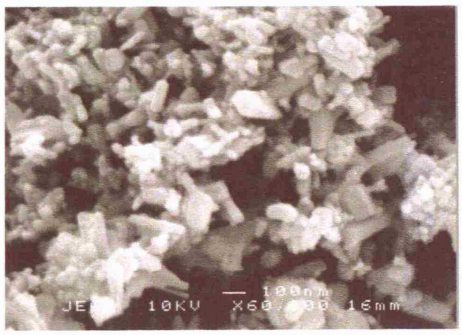

Figure 3.3: Scanning Electron Microscopy images of pure zinc oxide powders.

3.1.4 SEM Images of Mixed Zinc Oxide/Titanium Dioxide Powders

(A) Sample-**a**

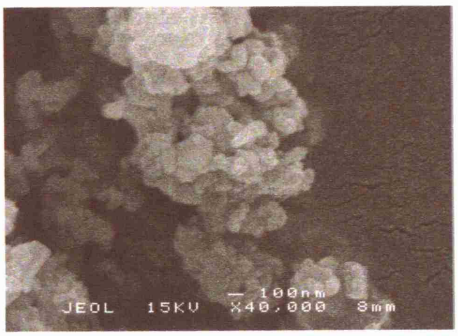

(B) Sample-**b**

(C) Sample-**c**

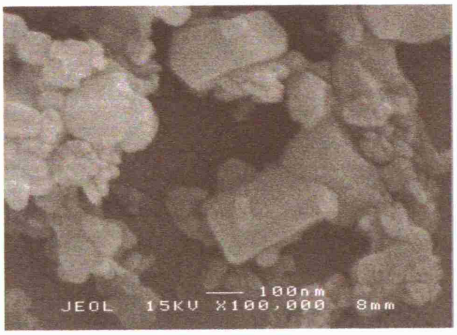

(D) Sample-**e**

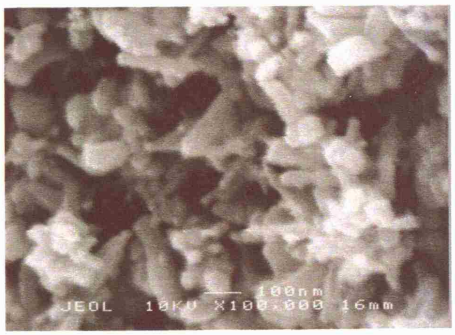

Figure 3.4: Scanning Electron Microscopy images of (A, B, C) sunscreen extracted mixed zinc oxide/titanium dioxide powders and extracted zinc oxide (D).

Table 3.1: Shape and particle size of pure zinc oxide and extracted mixed zinc oxide/titanium dioxide samples from Scanning Electron Microscopy.

Sample	Shape (from SEM)	Size/nm
a	Rod	50 – 200
b	Rod	50 – 200
c	Hexagonal	100 – 200
	Spherical	20 – 100
d	Hexagonal	50 –100
	Rod	50 -200
e	Hexagonal	50– 100
	Rod	50 – 200
f	Hexagonal	50 – 100
	Rod	50 – 200

The SEM images of the pure zinc oxide powders show mainly polyhedral aggregates of nanoparticles and in samples-**d, e** and **f**, there are mainly hexagonal and rod-like particles. The rectangular particles of the pure zinc oxide powders differ in uniformity and their lengths range from 50 – 200 nm in size (Figure 3.3 A, B and Figure 3.4 C).

The extracted zinc oxide and titanium dioxide mixtures (sample-**a**,**b**,**c**) also include a mixture of particle morphologies. Samples-**a** and **b** show mainly rod-like particles varying from 50 – 200 nm in length (Figure 3.4 A,B). Sample-**c** contains two distinct types of aggregates. The first are large rectangular shapes from 100 –200 nm in length and the other type of particle is much smaller (20 – 100 nm) and more spherical in shape (Figure 3.4 C). The difference in morphologies maybe due to the presence of two different inorganic oxides, titanium dioxide and zinc oxide in the powders.

The morphologies of zinc oxide particles are more complex and diversified compared to that of titanium dioxide. Their shape can be spherical, ellipsoidal, rod-like, needle-like and prismatic depending upon the manufacturing processes such as reactant temperature, pH and concentrations[82].

A limitation of SEM is that the morphologies of the titanium dioxide and zinc oxide particles can only be determined in accordance to the two dimensional image that is acquired from the surface of the sample. Another limitation of SEM is the range of magnification (3x – 150,000x) and resolution. A similar imaging technique which has a higher magnification and resolution is Transmission Electron Microscopy and would give more accurate information on the sizes and morphologies of these inorganic nanoparticles.

3.2 TRANSMISSION ELECTRON MICROSCOPY

TEM can provide topographical information for carefully prepared, oriented bulk samples regarding morphology, crystallite and aggregate size. From the images of the titanium dioxide powders extracted from sunscreens, five samples (Figure 3.6: D, E, F and G), contained particles that were acicular or needle-like in morphology. **S10** a pure powder also shows this characteristic, however, a more detailed analysis of the microstructure at higher magnification showed that the **S10** particles were actually ellipsoidal in shape (Figure 3.5 C (i) and (ii)).

3.2.1 TEM Images of Pure Titanium Dioxide Powders

(A) **S1**

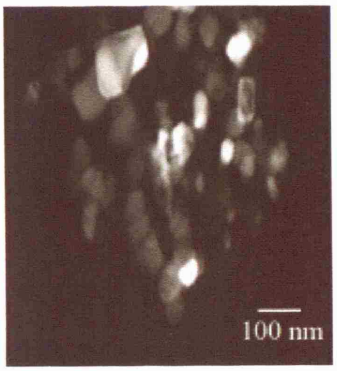

(B) (i) **S3**

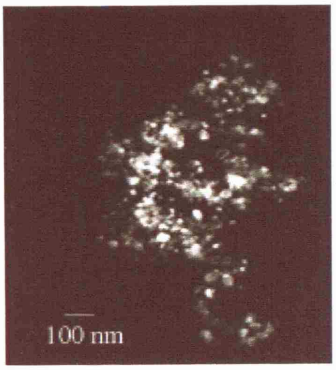

(B) (ii) **S3**

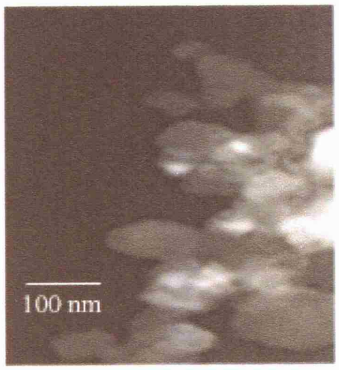

(C) (i) **S10**

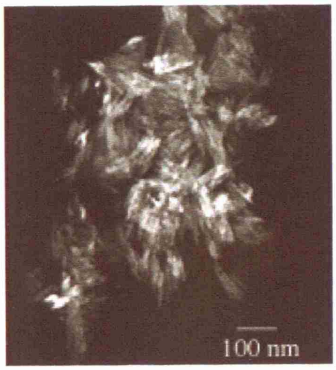

(C) (ii) **S10**

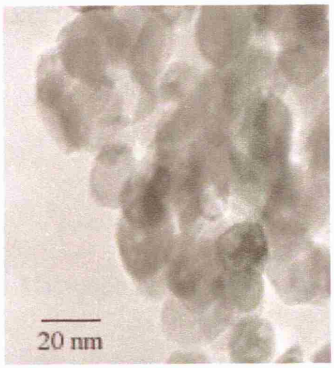

(D) **S12**

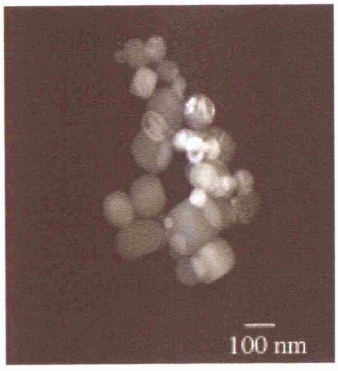

Figure 3.5: Transmission Electron Microscopy images of pure titanium dioxide powders.

3.2.2 TEM Images of Sunscreen Extracted Titanium Dioxide Powders

(A) **S2**

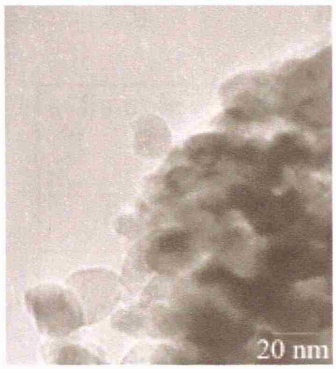

(B) **S4**

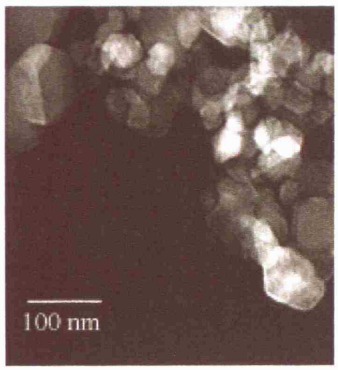

(C) **S5**

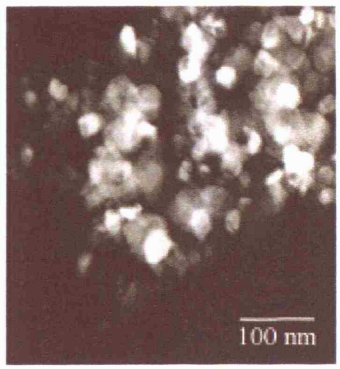

(D) **S6**

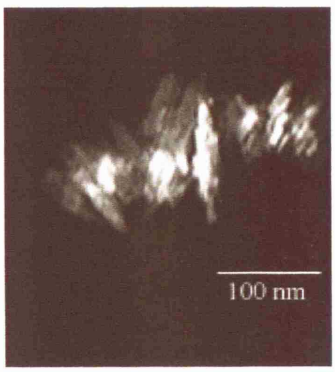

(E) **S7**

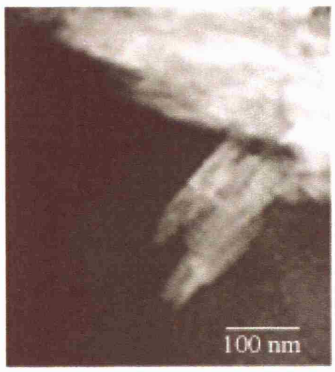

(F) **S9**

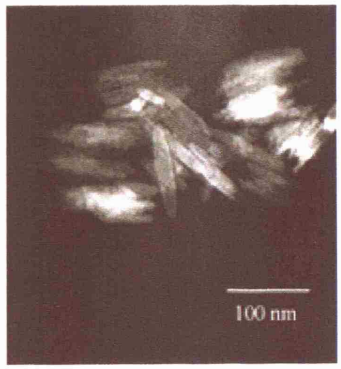

(G) **S11**

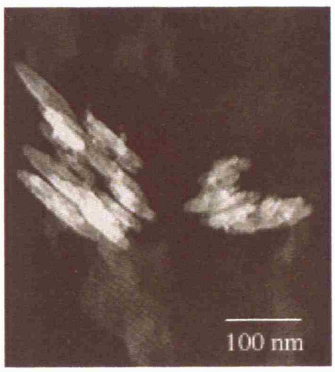

Figure 3.6: Transmission Electron Microscopy images of sunscreen-extracted titanium dioxide powders.

3.2.3 Comparison of SEM and TEM Data

Table 3.2: Summary of morphology and size of titanium dioxide powders from Transmission Electron Microscopy images and comparison to size determined from X-Ray Diffraction (see Section 3.3)

Sample	Shape (from TEM)	Size/nm (from TEM)	Size/nm (from XRD)
Pure			
S1	Spherical	20 – 50	30
S3	Ellipsoidal	50 – 100	21
S10	Ellipsoidal	20	10
S12	Spherical	60 – 134	14
Extracted			
S2	Hexagonal	16 – 20	17
S4	Hexagonal	30 – 60	11
S5	Spherical	20 – 50	23
S6	Acicular	30 – 50	16
S7	Acicular	50 – 80	13
S9	Acicular	80 – 110	16
S11	Acicular	50 – 100	14

The morphology or shape of the pure and isolated titanium dioxide particles varied from spherical to acicular (needle-like) as best determined by the resolution of the SEM and TEM used to picture these nanoscaled materials. Other researchers[83,84] have found that titanium dioxide as rutile usually possess a needle-like morphology whereas anatase particles are spherical. The diameters of the spherical and the length of the acicular particles were calculated by randomly selecting them from the images. All of the spherical particles had diameters below 50 nm and **S3** contained the smallest at 12 nm

in size. There were no single particles as they all formed larger aggregates of more than 50 – 100 nm in size. From these SEM and TEM images, there is no evidence of shelling whereby the coating is stripped from the core and resembles an amorphous mass around a crystalline particle. The processing/extraction method used here probably increased the agglomeration.

The photoactivity of titanium dioxide can critically depend on several factors including crystal type, particle size, manufacturing route, surface area, porosity and impurities. The shape and size of particles is important in a catalyst as the larger the surface area, the greater the number of active sites available for reaction. Besides catalytic activity, the shape of these nano-particles is important when taking into account light scattering and interaction. Pigmentary titanium dioxide (200 – 300 nm) strongly scatters visible light wavelengths (400 – 600 nm) whereas nanoscaled titanium dioxide such as those imaged by TEM and SEM (20 – 50 nm) interacts with ultraviolet light (200 – 400 nm).

The next section uses X-ray diffraction to analyse the crystal form and crystallite sizes of the titanium dioxide particles.

3.3 X-RAY DIFFRACTION

X-Ray diffraction (XRD) was used to provide crystal lattice information of the materials present in the powders and the characterisation of the crystalline forms present. The data was also manipulated to calculate crystallite size and particular orientation. The Debye-Scherrer equation was used to calculate the average crystallite size of the titanium dioxide present using the broadening of the (101) peak. Scherrer equation[85]:

$$D = \frac{K\lambda}{B_m \cos\theta}$$

where D is the crystallite size; K is the shape factor of the average crystallite and is usually 0.9, λ is the wavelength of the incident radiation = 1.5406 Å , B_m is the Full Width Half Maximum of the peak (in radians) and θ is the angle of incidence (half of 2θ).

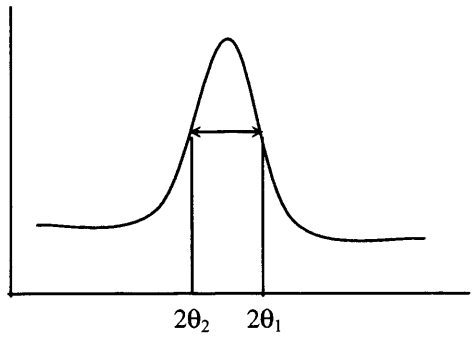

Full Width Half Maximum of a peak:

$$B_m = 2\theta_2 - 2\theta_1$$

The abundance ratio of the individual crystal types i.e. anatase and rutile, of a biphasic powder can also be calculated from the XRD spectra by measuring the relative peak intensity of their strongest diffraction peaks (I_A: anatase (101) and I_R: rutile (110)). For the weight percentage of anatase (W_A) in the powder[86]:

$$W_A = \frac{1}{[1 + 1.265\, I_R / I_A]}$$

Table 3.3 Summary of crystalline form and crystallite size of titanium dioxide particles from X-Ray Diffraction.

Sample	Crystalline Form	Crystallite Size from line broadening/nm
Pure		
S1	85% Anatase 15% Rutile	30
S3	85% Anatase 15% Rutile	21
S10	100% Rutile	10
S12	100% Rutile	14
Extracted		
S2	90% Anatase 10% Rutile	17
S4	85% Anatase 15% Rutile	11
S5	75% Anatase 25% Rutile	23
S6	100% Rutile	16
S7	100% Rutile	13
S8	100% Rutile	17
S9	100% Rutile	16
S11	100% Rutile	14

From all of the pure powders tested, two contained anatase and rutile mixed crystal forms whereas two samples contained titanium dioxide as 100% rutile. **S3**, **S10** and **S12** were reported in more detail in the following section. Of the sunscreen extracted powders, three samples were of mixed crystal form and the majority pure rutile. **S5** and **S11** were the only powders that had differing diffraction peaks to **S3** and **S10**, so their spectra were also shown and discussed. See Appendix A for the XRD spectra of **S2**, **S4**, **S6**, **S7**, **S8** and **S9**.

3.3.1 XRD of Pure Titanium Dioxide Powders

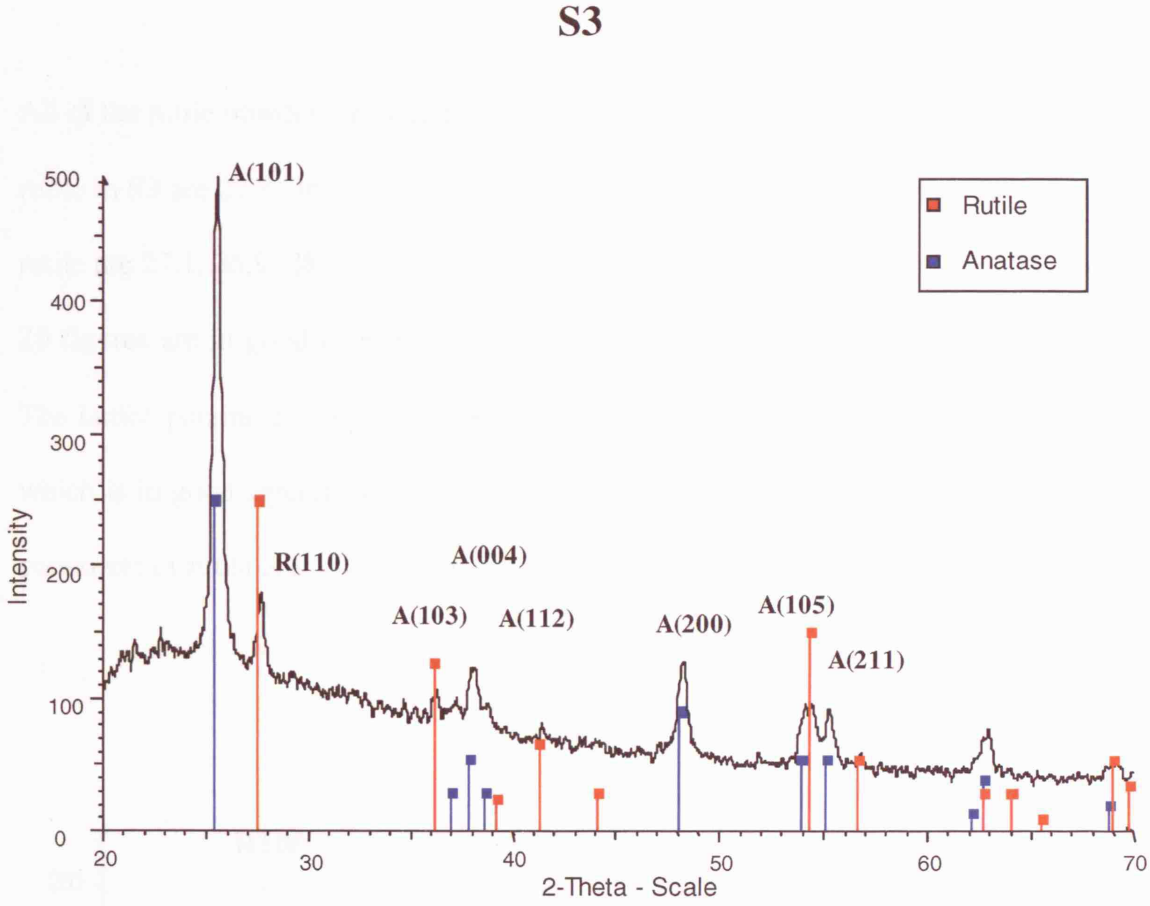

Figure 3.7: X-Ray Diffraction spectrum of **S3** with reference lines (red and blue) for each crystal peak.

S3 contains a mixture of crystalline titanium dioxide particles in the forms of 85% anatase and 15% rutile. The 2θ values for anatase in **S3** are 25.3, 37.0, 37.8, 38.8, 48.4, 54.8, 55.6 degrees (Figure 3.7). Literature values for anatase are 25.7, 37.5, 38.4, 48.8, 54.8, 55.9 degrees[87]. The dominant anatase reflection was from the (101) plane at $2\theta \approx 25.4°$, with additional minor reflections from (004) planes at $2\theta \approx 38°$ and (200) planes at $2\theta \approx 48°$. The lattice parameter of anatase in **S3** was calculated to be $a = 3.807$ Å and $c = 9.08$ Å which was in excellent agreement to the referenced data[87] with lattice

parameter values of $a = 3.807$ Å and $c = 9.09$ Å. The Miller indice for each reflection is shown above the peak.

All of the rutile powders showed peaks similar to the literature values. The 2θ values for rutile in **S3** are 27.3, 36.1, 38.3, 41.1, 44.0, 54.3, 56.6 degrees. Literature 2θ values for rutile are 27.1, 35.9, 38.7, 40.9, 43.5, 53.8, 55.8 degrees[88]. Both observed and literature 2θ figures are in good agreement. The dominant rutile peak was (110) at $2\theta \approx 27.5°$. The lattice parameter for rutile in **S3** was calculated to be $a = 4.58$ Å and $c = 2.93$ Å which is in good agreement with the referenced data[88] with observations for the lattice parameter of rutile at $a = 4.59$ Å and $c = 2.95$ Å.

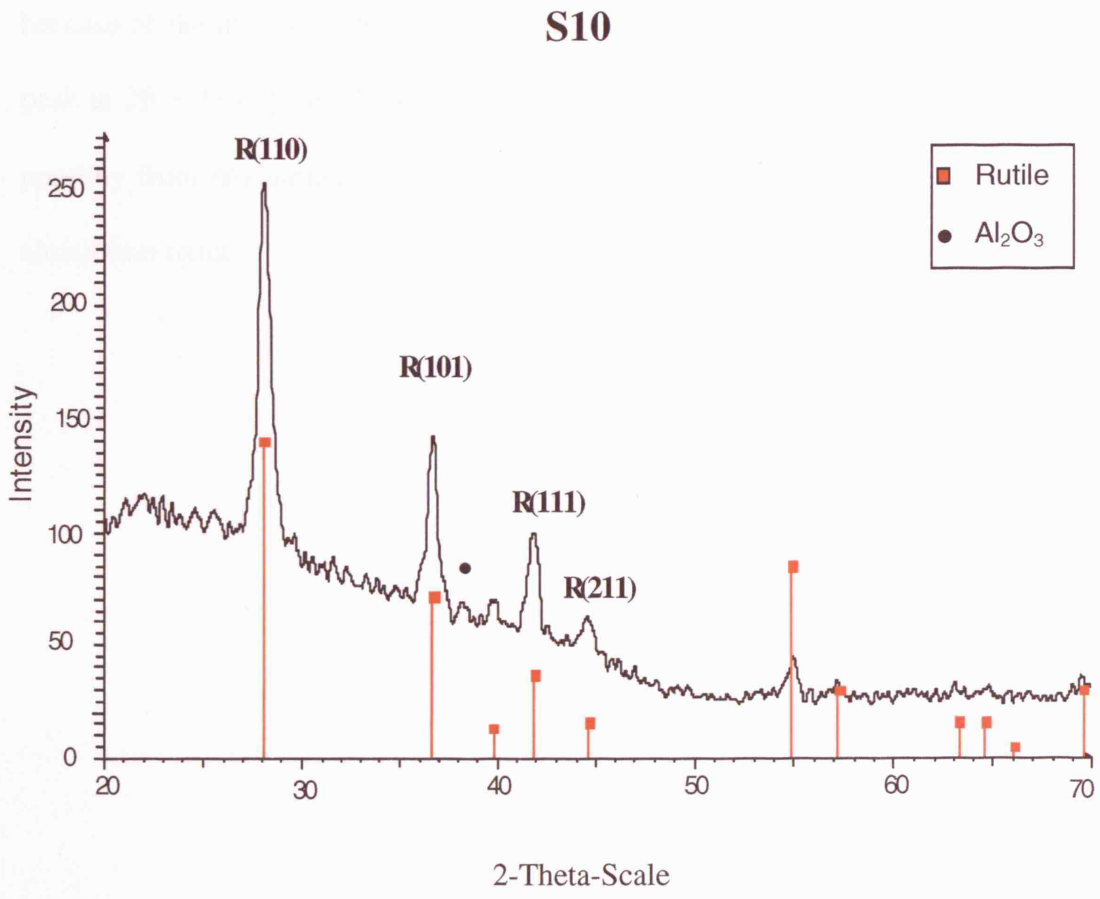

Figure 3.8: X-Ray Diffraction spectrum for **S10** with peaks comparing to reference lines (red).

The pure powder **S10** showed the characteristic XRD spectra of rutile with 2θ values at 27.3, 36.1, 38.3, 41.1, 44.0, 54.3, 56.6 degrees (Figure 3.8). These values correspond well to those in the rutile crystal form shown in **S3**. The Miller indice for each of the rutile reflections is shown above the corresponding peak. The small particle size of **S10** is seen by the non-defined baseline and the broad peaks of the spectra. **S6**, **S7**, **S8** and **S11** in Appendix A all show XRD spectra similar to that of **S10** with a rutile crystal structure. The lattice parameter values were also calculated for **S10** and were determined to be a = 4.50 Å and c = 2.92 Å, which are slightly less than the referenced values (a = 4.58 Å and c = 2.95 Å)[88]. This shift in the lattice values for **S10** indicates that there is the possibility that some aluminium has been incorporated into the bulk of the titanium dioxide core. Alumina itself is challenging to analyse far with XRD because of the myriad of poorly crystalline phases present. There is however, a small peak at 2θ = 38 degrees (Figure 3.8, symbol •) which does not belong to rutile and is possibly from α-alumina phase, which is the most thermodynamically stable form of aluminium oxide.

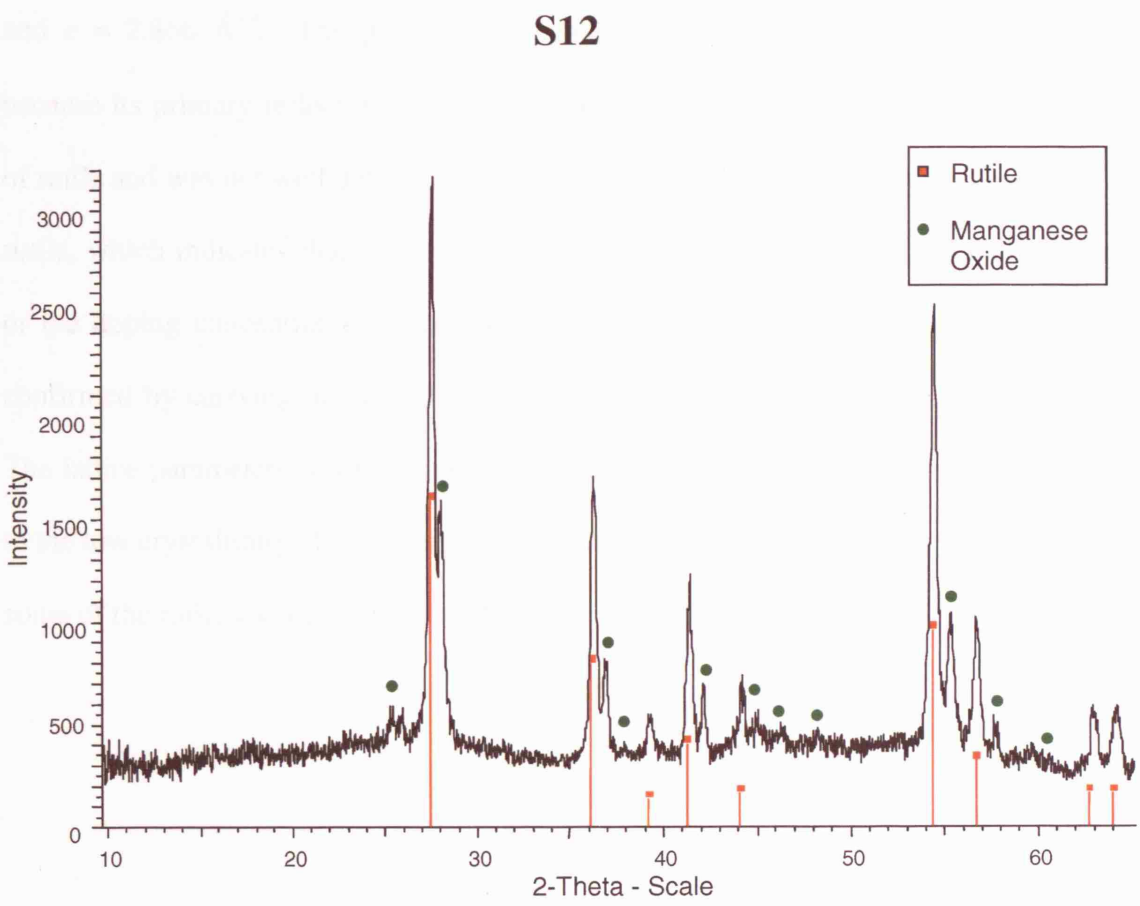

Figure 3.9: X-Ray Diffraction spectrum for **S12** comparing observed peaks with reference lines (red and green).

The pure powder **S12**, obtained directly from its manufacturers contains titanium dioxide as crystalline rutile as seen by its XRD spectrum in Figure 3.9. It is known that **S12** contains manganese oxide from its manufacturer's data sheet. The extra peaks (green lines) have been closely matched to that of manganese oxide as the mineral ramsdellite. The 2θ values for rutile were the same as that of the reference data stated previously. Typical diffraction peaks for MnO_2 at 2θ values 12.7°, 18.0°, 25.6°, 37.4°, 41.8° and 49.7°.

Reference data of the lattice parameters of manganese oxide are $a = 9.27$ Å, $b = 4.533$ Å and $c = 2.866$ Å[89]. The percentage of manganese oxide could not be determined because its primary reflection peak in the XRD spectrum of **S12** was very close to that of rutile and was not well defined. A shift in the lattice parameters was not observed for rutile, which indicates that manganese is probably not doped into the titanium dioxide or the doping concentration is too small to be detected. The lack of a shift was also confirmed by carrying out a Reitveld refinement calculation on the powder spectrum. The lattice parameters of the manganese oxide particles were difficult to elucidate due to the low crystallinity of the sample and the unresolved spectrum seen by the joining of some of the rutile and manganese oxide peaks.

3.3.2 XRD of Extracted Titanium Dioxide Powders

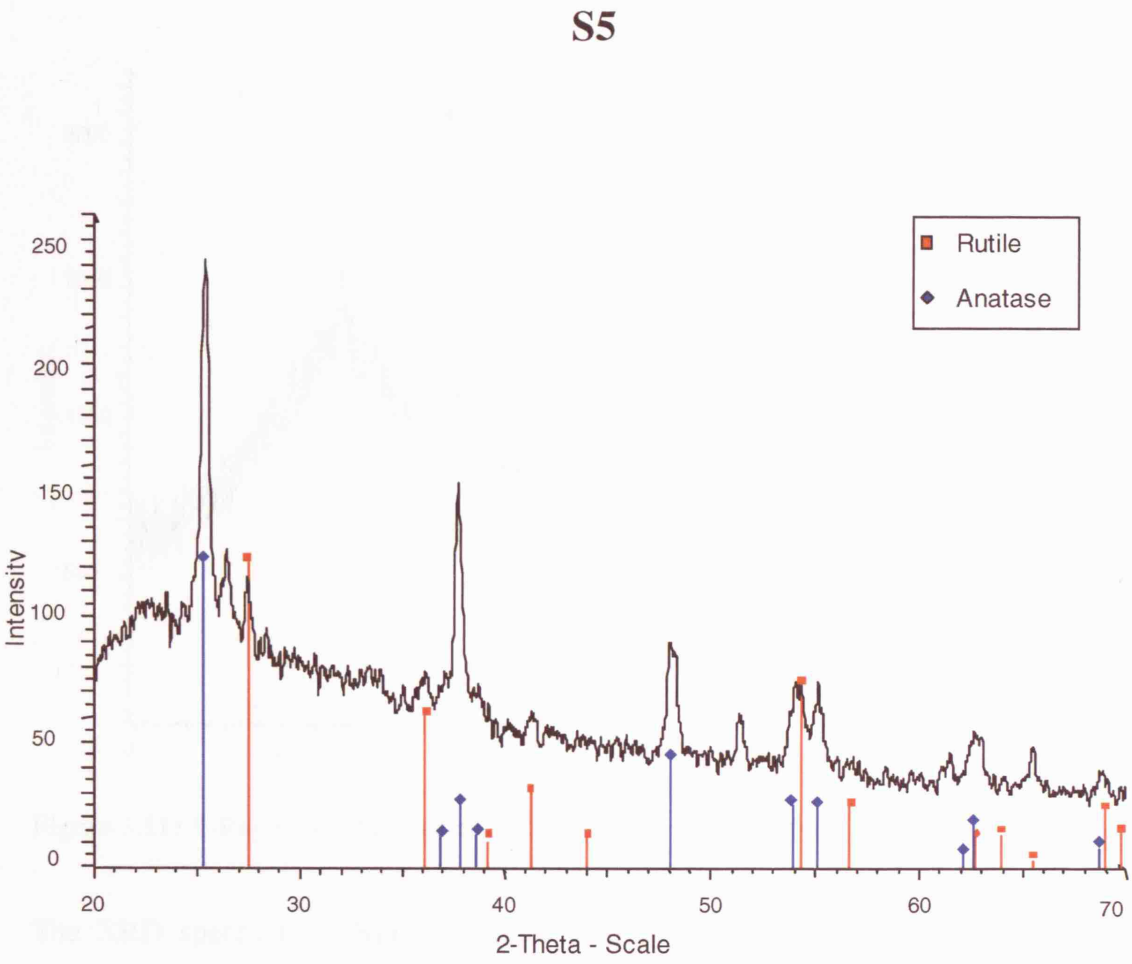

Figure 3.10: X-Ray Diffraction spectrum of **S5** with observed peaks compared to reference lines (red and blue).

The XRD spectra of the extracted sunscreen **S5** shows a mixture of anatase and rutile in a 4:1 ratio (Figure 3.10) as determined by the intensities of the main diffraction peaks. The 2θ reflection values for both anatase and rutile are similar to that of the sample **S3** (Figure 3.7) and the reference data. The Miller indices for both anatase and rutile are the same as those shown in Figure 3.7. The lattice parameter for anatase is the same as the literature values at $a = 3.807$ Å and $c = 9.09$ Å[87] and for rutile at $a = 4.58$ Å and $c = 2.95$ Å[88]. There are also two unknown extra peaks in the spectra at 2θ values 26.5 and 51.5°.

S11

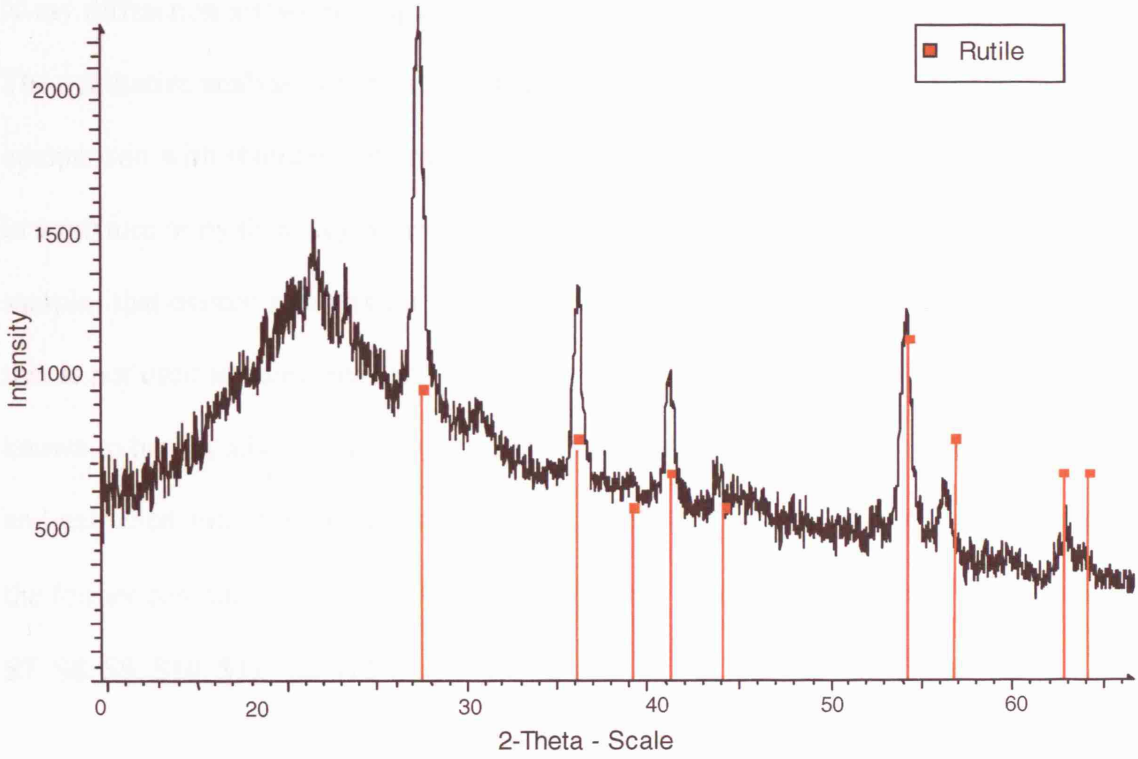

Figure 3.11: X-Ray Diffraction spectrum of sunscreen extracted **S11** with reference lines (red).

The XRD spectrum of **S11** clearly shows the presence of crystalline rutile as the titanium dioxide phase. However, there is also a broad peak at $2\theta = 21°$. The peak does not correspond with a rutile plane therefore it could be due to an alternative amorphous material present in the powder. The lattice parameters correspond to previously published data of $a = 4.58$ Å and $c = 2.95$ Å[88].

3.3.3 Comparison of X-Ray Diffraction Data

X-ray diffraction allows both qualitative and quantitative analysis of powered samples. The qualitative analysis involved the identification of particular phases in a specimen by comparison with standard patterns. Only two crystal forms of titanium dioxide, either in a mixture or by themselves, were present in these specimens. **S2**, **S3**, **S4** and **S5** were samples that existed as a mixture of anatase and rutile. **S1** is uncoated titanium dioxide that is not used in sunscreens and is only used as a control in this body of work. **S1** is known to have a mixed anatase and rutile crystal form. In Table 3.3, of the eleven pure and extracted sunscreen samples, four were comprised of both anatase and rutile with the former containing the majority, from 85 – 90%. The remaining seven powders, **S6**, **S7**, **S8**, **S9**, **S10**, **S11** and **S12** were 100% rutile.

The quantitative analysis of XRD data usually refers to the determination of the amounts of certain crystal forms present in multi-form samples. The experimental data itself was used to quantify structural characteristics such as crystallite size and lattice parameters for each phase. Crystallite size was calculated by measuring the broadening of the strongest planar reflection of the anatase (101) or rutile (110) peak from within the crystal unit cell. It is inversely related to the FWHM (full width half maximum) whereby the narrower the peak, the larger the crystallite size. This is due to the periodicity of the individual crystallite domains of the larger crystal, reinforcing the diffraction of the X-rays to form a narrow peak. The crystallite size varied from 10 – 23 nm excluding the uncoated **S1** sample which was 30 nm. The lines were fairly broad indicating small crystallites and more randomly oriented crystals or lower periodicity. The peak intensity decreases and the spectral line broadens with decreasing particle size (compare **S3** and **S10**).

The cell dimensions were calculated using the CMPR program for each powder spectrum[90]. The calculated cell dimensions for anatase and rutile in each of the samples were similar to that of the quoted reference except for **S10**. There was a definite shift in the lattice parameters of **S10** especially with regard to *a* which decreased from 4.58 to 4.50 (**S10**). With increasing amounts of some dopants, the cell parameter values usually decrease[91]. Apart from **S10**, there was no large deviation of the lattice parameters of the other powders. **S12**, a pure powder, is supposedly doped with manganese however its cell dimensions for rutile were the same as the reference. A powder that comprises of a solid solution would normally show a different XRD pattern because the doping atom such as manganese would be substitutionally or interstitially incorporated into the crystal lattice thereby distorting it from its original position, unless the doping concentration was extremely small. The XRD spectrum for manganese oxide in S12 was determined to have the closest match to the mineral ramsdellite[89]. Unfortunately, the crystal structures, and consequently, the powder diffraction patterns are similar for many of the Mn oxide minerals. The crystal structures are also poorly understood and there are several phases for which even the basic crystal structure is unknown. It is known that the basic building block for manganese oxide is the MnO_6 octahedron. These octahedra can be assembled into a large variety of different structural arrangements by sharing edges and/or corners. They fall into two groups, either chain or tunnel structures, or layer structures. Ramsdellite is made up of double chains of edge-sharing MnO_6 octahedra[92]. The $Mn(IV)O_6$ octahedra are linked into double chains, each of which consists of two adjacent single chains that share octahedral edges. The double chains, in turn, link corners with each other to form a framework having tunnels with rectangular shaped cross sections.

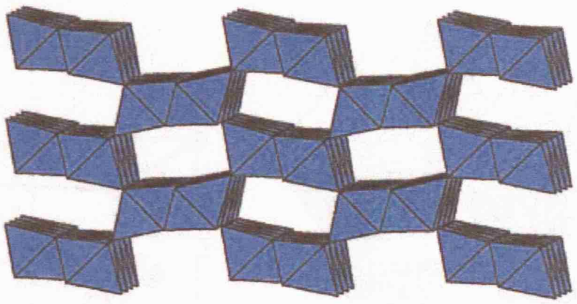

Figure 3.12: Crystal structure of manganese oxide as ramsdellite[89]

Both anatase and rutile have D_{4h} tetragonal symmetry but their space groups are different. The space group of anatase is $I4_1/amd$ indicating that the crystal lattice is body centred tetragonal. Rutile has a primitive tetragonal Bravais lattice with a $P4_2/mnm$ space group. Both structures contain a sublattice of titanium with an octahedral coordination of six O^{2-} ions about the central Ti^{4+} cation. This is the maximum number of oxygen ions that can fit around the smaller titanium ion. The two structures differ only by the distortion inside each octahedron and by their assembly. In an anatase structure, each octahedron is in contact with eight neighbours (four sharing an edge and four sharing a corner), while rutile has a coordination number of ten (two sharing an edge and eight sharing a corner)[93]. The octahedron in rutile shows a slight orthorhombic distortion. The octahedron in anatase is significantly distorted, so that its symmetry is lower than orthorhombic (Figure 3.13).

(A)

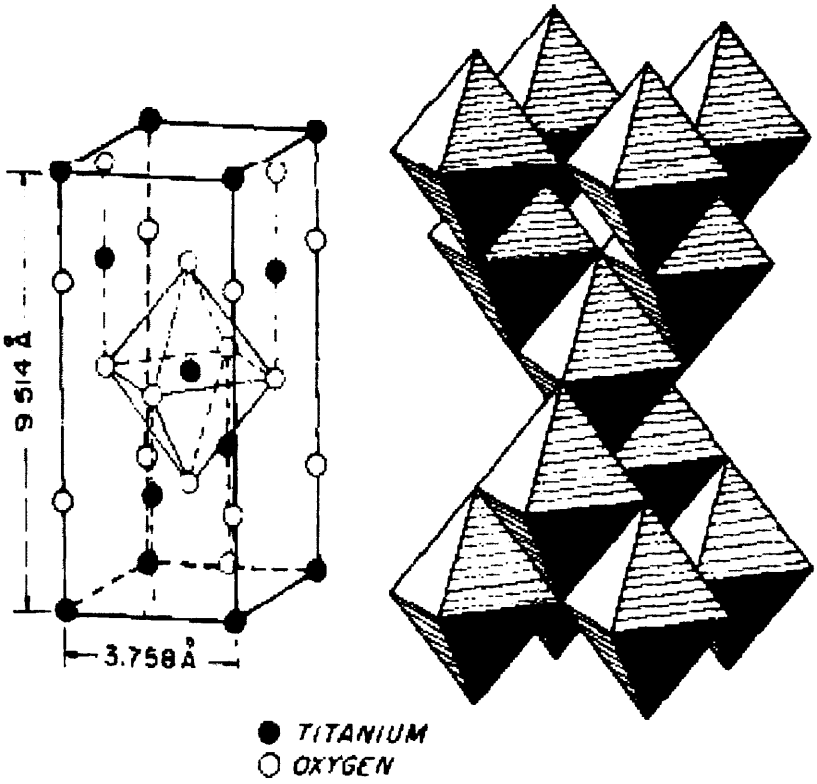

(B)

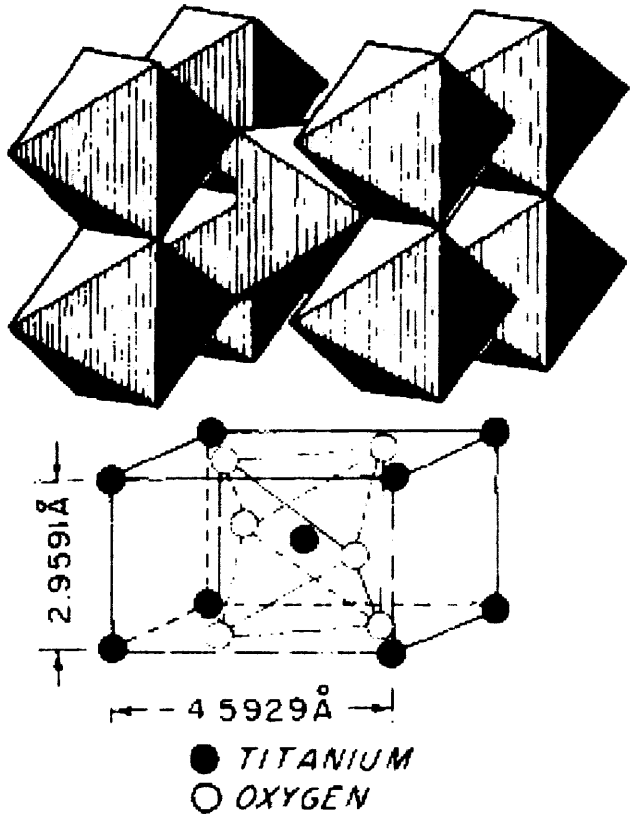

Figure 3.13: Anatase (A) and Rutile (B) Crystal Structure [94]

XRD was successfully used to determine the qualitative and quantitative aspects of the powders however these samples do not only contain titanium dioxide whether in the anatase or rutile crystal form. There should be a small percentage of the coating material present in each of the powders that need to be determined. A key limitation of XRD is its inability to identify amorphous materials, as they do not diffract. This is seen in Figure 3.11 for **S11**, where there is an unidentifiable broad peak. X-ray Photoelectron Spectroscopy or XPS is a technique which can be used to determine different elemental components in a solid sample, and it does not depend upon its crystallinity. This surface technique is used in the next section to analyse the titanium dioxide powders.

3.4 X-RAY PHOTOELECTRON SPECTROSCOPY

X-ray photoelectron spectroscopy (XPS) was used to determine the chemical species and quantity of the coating on the surface of the titanium dioxide core. XPS uses soft X-ray (200 – 2000 eV) radiation which is energetic enough to eject electrons from the core orbitals thereby allowing core energy levels to be probed. In XPS, the initial energy of the photon is compared to the kinetic energy of the emitted electron. The difference in energy is accounted for by the amount of attraction that the electron has with the nucleus (binding energy) and the amount of energy which is lost in transit from the sample to the analyser (work function). The work function is the same for each sample in a specific XPS analyser whereas the binding energy is dependent upon the atom from which it came, as well as its chemical environment. As each element has a unique range of binding energies, XPS can be used to determine and quantify the concentration of the elements on the surface. XPS depth profile analysis into the particle gave an indication of its surface chemistry.

Three of the pure powders obtained directly from the manufacturers, **S3**, **S10** and **S12** are reported in this section and similar extracted sunscreen samples were compared and contrasted to the pure samples. The extracted powders **S2**, **S4** and **S5** have the same XPS spectrum as the pure powder **S3**, obtained from its manufacturer. They all possess a coating which contains silicon. The extracted powders **S6** and **S8** both contain silicon and aluminium in their coating and are discussed. The extracted powders **S7**, **S9** and **S11** show similar XPS spectra to that of the pure powder **S10**. The XPS spectra of the powders **S3**, **S6**, **S8**, **S10**, **S12** are shown in this chapter. The spectra for **S2**, **S4**, **S5**, **S7**, **S9** and **S11** are shown in Appendix B.

3.4.1 X-Ray Photoelectron Spectroscopy of S3

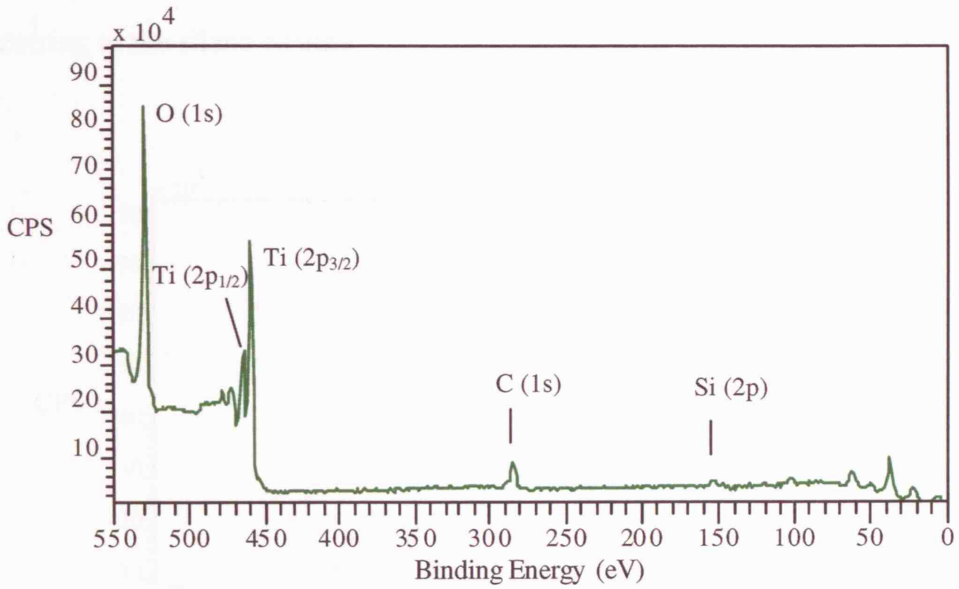

Figure 3.14: X-Ray Photoelectron survey for **S3**.

Table 3.4: X-Ray Photoelectron binding energies for **S3** components.

Binding Energy/eV	Species
529.2, 531.4	O (1s)
464.5	Ti^{4+} ($2p_{1/2}$)
458.9	Ti^{4+} ($2p_{3/2}$)
284.5, 285.0, 288.0	C (1s)
153.1	Si (2s)
102.2, 102.8	Si ($2p_{3/2}$)
37.6	Ti (3p)
22.15	Ti (2s)

S3 is titanium dioxide with an organosilane outer coating. This is known in the manufacturer's sheet and states that the coating is trimethoxycaprylylsilane. The Si ($2p_{3/2}$) peak at binding energy 102.8 eV is indicative of silicon oxides SiO_x/Si or silane or a silicon atom in a polymer[95]. It is also noted that as the etching depth is increased,

the percentage of Si decreases and that of Ti increases. This is to be expected as the coating is only a few atomic layers thick and would disappear after a few etchings. The titanium dioxide core would be more visible after etching deeper with the converse occurring to the silane coating.

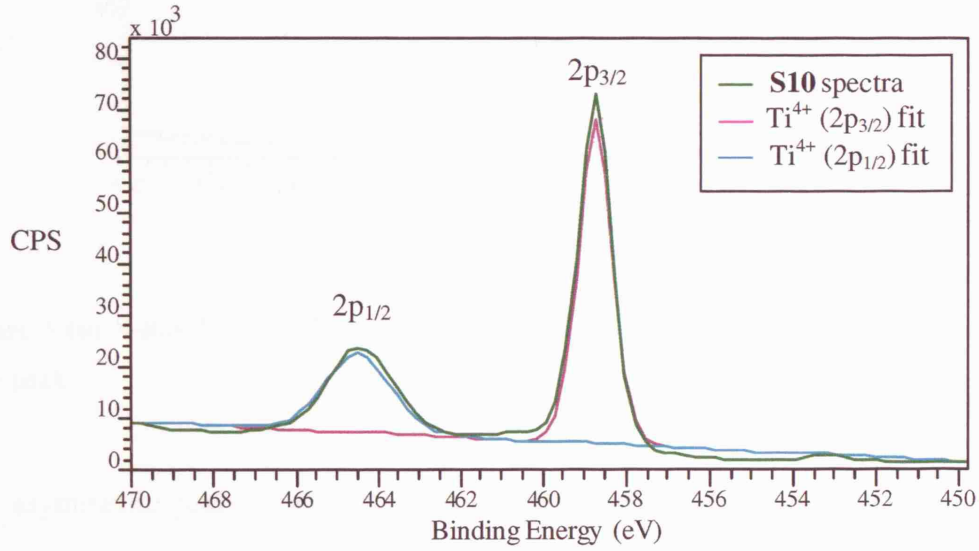

Figure 3.15: X-Ray Photoelectron spectra for titanium (2p) in **S3** with calculated fits for each peak.

The XPS spectra of Ti (2p) region for the surface of **S3** is shown above in Figure 3.15. The spectrum shows a closely spaced doublet. The two pronounced features at binding energies 464.5 eV and 458.9 eV are evoked by the Ti ($2p_{1/2}$) and the Ti ($2p_{3/2}$) spin orbit components respectively. Reference values for Ti ($2p_{1/2}$) and ($2p_{3/2}$) are 464.5 eV[96] and 458.9 eV[97]. The single peak at 458.9 eV, the Ti ($2p_{3/2}$) component indicates the presence of a single oxidation state of Ti (Ti^{4+}) typical of the TiO_2 lattice. All of the other titanium dioxide samples except **S12** show XPS peaks like those in Figure 3.15 so their spectra are not shown.

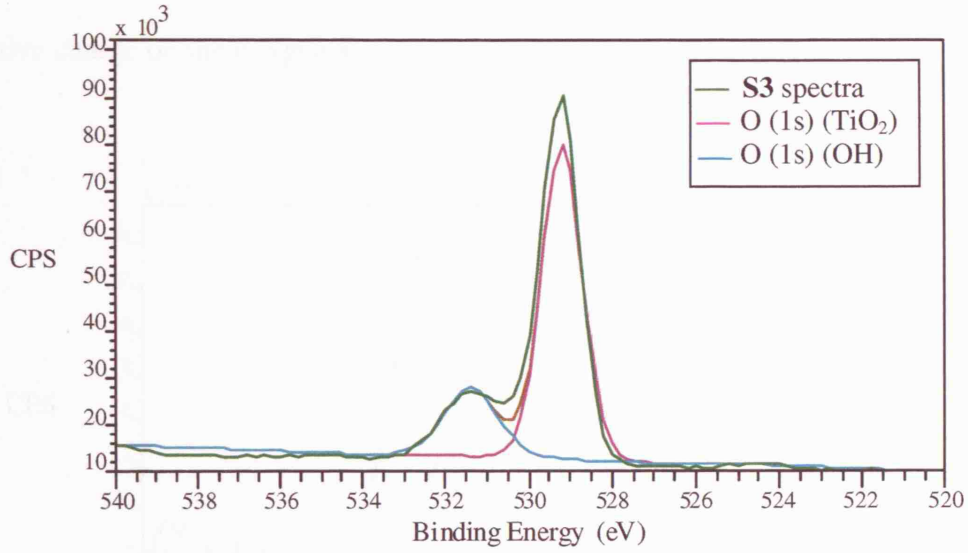

Figure 3.16: X-Ray Photoelectron spectra for oxygen (1s) region in **S3** with calculated fits for each peak.

The asymmetric peaks of the O(1s) can be split into two different components. The broad peak shows that there is more than one oxygen species present. From previous XPS work[98], the more intense peak at binding energy 529 eV is due to oxygen in the bulk thus arising from the titania, whereas the smaller peak is due to surface oxygen species. As most of the atoms in small particle clusters are surface atoms, the oxidation state measured will also reflect some bulk oxidation state. The blue line showing a shoulder at 531.4 eV is indicative of surface hydroxyl species[98]. If the surface of the titanium dioxide core were not completely covered with the inert coating then there would exist some Ti–OH on the surface. This is because when titanium dioxide powders are exposed to air they become hydroxylated in order to reduce the surface potential. The binding energy of 531.4 eV could also be that of the mixed oxide bond Ti – O – Si as it is the intermediate of an Si – O – Si (532.9 eV) and Ti – O – Ti (530.7 eV) bond. The binding energy of the oxygen in a Si – O – Si bond is usually at 532.9 eV

however, replacement of the silicon atom with a titanium atom would increase the negative charge on the oxygen atom causing a shift in O (1s) values.

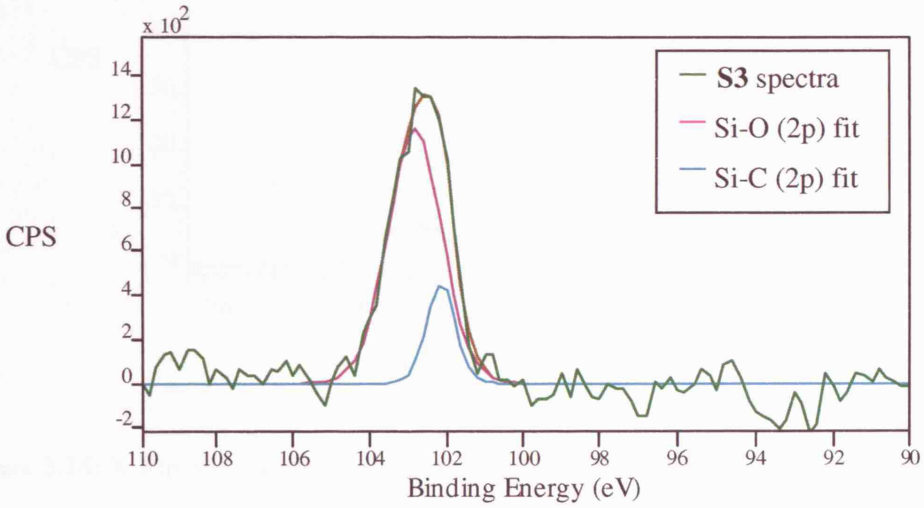

Figure 3.17: X-Ray Photoelectron spectra for the silicon (2p) region of **S3**.

The peak for Si (2p) shows two different environments for silicon. The Si (2p) peak position for a silicon oxide, SiO_2 is at 103.4 eV [99] whereas the main Si (2p) peak in **S3** is at 102.8 eV. The less intense value at 102.2 eV can also denote the presence of an organosilane like triethoxysilane[95]. This chemical shift to lower binding energies may also indicate a decrease in the ionicity of the complex caused by the bond to an ionic atom. It is possible that there is a decrease in the effective positive charge on the silicon atoms due to the formation of a mixed metal oxo bond i.e. Ti – O – Si. This is in agreement with the binding energy for the O(1s) seen in Figure 3.16.

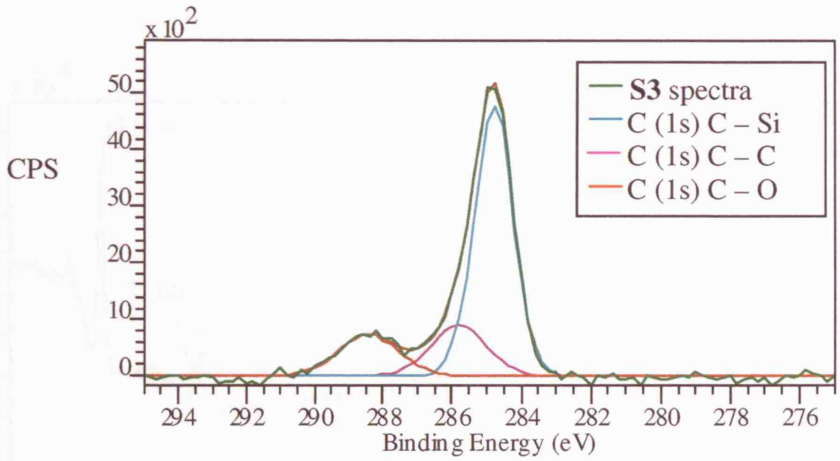

Figure 3.18: X-Ray Photoelectron spectra for the carbon (1s) region in **S3** with calculated fits.

Deconvolution of the carbon spectra revealed the existence of three different chemical environments for carbon. The values of the three C (1s) peaks in **S3** are 284.5, 285 and 288 eV. The least intense peak at binding energy 284.5 eV can be assigned to C – Si [100]. The largest peak in the carbon region at 285 eV is due to C – C and C – H bonds[101] and the peak with the highest binding energy is assigned to the C – O peak[102]. The values at 284.5 eV and 288 eV have also been found in aliphatic carbon atom and carbon atoms attached to silicon atoms such as silanes[103].

3.4.2 X-Ray Photoelectron Spectroscopy of S6

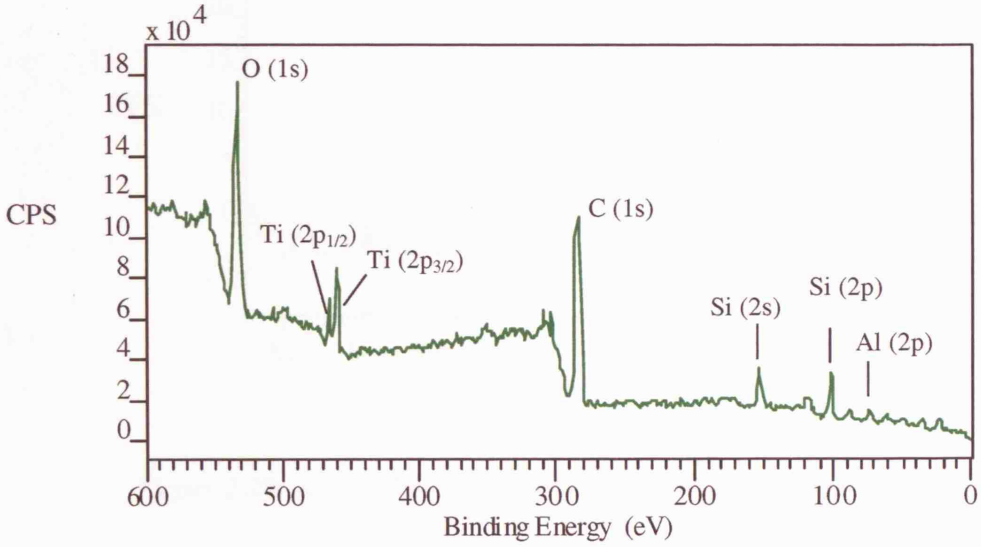

Figure 3.19: X-Ray Photoelectron survey of **S6**.

Table 3.5: X-Ray Photoelectron binding energies of **S6** components.

Binding Energy/ eV	**Species**
531.0, 532.1, 532.2, 534.0	O (1s)
466	Ti^{4+} ($2p_{1/2}$)
460.9	Ti^{4+} ($2p_{3/2}$)
285.0	C (1s)
153	Si (2s)
119.21	Al (2s)
102.2, 102.8	Si ($2p_{3/2}$)
73.7, 74.4	Al ($2p_{3/2}$)
49	Mg (2p)
36.2	Ti (3p)

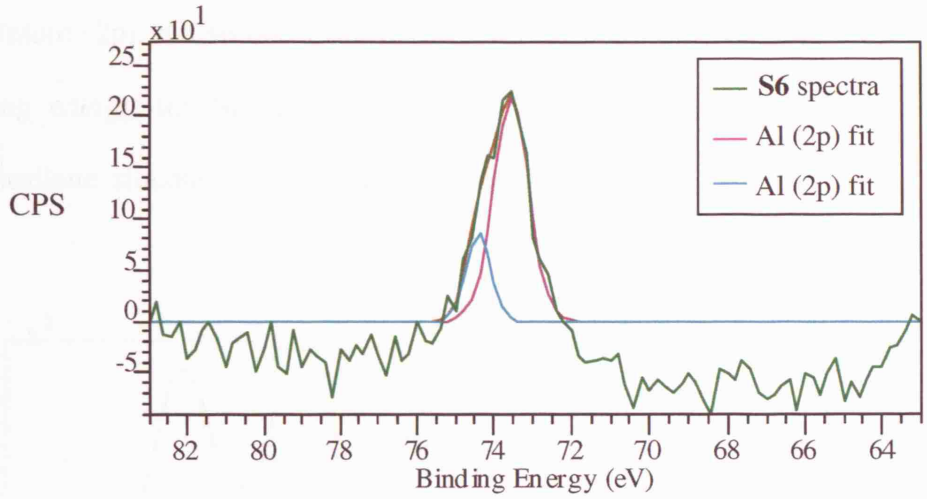

Figure 3.20: X-Ray Photoelectron spectra of the aluminium (2p) region of **S6**.

The peak at 73.7 eV is indicative of the Al (2p) region of aluminium oxide[104], Al_2O_3.

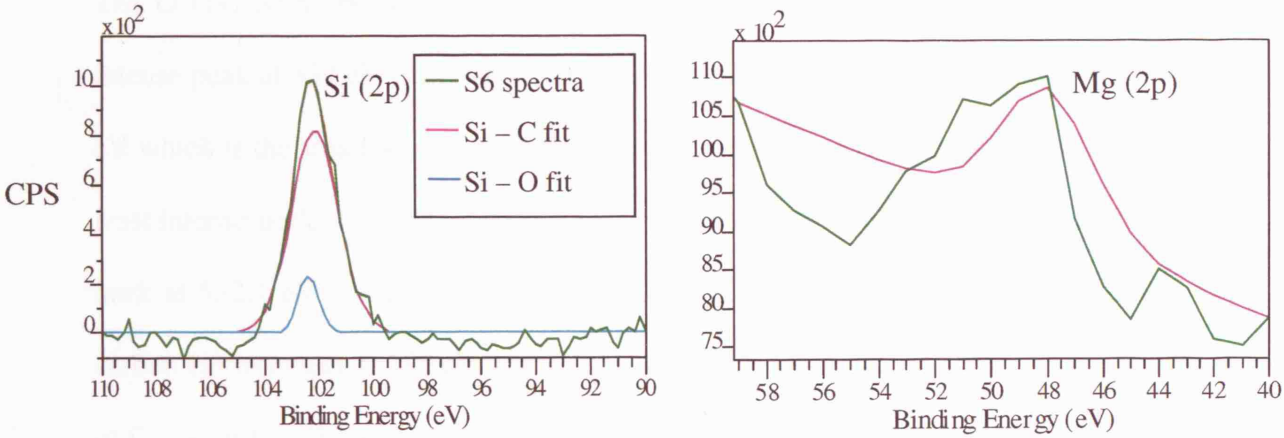

Figure 3.21: X-Ray Photoelectron spectra of the silicon (2p) and the magnesium (2p) regions of **S6**.

From Figures 3.20 and 3.21, it is possible that the coating for **S6** contains both silica and alumina with a smaller amount of the latter present on the particle as noted by the variation in intensity of the peaks. The Al (2p) component at 74.5 eV combined with the peaks at 102.2 eV (Si (2p)) and 49 eV (Mg (2p))[97] suggests the presence of small

amounts of magnesium aluminium silicate with the first binding energy being from aluminium (2p), the second from magnesium (2p) and the last from silicon (2p). The binding energy for Si (2p) at 102.8 eV could also indicate the presence of an organosilane, silicone or even silica in the **S6** powder.

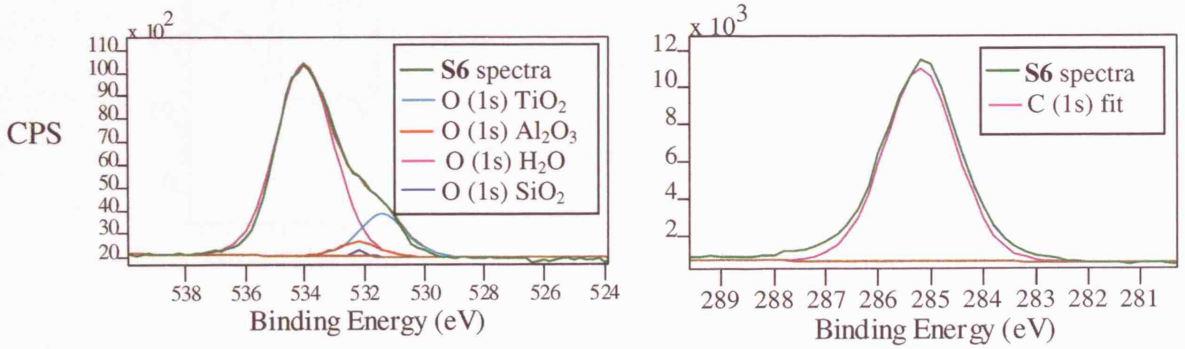

Figure 3.22: X-Ray Photoelectron spectra of oxygen (1s) and carbon (1s) regions of **S6**.

The O (1s) XPS spectrum is deconvoluted into four different components, the most intense peak at 534 eV is due to adsorbed H_2O on the surface; a less intense peak at 531 eV which is the smallest of the binding energies denotes oxygen in titanium dioxide; the least intense peak at binding energy 532.2 eV is suggestive of silicon oxide and the XPS peak at 532.1 eV is due to oxygen in alumina. The C (1s) spectrum shows only one carbon environment at 285 eV which is indicative of C – C bonds. There is no evidence of C – Si or C – O bonds present in **S6** unlike **S3** which has an organosilane coating.

3.4.3 X-Ray Photoelectron Spectroscopy of S7

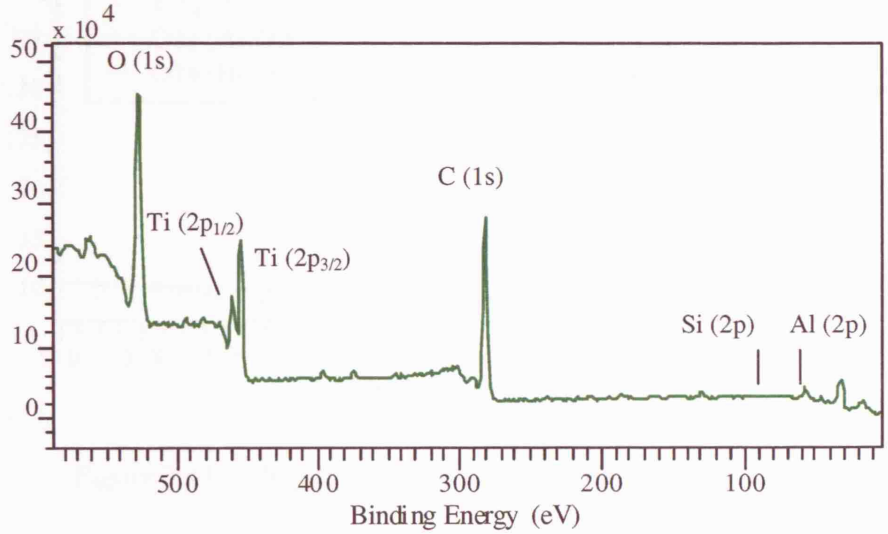

Figure 3.23: X-Ray Photoelectron survey for **S7**.

Table 3.6: X-Ray Photoelectron binding energies of **S7** components.

Binding Energy/eV	Species
530.0, 531.3, 532.6	O (1s)
464.4	Ti ($2p_{1/2}$) Ti^{4+}
458.2	Ti ($2p_{3/2}$) Ti^{4+}
285.0, 286.0, 288.0	C (1s)
134.0	P ($2p_{3/2}$)
102.0	Si (2p)
74.3	Al (2p)
62.2	Ti (3s)
36.3	Ti (3p)

The reference carbon shift is always a constant at 285.0 eV[101]. For **S7**, there was a shift of – 4 eV hence 4 eV was added on to correct the binding energies. The recalculated binding energies are tabulated above however the graphs still retain the old values.

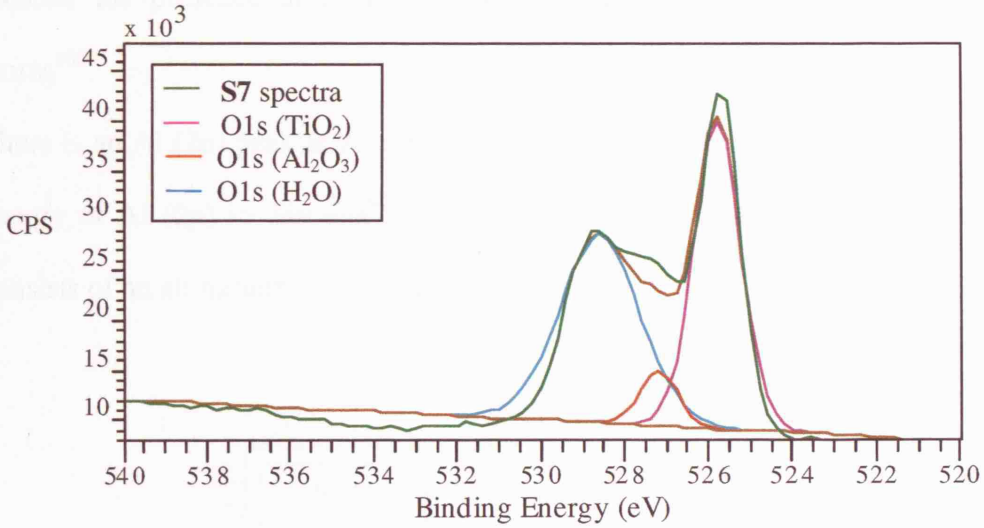

Figure 3.24: X-Ray Photoelectron spectra of oxygen (1s) region of **S7**.

The O (1s) spectra can be resolved into three peaks at 530.0, 531.3 and 532.6 eV. They are assigned to titanium dioxide lattice oxide, aluminium oxide and adsorbed water respectively.

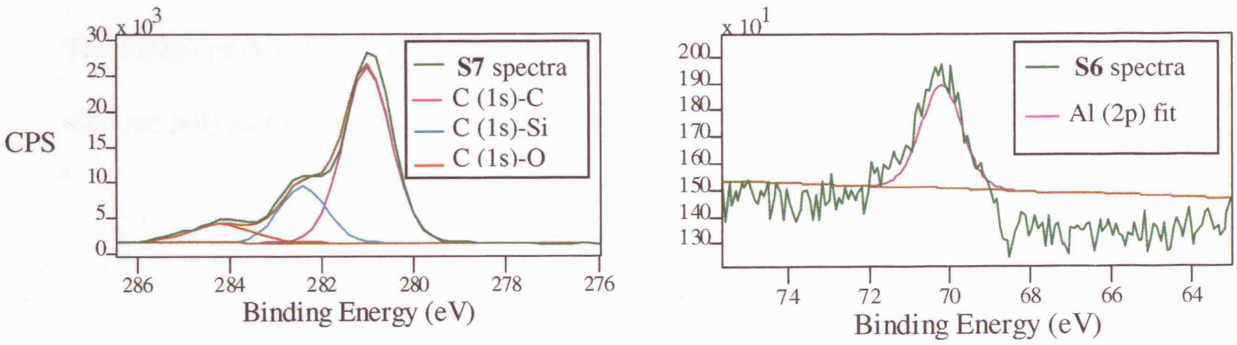

Figure 3.25: X-Ray Photoelectron carbon (1s) and aluminium (2p) regions of **S7** powder.

The carbon XPS spectrum (Figure 3.25) was resolved into three separate peaks. The most intense peak at 285 eV (corrected by +4 eV) is assigned to C – C bonds. The smaller peak at higher binding energy 286 eV (corrected by +4 eV) is suggestive of a long chain carbon polymer[105]. The highest binding energy is at 288 eV which could

indicate the presence of a carbonyl group[106] or a carbon atom attached to silicon atoms[103].

There is an Al (2p) peak at 74.3 V (Figure 3.25) which corresponds well to the binding energy of Al (2p) in alumina[97]. This may indicate that the titanium dioxide surface consists of an aluminium oxide coating.

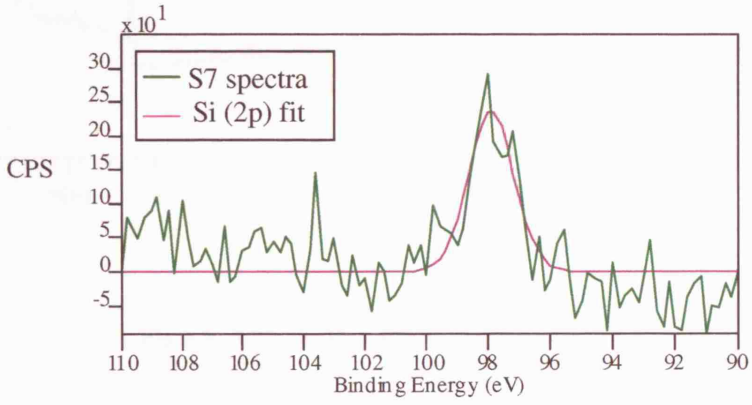

Figure 3.26: X-Ray Photoelectron spectra of Si (2p) region in **S7**.

The Si(2p) peak at binding energy 102.0 eV may be indicative of a small amount of silicone polymer in the S7 powder.

3.4.4 X-Ray Photoelectron Spectroscopy of S8

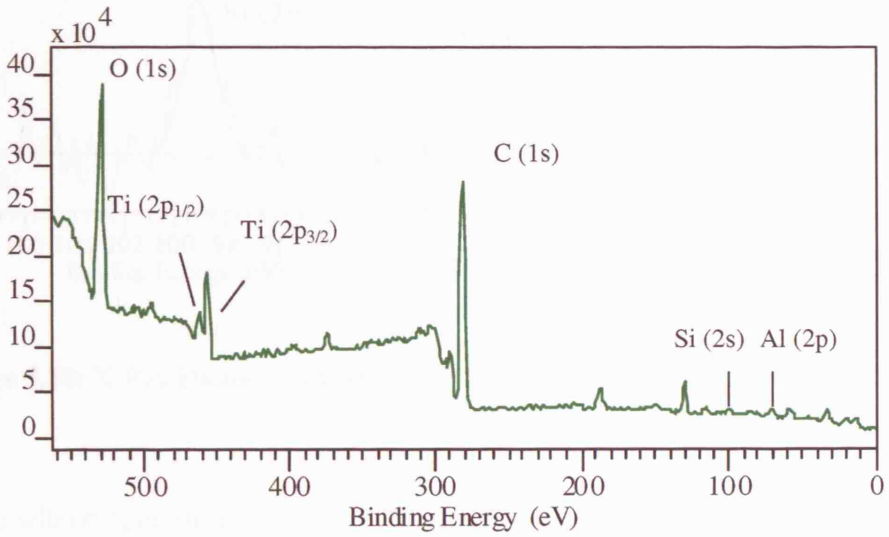

Figure 3.27: X-Ray Photoelectron survey of **S8**.

Table 3.7: X-Ray Photoelectron binding energies of **S8** components.

Binding Energy/ eV	Species
533.2, 531.7, 531.1	O (1s)
466.1	Ti ($2p_{1/2}$)
460.5	Ti ($2p_{3/2}$)
285.0	C (1s)
191.4	P (2s)
134.0	P ($2p_{3/2}$)
119.4	Al (2s)
103.0	Si ($2p_{3/2}$)
74.2; 75.7	Al (2p)
63.3	Ti (3s)
36.4	Ti (3p)

Correction: +3.6 eV

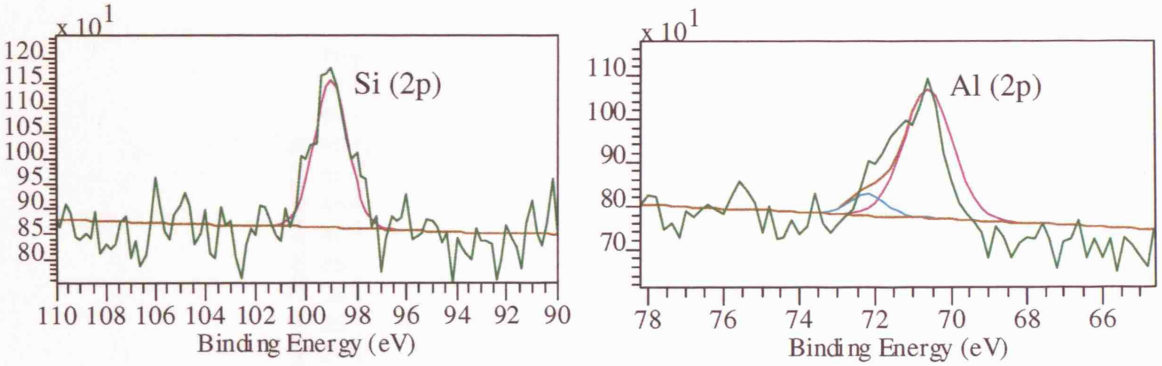

Figure 3.28: X-Ray Photoelectron spectrum of the silicon (2p) and aluminium (2p) region of **S8**

In the silicon spectrum of Figure 3.28, the Si (2p) peak at 103.0 eV (+3.6 eV correction) is ascribed to silica or silicon dioxide as it corresponds very well to reference values [97]. The aluminium region for **S7** shows that the peak can be resolved into one more intense peak at 74 eV with a small one at higher binding energy 75.7 eV. The graph shows that the aluminium is in two different environments. The peak at 74.2 eV is similar to the Al_2O_3 peak in **S7** indicating that the outer coating could be aluminium oxide based. The shoulder at 75.2 eV may correspond to aluminium in a small amount of magnesium aluminium silicate as seen in **S6**.

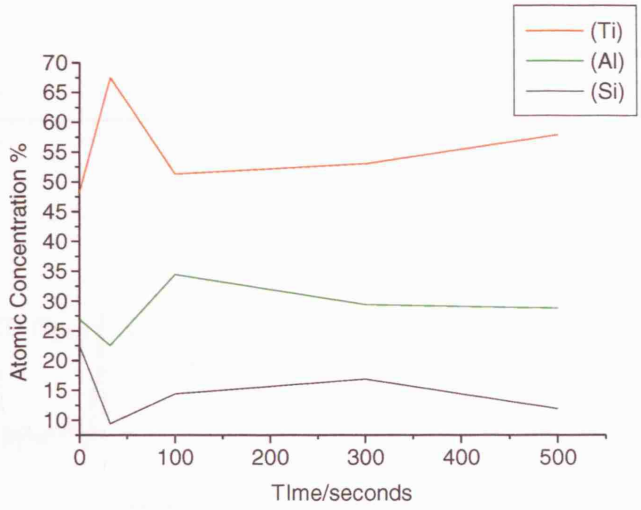

Figure 3.29: Depth profile of **S8**.

The depth profile showing the main metals present in **S8**, indicate that the silicon atoms follow the same trend as the aluminium atoms, which are part of the coating. Thus, silica may also be part of the coating material. Both materials decrease in intensity as the sample is sputtered.

3.4.5 X-Ray Photoelectron Spectroscopy of S10

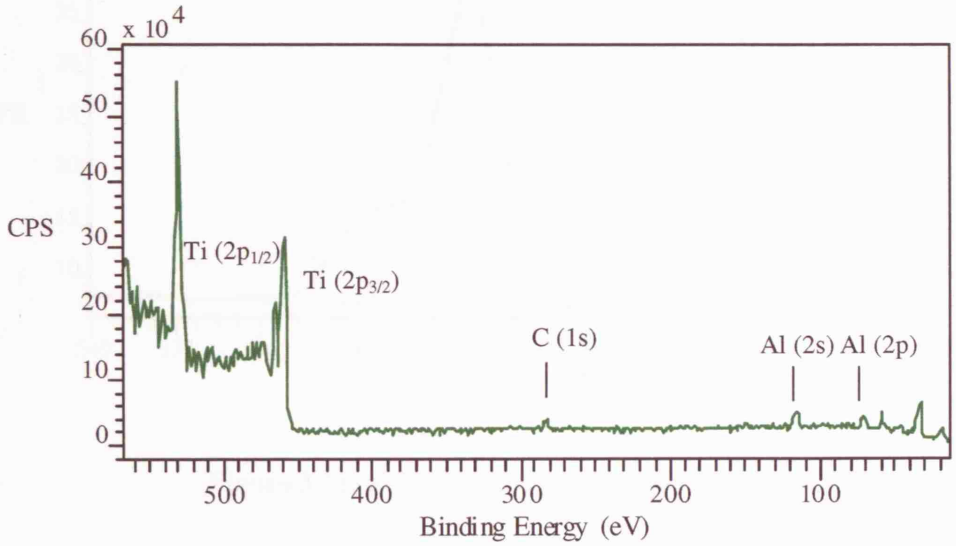

Figure 3.30: X-Ray Photoelectron survey for **S10**.

Table 3.8: X-Ray Photoelectron binding energies for **S10** components.

Binding Energy/eV	**Species**
465.5	Ti^{4+} ($2p_{1/2}$)
460.2	Ti^{4+} ($2p_{3/2}$)
529.0, 531.0, 533.0	O (1s)
285.0	C (1s)
116.1	Al (2s)
71.0	Al (2p)
33.0	Ti (3p)

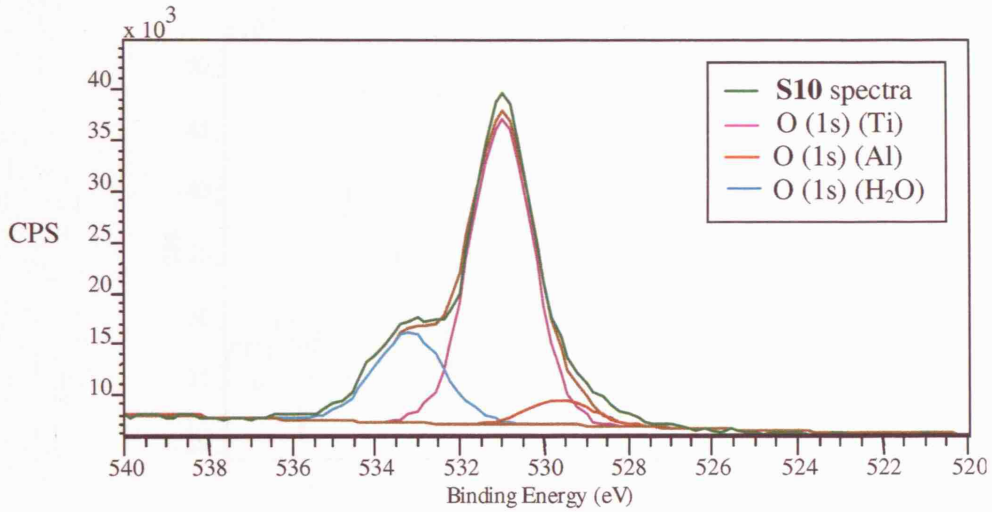

Figure 3.31: X-Ray Photoelectron oxygen (2p) for **S10**.

The XPS spectra for O (1s) is asymmetric which indicates that there is more than one kind of oxygen species present on the surface. The different species can be recognised by resolving the XPS curves. The main peak at 531 eV is characteristic of metallic oxides, which is in agreement with the O (1s) binding energy arising from the titania surface. The less intense peak at 529.6 eV and the smallest binding energy of the O (1s) region are due to the O (1s) of aluminium oxide. The component at 533 eV maybe ascribed to an adsorbed species such as oxygen chemisorbed or adsorbed water [107].

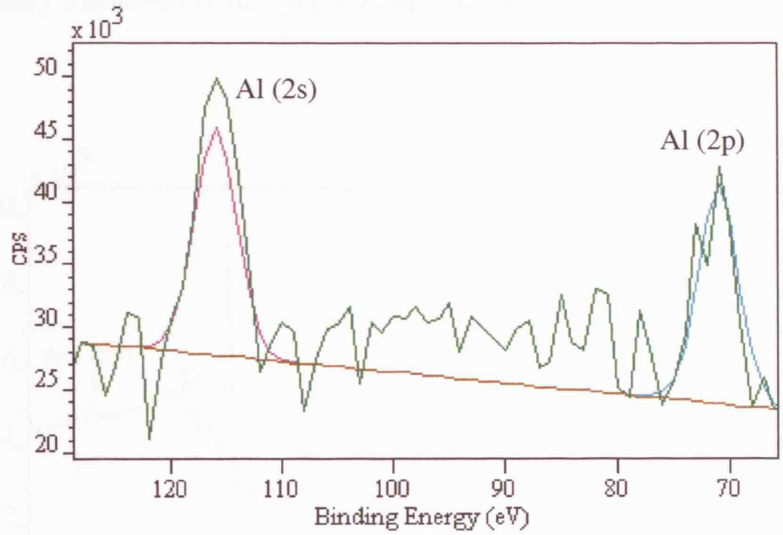

Figure 3.32: X-Ray Photoelectron spectra of aluminium (2p) and (2s) in **S10**.

There is only one main Al (2p) peak at 71.0 eV for **S10**, which is known to have aluminium oxide (alumina) as the outer coating to the core titanium dioxide. Reference values usually place the Al (2p) peak for alumina in the range 71-73 eV[97]. The depth profiling result also gives an indication of what metallic elements may be on the surface of the particles. As the etching depth is increased, the concentration of the elements on the surface of the particle will decrease as the titanium concentration increases. This is seen for **S10** in Figure 3.33.

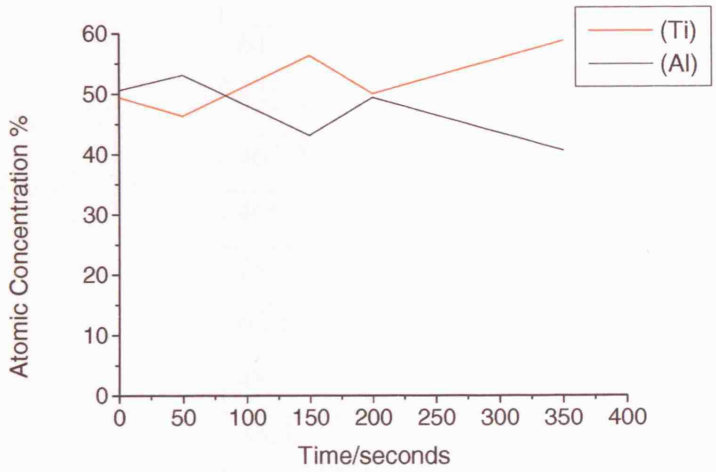

Figure 3.33: Surface etching profile of **S10**.

3.4.6 X-Ray Photoelectron Spectroscopy of S12

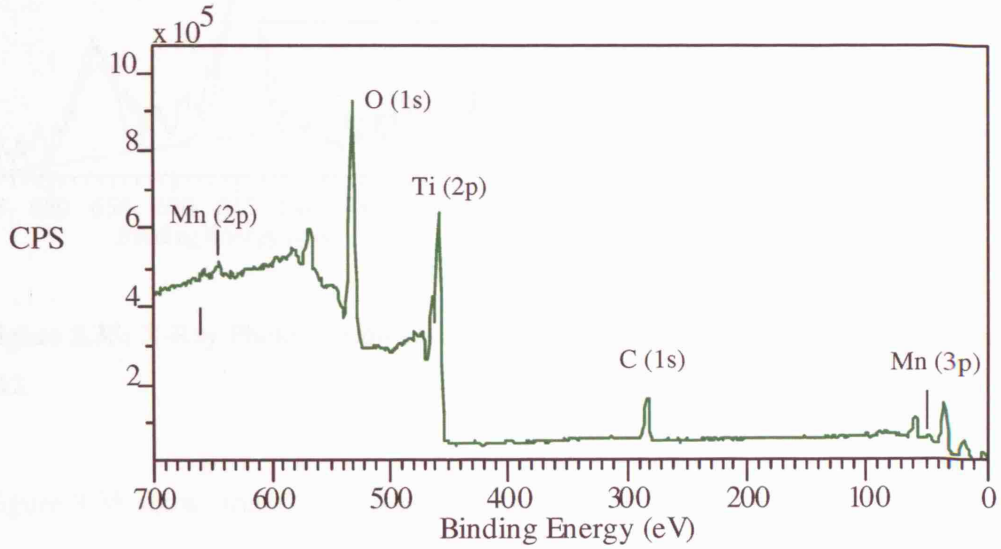

Figure 3.34: X-Ray Photoelectron survey of **S12**.

Table 3.9: X-Ray Photoelectron binding energies of **S12** components.

Binding Energy/ eV	Species
658.4	Mn ($2p_{1/2}$)
647.3	Mn ($2p_{3/2}$)
532.4	O (1s)
461.2	Ti^{4+} ($2p_{1/2}$)
466.8	Ti^{4+} ($2p_{3/2}$)
285.0	C (1s)
60.1	Ti (3s)
48.7	Mn (3p)
35.4	Ti (3p) Ti
5.25	Mn (DS-3s)

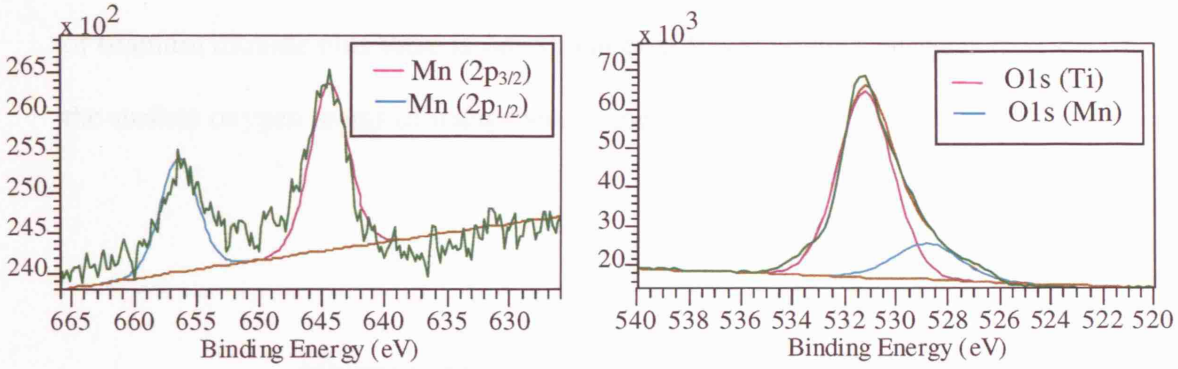

Figure 3.35: X-Ray Photoelectron spectrum of the manganese (2p) and oxygen (1s) region of **S12**.

Figure 3.35 shows that the manganese region of the spectrum is split into a doublet with the Mn ($2p_{1/2}$) and Mn ($2p_{3/2}$) spin orbit components, similar to that of titanium but at higher binding energies, 658.4 eV and 647.3 eV respectively. Reference values for manganese ($2p_{1/2}$) and ($2p_{3/2}$) in manganese oxide are 653.9 eV and 642.2 eV (± 3 eV)[108]. The value of the spin orbit splitting of the core level of an element in different compounds are nearly the same. In the case of manganese, the difference between the spin orbit components for the reference values is 11.7 eV whereas that of the observed values is 12.5 eV. In general, the higher the oxidation state, the higher the binding energy for the Mn ($2p_{3/2}$) region. Peaks at around 642 eV are assigned to Mn^{4+} cations[109]. However, there are no literature values for the binding energies that are close to such a high value of the Mn region seen in **S12**. This Mn^{4+} cation maybe in a different coordination environment and interacting with a different metal element. The observed binding energy values are higher than that of the reference values indicating that the manganese ion may be attached to a more electronegative atom or may have lost electrons from the surface.

The O (1s) peak in Figure 3.35 shows that there is one intense peak at 532 eV indicative of titanium dioxide plus there is one shoulder at lower binding energies (531 eV) due to the surface oxygen atoms of manganese oxide.

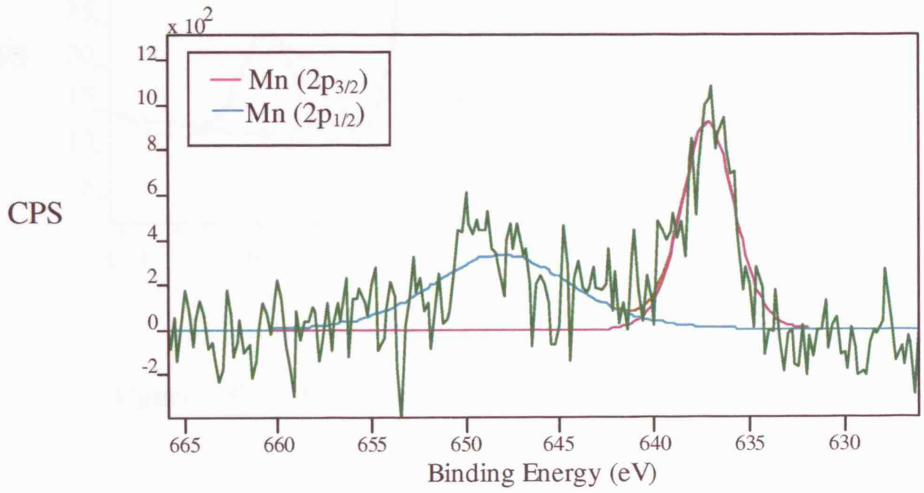

Figure 3.36: X-Ray Photoelectron spectrum of manganese (2p) in **S12** after etching.

After etching into **S12**, the XPS spectrum of manganese changed from Figure 3.35 to Figure 3.36. The binding energies for the Mn ($2p_{1/2}$) and Mn ($2p_{3/2}$) spin orbit components are now 639.0 eV and 650.8 eV, compared to 647.3 eV and 658.4 eV before etching. This decrease in the binding energies can correspond to manganese in the +2 oxidation state[110]. The decrease in binding energy can also indicate that the manganese ions are incorporated into the titanium dioxide lattice. The Mn^{4+}ions in manganese oxide would have a slightly greater pull on the outer electrons compared to Ti^{4+} therefore a decrease in the binding energy of the Mn ion may occur. Another more probable reason for the decrease in binding energy is the problem of sputter reduction, which occurs in higher valent oxides that are reduced to lower oxidation states.

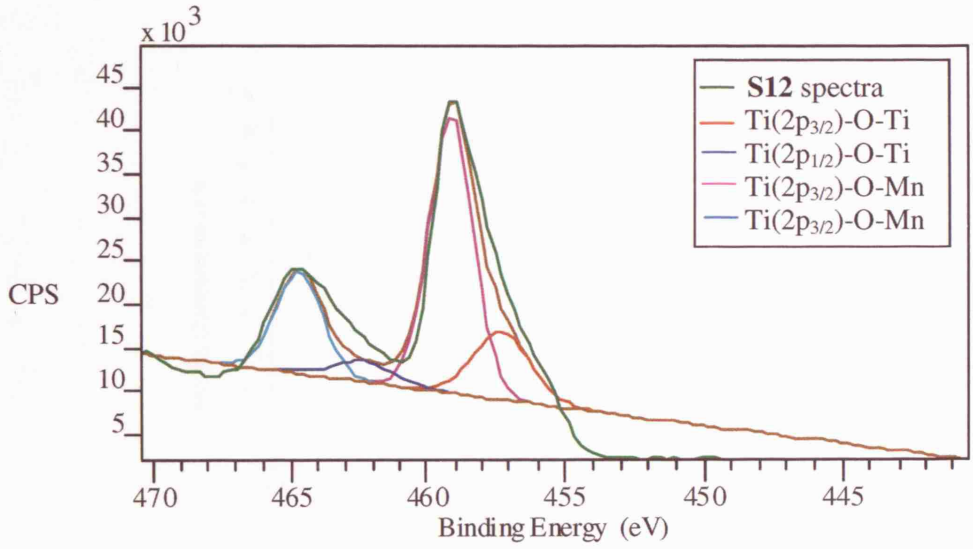

Figure 3.37: X-Ray Photoelectron of titanium (2p) region in **S12**.

From Figure 3.37, **S12** powder contains two different environments for titanium. There are two more intense peaks at 461.2 eV and 466.7 eV and two smaller peaks at 459.0 eV and 464.0 eV. The latter pair of peaks at the smaller intensity are due to the ($2p_{3/2}$) and ($2p_{1/2}$) spin orbit components of titanium in the +4 oxidation state. The doublet at higher binding energies may be indicative of titanium ions bonded to manganese to make a solid solution. These results for the titanium region in **S12** correlate with the lower binding energy of the manganese ions in Figure 3.36.

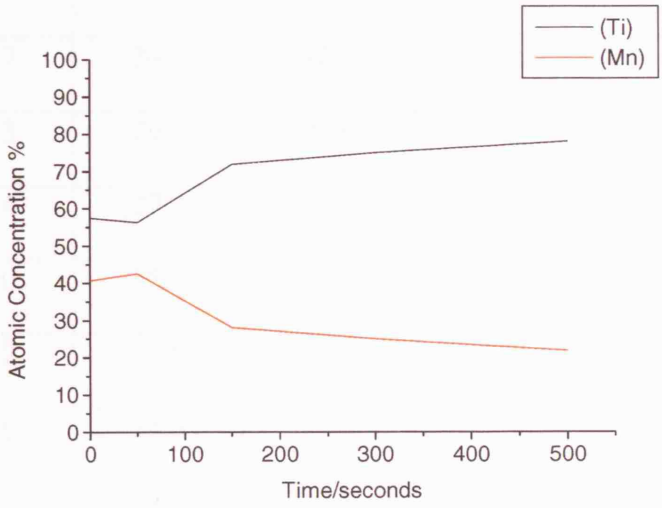

Figure 3.38: Depth profile of **S12**.

The presence of manganese before etching indicates that there is some manganese on the surface of the titanium dioxide particle.

The relative elemental concentration percentages were calculated by integrating the peak areas from the XPS spectra and applying significance factors (correlated with standards) and shown in Table 3.10.

Table 3.10: Concentrations of elements on the surface of each sample.

SAMPLE	O (1s)/%	Ti (2p)/%	C (1s)/%	Si (2s)/%	Al (2p)/%	Mn (2p)/%
S2	58.7	24.2	16.1	1.0	0	0
S3	62.3	29.8	5.6	2.3	0	0
S4	60.4	27.3	9.5	2.8	0	0
S5	55.0	25.1	17.6	2.3	0	0
S6	46.2	19.8	26.9	6.3	0.8	0
S7	61.0	16.9	20.0	1.1	1.0	0
S8	58.8	14.9	23.8	0.8	1.7	0
S9	45.3	15.3	30.2	0	1.2	0
S10	62.2	28.7	3.3	0	5.8	0
S11	46.7	20.2	31.8	0	1.3	0
S12	56.0	31.0	6.8	0	0	6.2

From the concentration results, the titanium dioxide particles seem to contain a small percentage (thin layer) of the coating material, which can be alumina, silica, organosilane or silicone in nature. The elemental percentages range from 0.8% of aluminium in **S6** to 5.8% in **S10**; also 0.8% of silicon in **S8** to 6.3% in **S6**. Even though the XPS technique can determine elemental compositions, some of these powders extracted from suncreams may have inorganic residues such as magnesium aluminium silicate, which is used as an absorbent in lotions. Magnesium was shown to be present in the XPS of **S6** and possibly **S8**. Therefore, unless the powder is a pure sample obtained directly from the manufacturers and has no other inorganic residues, the elemental percentages obtained here are not exact. This would explain why **S6** features such a large amount of silicon. This amount however is decreased as the S6 sample is

etched into, suggesting that silica maybe apart of the coating material on titanium dioxide.

Table 3.11: Si, Al and Mn/Ti Ratios before and after etching into the samples.

Sample	Si/Ti Ratio At surface	Si/Ti Ratio After etching	Al/Ti Ratio At surface	Al/Ti Ratio After etching
S2	0.04	0.006	-	-
S3	0.08	0.001	-	-
S4	0.1	0.04	-	-
S5	0.09	0.06	-	-
S6	0.32	0.22	0.04	0.02
S7	0.07	0.009	0.06	0.003
S8	0.05	0.03	0.11	0.03
S9	-	-	0.08	0.004
S10	-	-	0.2	0.01
S11	-	-	0.06	0.02
S12	-	-	0.2 **(Mn/Ti)**	0.26 **(Mn/Ti)**

The results shown in Table 3.11 are evidence for the coated particles. After etching into the samples, a decrease is seen in the Si/Ti and Al/Ti ratios. After sputtering the particles, the coating materials would be partly removed. If the titanium dioxide and silica or alumina particles existed as separate entities, a constant Si/Ti and Al/Ti ratio would be observed. The small percentage of silicon and aluminium present also indicates that they may be a thin layer coating material rather than a separate component present in the powders. The only powder which shows an increase in sputtering ratio after etching is **S12** which has a Mn/Ti ratio of 2.0 before etching and 2.6 after etching. This may indicate the presence of a solid solution of manganese oxide in titanium dioxide.

3.4.7 Comparison of XPS Data

XPS is quantitative technique for elemental composition, which produces reproducible XPS data with a resolution of 0.1 eV. The electrons that are excited by soft X-ray radiation have short mean free paths in the solid so that the majority of electrons detected are from the atoms at or near to the surface. These are the only electrons which can escape materials capture and travel to the detector[111]. Depending upon the matrix and the kinetic energies of the electrons, the first 10 atomic layers or roughly 2.5 nm are usually detected with XPS[112]. The depth profiling of all of these powders have shown that the main metallic element to be found at the surface is titanium. As the titanium dioxide particles are supposedly uniformly coated with aluminum oxide or an organosilane, unless the coating is patchy, this means that the outer coating is very thin and less than 2.5 nm.

There are variations in the binding energies from 0.1 eV to 10 eV, known as chemical shifts, which can give information about the different oxidation states of the ions as well as chemical environment. Chemical shifts are correlated with the overall charge of the atom, where a reduced charge gives an increase in binding energy. The two main factors that are associated with chemical shift are number of substituents and their electronegativity. **S8**, for example has a Si (2p) binding energy of 103.4 eV that is assigned to the presence of silica, as determined by literature values. **S3** has an organosilane outer coating and the Si (2p) binding energy is observed at the smaller value of 102.8 eV. This decrease in binding energy means that the silicon atom in **S3** is attached to a less electronegative atom than the silicon atom in **S8**. This is consistent with a Si – O bond in **S8** and a Si – C bond in **S3**.

Sputter depth profile analysis or depth profiling was also carried out by sputtering or continuous removal of the surface material by energetic noble gas (argon) ion bombardment. Deeper layers are thus exposed to the surface and subsequently analysed. This technique gave an estimate of the concentrations of different elements on the surface and in the bulk but near to the surface of the particles. However, as the powder is made up of non-uniform layers, the accuracy of the intensity/concentration of the elements determined by etching is dependent upon the uniformity of the layers. Sputter etching is also regarded as a destructive technique as it always leaves some damage. There is also the problem of sputter reduction as seen for Mn^{4+} in **S12**. This occurs in higher valent oxides which are reduced to lower oxidation states. This problem does not largely affect the work carried out here, as the surface components of the particles are the only real interest.

Despite the advantages of using XPS as a quantitative analysis technique, there are a few limitations. The monochromatic x-rays have a low flux and the sampling depth varies with electron kinetic energy and the material being analysed. The XPS spectra are also complicated with certain features such as x-ray satellites which are produced from non-monochromatic x-ray sources. Although not an important limitation in this body of work, XPS is insensitive in the detection of H and He.

3.4.8 Summary of XPS Data

3.4.8.1 Coatings containing aluminium

The samples that contain aluminium oxide in their outer shell are **S6**, **S7**, **S8**, **S9**, **S10** and **S11** as shown by the peak at approximately 74 eV, which corresponds to Al (2p) in Al_2O_3. The literature values for Al 2p range from 71.47 – 76.0 eV[113].

3.4.8.2 Coatings containing silicon

S3 has a trimethoxycaprylylsilane coating which contains mostly Si–O bonds and Si–C bonds. It is known from the manufacturer's data sheet that **S3** has this particular silane coating. The main indication of the silane coating in **S3** was a peak in the silicon 2p region of the XPS spectra at 102.8 eV. The Si (2p) peaks for **S2** (102.1 eV), **S4** (102.1 eV), **S5** (102.7 eV), **S6** (102.8) and **S7** (102.0) also fell in the region of a silane or a silicon polymer. The small difference suggests that both isolated sunscreen samples contain the same outer coating on their titanium dioxide cores. **S8** possessed silicon oxide (silica) as noted by the high Si (2p) peak at 103.4 eV.

Table 3.12: Summary of XPS Data

Sample	Binding Energy (eV)	Elements	Interpretation/Surface Coating
S2	464.4, 458.9	Ti^{4+} (2p)	Ti^{4+} in TiO_2 lattice
	102.7	Si (2p) – O	Silicone polymer/
	102.1	Si (2p) – C	Organosilane
S3	464.5, 458.9	Ti^{4+} (2p)	Ti^{4+} in TiO_2 lattice
	102.8	Si (2p) – O	Silicone polymer/
	102.2	Si (2p) – C	Organosilane
S4	464.4, 458.9	Ti^{4+} (2p)	Ti^{4+} in TiO_2 lattice
	102.1	Si (2p) – C	Silicone polymer
S5	464.7, 459.0	Ti^{4+} (2p)	Ti^{4+} in TiO_2 lattice
	102.7	Si (2p) – O	Silicone polymer/
			Organosilane
S6	466.0, 460.9	Ti^{4+} (2p)	Ti^{4+} in TiO_2 lattice
	102.8	Si (2p) – O	Silicon Dioxide/
			Silicone polymer
	73.7, 74.4	Al (2p) – O	Aluminium Oxide
S7	464.4, 458.2	Ti^{4+} (2p)	Ti^{4+} in TiO_2 lattice
	102.0	Si (2p) – O	Silicone polymer
	74.3	Al (2p) – O	Aluminium Oxide
S8	466.1, 460.5	Ti^{4+} (2p)	Ti^{4+} in TiO_2 lattice
	103.4	Si (2p) – O	Silicon Dioxide
	75.7, 74.2	Al (2p) – O	Aluminium Oxide
S9	464.4, 458.2	Ti^{4+} (2p)	Ti^{4+} in TiO_2 lattice
	76.4, 74.6	Al (2p) – O	Aluminium Oxide
S10	465.5, 460.2	Ti^{4+} (2p)	Ti^{4+} in TiO_2 lattice
	71.0	Al (2p) – O	Aluminium Oxide
S11	464.4, 459.0	Ti^{4+} (2p)	Ti^{4+} in TiO_2 lattice
	75.0	Al (2p) – O	Aluminium Oxide
S12	657.5, 645.3	Mn^{4+} (2p) – O	Manganese Oxide
	466.8, 461.2	Ti^{4+} (2p)	Ti^{4+} in TiO_2 lattice (possible solid solution of Mn – O – Ti)

3.5 SOLID STATE NUCLEAR MAGNETIC RESONANCE

3.5.1 Introduction

Nuclear Magnetic Resonance (NMR) involves the study of magnetic energies of those nuclei which possess nuclear magnetic moments, in the presence of a magnetic field. Solid state NMR (SSNMR) is a powerful tool for structure elucidation. It is a complementary technique to XRD as it does not require long-range order for analysis and is therefore particularly useful with amorphous solids. SSNMR deals with powdered samples i.e. samples with many crystallites having random orientations. Nuclear spin interactions which affect SSNMR spectra such as chemical shielding, dipole-dipole coupling and quadrapolar coupling are dependent on the crystallite orientation and are said to be anisotropic[122]. Therefore, the NMR spectrum of a powdered sample contains broad lines as all of the different molecular orientations give rise to different spectral frequencies.

One technique that is used to remove the effects of chemical shift anisotropy and to assist in the removal of heteronuclear dipolar coupling effects is Magic Angle Spinning (MAS). The sample is spun at an angle of 54.74° to the magnetic field. MAS also narrows the lines from quadrupolar interactions which arise in nuclei with $I > ½$ and are due to the interaction of the nuclear electric dipole moment with the field gradient around the nucleus[122].

Another technique which is used to aid in SSNMR is Cross Polarisation (CP). There are two main problems of SSNMR:

1. the nucleus of interest is of low natural abundance and/or sensitivity.
2. long spin-lattice relaxation times

Cross polarisation substantially increases the signal to noise ratio in the spectra of such magnetically dilute (rare) systems as ^{13}C and ^{29}Si. Cross polarisation enhances the magnetisation of the rare spins from that of the abundant spins (usually protons) and hence, the intensity of the spectrum of rare spin systems effectively depends on the relaxation of the proton spin system. The spin-lattice relaxation times of protons are shorter than those of rare spins[123].

In NMR spectroscopy, the shapes and positions of the spectral peaks indicate the nuclei in different chemical environments and the peak areas are proportional to the number of nuclei in each given symmetry.

3.5.2 Nuclei of Interest

The main materials studied were titanium dioxide particles with either an aluminium or silicon containing outer coating (as determined by XPS) hence ^{27}Al and ^{29}Si nuclei were used to determine the possible structures contained in the powders.

3.5.2.1 ^{29}Si NMR

^{29}Si (4.7% abundance) is a magnetically 'dilute' nucleus in all silicon compounds and thus may be investigated by CP/MAS techniques. The ^{29}Si CP MAS NMR technique is sensitive to silicon atoms around OH and CH_x (where x is the number of hydrogen

atoms) groups and has been regarded as the standard method of characterisation of silicate compounds[121]. ^{29}Si NMR spectroscopy provides direct information about the structure of materials from measurements of the isotropic chemical shifts. This parameter is influenced significantly by the co-ordination number of the Si, which in compounds coordinated to oxygen varies by approximately 50 ppm when going from 4 to 6 coordinate. Silicon in inorganic compounds is most commonly bonded to oxygen and prefers four fold co-ordination. Separate signals are observed for the ^{29}Si nucleus in the basic SiO_4 unit depending on the environment given by the four atoms attached to the oxygens at the corners of the SiO_4 tetrahedron in the second coordination sphere[123]. Silicon NMR uses the relationship between each silicon atom and its neighbours, counting the number of other silicon atoms to which each silicon atom is connected to, through an oxygen atom. Silicate structures can be regarded as being made up of tetrahedral units with varying degrees of polymerisation. These are described with the 'Q^n' notation where Q denotes a silicon atom bonded to four oxygen atoms. The superscript n, where n = 0 to 4 refers to the number of further silicon atoms (or Q units) attached to the tetrahedral corners.

- Q^0 — The silicon atom is not bonded to any other Si – O linkages. This characterizes the silicon in the monomeric silicate anion SiO_4^{-4}.
- Q^1 — The silicon atom is bonded to one other Si – O linkage. Examples are silicon atoms in a two-atom chain or at the ends of longer chains.
- Q^2 — The silicon atom is bonded to two other Si – O linkages. Examples are silicon atoms in the middle of a linear anion or silicon atoms that form a planar cyclic structure.

- Q^3 — The silicon atom is bonded to three other Si – O linkages. An example is silicon atoms at the corner of a three dimensional structure.
- Q^4 — The silicon atom is bonded to four other Si – O linkages. Examples are silicon atoms in the interior of polymeric colloidal silica or silicon atoms in the interior of silica gel particles.

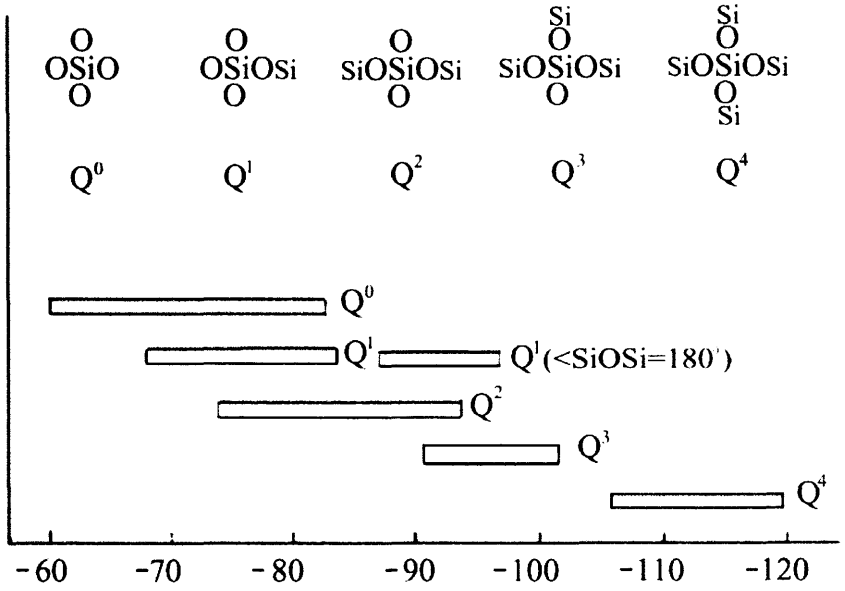

^{29}Si Chemical Shifts (ppm) w.r.t TMS[121]

Figure 3.39: ^{29}Si MAS Nuclear Magnetic Resonance Chemical shifts for various possible silicate configurations.

As seen in Figure 3.39, the ^{29}Si shift has a more negative chemical shift with an increase in the number of Q units. This is due to increased electronic shielding of the central silicon nucleus.

3.5.2.2 ^{27}Al NMR

Aluminium is a very favourable nucleus for NMR investigations because its isotope is 100% naturally abundant[121]. This feature will give much larger intensities than ^{29}Si NMR. The drawback of the aluminium nucleus is that its quadrupolar moment (I = 5/2) results in broad lines, distortion of the spectral peaks and displacement from the isotropic (true) chemical shift. Therefore, it is necessary to carry out the experiments at high magnetic field strengths where the quadrapole effects are minimised but not completely removed. If some of the coatings in this project are composed of solid solutions of silicon and aluminium, then there can be a range of possible aluminosilicate structural positions that are shown in Figure 3.40.

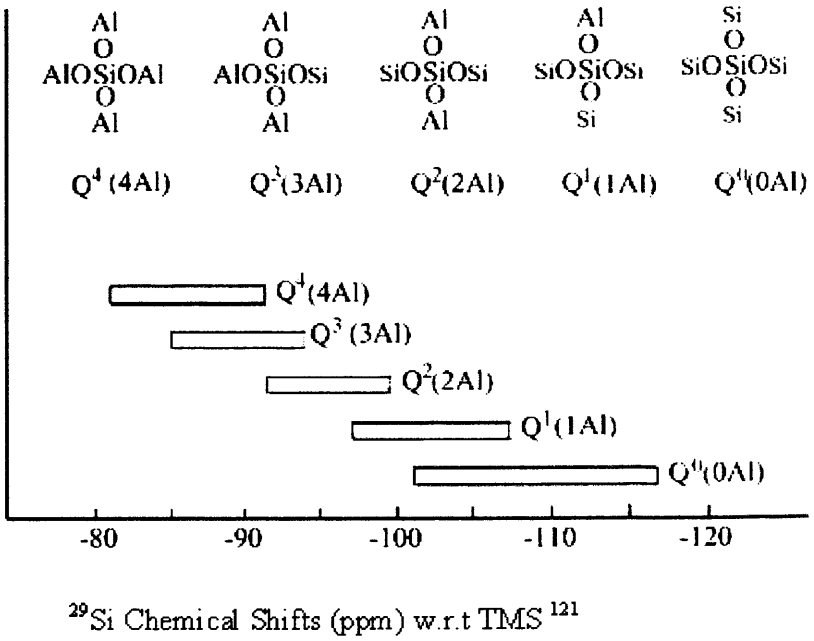

Figure 3.40: ^{29}Si Nuclear Magnetic Resonance Chemical shifts for possible configurations of aluminosilicates.

Changes in the next-nearest-neighbour element produces small but measurable shifts in the ^{29}Si spectra, usually in the order of ~10 ppm as seen in Figure 3.40 for aluminium. From Figure 3.39, there is a fair amount of overlap of the chemical shifts in the various groups which can lead to some uncertainty therefore the next nearest neighbour interaction must also be taken into account when making assignments.

This section describes NMR studies of titanium dioxide which has different structural forms and coatings. The different coatings on the titania particles is the main area of interest by using SSNMR. Of the 10 different samples (6 sunscreen isolated and 4 pure), 7 samples were tested (5 sunscreen isolated and 2 pure). **S12**, one of the pure samples was not tested because it contained neither silicon or aluminium atoms.

3.5.3 Solid State Nuclear Magnetic Resonance of Titanium Dioxide Pure Powders

3.5.3.1 Solid State Nuclear Magnetic Resonance of S3

3.5.3.1.1 ^{29}Si NMR

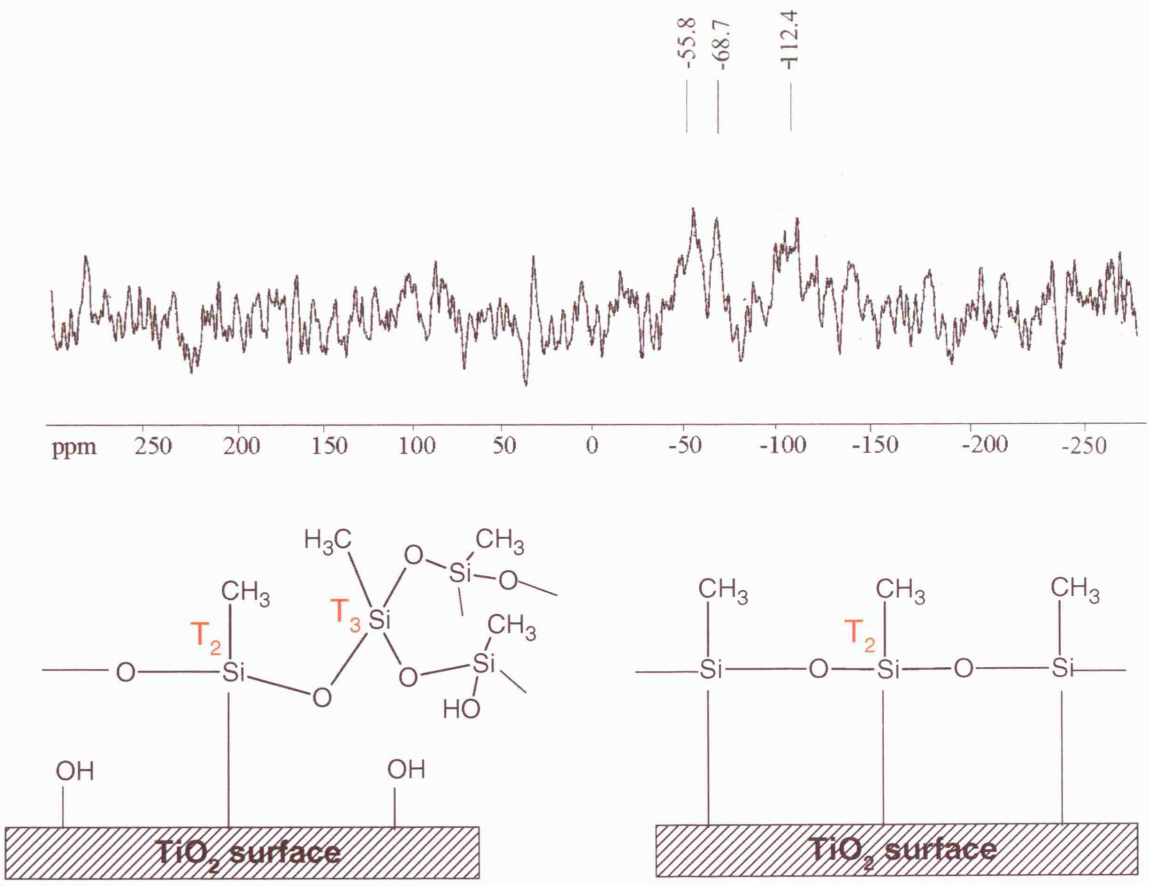

(A) *Vertical Polymersiation*

(B) *Horizontal Polymerisation*

Figure 3.41: ^{29}Si Nuclear Magnetic Resonance for **S3** showing trimethoxycaprylylsilane as the coating material and possible polymerisation structures, (A) vertical (B) horizontal polymerisation.

S3 is a pure powder from the manufacturers which shows a negligible amount of silicon present as the coating material since the peak intensities are almost indistinguishable from the background noise (Figure 3.41). The peaks at -55.8 and -68.7 ppm are much

lower than the shifts seen in Figure 3.39 which shows the usual shifts for Q^n silicon species. There is the possibility that the latter could be due to Q^0 species which appear at chemical shifts from -60 ppm to -80 ppm, however -55.8 ppm falls just below this region.

With respect to condensed or grafted organosilanes, signals can be observed in the -45 to -50 ppm, -55 to -60 ppm and -65 to -70 ppm regions and are assigned to mono(T1)-, bi(T2)-, and tri(T3)-fold Si–O-linked silicones, respectively[124]. According to the assignments of silicones, **S3** would possess T2 and T3 Si – O linkages due to the peaks at -55.8 ppm and -65.7 ppm. The organosilane coating on the titanium dioxide surface of **S3** could possibly have the structure shown in Figure 3.41 (A).

The silanisation process onto the titanium dioxide surface produced vertical polymerisation giving polycondensed structures. If the silane had assembled onto the titania surface horizontally, only the presence of T2 linkages would be detected via NMR (Figure 3.41 (B)).

There is also evidence of a small amount of Q^4 siloxane from the peak at –112 ppm which falls within the Q^4 range –108 to –120 ppm for conventional Q^n assignments and signifies a silicon atom bonded to four other silicon atoms. Such a compound would not be grafted onto the surface of the titanium dioxide core and could be residues from the manufacturing process. However, due to the low signal to noise ratio of the ^{29}Si NMR spectrum of **S3**, the exact structures are difficult to determine and those shown in Figure 3.41 are only possible structures. As expected, the ^{27}Al NMR spectra showed no aluminium in the **S3** powder.

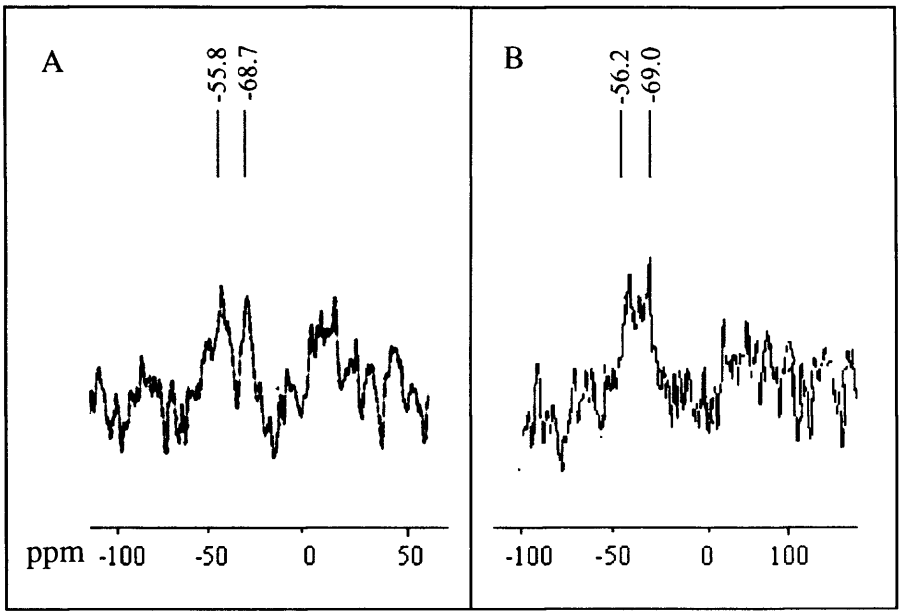

Figure 3.42: Comparison of **S3** (A) before and (B) after solvent extraction.

The pure powder, **S3** was put through the solvent extraction process as it contains an organosilane coating to determine whether the process was destructive to the coat. The two main peaks of the ^{29}Si NMR are comparable (error of ± 1 ppm) however, it is more difficult to distinguish between them due to the low quantity of silicon present in the coating material. ^{13}C is a better nucleus to test whether the organic part of the coating was removed or chemically altered during the extraction process. As seen from Figure 3.43, the peaks present in the original powder and the extracted powder are the same confirming that the coating was not chemically damaged during the chemical wash procedure. The ^{13}C NMR peaks are from the alkyl groups attached to the silicon atom of the trimethoxycaprylylsilane coating. The low intensity resonances between -40 to 0 ppm indicates that there are only alkyl species present[125].

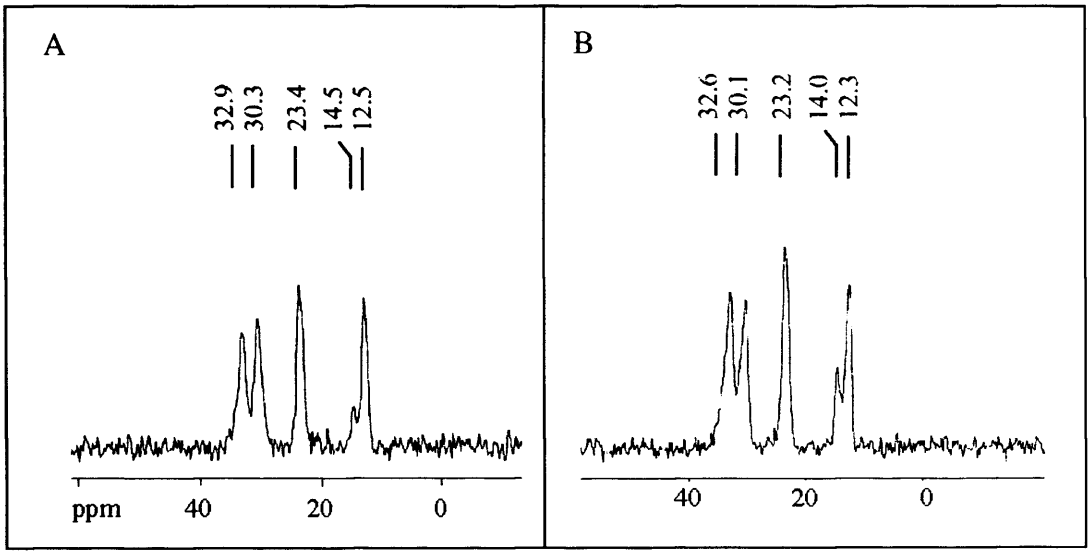

Figure 3.43: Comparison of ^{13}C nuclei for **S3** (A) before and (B) after solvent extraction.

^{13}C NMR was carried out for all samples and **S3** is illustrated to show that the extraction process did not damage the coating.

.

3.5.3.2 Solid State Nuclear Magnetic Resonance of S10

3.5.3.2.1 ^{27}Al NMR

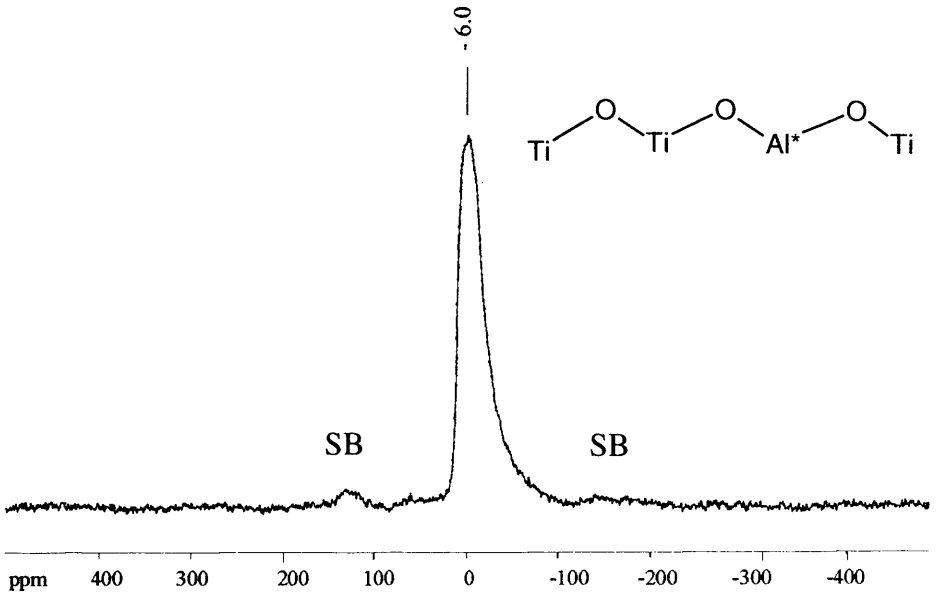

Figure 3.44: ^{27}Al Nuclear Magnetic Resonance of **S10**. SB = Spinning Side Bands

As for ^{29}Si, isotropic shifts for ^{27}Al in oxides are most strongly influenced by coordination number. ^{27}Al is capable of unambiguously distinguishing between tetrahedrally and octahedrally co-ordinated aluminium by their clear difference in chemical shift ranges. These resonances are shifted by complexation which induces a change in the electronic environment of the Al atom i.e. a shielding of its local magnetic field. The range for AlO_4 units is 50 to 80 ppm[3], while AlO_6 units have a chemical shift range of –10 to 20 ppm w.r.t. $Al(H_2O)_6^{3+}$. Aluminium oxide shows a ^{27}Al MAS NMR spectrum with a peak around 12 ppm[126]. The large single peak at -6.0 ppm (Figure 3.44) maybe indicative of an Al attached to an inorganic anion such as Al, which is substituted in the TiO_2 lattice of the rutile crystal structure. Such a substitution can be in the range of -1 to -7 ppm[127]. Generally, substitution increases chemical shielding thus making the chemical shift more negative[126]. This is a well-known characteristic for

silicon and aluminium atoms. From the XRD measurements, aluminium oxide as α-alumina was determined to be present in **S10**. In this structure, 6 oxygen atoms surround each aluminium atom octahedrally, and each oxygen atom is surrounded by four aluminium atoms. So there is no tetrahedral aluminium coordination involved in this structure.

Spinning side bands are noticed on the aluminium NMR spectrum. These are lines with a centre band at the isotropic chemical shift. For magic angle spinning to reduce the broad lines from the powder to a single line at the isotropic chemical shift, the rate of spinning the sample must be fast compared to the anisotropy of the interactions being spun out. (~3-4 x anisotropy) Slower spinning causes side bands in addition to the spectral line[122].

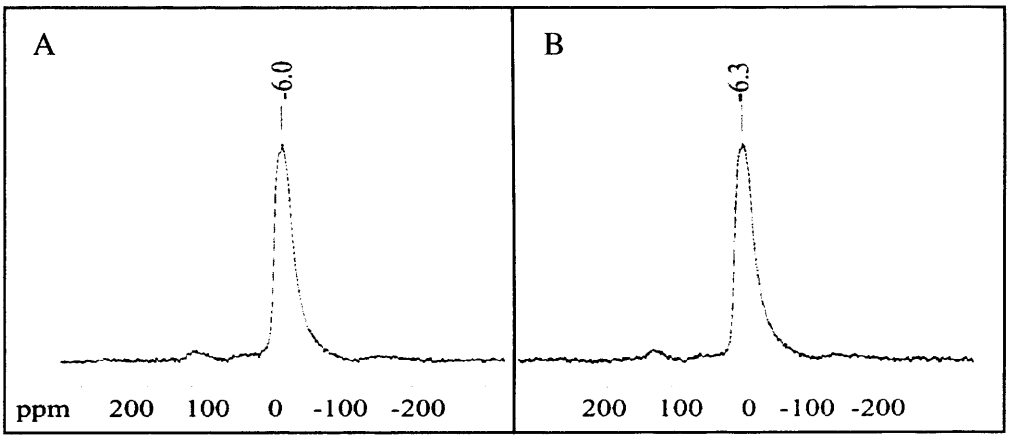

Figure 3.45: Comparison of (A) **S10** in its natural state and (B) **S10**-EX, after chemical extraction.

Figure 3.45 shows **S10** before and after solvent washing. The chemical shifts are the similar indicating that the powder seemed to be chemically unchanged by the extraction procedure.

3.5.4 Solid State Nuclear Magnetic Resonance of Titanium Dioxide Extracted Powders

3.5.4.1 Solid State Nuclear Magnetic Resonance of S4

3.5.4.1.1 ^{29}Si NMR

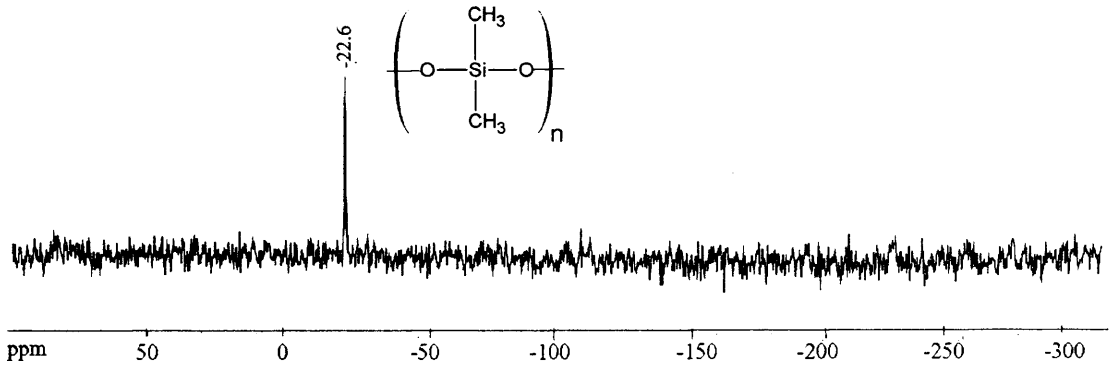

Figure 3.46: ^{29}Si Nuclear Magnetic Resonance spectrum of **S4** showing the presence of a polysiloxane.

The ^{29}Si shift at -22.6 ppm shows a narrow peak that indicates the existence of the repeat unit of polysiloxane chains $-(O\text{-}Si(CH_3)_2\text{-}O\text{-})_n$ present in **S4** which could be part of the coating material (Figure 3.46). Research has shown that a titanium atom attached to a polysiloxane yields a sharp ^{29}Si peak at a chemical shift of -22 ppm[128].

The ^{27}Al spectra showed no peaks due to aluminium present in the powder.

3.5.4.2 Solid State Nuclear Magnetic Resonance of S6

3.5.4.2.1 ^{29}Si NMR

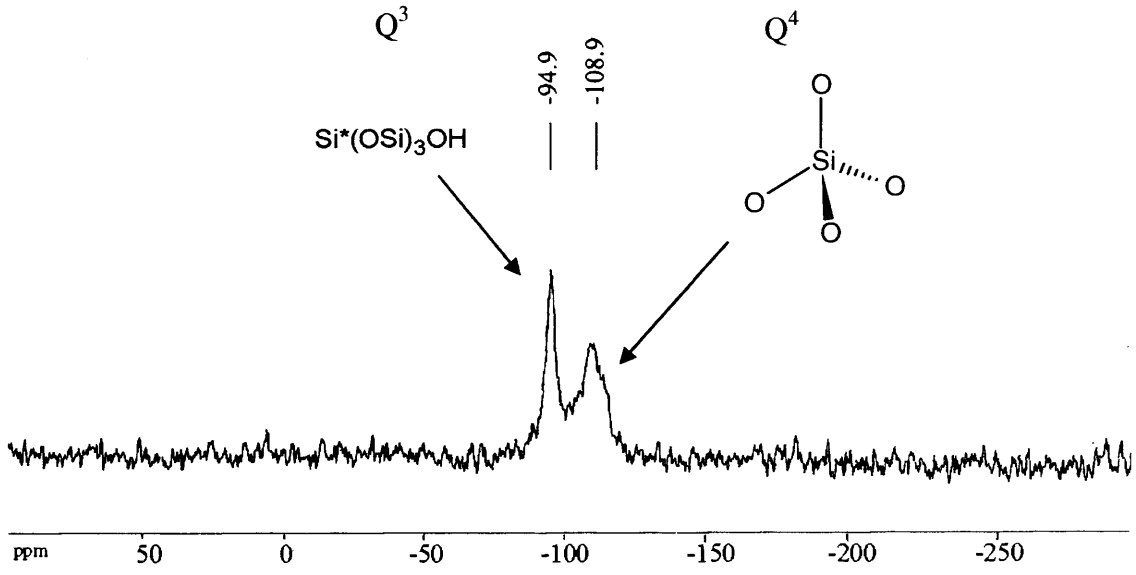

Figure 3.47: ^{29}Si Nuclear Magnetic Resonance of **S6**.

The ^{29}Si NMR Data indicates the presence of a Q^3 centre ($Si^*(OSi)_3(OH)$ at -94.9 ppm and a Q^4 ($Si^*(OSi)_4$) centre at -108 ppm which could both be due to the presence of magnesium aluminium silicate (Figure 3.47). Magnesium aluminium silicate or montmorillonite is a smectite clay which is used in cosmetics to thicken formulations and to produce a smooth texture. The basic crystal structure of smectites is an octahedral alumina sheet sandwiched between two tetrahedral silica sheets. Close-packed aluminosilicates have SiO_4 groups which are usually Q^3 or Q^4 and the shifts are also influenced by whether the attached groups are with silicon or aluminium centres[123]. The ^{29}Si resonances in zeolites shift by approximately 5 ppm per Al next nearest neighbour. In this case, the peak at -94.9 ppm is due to Q^3 (0Al) units which are SiO_4 units crosslinked in the tetrahedral sheets with no aluminium in the neighbouring tetrahedral. The less intense, broad, Q^4 ($Si^*(OSi)_4$) centre at 108 ppm corresponds to

three dimensional silica with no aluminium present (Q^4 (0Al)). The silica shown here is in an amorphous state since it was not observed in the XRD measurements. The peak is quite broad and seems to have a shoulder which could possibly be a second peak showing the presence of silica as the coating material. The varying line widths seen in the ^{29}Si NMR spectrum reflect varying degrees of crystallinity or structural order in the samples. A broad linewidth indicates an amorphous state with a substantial degree of short range order but no long range order.

3.5.4.2.2 ^{27}Al NMR

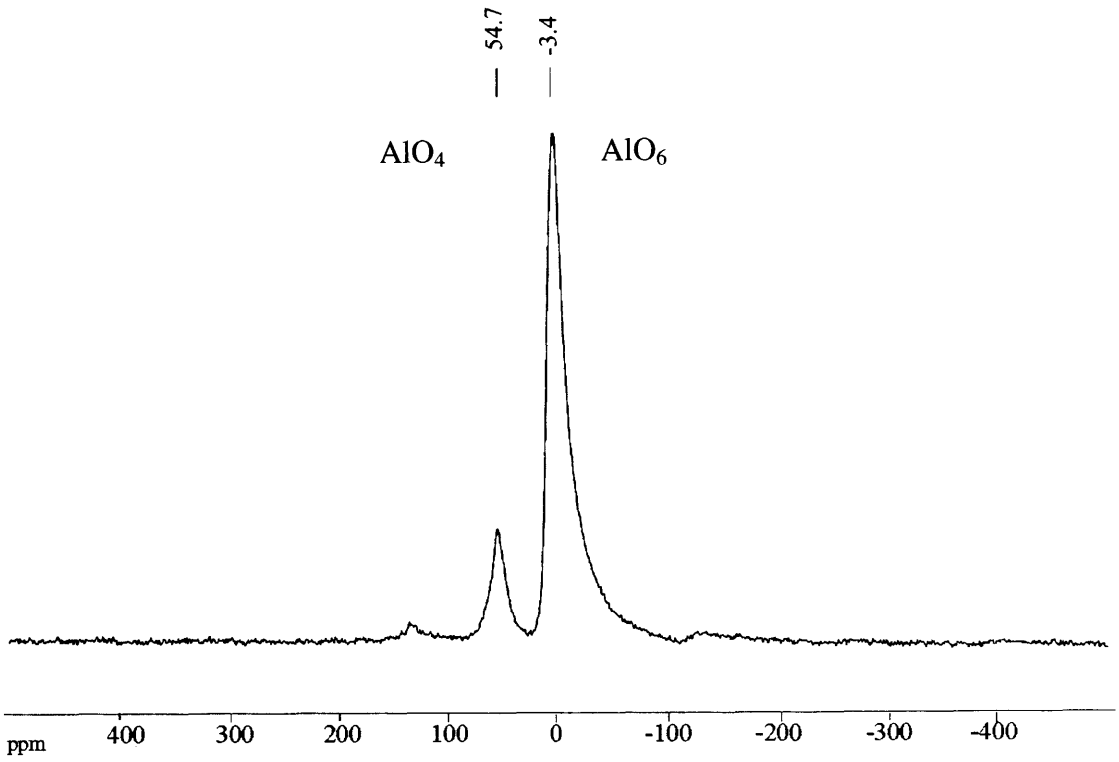

Figure 3.48: ^{27}Al MAS Nuclear Magnetic Resonance of **S6**.

The peak at +54.7 ppm (Figure 3.48) is due to the presence of 4 co-ordinate (tetrahedral) oxygen environments around aluminium (AlO_4). Magnesium aluminium silicate is one of the inorganic compounds which remained after the extraction

procedure. This was determined by cross-referencing the ingredients listing on the commercial sunscreen bottle to XPS. This type of clay has octahedral alumina sheets sandwiched between tetrahedral silica sheets. However, the aluminium often substitutes for the silicon which can give the ^{27}Al NMR peak at 54.7 ppm. It may also contributes to the signal at the -3.4 ppm showing octahedral aluminium as the AlO_6 octahedron in magnesium aluminium silicate which can exhibit an Al peak from -10 ppm to 20 ppm. The negative chemical shift at -3.4 ppm could also indicate an Al site substituted to a Ti site in the rutile structure[127] like **S10** and shows a clearly defined quadrupolar line shape with sharp upfield and downfield shoulders. However, the chemical shift of -3.4 ppm is at a slightly higher value than the octahedral aluminium in **S10** at -6.0 ppm but still lower than the chemical shift literature value of 12 ppm for 'free' α-alumina. Another possibility is that the aluminium oxide is attached to the titanium dioxide surface Al_2O – TiO_2 but not substituted into the lattice as a solid solution.

3.5.4.3 Solid State Nuclear Magnetic Resonance of S8

3.5.4.3.1 ^{27}Al NMR

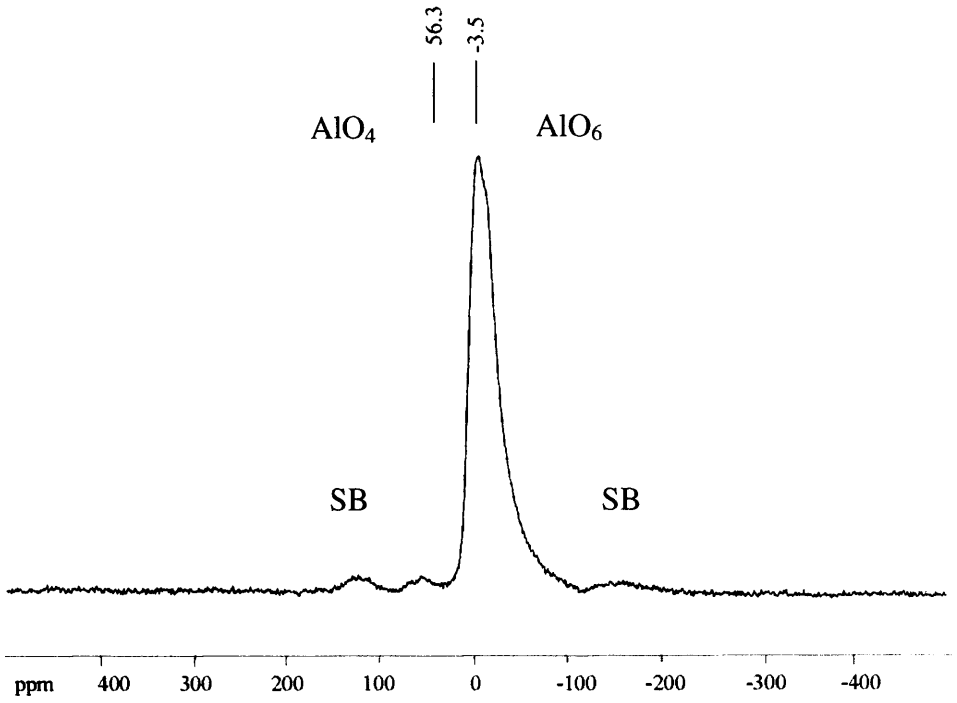

Figure 3.49: ^{27}Al MAS Nuclear Magnetic Resonance of **S8**.

The negative chemical shift at octahedral aluminium -3.5 ppm (Figure 3.49) indicates that **S8** may have an aluminium coating present on the rutile titanium dioxide particles. The resonance of the aluminium tetrahedron (AlO_4) is located at +56 ppm maybe due to magnesium aluminium silicate. Both signals are similar to that of **S6** shown previously.

3.5.4.3.2 ^{29}Si NMR

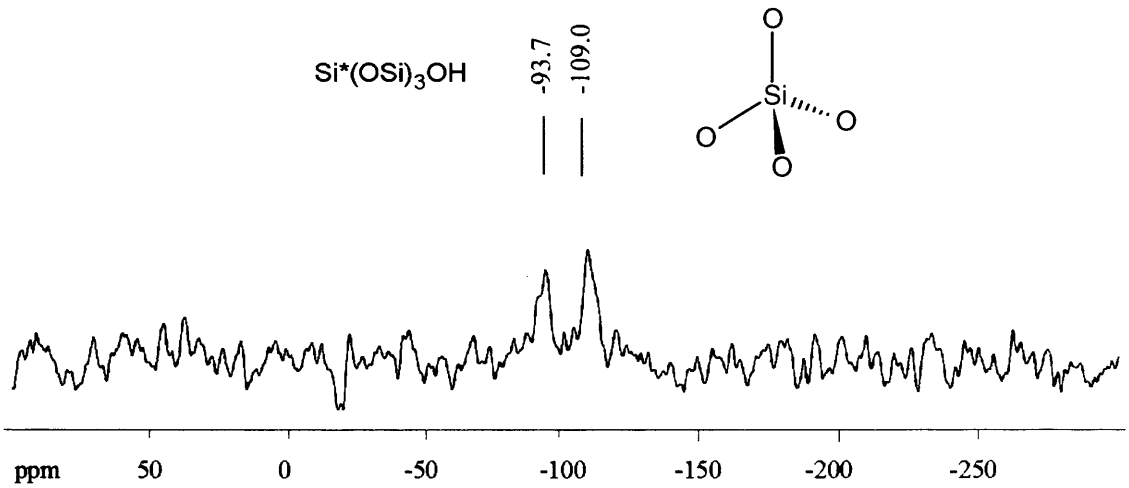

Figure 3.50: ^{29}Si MAS Nuclear Magnetic Resonance of **S8**.

The Si Q^3 signal indicates the presence of an aluminosilicate (Figure 3.50). The Q^4 signal suggests the presence of a fully cross-linked framework site, $Si(OSi)_4$. This is similar to the resonances found for **S6** which showed the presence of an aluminosilicate and silica. The peaks are not intense which suggests that there are small quantities of the silicon containing compounds in the powder.

3.5.4.4 Solid State Nuclear Magnetic Resonance of S9

3.5.4.4.1 ^{27}Al NMR

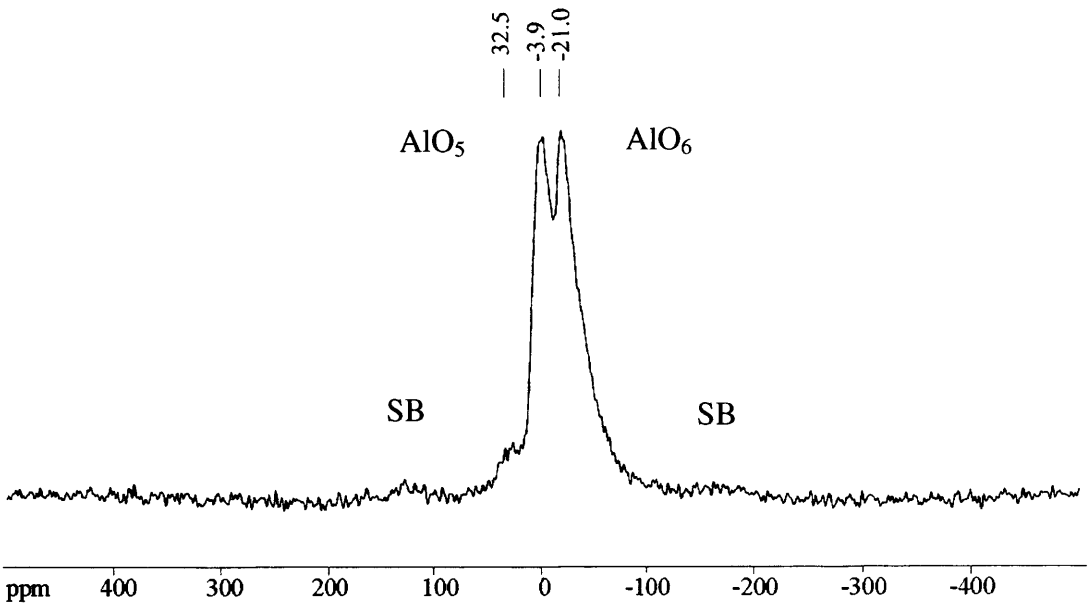

Figure 3.51: ^{27}Al MAS Nuclear Magnetic Resonance of **S9**.

The spectrum of **S9** shows a line shape in the form of a doublet at an octahedral site (Figure 3.51). This could be due to either two different aluminium environments or aluminium's quadrupolar nuclei. Quadrapolar nuclei such as Al (nuclear spin of 5/2) do not only interact with the magnetic field in which the sample is placed but also the electric field gradient. This interaction often causes the ^{27}Al peaks to broaden and split as seen in the spectra above. Magic angle spinning has been used to prevent the line broadening but it is only partially effective against half spin integers like ^{27}Al. The asymmetric peak could possibly be deconvoluted into two separate peaks whereby one is of octahedral aluminium (AlO_6) and the other is also octahedral Al but with Ti neighbours. The oxygen atoms adjacent to the aluminium atom would be electronically enriched if next to an electron rich atom such as titanium thereby shifting the ^{27}Al NMR peaks towards more negative values i.e. there is increased shielding. This would explain

the presence of aluminium hydroxide as the coating for **S9**. There are no peaks which indicate the presence of tetrahedral aluminium for **S9**. The small shoulder at 32 ppm is in the region of pentavalent aluminium, AlO_5 that has a range 30 – 40 ppm[129]. This resonance has been reported in poorly crystalline and amorphous aluminium containing materials[130,131]. There were no signals for ^{29}Si NMR with **S9**.

3.5.4.5 Solid State Nuclear Magnetic Resonance of S11

3.5.4.5.1 ^{27}Al NMR

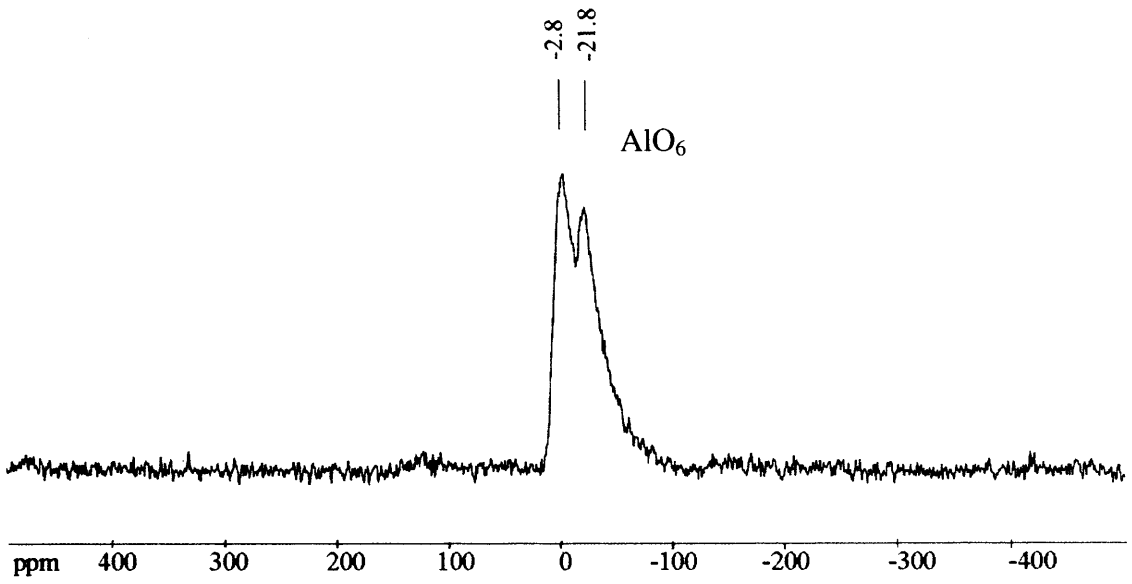

Figure 3.52: ^{27}Al MAS Nuclear Magnetic Resonance of **S11**.

A quadrapolar line that has formed a doublet or two different chemical aluminium environments is present at an octahedral Al site (Figure 3.52). This is similar to the spectra for **S9** which shows that the octahedron, aluminium hydroxide may be contained in the powder.

3.5.5 Summary of Solid State NMR Data

Solid state NMR was used to elucidate the nature of the different coating materials on the titanium dioxide nanoparticles. The coordination state and local symmetry of structural units were determined for each sample. Magic angle spinning made it possible to obtain high resolution NMR spectra of the different solids. The main atomic constituents of the coating are silicon and aluminium therefore; ^{29}Si and ^{27}Al nuclei were examined. Five of the seven samples tested had a coating that contained aluminium atoms. More specifically, **S6**, **S8** and **S10** had an aluminium oxide coating; **S9** and **S11** contained an aluminium hydroxide coating. However, **S6** and **S8** also contained silicon oxide as silica. **S4** possessed a polysiloxane coating and as known, organosilane coatings surrounded the pure **S3** titanium dioxide particles. The structure of the organosilane coating was elucidated from the ^{29}Si NMR nuclei as being likely vertically polymerised onto the surface of the titania with T2 and T3 Si – O linkages.

Other nuclei could also be used to determine the structures present in the powders such as ^{47,49} Ti and ^{17}O. The quadrupolar Ti nuclei however would be much more difficult to probe because they have low natural abundance at ^{47}Ti at 7.28% and ^{49}Ti at 5.51%. This problem would decrease the detection sensitivity of the titanium nuclei. The large quadrupolar moment of these isotopes would also result in significant broadening of the signal peaks. Another problem is that these two isotopes have similar relaxation times resulting in resonance frequencies that differ by only 9 kHz and therefore some overlapping of the spectra[128].

Using ^{29}Si and ^{27}Al to distinguish X-O-Ti and X-O-X bonds (X = Si or Al) is sometimes quite difficult in providing a clear differentiation, however, using ^{17}O NMR, the oxygen environments in the linkages can be easily probed. The chemical shift range of ^{17}O is large at 1500 ppm and the resonances of different oxo-bridges such as Si-O-Si and Ti-O-Si appear at very different values (97 vs. 332 ppm). A negative aspect is the low natural abundance of the ^{17}O nuclei (0.037%)[128].

A summary of the SSNMR data is given in Table 3.13. The data agrees well with the other techniques used such as XPS. However, XPS could not define whether some of the powders consisted of an organosilane coating or silicone polymer coating due to the proximity of their Si (2p) binding energies. SSNMR was able to elucidate the structure of the coatings which contained silicon compounds, giving a clearer view of their nature on each sample tested.

Table 3.13: Summary of Solid State Nuclear Magnetic Resonance Data.

Sample	Nuclei Tested	Chemical Shift (ppm)	Interpretation	Possible Coating
S3	^{29}Si	-55.8 -69.7 -112.4	Bi(T2)-Si – O linked silicone Tri(T3)-Si – O linked silicone Q^4 siloxane	Organosilane/ Silicone Polymer
S4	^{29}Si	-22.6	Polysiloxane chains $-(O-Si(CH)_3-O)_n$	Silicone Polymer
S6	^{29}Si	-94.9 -108.9	Q^3 $Si(OSi)_3OH$ Q^4 $Si(OSi)_4$	Silica
	^{27}Al	54.7 -3.4	Tetrahedral AlO_4 Octahedral AlO_6	Aluminium Oxide
S8	^{29}Si	-93.7 -109.0	Q^3 $Si(OSi)_3OH$ Q^4 $Si(OSi)_4$	Silica
	^{27}Al	56.3 -3.5	Tetrahedral AlO_4 Octahedral AlO_6	Aluminium Oxide
S9	^{27}Al	32.5 -3.9 -21.0	Pentavalent AlO_5 Octahedral AlO_6	Aluminium Hydroxide
S10	^{27}Al	-6.0	Octahedral AlO_6	Aluminium Oxide
S11	^{27}Al	-2.8 -21.8	Octahedral AlO_6	Aluminium Hydroxide

3.6 RAMAN SPECTROSCOPY

Raman spectroscopy is a form of vibrational spectroscopy, much like Fourier Transform Infra-Red (FTIR) and is useful for chemical identification, characterisation of molecular structures and effects of bonding. However, whereas FTIR bands arise from a change in dipole moment, Raman bands arise from the change in polarisability. In many cases, vibrations that are forbidden in FTIR are active in Raman spectroscopy and vice versa therefore making the techniques complimentary. Titanium dioxide is a very strong Raman scatterer and the different crystal forms can easily be identified using Raman spectroscopy because the peaks of each phase are clearly separated in frequency.

3.6.1 Raman Spectrum of S10

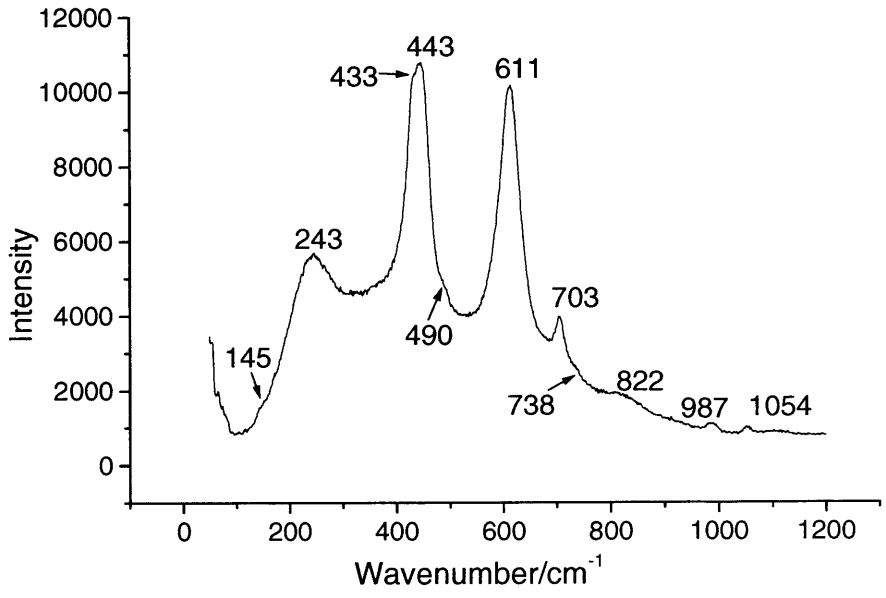

Figure 3.53: Raman spectrum for **S10**, alumina coated rutile.

Figure 3.53 shows the Raman spectrum for **S10**, alumina coated rutile with values at 145, 243, 431, 444, 490, 611, 703, 738, 822, 987 and 1054 cm^{-1}. The literature values for a pure rutile powder[114] are 143, 232, 447, 612 and 826 cm^{-1}. The space group of rutile is D_{4h} ($P4_2/mnn$) implying a total of 15 vibrational modes with the following irreducible representation: $A_{1g} + A_{2g} + A_{2u} + B_{1g} + B_{2g} + 2B_{1u} + E_g + 3E_u$. Of these there are four Raman active modes, $A_{1g} + B_{1g} + B_{2g} + E_g$ observed at 143, 447, 612 and 826 cm^{-1} respectively[115]. The broad peak at 243 cm^{-1} is assigned to a combination rather than a fundamental one phonon process due to the overlapping of two modes of A_{1g} and B_{2g} symmetry[116,114]

All of the bands for **S10** show a shift compared to the literature data particularly the resonance at 232 cm^{-1} for uncoated rutile shifting to 243 cm^{-1} for **S10**. This blue shift is indicative of a change in the typical rutile lattice. There are also some additional weak peaks at 433, 490, 703, 738, 987 and 1054 cm^{-1} which can be attributed to Al – O – Al vibrations in aluminium oxide[117] as α-Al_2O_3. This is evidence that **S10** may be made up of a solid solution of aluminium oxide doped titanium dioxide.

3.6.2 Raman Spectrum of S1 (P25)

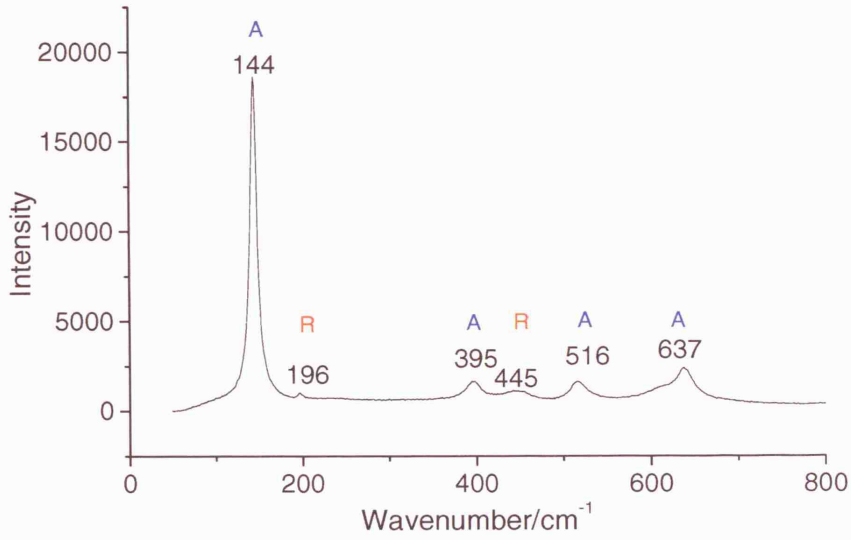

Figure 3.54: Raman spectrum of Degussa P25 (**S1**) showing a mixture of anatase (A) and rutile (R) peaks.

Both **S1** (Degussa P25) and **S3** both exhibit the same Raman spectra. The vibrations are characteristic of titanium dioxide as anatase. Bands are observed at 143, 197, 396, 516 and 638 cm^{-1} which correspond well with published data. The peak at 516 cm^{-1} has a shoulder at ~ 520 cm^{-1}. Literature values have cited the frequencies due to the anatase crystal form as 143, 197, 397, 516 and 637 cm^{-1}. Anatase has a space group D_{4h} ($I4_1/amd$) and group analysis shows that there are six Raman active modes ($A_{1g} + 2B_{1g} + 3E_g$). These are identified as 143 cm^{-1} (E_g), 197 (E_g), 395 cm^{-1} (B_{1g}), 513 cm^{-1} (A_{1g}), 519 cm^{-1} (B_{1g}) and 637 cm^{-1} (E_g) [116].

From XRD studies, **S1** and **S3** both contain a mixture of anatase and rutile crystal forms. However, only the anatase phase is dominant in the spectra as P25 contains 85% anatase and only 15% rutile (as determined by XRD measurements). **S3** is an organosilane coated mixed crystal form of titania powder and a Ti – O – Si bond

should be observed at around 950 cm^{-1}, however, no such peak is observed in its Raman spectrum. The small concentration of the organosilane present is the most likely the reason for the lack of mixed oxo metal bonds vibrations.

3.6.3 Raman Spectrum of S2

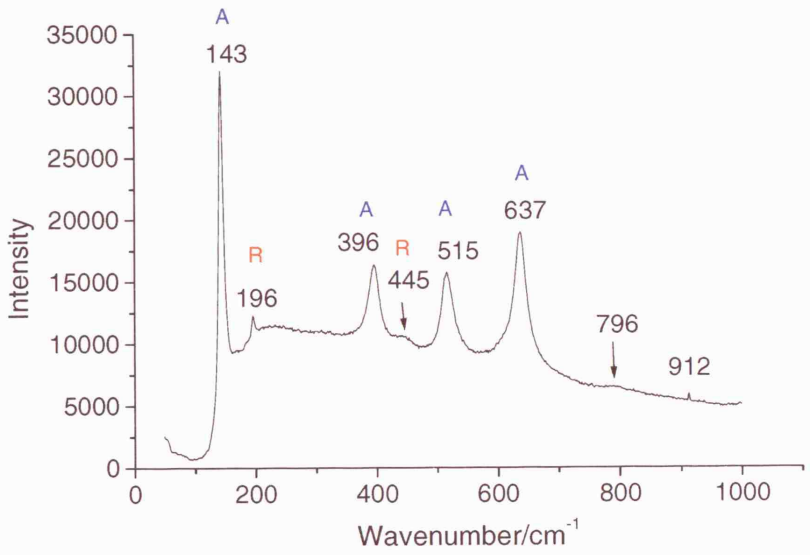

Figure 3.55: Raman spectrum of **S2** showing a mixture of anatase and rutile.

S2 is an extracted sunscreen titanium dioxide powder, which has the same composition as **S1** and **S3** i.e a mixed anatase and rutile crystal powder. The Raman spectrum shows that same strong peaks as Figure 3.55 however the anatase peaks are more intense than the rutile peaks. From the XRD calculations, **S2** contained 90% anatase and 10% rutile which can explain the difference in intensities of the two crystal forms. There are also two extra frequencies at 796 cm^{-1} and 912 cm^{-1} in the Raman spectrum of **S2** compared to **S3**. The vibration at 796 cm^{-1} can be assigned to the Si – O – Si bending mode and the latter peak at 912 cm^{-1} can signify the presence the stretching of the Ti – O – Si linkages[118].

3.6.4 Comparison of Raman Spectroscopy Data

Raman spectroscopy is advantageous because it is very specific and the resulting spectra are fingerprints for characterising materials. The crystal forms anatase and/or rutile were precisely identified in all the tested samples due to their strong Raman scattering. Both the Raman and XRD results show that of the 12 powders tested, 5 contained a mixture of the anatase and rutile crystal forms whereas the remaining 7 consisted of titanium dioxide as pure rutile. Although the crystal types were deduced, the vibrations of the connecting bonds from the titanium dioxide lattice to the coating material could not be identified in the pure samples, **S3** and **S10**. This could be due to the very small concentration of coating present in the powder resulting in a small quantity of Ti – O – Al and Ti – O – Si bond vibrations. In the extracted powder, **S2**, a weak peak was observed in the region of Ti – O – Si linkages (912 cm^{-1}). Si – O – Si bonds (stretch) were observed in the sunscreen extracted, **S2** sample at vibrational frequency 796 cm^{-1}. Si – O – Si stretches can occur between 600 – 1200 cm^{-1} and is seen for **S2** and **S7** but not for the other samples which have an organosilane, silica or silicone polymer coating such as **S3**, **S4**, **S5**, **S6** and **S8**. Three powders exhibited vibrations due to aluminium oxide linkages. The vibration observed at 995 cm^{-1} for **S9** and **S11** is due to an Al – O – Al stretch[119]. **S10**, the pure powder, which has an aluminium oxide coating, produced Raman frequencies at 433, 703, 738, 987, 1054 cm^{-1} due to the stretching and bending modes of aluminium oxide [117,120].

Table 3.14: Summary of collected Raman Data.

Sample	Raman Shift/cm^{-1}	Interpretation
S1	144, 395, 516, 637 196, 445	Anatase Rutile
S2	143, 396, 515, 637 196, 445 796 912	Anatase Rutile Si – O – Si stretch Ti – O – Si stretch
S3	144, 396, 516, 639 197	Anatase Rutile
S4	143, 397, 519, 639 197	Anatase Rutile
S5	143, 397, 519, 639 197	Anatase Rutile
S6	241, 444, 611	Rutile
S7	239, 443, 611 1067 1135	Rutile Al – O – Al bend Si – O
S8	237, 447, 610	Rutile
S9	243, 439, 611 995	Rutile Al – O – Al stretch
S10	243, 443, 611 433, 703, 738, 987, 1054	Rutile Al – O – Al (Al_2O_3)
S11	243, 439, 611 995	Rutile Al – O – Al stretch
S12	243, 439, 613	Rutile

The Raman spectra of the titanium dioxide powders gave the same crystal form composition as the X-ray diffraction results. Additional information about bonding of other materials present in the powder was also acquired from this technique.

3.7 SPECIFIC SURFACE AREA MEASUREMENTS

This last section of the analysis chapter deals with the specific surface areas of the powders. The surface area of a photocatalytic powder such as titanium dioxide is important because it is the means by which the solid interacts with its surroundings. The decrease in particle size increases the surface area per unit volume (or mass). Generally, with a larger surface area, there are more sites which are able to react and the activity of the catalytic powder increases.

3.7.1 Methodology

There are usually different methods used to measure the surface area of solids and most yield different results. The majority use the isothermal adsorption of nitrogen gas, N_2 with a singlepoint or multipoint method. The cost effective singlepoint method was used to measure the specific surface areas, pore volumes and pore sizes of three extracted sunscreen powders **S5**, **S6** and **S9**.

The dried powders were degassed and cooled to the temperature of liquid nitrogen, 77 K. At this temperature, an inert gas such as nitrogen will physically adsorb on the surface of the particles with the process being reversible. An adsorption isotherm (constant temperature) is recorded of the adsorbed gas vs. relative pressure (standard pressure/saturation vapour pressure). The data points of the adsorption isotherm is measured and the Braunaur Emmet Teller (BET) equation used to calculate the surface area[132]. The BET equation actually gives the volume of gas needed to form a

monolayer on the surface of the particles and the surface area is calculated from the size and number of adsorbed molecules.

BET Equation:

$$\frac{P}{n_{ads}[(P_0 - P)]} = \frac{1}{n_m C} + \frac{(C - 1)}{n_m C}\frac{P}{P_0}$$

where

P/P_0 = relative pressure (standard pressure/saturation vapour pressure)

n_{ads} = moles of nitrogen adsorbed at a given P/P_0

n_m = moles of gas to give monolayer of adsorption per gram of sample solid

C = constant related to heat of adsorption.

The slope and intercept are used to determine the quantity of nitrogen adsorbed on the monolayer and the surface area calculated.

Surface Area (m^2/g) = $n_m N A_{cs}$

A_{cs} = Area occupied by one molecule (for N_2 at 77 K) = 16.2 $Å^2$

N = Avogardro's number (molecules/mol)

The BET equation assumes that only the uppermost layers of a multilayered absorbate are in dynamic equilibrium with the vapour and some particular point on the isotherm represents a complete monolayer.

3.7.2 Results

Table 3.15: Comparison of surface area, pore volume and pore size of some pure (**S1**, **S3**, **S10**, **S12**) and extracted titanium dioxide powders (**S5**, **S6**, **S9**).

Sample	Surface Area m^2/g	Pore Volume cm^3/g	Pore Size Å
S1	45	-	-
S3	50	-	-
S5	12.6	0.0056	18.43
S6	77.9	0.037	18.91
S9	13.8	0.0062	18.02
S10	40	-	-
S12	20	-	-

S1, S3, S10, S12 – Surface areas known from manufacturer's data sheet.
S5, S6, S9 – Surface areas measured by BET.

A larger surface area can increase the rate of a reaction as a greater proportion of the particles are exposed. Pore size defines the ability of an analyte molecule to penetrate into the particle and interact with its inner surface. It refers to the part of the bulk that is filled with pore or void space. The nitrogen adsorption/desorption method is usually used to determine the pore size of particles between 10 – 300 Å and was therefore used to analyse **S5**, **S6** and **S9**. For particles with larger pore radius (50 Å - 55μm), the mercury porosimetry technique is utilised. This is because mercury has a very high surface tension and is therefore a non-wetting liquid on most substrates. The amount of mercury forced into the pores as a function of pressure is used to determine the pore size and volume[133]. The pore sizes of the extracted sunscreen powders are all approximately 18 Å, which is an intermediate size and is referred to as mesopores. The pore volume is the average volume of all pores in 1 gram of powder. Only the internal pore volumes inside the particles are counted.

S5 and **S9** possess similar surface areas at 12.6 m^2/g and 13.8 m^2/g (Table 3.15). However, **S5** is an anatase and rutile mixed crystal form with a dimethicone coating and **S9** has a rutile crystal form with an aluminium hydroxide coating. **S6** has a mixed silica and alumina coating and is also comprised of rutile. However, **S6** has the highest surface area of all the powders at 77 m^2/g and the greatest pore volume of all the measured powders.

3.8 ANALYTICAL RESULTS AND COATING MATERIAL

The X-Ray Photoelectron results show the greatest evidence for the elemental composition of the coating material. The surface coatings of the titanium dioxide nanoparticles contained either silicon or aluminium compounds as observed by the decrease in the sputtering ratio of Si/Ti and Al/Ti. As the powder was etched into, the surface coating is removed and a greater amount of titanium revealed. The percentages of silicon and aluminium observed in the powders are approximately 2.5%, which is small enough to indicate the amount present in a coating material a few nanometers thick.

The SEM and TEM images also show mostly uniform particles in both the pure and solvent extracted powdered samples. If silica or alumina existed as separate compounds instead of as a coating on titanium dioxide, a large difference in particle size would be observed in these images.

Table 3.16: Summary of Analytical Results

Sample	XRD	XPS	Raman	SSNMR	Interpretation/ Possible coating	Future Code of Identification
S1	85% Anatase 15% Rutile	Ti, O	Anatase Rutile	-	None	A&R+no coat
S2	90% Anatase 10% Rutile	Ti, O, Si (1%), C	Anatase Rutile Si – O – Si Ti – O – Si	-	Organosilane/ Silicone Polymer	A&R+Si coat
S3	85% Anatase 15% Rutile	Ti, O, Si (2.3%), C	Anatase Rutile	Bi(T2)-Si – O linked silicone Tri(T3)-Si – O linked silicone Q^4 siloxane	Organosilane/ Silicone Polymer	A&R+Si coat
S4	85% Anatase 15% Rutile	Ti, O, Si (2.8%), C	Anatase Rutile	Polysiloxane chains $-(O-Si(CH)_3-O)_n$	Silicone Polymer	A&R+Si coat
S5	75% Anatase 25% Rutile	Ti, O, Si (2.3%), C	Anatase Rutile	-	Organosilane/ Silicone Polymer	A&R+Si coat

Sample	XRD	XPS	Raman	SSNMR	Interpretation/ Possible coating	Future Code of Identification
S6	100% Rutile	Ti, O, Al (0.8%), Si (6.3%), C	Rutile	Q^3 $Si(OSi)_3OH$ Q^4 $Si(OSi)_4$ Tetrahedral AlO_4 Octahedral AlO_6	Silica Aluminium Oxide	A&R+Al+Si coat
S7	100% Rutile	Ti, O, Al (1.0%), Si(1.1%), C	Rutile Al – O – Al Si – O	-	Aluminium Oxide Silicone polymer	R+Al+Si coat
S8	100% Rutile	Ti, O, Al (1.7%), Si (0.8%), C	Rutile	Q^3 $Si(OSi)_3OH$ Q^4 $Si(OSi)_4$ Tetrahedral AlO_4 Octahedral AlO_6	Silica Aluminium Oxide	R+Al+Si coat
S9	100% Rutile	Ti, O, Al (1.2%), C	Rutile Al – O – Al	Octahedral AlO_6	Aluminium Hydroxide	R+ Al coat
S10	100% Rutile	Ti, O, Al (5.8%), C	Rutile Al – O – Al (Al_2O_3)	Octahedral AlO_6	Aluminium Oxide	R+ Al coat
S11	100% Rutile	Ti, O, Al (1.3%), C	Rutile Al – O – Al	Octahedral AlO_6	Aluminium Hydroxide	R+Al coat
S12	100% Rutile	Ti, O, Mn (6.2%)	Rutile	-	Manganese oxide	R+Mn doped

Chapter 4 – Electron Paramagnetic Resonance

This chapter details the use of Electron Paramagnetic Resonance (EPR) in the solid state to determine if UV irradiation of coated titanium dioxide powders produces free radical species. This type of research has never been done before and it directly detects the free radicals produced from modified titanium dioxide powders used in sunscreens. Previous work on titanium dioxide powders[134] were carried out using liquid spin trapping agents which indirectly measured the free radicals generated. This method can sometimes give misleading information as an adduct of the radical species and not the actual radical is being measured[135]. However, it is generally known that reactive oxygen species are produced by the irradiation of uncoated titanium dioxide[136] but what remains unclear is whether the coatings on the titania particles prevent these free radicals from being created.

4.1 INTRODUCTION

Electron Paramagnetic Resonance or EPR is a branch of spectroscopy in which electromagnetic radiation of microwave frequency is absorbed by atoms in molecules or solids, which possess unpaired electrons. EPR can be used to detect unpaired electrons, free radicals, transition metal cations and triplet states.

In EPR, the change in the electron spin m_s, is observed. The different values for m_s are +1/2 (a high energy state where the magnetic moment is aligned anti-parallel to the applied magnetic field) or –1/2 (a low energy state where the magnetic moment is aligned parallel to the applied magnetic field). As the lower energy spin state is more

populated, microwave energy absorption occurs during transitions to the higher energy state at resonance.

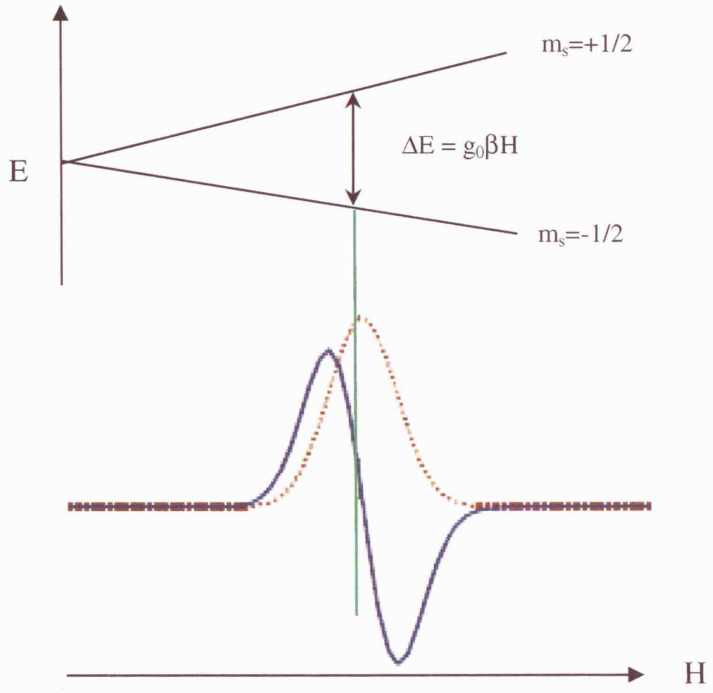

Figure 4.1: Change in spin state as a function of the applied magnetic field.

The free radicals are promoted from the –1/2 spin state to the +1/2 spin state by absorption of the microwave radiation (Figure 4.1). This happens at resonance when $\Delta E = h\nu = g\beta H$, where h is Planck's constant, ν is the operating frequency of the microwave radiation, β is the Bohr magneton, H is the applied magnetic field strength and g is the g-factor, a proportionality constant.

$$g = \frac{h\nu}{\beta H} = 0.07145 \frac{\nu\,(\mathrm{GHz})}{H\,(\mathrm{T})}$$

The g factor is an inherent property of a system containing an unpaired electron. It is similar to the chemical shift observed in a NMR spectrum. The g value for a single

unpaired electron (free electron-g_e) has been calculated and experimentally determined to be 2.0023[137].

Since some free radicals are not very long-lived due to their high reactivity, a sufficient concentration of the species is not usually present. Thus in order to be detected, the irradiations should ideally be carried out *insitu* and at low temperature, 77 K. It is well known that upon UV irradiation of titanium dioxide particles, the photogenerated electrons and holes are ultimately responsible for the photocatalytic redox reactions. Therefore, the EPR technique is ideally suited to measuring oxygen species that are trapped on the surface of these particles. The following are a set of reactions which can occur during UV irradiation of titanium dioxide[134,138].

1. The absorption of photons leads to the formation of photogenerated electron and hole pairs in the bulk oxide.

$$TiO_2 + h\nu \longrightarrow TiO_2\,(h^+ + e^-)$$

2. The photogenerated electron can reduce Ti^{4+} sites at the bulk or surface.

$$Ti^{4+} + e^- \longrightarrow Ti^{3+}$$

3. The photogenerated holes can be trapped at lattice anions.

$$Ti^{4+} - O^{2-} - Ti^{4+} - OH^- + h^+ \longrightarrow Ti^{4+} - O^{\bullet -} - Ti^{4+} - OH^-$$

4. The trapped holes can react with surface oxide ions.

$$Ti^{4+} - O^{2-} - Ti^{4+} - OH^- + h^+ \longrightarrow Ti^{4+} - O^{2-} - Ti^{4+} - O^{\bullet -}$$

5. Photogenerated positively charged holes could also be trapped at surface hydroxyl groups forming hydroxyl radicals.

$$Ti^{4+} - OH^{-} + h^{+} \longrightarrow Ti^{4+} - OH^{\bullet}$$

6. The interfacial electron transfer from trapped electron sites at the surface to adsorbed oxygen can then form superoxide anions.

$$Ti^{3+} + O_2 \longrightarrow Ti^{4+} - O_2^{-}$$

7. The superoxide anions then react with protons on the hydrated surface to form hydroxy anions.

$$Ti^{4+} - O_2^{-} + H^{+} \longrightarrow Ti^{4+} - O_2H^{\bullet}$$

4.2 EXPERIMENTAL

The powders (5.0 mg) were placed in an EPR tube and the air evacuated from the tube (10^{-4} torr) at room temperature (RT) for 20 minutes. A 1000 W Oriel Instrumentals UV lamp, incorporating a Hg/Xe arc lamp (250 nm to > 2500 nm), was used for all irradiations in the presence of a water filter and also a 350 nm cut-off filter. The powders were irradiated for 40 minutes *in situ* at 77 K. Oxygen (10 T) was added to the tube at RT, the excess oxygen subsequently evacuated and the EPR spectra recorded at 77 K. The EPR spectra were recorded on a Bruker ESP-300e series spectrometer at X-band frequencies (≈ 9 GHz), 100 kHz field modulation and 10 mW microwave power at 77 K. The *g* factor values were obtained using a DPPH standard[139].

4.3 EPR RESULTS AND DISCUSSION

All of the sunscreen extracted and pure powders were irradiated with UVA light (> 350 nm) and the various paramagnetic species and free radicals measured. However only **S2**, **S3**, **S4**, **S10** and **S12** are compared in this section as they contain the most information.

4.3.1 S2 (Anatase & Rutile + Organosilane coat)

4.3.1.1 UVA Irradiation of S2

In the following sample (**S2**) the extracted sunscreen powder was irradiated with UV light and the different paramagnetic centres recorded. No oxygen centred species are expected at this point because there was no oxygen present to react with. After irradiation, the white powder was slightly blue/grey in colour indicating the existence of trapped electrons rather than free electrons in the conduction band[134].

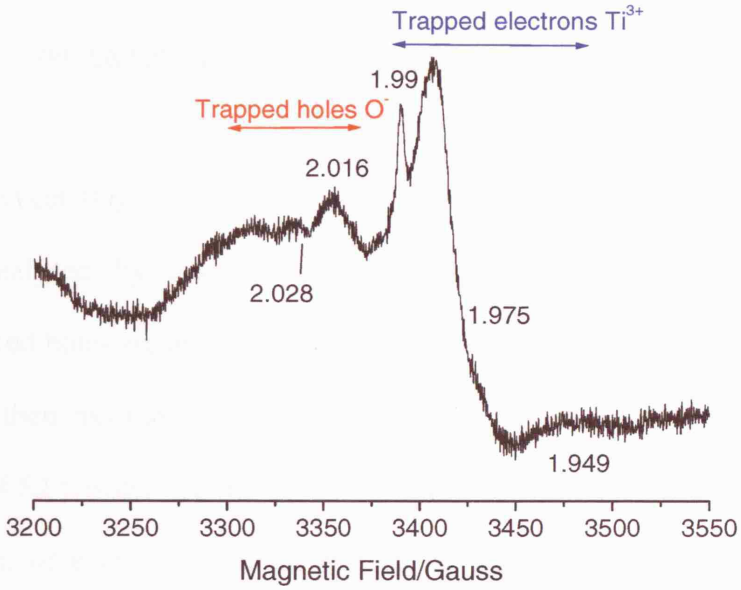

Figure 4.2: Electron Paramagnetic Resonance spectrum of UVA irradiated **S2** powder at 77 K for 40 minutes.

Electrons and holes can be trapped both at the surface and at interior sites of the titanium dioxide lattice. Howe and Gratzel[134] observed EPR spectra of electrons trapped on Ti^{4+} ions and characterised this as Ti^{3+} centres in TiO_2. The signals at $g < 2$ can be assigned to the capture of electrons on titanium ions. The structural geometry of anatase and rutile are sufficiently different that paramagnetic properties of trapped

electrons in the two crystal forms are distinct and can be differentiated using EPR. From the spectrum of **S2** in Figure 4.2, the g-components show the presence of Ti^{3+} (g = 1.99) ions from anatase and Ti^{3+} ($g_{\perp}$ = 1.975 and $g_{\parallel}$ = 1.949) ions from rutile[140]. For each electron that is produced, there should also be a photogenerated hole but these are more difficult to detect as they decay quickly in the dark or upon warming to RT. Despite this, $O^{\bullet-}$ species were detected during the irradiation of the **S2** powder. The g-components of a surface trapped hole $Ti^{4+} - O^{2-} - Ti^{4+} - O^{\bullet-}$ is located at g_{zz} = 2.028, g_{yy} = 2.016 and g_{xx} = 2.002[141].

*4.3.1.2 UV irradiation of **S2** powder followed by addition of oxygen*

Molecular oxygen (O_2) is the oxidising reagent for many of the photocatalytic processes that are catalysed by titanium dioxide. Oxygen is an electron scavenger and photogenerated holes are able to exist for longer lifetimes when O_2 is present due to the reduction in their recombination rate with electrons. After irradiation, O_2 was added to the sample of **S2** powder and the excess O_2 degassed from the tube. If the spectrum was taken with the unreacted oxygen gas present, the reactive oxygen species formed would not be detected due to the high concentration of paramagnetic oxygen atoms which cause line broadening.

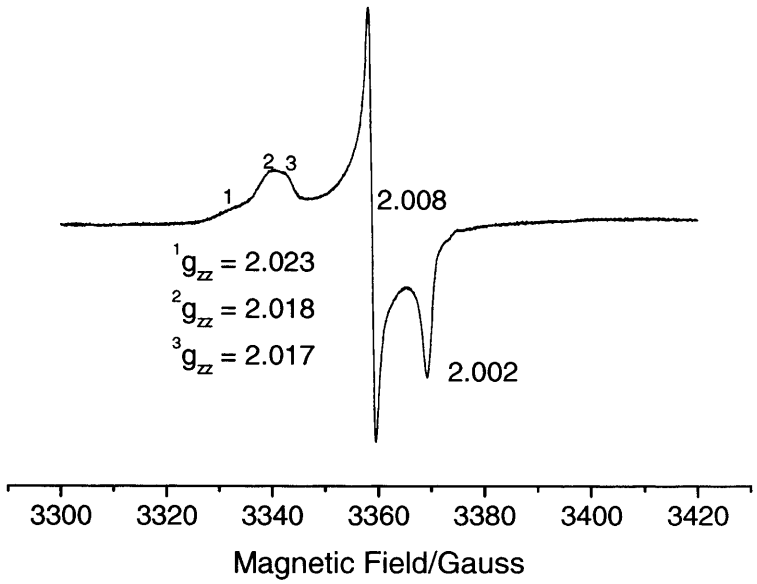

Figure 4.4: Electron Paramagnetic Resonance spectrum of **S2** powder after UVA irradiation followed by addition of oxygen and outgassing.

The spectrum in Figure 4.4, after addition of oxygen and degassing, shows a typical superoxide rhombic ($g_x \neq g_y \neq g_z$) powder spectrum with g components g_{xx} = 2.002, g_{yy} = 2.008 and g_{zz} = 2.017, 2.018, 2.023. The observed g-values correspond to literature values[136,141]. The three values for g_{zz} indicate that there is more than one stable adsorption site for the superoxide anion on the **S2** surface. The formation of superoxide anions on Ti^{4+} sites signifies that the surface of the **S2** powder (extracted from sunscreen) is freely accessible to oxygen molecules.

Table 4.1: Summary of Electron Paramagnetic Resonance parameters and assignment of the reactive species observed along with literature values for similar species.

Species	**EPR Parameters**			
Assignment	g_{zz}	g_{yy}	g_{xx}	**Reference**
Surface oxygen anion $Ti^{4+} - O^{2-} - Ti^{4+} - O^{\bullet-}$	2.028	2.016	2.002	[141] This work
Subsurface oxygen anion radical $Ti^{4+} - O^{\bullet-} - Ti^{4+} - OH^-$	2.024	2.013	2.003	[141]
	2.024	2.014	2.007	[142]
	2.023	2.014	2.003	This work
	2.018	2.014	2.004	[143]
Superoxide anion $Ti^{4+} - O^{2-}$	2.017, 2.018 2.023	2.008	2.002	This work
	2.019 2.022 2.025	2.008	2.002	[136]
Hydroperoxy radical $^{\bullet}HO_2$	2.034	2.008	2.002	[136]
	$g_{\perp}$	$g_{\parallel}$		
Surface and bulk Ti^{3+} Anatase	1.99	1.957		[140] This work
Surface and bulk Ti^{3+} Rutile	1.975	1.949		[140] This work
Local conduction electrons	2.0023			

4.3.2 Comparison of EPR Spectra of UVA Irradiated S3 (Anatase and Rutile with Organosilane Coat) and S10 (Rutile with Alumina Coat)

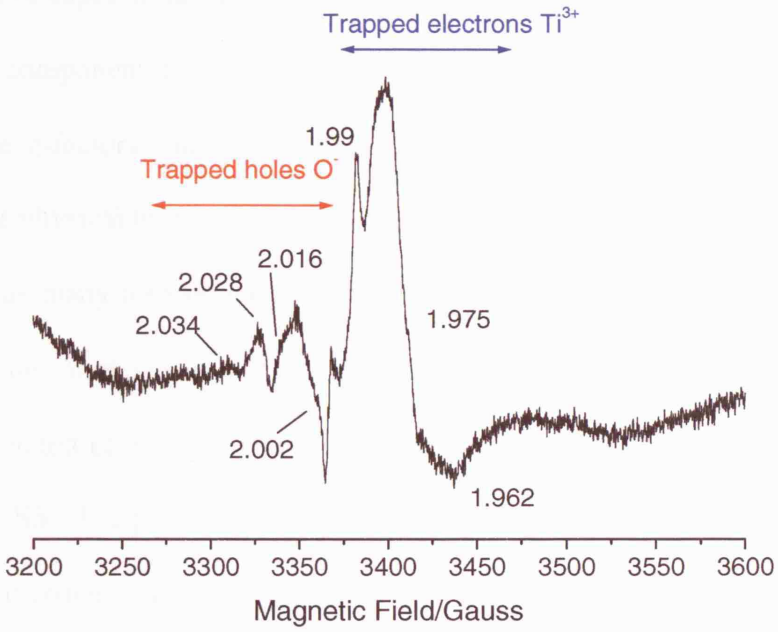

Figure 4.5: Electron Paramagnetic Resonance spectrum of UV irradiated **S3**.

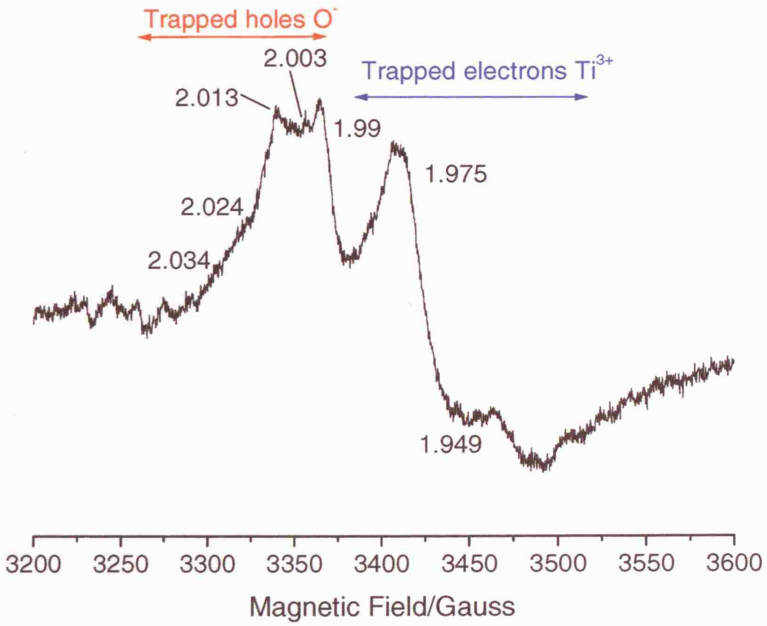

Figure 4.6: Electron Paramagnetic Resonance spectrum of UV irradiated **S10**.

S3 (Figure 4.5), the pure powder obtained directly from its manufacturers (with an anatase and rutile mixed crystal form) shows a mixture of many surface radicals such as both trapped electrons as Ti^{3+} centres and trapped holes as $Ti^{4+} - O^{2-} - Ti^{4+} - O^{\bullet}$; a small amount of superoxide anions and the hydroperoxy radical (g = 2.034). Figure 4.5 shows the g-component features $g_{\perp}$ = 1.975 and $g_{\parallel}$ = 1.941 typical of a pure rutile powder. The g-factors can sometimes vary slightly for the same compounds which have different physical properties such as surface area[136]. In comparison to **S3**, **S10** does not generate as many trapped electrons as Ti^{3+}. This could be due to fewer vacancies such as Ti^{4+} sites on the rutile surface because of the alumina coating, which would trap the photogenerated electrons. The holes in the rutile sample are trapped at a different site to that of **S3**. The positive holes generated by the irradiation of **S10** are trapped by the subsurface oxide in the lattice ($Ti^{4+} - O^{\bullet-} - Ti^{4+} - OH^{-}$) whereas in **S3**, they are trapped at surface oxide sites ($Ti^{4+} - O^{2-} - Ti^{4+} - O^{\bullet-}$). The hydroperoxy radical is indicated in the spectrum of **S10** at g = 2.034 however the signal is almost non-existent.

4.3.3 UVA Irradiated EPR Spectrum of S12 (Manganese doped Rutile)

S12 is manganese doped titanium dioxide with a unique EPR spectra consisting of two sets of six hyperfine line absorptions. This corresponds to Mn^{4+} ions incorporated into a rutile structure. Upon calcinations, the Mn^{2+} begins to oxidise to Mn^{4+} which is substitutionally incorporated into the rutile structure. The double sextet resonances observed at g = 2.0 and 4.3 are assigned to the fine structure transitions of the Mn^{4+} ions which occupy a substitutional site in the rutile lattice with associated hyperfine splittings from the interaction with the ^{55}Mn nucleus (I = 5/2, 100% abundance). [144,145].

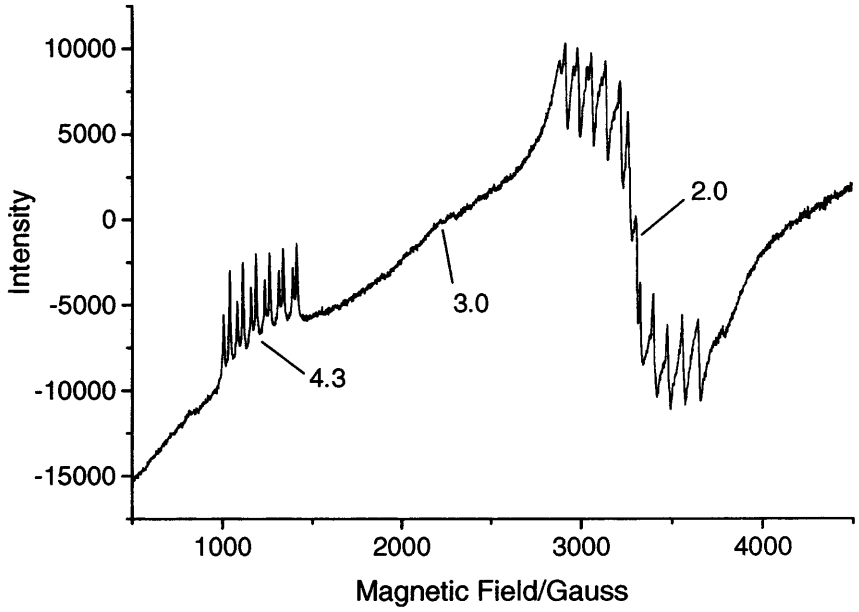

Figure 4.7: Electron Paramagnetic Resonance spectrum of UV irradiated **S12**.

There is a broad peak at g ≈ 3 which may be assigned to substitutionally incorporated Mn^{2+} ions due to the reduction of substitutionally incorporated Mn^{4+} ions[146].

There are no Ti^{3+} centres observed during the irradiation of the manganese doped rutile powder. This could be due to the stronger manganese signal which occurs in the same region as Ti^{3+} ($g \approx 2$) or because there were no Ti^{3+} centres formed during the irradiation.

4.3.4 Stability of Photogenerated Species on S2 Surface

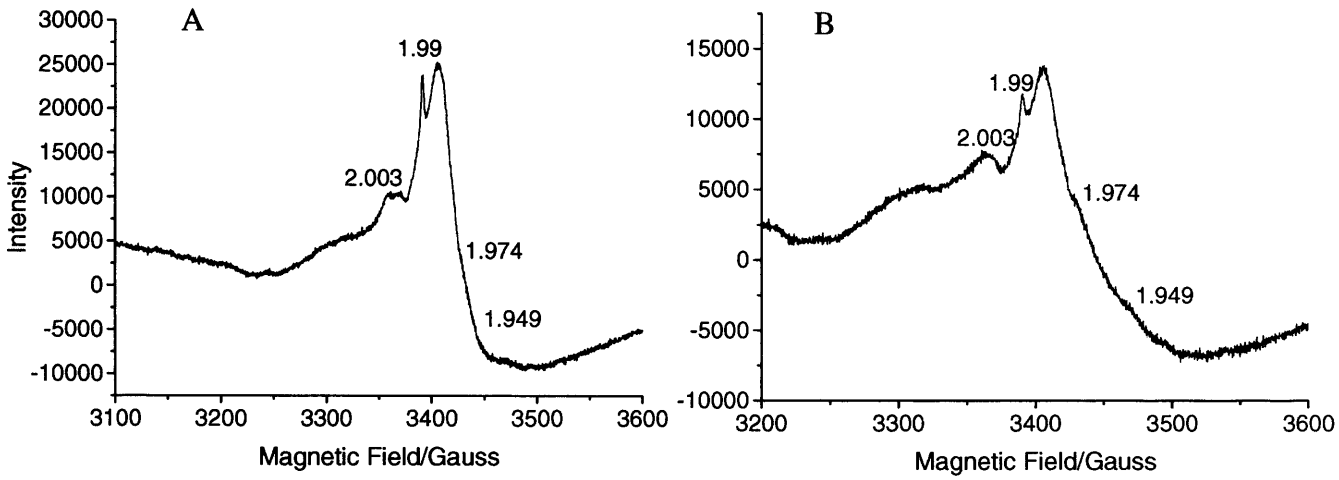

Figure 4.8: Electron Paramagnetic Resonance of **S2** (A) After irradiation of evacuated sample (B) Warming sample to RT.

After warming a sample of **S2** to RT, followed by cooling to 77 K, paramagnetic species remained, albeit in smaller quantities. These species are usually lost when increasing the temperature due to recombination of the electrons and holes and increased reactivity with adsorbed species on the surface. However, Figure 4.8 shows that the trapped photogenerated electrons and holes are stable on approximately 50% of the absorption sites on this mixed anatase and rutile powder with an organosilane coating after being at RT for 15 minutes.

4.3.5 Comparison of the Concentration of Superoxide Anions Formed with Coated Titanium Dioxide Powders

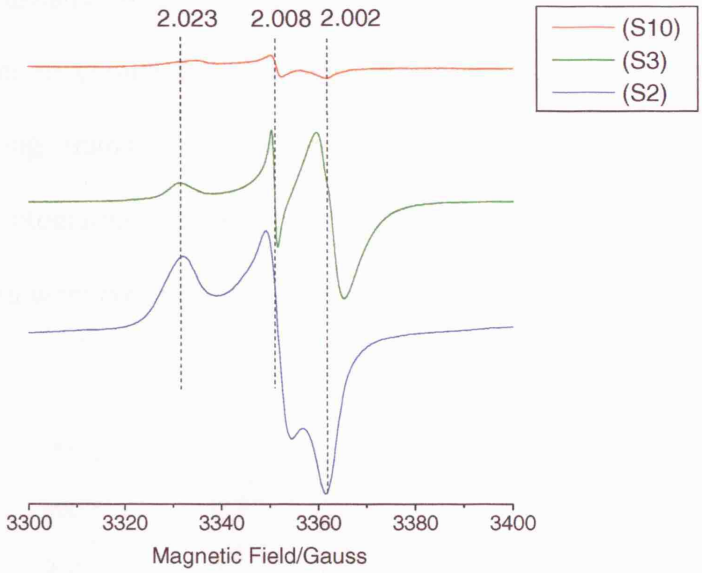

Figure 4.9: Comparison of superoxide anions generated by equal masses of **S2**, **S3** and **S10**.

Three powders of equal mass, one extracted from sunscreen **S2** and two pure powders obtained from their manufacturers, **S3** and **S10**, were irradiated with UVA light. The irradiated particles were allowed to react with oxygen to produce superoxide anions. The different concentrations of the reactive oxygen species formed by the coated powders are shown in Figure 4.9. **S2** and **S3**, both of which comprise of an anatase and rutile mixed crystal form with an organosilane coating, produced a greater amount of superoxide anions than **S10**, the rutile particles with an alumina coating.

4.3.6 Comparison of the Amounts of Ti^{3+} Ions Formed during UV Irradiation of Coated Titanium Dioxide Powders

Although EPR is usually used as a qualitative technique, some quantification was carried out in order to compare the different powders. The concentrations of Ti^{3+} centres formed during irradiation of the samples were calculated per gram for **S1**, **S2**, **S3**, **S4** and **S10** by integrating the area under the Ti^{3+} peaks. The total number of scans and the receiver gain were taken into account when calculating the concentrations.

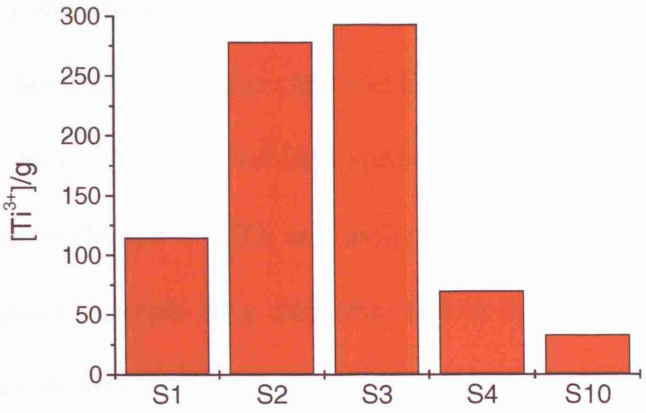

Figure 4.10: Bar graph of Ti^{3+} concentration for irradiated powders.

The bar graph in Figure 4.10 shows that **S2** and **S3** generated the highest concentration of Ti^{3+} centres during UV irradiation. This explains the greater number of superoxide anions seen for **S2** and **S3** in Figure 4.9. An equal number of photogenerated holes would have also been produced with the photogenerated electrons. **S1** is Degussa P25 and as it is uncoated should produce the greatest concentration of e^-/h^+ pairs, however **S1** was the third most radical generating powder after **S2** and **S3**. **S10**, the alumina coated rutile powder, is shown in Figure 4.10 to produce the least amount of Ti^{3+}

centres, however both Figure 4.9 and 4.10 show that a small quantity of reactive oxygen species are nonetheless being created.

4.4 DISCUSSION

The irradiation of the titanium dioxide powders produced photogenerated charge carriers which were detected via solid state EPR. The photogenerated electrons were trapped on Ti^{4+} sites in the bulk and on the surface to form Ti^{3+} ions. In the presence of oxygen, the reactive oxygen species, superoxide radical anions were formed from the reduction of the oxygen molecules by the Ti^{3+} centres on the surface. In the literature, the fate of photogenerated holes is less clear and EPR spectra with different signals have been reported. Anpo *et al*[147] observed EPR spectra of trapped holes ($g_{\perp}$ = 2.015 and $g_{\parallel}$ = 2.003) following irradiation of TiO_2 and assigned the signals to the hydroxyl ($^{\bullet}OH$) radical. Corresponding signals were also observed in this body of work (Table 4.1). However, other researchers[148,142] have carried out similar experiments and assigned the trapped hole to a subsurface oxygen anion radical ($Ti^{4+} - O^{\bullet-} - Ti^{4+} - OH^{-}$).

When the TiO_2 surface is hydrated, the photogenerated holes can be trapped at surface hydroxyl groups forming the hydroxyl radical. The hydroxyl radical is not usually observed in these types of solid-state experiments[141]. This is because other competing reactions can also occur, which can lead to a decrease in surface radical formation, such as the recombination of hydroxyl radicals to form hydrogen peroxide (equation 8) and additional radical species (equation 9).

8. $2OH^{\bullet} \rightarrow H_2O_2$

9. $H_2O_2 + OH^{\bullet} \rightarrow {}^{\bullet}HO_2$

As the hydroxyl radical is extremely reactive, these reactions would occur easily especially when the recombination processes are retarded by, for example, a coating material. Any organic material at the surface is a potential reactant for the photogenerated charge carriers. The production of diamagnetic species which are not detectable by EPR can also reduce radical formation ($O_2^- + e^- \rightarrow O_2^{2-}$).

The hydroperoxy radical observed in the anatase and rutile sample with an organosilane coat, **S3** is most possibly formed via the reaction with surface hydroxy groups (reaction 7) or via the reaction of diamagnetic hydrogen peroxide (reaction 8,9). There was no pre-treatment of the powders and they were used as received from the manufacturers. The formation of the hydroperoxy radical on **S3** shows that the surface of the titanium dioxide particle in this sunscreen powder does not only have an organosilane coating but also OH groups attached to the TiO_2. This may be an indication that the coating on the **S3** powder is patchy. The lack of the hydroperoxy radical on the surface of **S10**, the rutile powder with an alumina coating signifies that this coating may be more uniform as they are no OH groups on the surface. However, more likely is the fact that there were less Ti^{3+} centres formed in **S10** thereby inhibiting the reduction of oxygen molecules to superoxide anions and ultimately there is less of a chance of hydroperoxy formation.

Spin trapping experiments have been used to detect the presence of the hydroxyl radical during the irradiation of titanium dioxide[149]. These experiments are carried out at the solid-liquid interface rather than the gas-solid. It involves the use of a spin trap agent,

which is usually an organic compound that reacts with the radicals being formed from the system under study. This reaction produces an adduct which is readily detectable by EPR. As an adduct of the radical species and not the actual radical is measured using spin trapping, there is a loss of information compared to direct EPR detection. Side reactions and even oxidation of the spin traps can occur during spin-trap experiments of photocatalytic systems[135].

There was a difference between the site to which the photogenerated hole was trapped at in **S3** and **S10**. In **S10**, the h^+ was stabilised by the oxide in the sub-lattice of titanium dioxide, $Ti^{4+} - O^{\bullet-} - Ti^{4+} - OH^-$ whereas in **S3**, it was trapped at the surface of the titanium dioxide lattice, $Ti^{4+} - O^{2-} - Ti^{4+} - O^{\bullet-}$. This difference may affect the photocatalytic ability of the powders as the radical anion at the exterior would be able to react with any chemical compound in the vicinity of the particle surface. Hence, **S3** may be a better photocatalyst then **S10**. To determine which of the powders are more photocatalytically active, methylene blue degradation experiments were carried out in the presence of UV light and the titanium dioxide powders. The results are discussed in the next chapter.

Chapter 5 – Photocatalysis of Titanium Dioxide Powders

The purpose of this chapter is to determine the photocatalytic abilities of the modified titanium dioxide powders by the photodegradation of methylene blue dye under UVA irradiation. Methylene blue dye is a common organic pollutant found in the wastewaters of textile, paper and other industries. The irradiation of such waters in the presence of the photocatalyst titanium dioxide has become an efficient treatment for removal of resistant pollutants such as methylene blue. The use of methylene blue dye to test the photocatalytic strength of powders such as titanium dioxide is becoming a common technique.

5.1 PHOTOCATALYTIC DEGRADATION OF METHYLENE BLUE DYE BY MODIFIED TITANIUM DIOXIDE PARTICLES

The change in the concentration of the dye in aqueous titanium dioxide dispersions was monitored via the variation in the maximum absorption of the dye at 660 nm. In the absence of titanium dioxide, there was no significant degradation of methylene blue (MB) under UV irradiation or in the dark. After leaving the suspension to equilibrate overnight, there was generally a slight decrease in concentration at 660 nm. This is due to the adsorption of dye molecules on the surface of the titanium dioxide. Consequently, the equilibrium value was taken as the initial dye concentration. Initially, the reaction is fast due to the quick removal of the methyl groups (Figure 5.1 methylene blue → thionine). Towards the end of the photocatalytic reaction, the rate slowed down. The formation of intermediate groups, which would compete with the

dye molecules in the photocatalytic process and the slow degradation of the aromatic part of the dye could both be reasons for the decrease in reaction rate[150]. All experiments were carried out at the natural pH of the solution (pH 6.7).

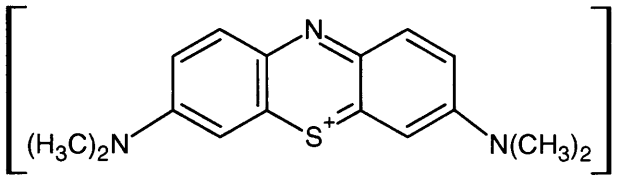

Methylene Blue (blue)

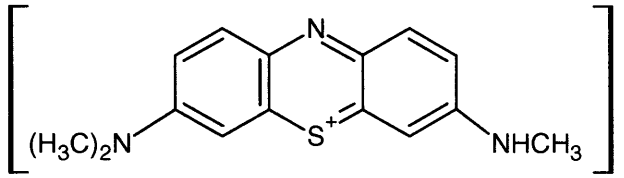

Azure B (blue)

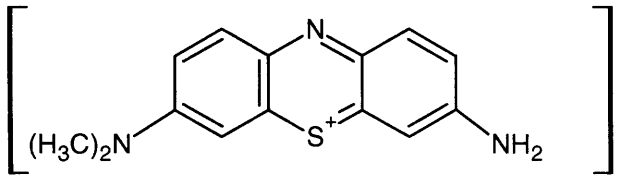

Azure A (blue)

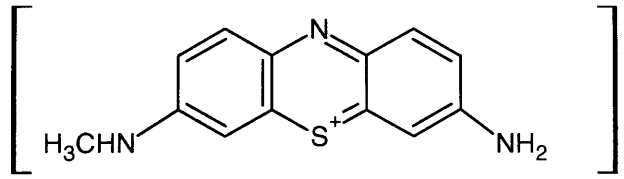

Azure C (blue)

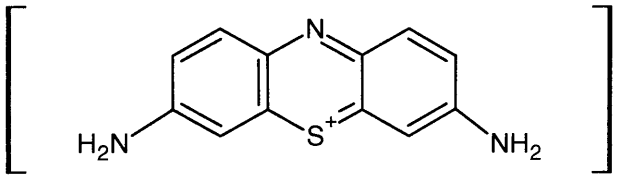

Thionine (violet)

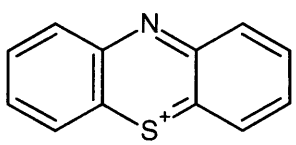

Phenothiazine (yellow)

Figure 5.1: Chemical structures of the degradation of methylene blue via N-demethylation including Phenothaizine[150].

The exact mechanism of the oxidation is still unclear however; the methyl groups which are weak electron-donor substitutes can facilitate an attack on methylene blue by electrophilic species such as $^{\bullet}OH$ or a trapped hole, O^{-}. As the $^{\bullet}OH$ and $^{\bullet}OOH$ radicals are very short-lived due to high reactivity, they are unlikely to migrate far from the titanium dioxide surface therefore the degradation of methylene blue is liable to occur at the surface or within a few monolayers around the photocatalytic surface[151].

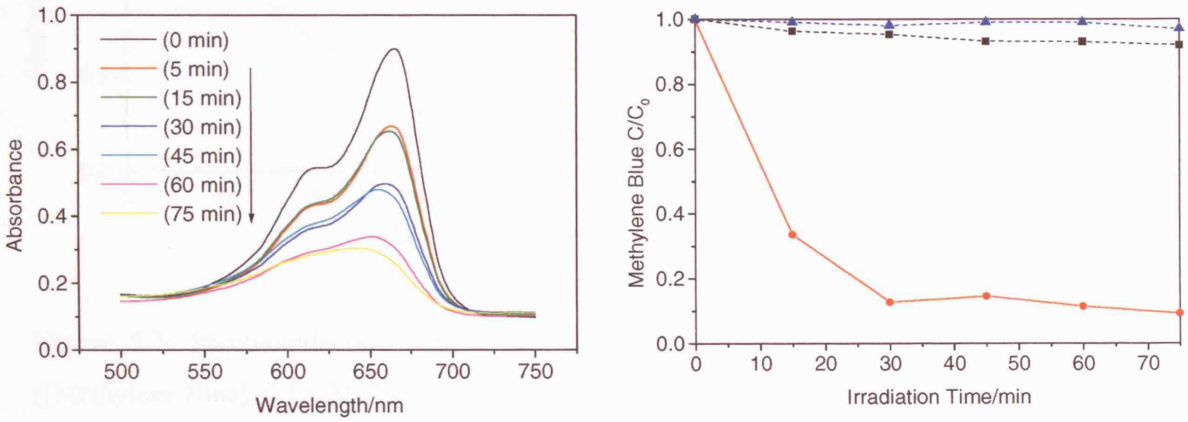

Figure 5.2: (A) UV absorbance changes of methylene blue at 660 nm during irradiation. (B) Comparison of the photo-oxidation of methylene blue in the absence and presence of 10 ml dispersions of TiO_2 under UV irradiation: UV without TiO_2 (Degussa P25) (■); UV with TiO_2 (Degussa P25) (●); in the dark with TiO_2 (▲) ([Methylene Blue], 0.1 mM; TiO_2 loading, 10 mg; UV irradiance, 35 W/m^2 at λ_{max} = 365 nm).

As seen in Figure 5.2(B), both UV light and titanium dioxide are needed for the photo-oxidation of methylene blue to occur. The small decrease in concentration seen in the UV irradiated methylene blue-only control is due to the oxidising action of molecular oxygen present in the air, under the UVA light. As the reaction progresses a blue shift of the absorption bands is noticed. This hypsochromic effect would account for the observed reduction of the blue colour as the irradiation time increases which is due to the N-demethylation of methylene blue [150].

5.1.1 Comparison of the Photocatalytic Activity of Titanium Dioxide Pure Powders

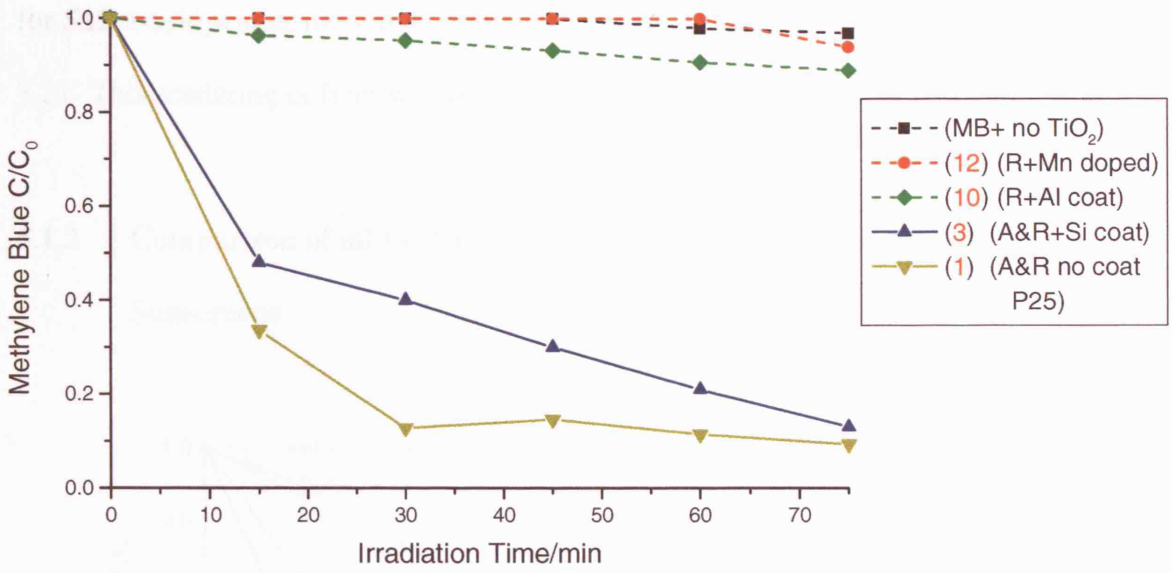

Figure 5.3: Photo-oxidation of methylene blue in the presence of the pure TiO_2 powders. ([Methylene Blue], 0.1 mM; TiO_2 loading, 10 mg; UV irradiance, 35 W/m^2 at λ_{max} = 365 nm). Refer to Table 5.6 for specifics on the sample numbers in the legend. Numbers coloured red in the legend are the sample numbers e.g. (12) is **S12**. (3) A&R+Si coat is **S3** with an Anatase and Rutile crystal mix and organosilane coat.

There is a clear difference in the photocatalytic abilities of **S1** (P25) and **S3** to **S10** and **S12** (Figure 5.3). Degussa P25, the industry standard and most active in this photo-oxidation process, takes 11.5 minutes to reduce the methylene blue dye to 50% of its concentration, whereas it takes more than 2 hours for **S12** to do the same. The silane coated mixed anatase/rutile **S3** degraded methylene blue in 12.2 minutes to its 50% concentration, one minute more than the industry standard which is uncoated. The alumina coated powder, **S10**, degraded the dye in more than 2 hours with a slightly higher activity than the methylene blue-only control. In contrast, the manganese-doped **S12** exhibited almost the same rate of degradation as the control (MB + no TiO_2). This

could have been due to the larger size of the **S12** particle, which would scatter more light according to Raleigh's law which states that the scattering intensity is proportional to the sixth power of the particle diameter[152]. Therefore, a particle of diameter 60 nm for **S12** would scatter more light than a particle of 20 nm, like **S10** (TEM from Section 3.2). This scattering of light would then allow minimal photon interaction with the dye.

5.1.2 Comparison of all the Extracted Titanium Dioxide Powders from Sunscreens

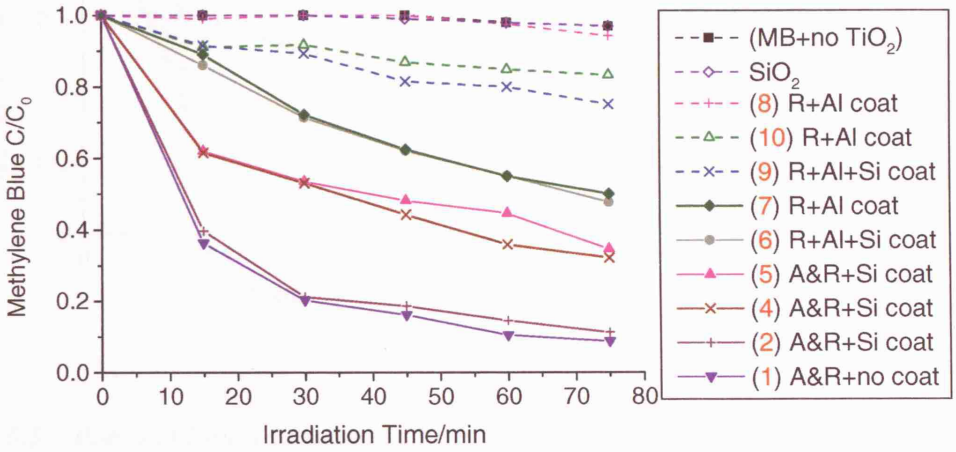

Figure 5.4: Photocatalytic degradation of methylene blue in the presence of sunscreen extracted TiO_2 powders under UVA illumination ([Methylene Blue], 0.1 mM; TiO_2 loading, 10 mg; UV irradiance, 35 W/m^2 at λ_{max} = 365 nm). Refer to Table 5.6 for specifics on sample numbers in red in the legend.

The inorganic powders used in these sunscreens are coated to reduce their photocatalytic activity. The powder isolated from **S2** showed the highest activity, reducing the methylene dye to its half-life within 11.5 minutes (Figure 5.4). The other extracted powders, which had moderately destructive effects, were **S4** and **S5** producing a half-life of 35 and 40 minutes respectively. Two powders, **S9** and **S11** showed only

slight photocatalysis of the dye. All of these samples (**S2**, **S4** and **S5**) all have the common factor of an anatase and rutile crystal mix with either an organosilane (**S2**, **S5**) or dimethicone coat (**S4**).

5.1.3 Comparison of all the Titanium Dioxide Powders (Pure and Extracted)

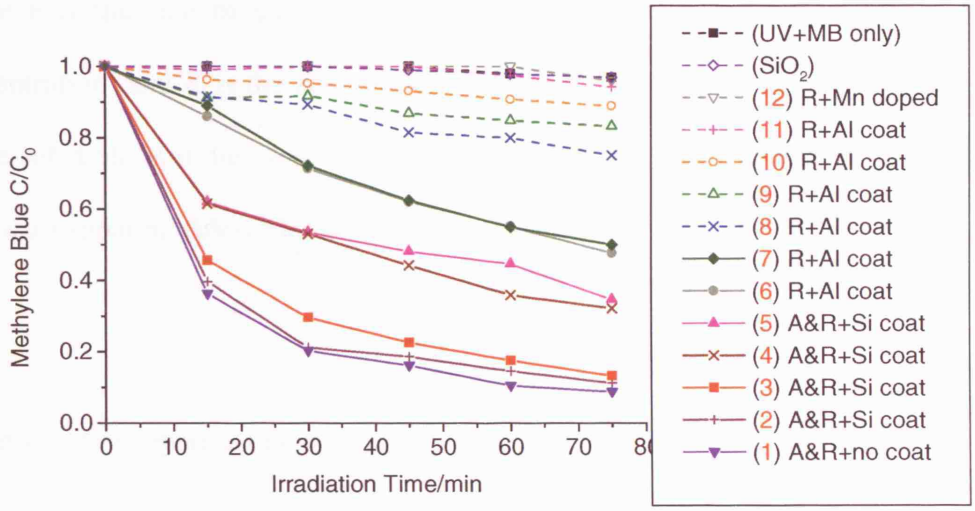

Figure 5.5: Photocatalytic degradation of methylene blue in the presence of coated titanium dioxide nanoparticles; TiO_2 dispersion 10 mg in 10 ml; [Methylene Blue] = 0.1 mM; UV irradiance, 35 W/m^2 at λ_{max} = 365 nm).

From Figure 5.5, the most active powder is Degussa P25 (**S1**) which is expected as the particles are uncoated and used in various photocatalytic industrial processes. Surprisingly, several of the extracted sunscreens also had high activities on a scale comparable to P25 such as **S2** and **S3**, the former an extracted powder and the latter, a pure powder. Both samples contain anatase and rutile crystal forms with an organosilane coating.

5.1.4 Kinetics

The photocatalytic oxidation of several dyes -including methlylene blue (MB)- with titanium dioxide obey the Langmuir-Hinshelwood kinetics given by:

$$r = -\frac{d[MB]}{dt} = -\frac{kK[MB]}{1+K[MB]}$$

where r is the rate of dye mineralization, k is the rate constant, *[MB]* is the dye concentration, and K is the adsorption coefficient[153]. However, when the concentration of the substrate is in the scale of millimoles (as are the dye concentrations used in this work), an apparent first-order model can be assumed[154]:

$$r = -\frac{d[MB]}{dt} = kK[MB] = k'[MB]$$

where k′ is the apparent rate constant.

Integration of the rate law gives the relation of concentration to time:

$$\ln\left(\frac{[MB]}{[MB]_0}\right) = -kKe^{-k't} = -k't$$

$$[MB] = [MB]_o e^{-k't}$$

where $[MB]_0$ is the equilibrium concentration of the dye and $[MB]$ is the concentration at time t. After the adsorption of dye onto the powder, the remaining concentration is taken as the initial concentration, $[MB]_0$, for kinetic analysis. A linear relation for the graph of ln (C/C_0) vs t was plotted for all of the titanium dioxide powders where the gradient equals the rate constant, k' (Figure 5.6). From the graph in Figure 5.6, the photocatalytic decolourisation of methylene blue seems to follow a gross approximation of pseudo first order kinetics with respect to [MB].

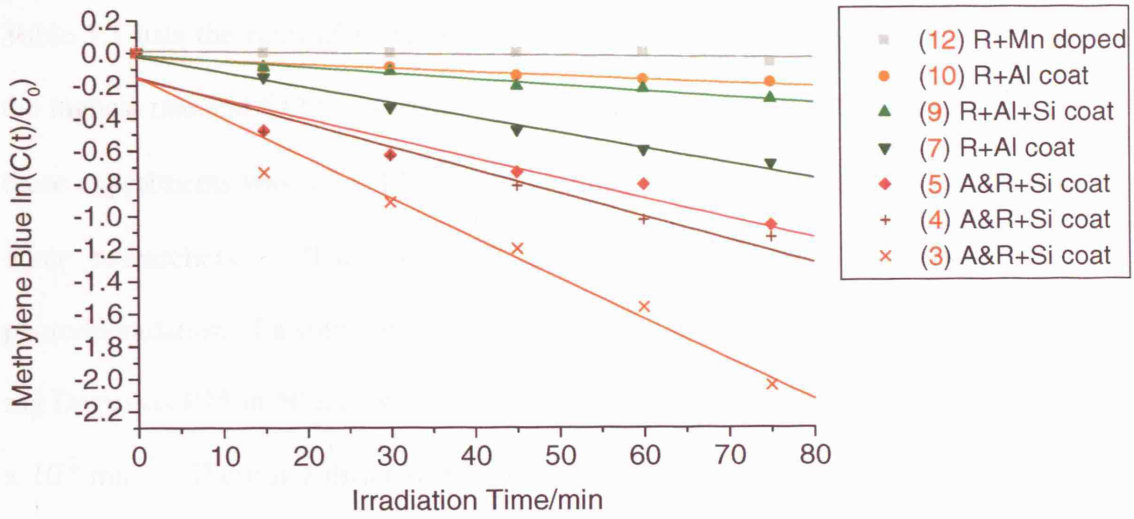

Figure 5.6: Photobleaching rates of methylene blue dye with a few selected pure and extracted titanium dioxide powders. Numbers coloured red in the legend are the sample numbers e.g. (12) is **S12**. (3) A&R+Si coat is **S3** with an Anatase and Rutile crystal mix and organosilane coat.

Table 5.1: Comparison of the rates of degradation of a 0.1 mM solution of methylene blue with titanium dioxide.

Sample	Rate Constant, k (10^{-2} min^{-1})	Rate of reaction (10^{-8} Ms^{-1})
S1	3.8	6.37
S2	3.2	5.30
S3	2.7	4.57
S4	1.7	2.82
S5	1.5	2.52
S6	1.0	1.63
S7	0.8	1.38
S8	0.4	0.65
S9	0.2	0.37
S10	0.09	0.13
S11	0.04	0.067
S12	0.03	0.050
Control (no TiO_2)	0.025	0.042

Table 5.1 lists the rates of reaction calculated for each of the powders with **S1** having the highest rate and **S12** the lowest. The calculated value of the rate constant for P25 in these experiments was 3.8 x 10^{-2} min^{-1} (± 0.003) which is comparable to work done by other researchers. Zhang *et al*[150] have calculated the rate constant of the photodegradation of a solution of 0.1 mM methylene blue dye with a dispersion of 100 mg Degussas P25 in 50 ml solution under 36 W/m^2 irradiance of 360 nm light to be 3.9 x 10^{-2} min^{-1}. There is a difference in the rate constant values quite possibly due to the greater UVA irradiance used by Zhang (36 W/m^2 vs. 35 W/m^2) and the higher amount of titanium dioxide (2g dispersed per litre of dye solution vs. 1g per litre) employed. However, the numbers within the error are the same.

5.1.4.1 Effect of Catalyst Amount

To determine the effect of catalyst amount on oxidation of methylene blue efficiency, experiments were performed with varying quantities of titanium dioxide (**S5**) at an initial concentration of 0.1 mM methylene blue.

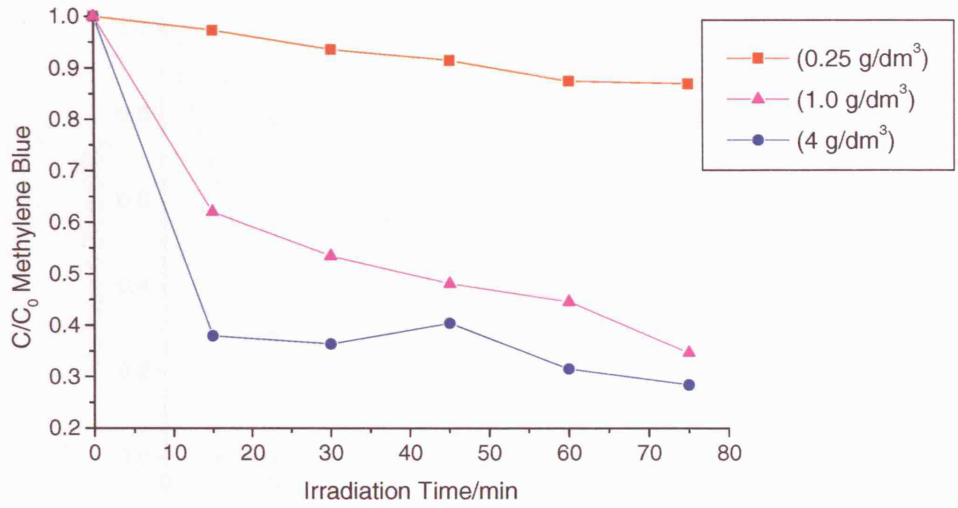

Figure 5.7: Effect of titanium dioxide (**S5**) amount on methylene blue.

When the amount of **S5** was increased from 0.25 g/dm^3 to 4 g/dm^3, the degradation efficiency of the dye increased from 2.7 % to 62.1 % after 15 minutes of UVA irradiation. As the number of molecules of titanium dioxide is increased, there is greater adsorption of the dye molecules onto their surfaces. The number of photons absorbed is also enhanced due to the higher density of titanium dioxide particles in the illuminated area. This in turn leads to an increase in photogenerated charge carriers which can degrade the methylene blue dye.

5.1.4.2 Effect of Initial Methylene Blue Concentration

The effect of the initial methylene blue dye concentration on the degradation rate was investigated in the range 10 – 100 μM for methylene blue in the presence of 1g/dm^3 of Degussa P25.

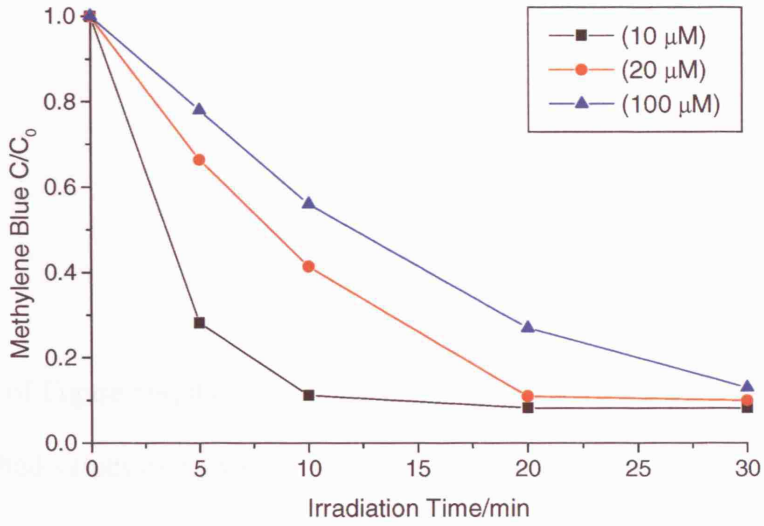

Figure 5.8: Effect of initial dye concentration on the rate of reaction. Increasing the concentration of dye decreases its photocatalytic rate of degradation.

Increasing the concentration of methylene blue from 10 μM to 100 μM decreased the decolourisation efficiency from 92% to 87% in 30 minutes (Figure 5.8). It is possible that increasing the concentration of the dye allows less UV penetration through the dye molecules to reach the titanium dioxide surface.

Table 5.2: Rate constant for the photodegradation of methylene blue decreases with increasing initial dye concentration.

Initial Methylene Blue Concentration	**Rate Constant/min^{-1}**
10 μmol/dm^3	0.108
20 μmol/dm^3	0.087
100 μmol/dm^3	0.041

In general, the photocatalytic reaction followed the Langmuir-Hinshelwood mechanism for diluted solutions where the reaction was apparently first order. This proposed

mechanism was confirmed by a linear plot of the Langmuir-Hinshelwood expression (Figure 5.9):

$$\frac{1}{R_0} = \frac{1}{k} + \frac{1}{kK[MB]_0}$$

From the plot of Figure 5.9, the values of k and K were calculated from the gradient and intercept and had values of 3.38 x 10^8 mol/dm^{3}s^{-1} and 3.92 x 10^{-3} dm^3/mol^1 respectively. This is in good agreement with work done by Lakshmi *et al*[154], who calculated a value of 3.36 x 10^8 mol/dm^{3}s^{-1} for k, the proportionality constant.

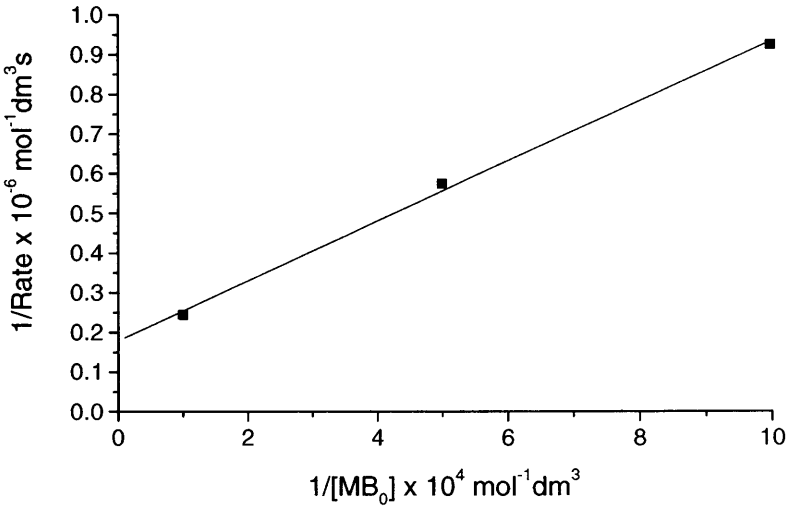

Figure 5.9: Langmuir adsorption isotherm showing linear relationship between reciprocal rate and reciprocal initial methylene blue concentration (10 mg TiO_2, natural pH).

5.1.5 Solar Illumination

The UVA lamp (365 nm monochromatic) used in the laboratory tests had an intensity of 35 W/m^2, and is an appropriate substitute for UVA occurring in natural sunlight, most

closely approximating to natural UVA irradiance during early to mid summer /autumn (average 37 W/m^2) in the UK[155]. In a direct test for the appropriateness of the experimental system, an anatase/rutile crystal mix, organosilane-coated particles isolated from **S2** (Table 5.4) was exposed to natural sunlight in a methylene blue solution. The photo-oxidation of methylene blue was carried out on a sunny, cloudless day in September (London, UK) latitude 52° between 11am and 2 pm. There was a Solar UV Index of 3 recorded for that day. The Solar UV Index is used to express the strength of the sun's ultraviolet radiation and expected risk of overexposure. Levels are predicted on a scale of 0 to 10+ where 0 is minimal risk of overexposure and 10+ is high risk. A UV Index of 3 means that a fair skinned person of Type 1 would have a low to medium risk of skin damage and would burn in more than 1 hour[156]. This experiment was done to give an indication of how the light irradiance from the UVA lamp would compare to direct sunlight.

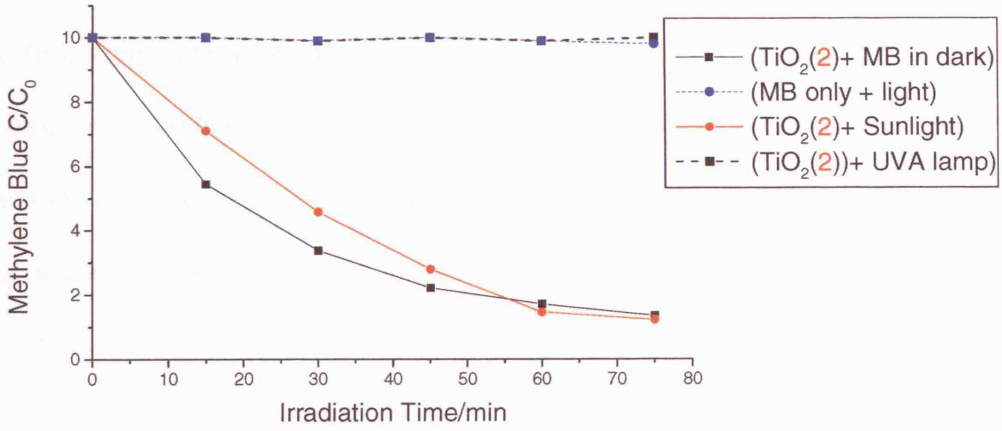

Figure 5.10: Photodegradation of methylene blue (0.01 mM; TiO_2 loading 1g/dm^3) with UVA lamp (35 W/cm^2) and natural sunlight.

Under the same conditions, the photocatalytic activities produced by the lamp and sunlight were very similar. After 75 minutes, the BLB lamp had degraded 88% of methylene blue whereas natural sunlight had removed 86% (Figure 5.10).

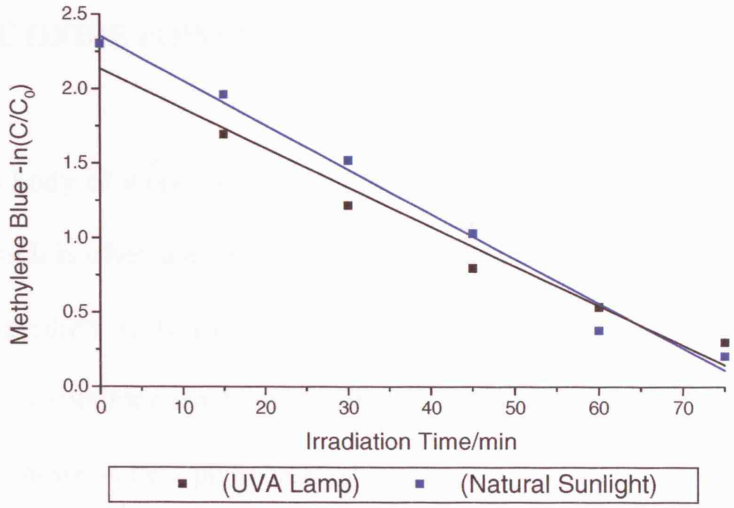

Figure 5.11: Comparable rate of degradation of methylene blue with natural sunlight and the UVA lamp.

The photo-oxidation of methylene blue in the presence of sunlight also followed a pseudo first order rate of reaction as seen in Figure 5.11. The k' value from the UVA lamp plot was 0.0298 min^{-1} with a corresponding half-life of 18 minutes. In comparison, the rate constant, k' for the photo-degradation of the dye under direct sunlight was determined with good accuracy ($R^2 = 0.99$) to have a value of 0.0293 min^{-1} and a half-life of 27 minutes.

The close comparisons of the light irradiance of the lamp to sunlight indicates that these results are significant and 75 minutes in the autumn sun is sufficient to activate titanium dioxide nanoparticles like **S2** into photo-degrading an organic compound such as methylene blue. It can then be assumed that during the summer months, the difference

would be even smaller between the two light sources and the direct sunlight may emit a stronger irradiance than the lamp.

5.2 PHOTOCATALYTIC DEGRADATION OF METHYLENE BLUE BY ZINC OXIDE POWDERS

Although this body of work focuses on titanium dioxide, another inorganic compound, zinc oxide which is often used in sunscreens, could not go unmentioned. Zinc oxide is used as an ingredient in suncreams as a UV reflector, and both titanium dioxide and zinc oxide are sometimes combined in creams to give broad UV spectrum protection. Zinc oxide is known is be a photocatalyst although not as strong as titanium dioxide[157]. The zinc oxide particles can also be coated with inorganic oxides and silicone polymers however; the uncoated powder is also marketed as a sunscreen ingredient. Methylene blue photodegradation experiments were carried out on both pure and extracted samples of zinc oxide and mixed zinc oxide/titanium dioxide powders and is discussed in the next section.

5.2.1 Comparison of the Photocatalytic Activity of Zinc Oxide and Mixed Zinc Oxide/Titanium Dioxide Powders

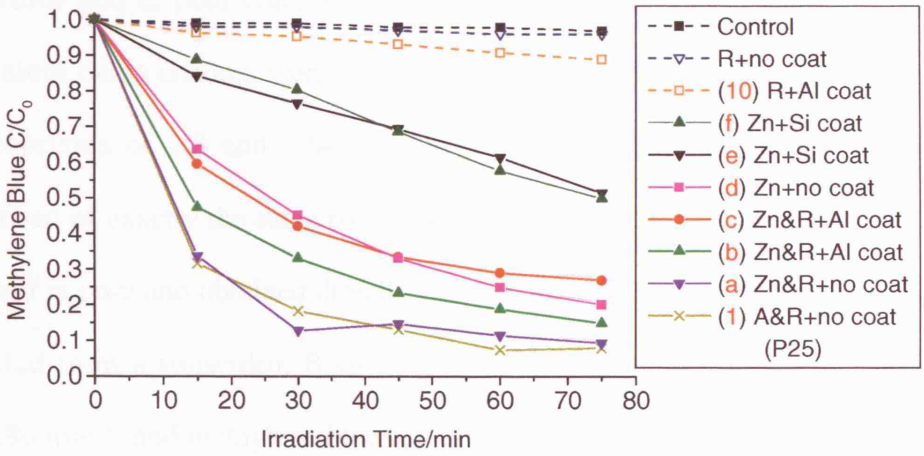

Figure 5.12: Photocatalytic degradation of methylene blue with extracted and pure zinc oxide (**d**,**e**,**f**) and extracted zinc oxide and titanium dioxide mixtures (**a**,**b**,**c**). (1) is S1 (P25); (10) is S10, Rutile with alumina coat.

Figure 5.12 shows all of the zinc oxide powders tested including the pure zinc oxide samples obtained directly from its manufacturer (**d** and **f**) which are uncoated and dimethicone coated respectively. Sample-**e** is a sunscreen extracted dimethicone coated zinc oxide powder. The coated zinc oxide particles (**e**, **f**) showed moderate photoactivity whereas all of the zinc oxide/titanium dioxide mixtures (**a**, **b**, **c**, **d**) exhibited high photoactivity towards methylene blue. Sample-**a**, uncoated mixed zinc and rutile showed similar rates of reaction as Degussa P25. With the analytical techniques used in this work, it was difficult to determine which of the metal oxides were coated or not in the titanium dioxide and zinc oxide mixed powders.

Degussa P25, uncoated titanium dioxide degraded 50% of the methylene blue concentration by 11 minutes. Sample-**a**, a mixture of zinc and rutile with possibly no discernible coating also photodegraded methylene blue to its half-life by 11 minutes. Samples-**b** and **c**, both composed of a mixture of zinc oxide and rutile but with an aluminium oxide coating, were comparatively as photocatalytically active as P25, with rate constants of 2.8 and 2.64 respectively (Table 5.3). Samples-**e** and **f** are both comprised of exactly the same particles-zinc oxide coated with dimethicone. However, sample-**f** is pure and obtained directly from its manufacturer and sample-**e** is chemically extracted from a sunscreen. Both samples (**f** and **e**) show similar rate constants (0.89 and 0.86 min^{-1}) and methylene blue half-lives (74 and 75 minutes).

The presence of zinc oxide under certain conditions is known to enhance the photoactivity of titanium dioxide[158] and can also produce free radicals itself[157]. This may explain why the mixed zinc oxide/rutile powders are more photocatalytically active than pure rutile (**S10**) and pure zinc (sample-**d**) seen in Figure 5.12.

Table 5.3: Calculated rate constants for the pure zinc oxide and mixed titanium dioxide/zinc oxide powders (Zn = zinc; R = Rutile; Al coat = aluminium oxide; Si = dimethicone). Samples **d** and **f** are pure, obtained directly from manufacturers. **a**, **b**, **c**, and **e** are extracted from sunscreens.

Zinc Oxide Sample	Identification Code	Rate Constant/min^{-1}
a	(Zn&R+no coat)	3.12
b	(Zn&R+Al coat)	2.80
c	(Zn&R+Al coat)	2.64
d	(Zn+no coat)	2.60
e	(Zn+Si coat)	0.89
f	(Zn+Si coat)	0.86

5.3 CONTROLS

Several controls were undertaken to unsure that the solvent wash extraction did not alter or chemically change the coatings on the titanium dioxide or zinc oxide particles.

1) In one test, a small amount of the pure titanium dioxide samples **S3** and **S10** obtained directly from its manufacturers were put through exactly the same solvent wash procedure as the sunscreen lotions. These 'washed' samples were then tested for a change in their photocatalytic activity with the methylene blue solution and compared to the unwashed samples. In Figure 5.13, these washed samples are labelled with the suffix –EX.

As seen in Figure 5.13, the rate of methylene blue destruction is near identical in the washed and unwashed **S3** and **S10**. If the solvents had removed the coating, then there would be no barrier to prevent reaction of the photogenerated electrons and holes. An increase in activity denoted by a sharper decrease in the concentration of the methylene blue solution would be seen with the washed powders. Therefore the alumina and the organosilane coats are seemingly unaffected by the extraction process.

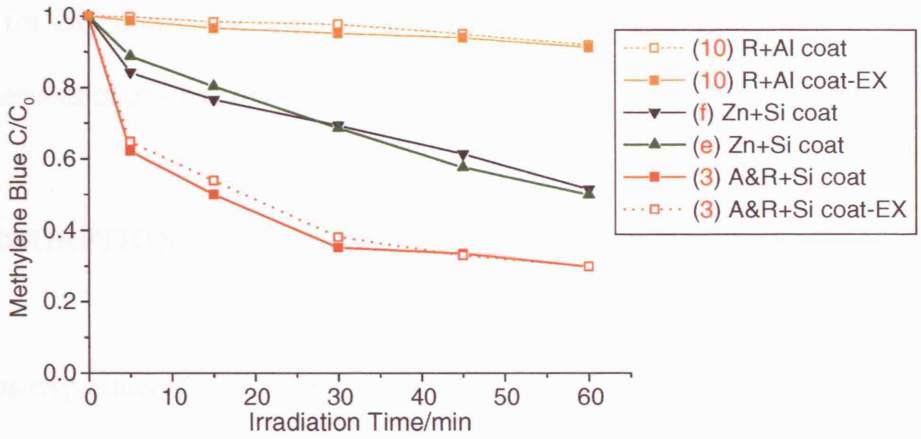

Figure 5.13: Control tests for the solvent extraction process. **S3** (A&R+Si coat) **S10** (R+Al coat) are pure powders obtained from their manufacturers. **S3**-(A&R+Si coat-Ex) and **S10**-(R+Al coat-Ex) are solvent extracted samples of the original pure powders. Sample-**e** is a sunscreen extracted powder of zinc oxide with dimethicone coating. Sample-**f** (Zn+Si coat) is a pure zinc oxide powder with dimethicone coating.

2) A second control test was carried out using the zinc oxide samples. Sample-**f** was obtained directly from the manufacturers and is known to be of zincite crystal form with a dimethicone coating. This was used in its original as-received form. A store-bought sunscreen, sample-**e**, with known active ingredient sample-**f**, was put through the wash procedure so that its own zincite crystal powder with dimethicone coating was extracted. Both sample-**f** (unwashed), obtained from the manufacturer and the extracted sample-**e** (washed) should be the same compound. Both samples were tested with methylene blue and the results are seen in Figure 5.13. They both show similar rates of methylene blue decolourisation and degradation indicating that the extraction process did not alter the dimethicone coating.

3) **S3** obtained from the manufacturer has shown to be one of the most active powders in the methylene blue experiments. In all of the experiments carried out in this

research, **S3** was used as received and was not put through the wash procedure (except for the control test in (1) above). Therefore, its high photocatalytic activity is independent of a solvent-washed altered coat.

5.4 ADSORPTION

The previous experiments have shown that the crystal form and the coating material on the titanium dioxide particles are both integral to their photocatalytic capabilities. The nature of the coating material may affect the adsorption properties of the particle itself, either adsorbing more or less of the methylene blue dye. As photocatalysis occurs on the surface of the titanium dioxide particle, there would be a higher rate of degradation occurring on the surface that adsorbs or is in contact with more of the dye molecules (assuming that other factors such as crystal form was constant).

Adsorption is a general term that refers to the disappearance of solutes from solution with the presumption of accumulation on a solid phase and may result from either physical or chemical interaction with the surface. Physical adsorption is a relatively weak bonding to the surface while chemical (chemisorption) is a stronger interaction which involves ionic or covalent bonding in addition to van der Waal's and dispersion forces operative in physical adsorption. *Adsorption* refers to attraction and bonding onto a surface, while *absorption* is a process in which the solute is taken up into a structure or across a membrane. Methylene blue adsorbs onto the titanium dioxide surface via electrostatic interactions. The amount of adsorption of the dye per unit mass of titanium dioxide (sorbate) was calculated by using the equation below in units of mmol/g:

$$\text{Amount Adsorbed} = \frac{(C_i - C_f)\, V_{sol}}{M_{adsorbate}}$$

where C_i is the initial concentration of methylene blue, C_f is the final concentration of methylene blue, V_{sol} is the volume of solution and $M_{adsorbate}$ is the mass of titanium dioxide. There are several factors which would affect adsorption or absorption onto a surface such as surface area, pore size and chemical composition.

Table 5.4: Adsorption amounts (mmol/g) of methylene blue (100ppm) and each titanium dioxide sample.

SAMPLE	ADSORPTION AMOUNT (mmol/g)
S1	16.1
S2	25.7
S3	11.6
S4	41.2
S5	23.2
S6	73.1
S7	70.7
S8	48.0
S9	4.2
S10	4.0
S11	3.8
S12	8.4
Control	-

The results in Table 5.4 show the adsorption amounts of methylene blue with the various modified titania compounds. With the exception of **S6**, **S7** and **S8**, the organosilane and dimethicone coated particles **S2**, **S3**, **S4** and **S5** adsorb more of the dye (11.6 – 41.2 mmol/g) whereas the alumina coated samples **S9**, **S10** and **S11** adsorb

considerably less of the methylene blue (3.8 – 4.2 mmol/g). From XPS and SSNMR, it is known that **S6** and **S8** both contain the clay, magnesium aluminium silicate that can also adsorb a large amount of the dye thereby giving a false indication of the amount of adsorbed molecules on the titanium dioxide particles. **S6**, **S7** and **S8** are also the only samples which also contain a mixture of both silica (dimethicone for **S8**) and alumina in their coatings. Nonetheless, there seems to be a correlation between the amount of dye adsorbed onto the surface and the photocatalytic ability of that particle, with generally higher adsorption on a single coated particle equaling a greater photocatalytic activity.

5.4.1 Isoelectric Point

The different adsorption properties of the silicon and aluminium coating materials are directly related to their surface charges in aqueous solution. The surface charge of a pigment such as titanium dioxide is often given as the isoelectric point or point of zero charge, which is the pH at which the surface charge of the pigment is zero[159,160].

The surface becomes negatively charged in an environment where the pH is higher than its isoelectric point.

$$M-OH + OH^- \leftrightarrow M-O^- + H_2O$$

At lower pH than the compound's isoelectric point, the surface becomes positively charged.

$$M-OH + H^+ \leftrightarrow M-OH_2^+$$

Table 5.5: Isoelectric points of compounds used in this work[160, 161]

Pigment	Isoelectric Point (pH)
Anatase	6.0
Rutile	6.7
Silica	2
Alumina	9.3
Zinc	9.0
Manganese (IV) Oxide	2.8 – 4.5

All of the methylene blue experiments were carried out at pH 6.7. Although silica has an isoelectric point of 2 (Table 5.5), the value of organosilane and siloxanes are not much higher at pH 3 – 4[161]. Therefore, the surfaces of the organosilane and dimethicone coated titanium dioxide particles possess a negative charge when dispersed in the neutral methylene blue solution. As methylene blue is a cationic dye, there would be an attraction to the negatively charged silane coated titania surface. This attraction may also occur between the uncoated surface of Degussa P25 (**S1**) and methylene blue dye, as the isoelectric point of P25 is between 6.0 – 6.7.

As alumina has an isoelectric point of 9.3, its surface would acquire a net positive charge in the neutral methylene blue solution. Consequently, there would be a slight repulsion between the cationic methylene blue and the positively charged alumina surface.

In summary, the absorption characteristics of these coated titanium dioxide particles can be correlated to the charge state and chemical composition of the surfaces. The organosilane and siloxane coated titania powders have a greater attraction to the positively charged methylene blue dye, which is seen in the adsorption amounts of **S1** –

S5 in Table 5.4. The low isoelectric point of silica (pH 2) may also explain the extremely high adsorption amounts calculated for **S6** and **S8** as they both contain silica coatings. The alumina and manganese oxide coatings for **S9**, **S10**, **S11** and **S12** become positively charged in neutral pH methylene blue solution and repel the dye molecules thereby adsorbing a low amount of the dye. As seen in Table 5.4, the greater the adsorbed amount of dye for the particles with a single coat (excluding **S6** and **S8**), the better their photocatalytic degradation of methylene blue. The crystal form alone cannot explain the difference in photocatalytic activities observed in the powders. **S6** and **S8** both comprise of titanium dioxide as rutile. However, unlike the other rutile powders like **S10** and **S11**, **S6** and **S8** are moderately active. The difference between the powders is that **S6** and **S8** posses a mixed coat of alumina and silica and have very high dye adsorption amounts (73.1 mmol/g for **S6** vs. 4.0 mmol/g for **S10**). It is possible that the rate of dye degradation would be greater for the rutile powder that has more dye molecules attached to its surface.

5.5 SUMMARY

Table 5.6: Summary of methylene blue experiments - crystal form, coating and kinetics of the different titanium dioxide powders (A=Anatase; R=Rutile).

SAMPLE	FORM	COATING	MB (½ -life) (min)	Rate of reaction (10^{-8} mol/dm^3/s)	ADSORPTION AMOUNT (mmol/g)
S1	85% A 15% R	Uncoated	11	6.37	16.1
S2	90% A 10% R	Tri-methoxycaprylysilane	11.5	5.30	25.7
S3	85% A 15 % R	Tri-methoxycaprylysilane	12.2	4.57	11.6
S4	85% A 15% R	Dimethicone	35	2.82	41.2
S5	75% A 25% R	Tri-methoxycaprylysilane	40	2.52	23.2
S6	100% R	Alumina and Silica	68	1.63	73.1
S7	100% R	Alumina and Dimethicone	90	1.38	70.7
S8	100% R	Alumina and Silica	> 120	0.65	48.0
S9	100% R	Aluminium hydroxide	>120	0.37	4.2
S10	100% R	Alumina	> 120	0.13	4.0
S11	100% R	Aluminium hydroxide	> 120	0.067	3.8
S12	100% R	Mn Doped	> 120	0.050	8.4
Control	-	-	> 120	0.042	-

Both titanium dioxide and zinc oxide powders were either chemically isolated from store-bought sunscreens or they were obtained directly from its manufacturer. They were all tested to rate their photocatalytic strength via the photodecolourisation and degradation of methylene blue solution. The majority of the zincite/rutile crystal form mixtures which were isolated from sunscreens showed very high activity, some close to

(sample-**b**,**c**,**d**) and one very similar (sample-**a**) to that of P25. Under certain conditions, zinc oxide is a photocatalyst and when doped with titanium dioxide, can exhibit higher photocatalytic abilities.

The photocatalytic degradation followed the Langmuir-Hinshelwood adsorption mechanism and was dependent upon the concentration of the initial methylene blue solution and the amount of titanium dioxide. The most active sample was P25, uncoated titanium dioxide with an 85:15 anatase to rutile mixed crystal form. However, of the titanium dioxide samples, the sunscreen-isolated **S2**, an organosilane coated 90:10 anatase to rutile mixed crystal form was similarly active to P25. The pure sample, **S3** which was obtained directly from the manufacturer and used as received, was also comparable in photocatalytic strength to **S2** and P25. **S4** and **S5** showed moderate destructive abilities. **S3**, **S4** and **S5** all have a mixed anatase and rutile crystal form with an organosilane (**S3**, **S5**) or silicone coat (**S4**).

From Table 5.6, there are definitely two criteria, which determine the activity of the titanium dioxide powders. The first is the crystal form. The 100% rutile powders are all less photocatalytically active than the anatase/rutile mixed nanoparticles. Anatase is generally known to be a better photocatalyst than rutile[158]. The complete reasons have not yet been identified but there are a few theories. The different manufacturing techniques used to process the particles would give them variable adsorption and acid-base properties. In addition, the smaller bandgap of rutile (3.0 eV) compared to anatase (3.2 eV) would increase the rate of electron-hole recombination thereby resulting in less photogenerated species to initiate reactions.

The second criterion is the type modification carried out on the titanium dioxide core. In these experiments, the different coated TiO_2 particles were more photocatalytically active than the manganese doped titania. The type of coating either contained silicon or aluminium. The alumina and aluminium hydroxide-coated samples all seemed to inhibit the activity of the titanium dioxide core more efficiently than the organosilane and silicone-coated titania particles. This could be due to the adsorption properties of the two different types of compounds.

The powders which contained anatase were able to photodegrade methylene blue much faster than the rutile powders. However not all of the rutile samples were completely inactive such as **S6**, **S7** and **S8**. Therefore, the coatings on the titania surface that affects the adsorption properties of the particles must play an important part in its photocatalytic activity. The organosilane, dimethicone and silica coatings all adsorb more of the dye compared to the alumina coatings. Giles et al[162] have confirmed this observation with the adsorption of methylene blue on each of the different metal oxide surfaces $SiO_2 > TiO_2 > Al_2O_3$. The low isoelectric points for silica, organosilane and dimethicone coatings induce a negative charge on the particle surface which attracts the cationic methylene blue. The opposite occurs with the alumina coated particles, where a high isoelectric point creates a positive charge on the surface and repels the dye.

It seems that a combination of crystal form of the titanium dioxide core and chemical nature of its outer coating, which affects its adsorption properties, are the most important factors in determining the photocatalytic capabilities of modified titania particles used in sunscreens.

The chemical experiments have shown some of the titanium dioxide powders to be as photocatalytically active as Degussa P25, a well-known photocatalyst, in degrading methylene blue dye. The next step was to determine whether these powders had the ability to adversely affect living cells as they are used in creams applied to human skin. Chapter 6 details the biological techniques and background used in the experiments and Chapter 7 gives an account of the results.

Chapter 6 – Biological Experimentation

This chapter is the beginning of the biological segment to this work. It describes the background to the main cell biology topics that are focussed on in this research, such as apoptosis or cell death. The biological techniques such as fluorescent staining and managing cell cultures are also explained in detail in the introductory section. The procedures of the different biological experiments are stated in the remainder of the chapter. In Chapter 7, the results of the biological experiments are given.

6.1 INTRODUCTION

6.1.1 Apoptosis

Apoptosis is one of the main types of cell death. It is a process of deliberate suicide of an unwanted cell in a multi-cellular organism. The other more common form of cell death is necrosis, which is accidental death due to cell injury or disease. In contrast, apoptosis is an ordered process that has many advantages to an organism's development. Apoptosis occurs throughout a vertebrate's lifespan and it is especially critical in embryogenesis (development and growth of an embryo), for example sculpting finger webs and eyelids[162]. Aging cells also undergo apoptosis, as do many cells damaged by ionising and non-ionising radiation. Since the 1990s, studies on cell death have been extensively carried out so typical active physiological changes during cell death, leading to apoptosis, are well known[163]. These changes include cell and nuclear shrinkage, phosphatidylserine externalisation, caspase activation, internucleosomal DNA fragmentation and disassembly into membrane-enclosed vesicles (apoptotic bodies). In vivo, this process terminates with the engulfment of apoptotic bodies by other cells, preventing release of intracellular contents[163].

As these markers seem to be characteristic and exclusive to apoptosis, they can be used to identify this mode of cell death by techniques such as microscopy. Therefore, measuring apoptosis is a recognised assay for determining cell death due to external factors. In this research, the external factor is the inorganic compound, titanium dioxide, when exposed to ultraviolet A radiation. If the particles are harming the cells then an increase in the number of apoptotic nuclei should be observed in the presence of UVA irradiation. If the particles are protecting the cells, as is part of their function in sunscreens, then there should be a decrease in the number of dying cells as compared to cells exposed to UVA alone.

6.1.2 Fluorescent Staining

Florescence is a luminescence in cold bodies where a molecule absorbs a high-energy photon and re-emits it as a low-energy (longer wavelength) photon. This property can be combined with histochemical or cytochemical skining to view/examine structures in biological tissues or cells respectively with the aid of a microscope[164]. Fluorescent labelling can be achieved via methods using fluorescent dyes and fluorescently-labelled antibodies. The cell staining procedure can be divided into four steps:

1. Cell or tissue preparation
2. Fixation and Permeabilisation
3. Antibody binding or dye staining
4. Detection

As living tissues are fluid, dynamic structures, fixation is required to immobilise and preserve the antigens while retaining cellular/subcellular architecture. Cells can be fixed by either solvent fixation or by chemical cross-linking[164]. Cell membrane permeabilisation allows antibody access to intracellular antigens. This is achieved either with inorganic solvents or anionic detergents. Antibodies are used because of their ability to specifically recognise antigens on proteins and other biological structures of interest to which they have been raised (see Figure 6.1). They are usually directly or indirectly coupled to a fluorescent molecule to aid in imaging the target. The cells are incubated with an antibody which is specific for the protein of interest and which at the correct concentration should not bind to non-specific proteins in the cell. Unbound antibody is removed by washing and the bound antibody detected directly (if the primary antibody is labelled) or indirectly by using a labelled secondary antibody that binds to the primary antibody.

Antibodies can be made in the laboratory by injecting an animal (usually a mouse, rabbit, sheep, or goat) with antigen A.

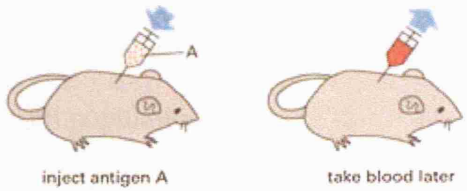

Repeated injections of the same antigen at intervals of several weeks stimulates specific B cells to secrete large amounts of anti-A antibodies into the bloodstream.

Figure 6.1: Raising antibodies in animals[165]

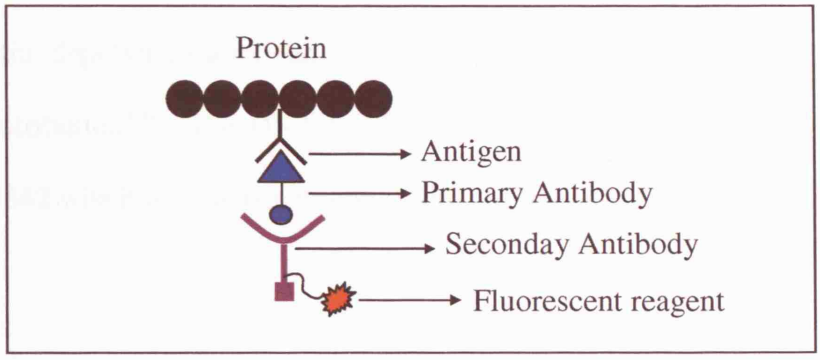

Figure 6.2: Fluorescent staining by antibody binding.

When a fluorescent antibody dye complex is added to a permeabilised cell, it will bind to the corresponding antigen, which will then be visibly labelled when illuminated by the exciting wavelength. This is known as *immunofluorescence*.

Many large structures of interest can be visualised by *affinity fluorescence*, i.e. the spontaneous localisation of fluorophores to or within a structure by virtue of their combined chemical properties. The fluorescent dyes and stains are class-specific to structures such as DNA and proteins and are used to quantify or qualify the presence of a specific compound. Stains may be used to examine bulk tissues such as muscle fibres or as in these experiments, cell populations.

In these experiments, affinity fluorescence is utilised where the DNA and Filamentous actin (F-actin) of the cells have been stained for viewing. When cells go through apoptosis, the DNA and F-Actin change structurally and these changes can be observed by fluorescent staining. F-actin is the polymer form of the protein actin, which is the main constituent of the thin filaments of muscle fibres. It provides mechanical support for the cell, determines the cell shape and enables cell movement[164]. F-actin can be

viewed by specific binding of phalloidin, a toxin from the Death Cap mushroom which inhibits actin depolymerisation and is thus an important tool in determining actin filament distribution[164]. The DNA has been labelled with a fluorescent Hoechst dye, Hoechst 33342 which is a bis-benzimide (Figure 6.3).

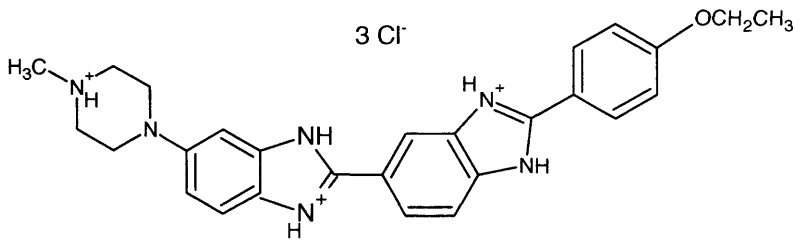

Figure 6.3: Chemical structure of Hoechst 33342 a bis-benzamide[166] with molecular formula $C_{27}H_{28}N_6O.3HCl.3H_2O$

The dye in Figure 6.3 can permeate cell membranes excited by light at 351-364 nm, and emits blue/cyan fluorescence light around an emission maximum at 465 nm when bound to DNA[167]. Hoechst may be used to stain live or fixed cells as it is relatively non-toxic.

6.2 MATERIALS

Dulbecco's Modified Eagle Medium High Glucose (DMEM), Eagle's Minimum Essential Medium Low Glucose (EMEM), Penicillin/Streptomycin, Fetal Bovine Serum (FBS), Formaldehyde, Phosphate Buffered Saline (PBS), Triton X-100 (Tx), Antibody Diluting Solution (Abdil which consists of 2% w/v bovine serum albumin, 0.1% v/v Tx and 0.1% sodium azide in PBS).

Alexa Fluor® 594 Phalloidin, Hoechst 33342, Annexin V, Sytox Green, Rabbit active Caspase 3, Goat anti-rabbit secondary antibody, Zvad-FMK, Mouse Antiphosphohistone 2AX, FITC-goat-anti-mouse secondary antibody.

6.3 METHODOLOGY

Cell types used in throughout the experiments:

1. MDCK-I (Madin-Darby Canine Kidney)
2. PtK2 (*Potorous tridactylis* (potoroo or kangaroo rat) kidney)
3. HaCaT (Human keratinocyte)

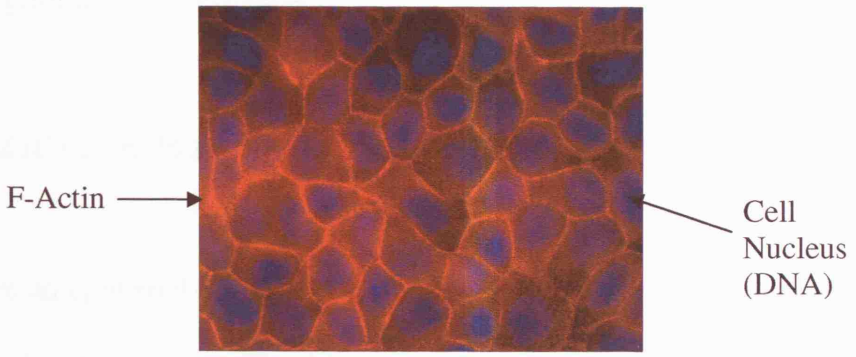

Figure 6.4: Fluorescent stained micrograph of a monolayer of HaCaT cells. The cell nucleus is stained blue with Hoechst and the F-actin is stained red with phalloidin. All of the cell lines used in these experiments look similar to this image when stained for the appropriate structures.

6.3.1 Cell Culture

6.3.1.1 MDCK-I (Madin-Darby Canine Kidney)

MDCK-I cells are epithelial cells derived from the kidney of a canine. These cells form monolayers with characteristics of tight cell-cell junctions. The cells were routinely maintained at 37 °C/10 % CO_2 in DMEM (Dulbecco's Modified Eagle Medium) (high glucose) supplemented with 1% (v/v) penicillin/streptomycin and 10 % (v/v) fetal bovine serum (FBS). The cultures were expanded in T-75 flasks and the medium was exchanged when necessary, usually after two days and the cells were split 1:6 when confluent. The cells grew as a monolayer on 13 mm glass coverslips in a 6 cm dish and were seeded at a density of 3x 10^4 and 5 x 10^4 cells/ml for 72 hours and 36 hours respectively, prior to the experiments.

6.3.1.2 PtK2 (Potorous tridactylis (potoroo or kangaroo rat) kidney)

PtK2 cells are an epithelial-like cell line which was established from the kidney tissue of an adult male rat kangaroo. The cells were maintained at 37 °C/5 % CO_2 in EMEM (Minimum Essential Medium) (low glucose) supplemented with 10 % fetal bovine serum (FBS), 1 % (v/v) penicillin/streptomycin and 1.5% glutamine and split 1:4 every four days. The cells grew as confluent monolayers on 13 mm glass coverslips in a 6 cm plastic dish and were seeded at a density of 5 x 10^4 cells/ml for 36 hours prior to the experiment.

6.3.1.3 HaCaT (Human Keratinocyte)

HaCaT is a human epidermal keratinocyte cell line that exhibits a cobblestone like morphology. HaCaT cells are often used in epidermal studies, as it is representative of normal keratinocytes. The cells were routinely maintained at 37 °C/5 % CO_2 atmosphere in DMEM (low glucose) supplemented with 1 % (v/v) penicillin/streptomycin and 10 % (v/v) fetal bovine serum (FBS). The cultures were expanded in T-75 flasks and split 1:4 every three days. The cells attained confluence after three days following seeding at 9 x 10^5 cells/ml in a 50/50 mixture of conditioned and fresh media. The use of conditioned media was to ensure that the cells would adhere to the glass coverslips. Fresh media was then exchanged within 24 hours and the cells allowed to grow to confluency.

Optimum conditions had to be determined for each of the cell cultures. Early experiments showed that the cells went through apoptosis at different rates and cell density seemed to be an important criterion affecting the final number of apoptotic cells. A larger number of cells on the coverslip would result in an increase the number of apoptotic cells after irradiation. In order for variables to be reduced for each experiment, the number of cells in each experiment had to be roughly the same. Therefore, the initial seeding density of the cells for a particular cell type was equal for each test.

6.3.2 UVA Irradiation of Cultured Cells

6.3.2.1 Titanium Dioxide Loading

To devise appropriate laboratory tests, the amount of titanium dioxide within sunscreen lotions was considered. The recommended sunscreen application that is used to determine its SPF value is 2 mg/cm^2 of skin. In Europe, up to 0.5 mg/cm^2 (25%) of titanium dioxide is allowed in sunscreens[168]. The titanium dioxide particles were consequently tested at less than the recommended amount- 0.1 mg/cm^2 and 0.4 mg/cm^2.

6.3.2.2 Light Source

The UVA lamp (365 nm monochromatic) had an intensity of 35 W/m^2, and is an appropriate substitute for UVA occurring in natural sunlight; it most closely approximates the natural UVA irradiance during early to mid summer /autumn (average 37 W/m^2) in the UK[169].

6.3.2.3 Apoptosis Assay

The biological effect of the titanium dioxide powders was investigated by quantifying the amount of apoptosis induced in cells, which have been exposed to ultraviolet A light in the presence of these powders. A monolayer of MDCK, PTK2 and HaCaT cells were used as *in vitro* models of simple epithelia. 1 and 3 mg of the titanium dioxide powder was suspended in 750 µl chamber media (DMEM/F-12, 1% (v/v) penicillin/streptomycin and 10% (v/v) fetal bovine serum) and sonicated for 5 minutes in order to enhance its distribution. The suspension was then added to the monolayer of

cells grown on a 13 mm glass coverslip which was in a 3 cm plastic dish (area 7.07 cm^2). The inorganic particles sank to the bottom of the dish, which was gently rocked from side to side to evenly coat the cells with the powder. The particles remained fixed on the cells. Final amounts of 0.1 mg/cm^2 and 0.4 mg/cm^2 titanium dioxide were used in these experiments.

Irradiation was carried out with a BLB lamp with a spectral output peaking at 365 nm. A series of exposure times were evaluated (15, 30, 45, 60, 90, 120 minutes) combined with a series of incubation times (60, 120, 150, 165, 180 minutes) to determine the optimum conditions for UVA induction.

To replicate the effects of being in the sunlight, the cells were irradiated with 3.5 mW/cm^2 of 365 nm (UVA) light for 2 hours, adding 150 µl of media to the dish every 30 minutes to account for evaporation losses. After irradiation, the media was removed and the cells were rinsed with warm PBS (Phosphate Buffered Saline) until the majority of the titanium dioxide powder was removed. 1.5 ml DMEM was added to the cells, which were then incubated for 3 hours in the respective atmosphere for that particular cell line. Control cells were also set-up for each experiment. The controls consisted of cells ± UV and cells – UV + titanium dioxide. After incubation, the cells were fluorescently labelled for microscopy analysis. In this procedure, the cells were chemically fixed (denaturing of proteins to fix them into place) with 4% formaldehyde in PBS for 20 minutes then washed three times with PBS. The cells were rinsed with 0.1% Triton X-100 in PBS (Tx), permeabilised for 10 min with 0.5% Tx, rinsed with 0.1% Tx, blocked with Antibody Diluting Solution (Abdil which consists of 2% w/v bovine serum albumin, 0.1% v/v Tx and 0.1% sodium azide in PBS) for 20 min, stained

for F-Actin with Alexa Fluor® 594 phalloidin for 20 min, washed with 0.1% Tx and finally stained for DNA with 1 μg/ml Hoechst 33342 in Abdil for 2 min.

The stained coverslips were mounted onto glass slides and were subsequently viewed by florescence microscopy. Florescence micrographs were obtained using a Nikon eclipse e800 microscope and captured using a SynSys cooled charge-coupled device (CCD) camera (Roper Scientific). A total of 1000 cells were counted per coverslip and the average over 3 or 4 experiments was calculated.

6.3.3 Annexin V and Sytox Green experiment

Cells were treated with 1 mg of Degussa P25 in 750 μL of chamber media at 37 °C and irradiated with 3.5 mW/cm^2 of UVA (365 nm) light for 2 hours, adding 150 μL of chamber media at 37 °C every 30 minutes. Controls of untreated cells (no TiO_2, no UV) and TiO_2 treated cells with and without UVA were also carried out in parallel. A coverslip of MDCK-1 cells irradiated with 312 nm (UVB) light for 7 minutes was used as a positive control. After irradiation, the titanium dioxide particles were washed from the cells; the chamber media replaced with 1.5 ml growth media and the cells were then incubated for 3 hours. The coverslips were transferred to a cell-staining chamber and incubated with 18 μL of Annexin V per 50 μL of chamber media combined with 0.5 μM of Sytox Green for 20 minutes at 37°C/10% CO_2. The cells were washed with DMEM, rinsed with PBS then fixed with 4% formaldehyde for 20 minutes. The staining procedure for DNA and F-Actin was then carried out. The cells were rinsed with 0.1% Triton X-100 in PBS (Tx), permeabilised for 10 min with 0.5% Tx, rinsed again with 0.1% Tx, and blocked with Abdil for 20 min. F-Actin was labelled with

Alexa Fluor®-594 phalloidin for 20 min followed by a final washed with 0.1% Tx and lastly DNA was stained using 1 μg/ml Hoechst 33342 in Abdil for 2 min. The coverslips were then drained, mounted, sealed and viewed by fluorescence microscopy.

6.3.4 Antibody Specific Caspase 3 Detection

Cells were treated with 1 mg of Degussa P25 in 750 μL of chamber media at 37 °C and irradiated with 3.5 mW/cm^2 of UVA (365 nm) light for 2 hours, adding 150 μL of chamber media at 37 °C every 30 minutes. Controls of untreated cells (no TiO_2, no UV) and TiO_2 treated cells with and without UVA were also carried out in parallel. A coverslip of MDCK-1 cells irradiated with 312 nm (UVB) light for 7 minutes was used as the positive control. After irradiation, the cells were rinsed with PBS then fixed with 4% formaldehyde for 20 minutes. The staining procedure for the detection of Caspase 3 and DNA was then carried out. The cells were rinsed again with 0.1% Triton X-100 in PBS (Tx), permeabilised for 10 min with 0.5% Tx, rinsed with 0.1% Tx then blocked with Abdil for 30 min. The primary antibody, *rabbit active caspase 3*, was added to the cells at a 1 in 20 dilution. After 1 hour, the cells were thoroughly washed and incubated with *goat anti-rabbit* secondary antibodies conjugated to Alexa Fluor® 488 for 40 minutes. The cells were washed with 0.1% Tx for 5 minutes, incubated with Hoechst for 2 minutes, washed again with 0.1% Tx for 10 minutes and finally rinsed with PBS. The coverslips were drained, mounted and sealed on microscope glass slides for fluorescent microscopy.

6.3.5 Broad-Spectrum Caspase Inhibitor (Z-VAD-FMK)

The MDCK-I cells were grown on 13 mm coverslips and pre-incubated with 8 μM Zvad-fmk in DMEM for 1 hour. 1.7% Degussa P25 as the titanium dioxide powder was uniformly sprinkled onto the cells which were then irradiated for 2 hours with 3.5 mW/cm^3, 365 nm light. 150 μl of chamber media was added to the dish every 30 minutes to account for evaporation losses. The controls were cells + UV ± Zvad-fmk and cells – UV ± Zvad-fmk ± TiO_2. After irradiation, the cells were incubated with the caspase inhibitor for 3 hours, then fixed in formaldehyde and stained for DNA and F-Actin as described in the Annexin V and Sytox Green experiment.

6.3.6 DNA Damage Assay

MDCK-I cells were prepared as above and irradiated for 2 hours with 3.5 mW/cm^3, 365 nm light. 150 μl of chamber media was added to the dish every 30 minutes to account for evaporation losses. Cells were tested after 3 hours and 24 hours incubation. After the respective incubation time, the cells were fixed in methanol at –20 °C for 5 minutes, rinsed with PBS, washed with 0.1% Triton X-100 in PBS (Tx), permeabilised for 10 min with PBS-0.5% Tx, rinsed with PBS-0.1% Tx and blocked with Abdil for 20 minutes. The primary antibody, *mouse antiphosphohistone 2AX* was added at a dilution of 1 in 75 for 45 minutes. The cells were washed thoroughly and the secondary antibody, *FITC-goat-anti-mouse* was added at a 1/50 dilution for 30 minutes. The cells were washed with PBS-0.1% Tx, incubated with Hoescht in Abdil for 5 minutes and finally washed with PBS-0.1% Tx and rinsed with PBS. The coverslips were then drained, mounted and sealed onto glass slides in preparation for imaging.

Chapter 7 – Biological Results

The purpose of this chapter is to test any damaging effect on cells induced by UVA-activated modified titanium dioxide particles. Two separate approaches were used: cellular damage assayed by apoptosis and activation of the DNA-damage-response pathway. This type of cellular research using apoptosis markers and fluorescent microscopy on inorganic powders like titanium dioxide has never been carried out before. In this work, the definite morphology of a cell's nucleus, which goes through apoptosis or programmed cell death, is used as a marker for dying cells. A few minutes irradiation with the highly energetic UVC (λ: 100 – 280 nm) light alone is a standard experimental method to induce apoptosis in cultured cells within 2-4 hours post-irradiation, with well-characterised alterations in cell morphology, including nuclear condensation and fragmentation[170]. However, the timing and morphology of apoptotic nuclei induced by the less energetic, more penetrative UVA is less well characterised. The UVA irradiations induced a non-fragmented or hyper-condensed type of cell nucleus, which was more prominent in the presence of titanium dioxide. These new type of nuclei, which may be part of a novel cell death pathway, are also analysed and characterised in this chapter.

Three different cells lines from animals and human were tested with the UVA irradiated titanium dioxide particles and the results of all cell lines are discussed in this chapter.

7.1 ANALYSIS OF HYPER-CONDENSED NUCLEI

7.1.1 Morphologies of UVA Irradiated Cells in an Epithelial Monolayer

7.1.1.1 Introduction

In most apoptosis studies, the usual treatment for cells is UVB and UVC radiation, which results in some of the nuclei going through the structural changes seen in Figure 7.1 (B-D). One of the early events of cell death is dehydration, which causes a change in the cell size and shape. The cells may become elongated and generally smaller. A more characteristic marker of apoptosis is nuclear chromatin condensation as seen in Figure 7.1 (B-D) where the DNA takes on a concave shape, finally separating into small spherical nuclear fragments, known as 'apoptotic bodies'. The final step in the apoptotic pathway is the removal of the dead cell. In simple epithelia the dying cell is extruded from the monolayer [171]. Lastly, 'eat me' signals are expressed on the apoptotic cell surface, which summons phagocytic cells to engulf and remove the dying cell.

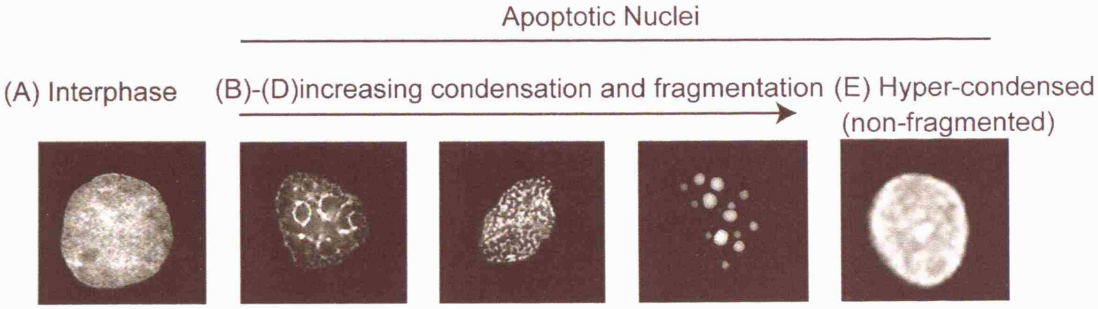

Figure 7.1: Morphological changes of a cell's nucleus undergoing apoptosis. (Images taken from MDCK cells but observed in all cell lines). (A) Interphase or a normal nuclei (B)-(D) is normal apoptotic change from early to late phase where the nuclei is completely fragmented (E) hyper-condensed nuclei observed in UVA irradiation. (images not to scale)

UVA induced apoptosis has not been as widely researched because the effects of all the different wavelengths of ultraviolet radiation on living tissue were thought to be similar[172].

7.1.1.2 Morphology Results and Discussion

In these experiments, all cells were irradiated with monochromatic UVA light, which resulted in a few nuclei going through the normal apoptotic pathway seen in Figure 7.1 (B-D). However, a number of hyper-condensed nuclei were also observed (Figure 7.1E). They were usually half the size of an interphase nuclei and their DNA were very brightly stained due to the compactness of their composition. These structures were observed for all three cell lines (MDCK, PtK2 and HaCaT) examined. The morphological changes in Figure 7.1 were also observed when cells were irradiated in the presence of titanium dioxide however, a much higher percentage of the cells resembled Figure 7.1E.

These hyper-condensed nuclei are not normally observed in such vast numbers in UVB and UVC irradiations compared to those seen with UVA illumination in the presence of titanium dioxide. As there is no information about this nuclear phenotype in the available literature, it is unknown as to whether the hyper-condensed nuclei are apoptotic (dying) or not. Since a single apoptosis assay is often not sufficient to demonstrate apoptosis, it is recommended that determination of apoptosis be analysed by a variety of methods:

1. Morphology
2. Annexin V (binding to externalised phosphatidylserine)

3. Caspase 3 activation
4. Inhibition of caspase activity – Zvad-fmk

The morphology of an apoptotic nucleus was discussed in Section 7.1. An apoptotic nucleus usually shrinks to about half its original size due to condensation of its nuclei. This hallmark characteristic of apoptosis is seen in the hyper-condensed nuclei. However fragmentation of the DNA into apoptotic bodies does not occur. Other studies have shown that the precise apoptotic phenotype can vary considerably depending on the cell type, cell cycle and the initiating factors[173]. However, the hyper-condensed nuclei were observed in all three cell lines and in every experiment. The other three methods used to determine whether the hyper-condensed nuclei are going through the apoptotic cell death pathway is discussed in Section 7.1.2 – 7.1.4.

7.1.2 Annexin V and Sytox Green experiment

7.1.2.1 Introduction

During apoptosis, there are many different morphological and biochemical changes. In normal viable cells (human and animal), phosphatidylserine (PS) is located on the cytoplasmic surface of the cell membrane. In apoptotic cells, PS is externalised from the inner to the outer part of the cell membrane in order to recruit phagocytes and induce phagocytosis[174,175]. This membrane asymmetry can mark the cell as being apoptotic. Annexin V is a member of the calcium and phospholipid binding family of proteins. It is a human vascular coagulant that has a high affinity for phosphatidylserine therefore it can be used to identify apoptotic cells[176]. A positive staining of the hyper-condensed nuclei (red colour) when incubated with Annexin V would indicate that this nuclear phenotype is most likely apoptotic.

7.1.2.2 Annexin V and Sytox Green Results and Discussion

In this assay, HaCaT cells were UVA irradiated in the presence of **S3**, anatase and rutile titanium dioxide with organosilane coating, as it is one of the most photoactive powders. The cells were incubated with Annexin V and Sytox Green to determine whether the hyper-condensed nuclei produced from the irradiation were dying via apoptosis. The FITC-Annexin V (red) labelled only the mid to late stage apoptotic cells whereas the early staged apoptotic cells were not stained at all. This is consistent with other research[175] which has shown that binding of Annexin V only coincides with chromatin condensation of cells i.e. during later stages of apoptosis. In this assay, the hyper-condensed nuclei were brightly stained with the FITC-Annexin V conjugate (Figure 7.2). This signifies that phosphatidylserine was exposed on the outer envelope and seemingly that the hyper-condensed nuclei is a late phase of apoptosis.

Sytox Green is a high-affinity DNA stain that does not cross the membranes of live cells yet easily permeates the compromised plasma membranes of dead cells[177]. Sytox Green stains late stage apoptotic cells and necrotic cells with an intense green fluorescence. Some of the cells (hyper-condensed and normal apoptotic) stained with the Annexin V also concurrently stained with Sytox Green (Figure 7.2 C, B) indicating that Annexin V is a marker for membrane damage. Therefore, the pictures in Figure 7.2 show that the hypercondensed nuclei which are formed during UVA irradiation with titanium dioxide, have damaged membranes and are most likely late stage apoptotic.

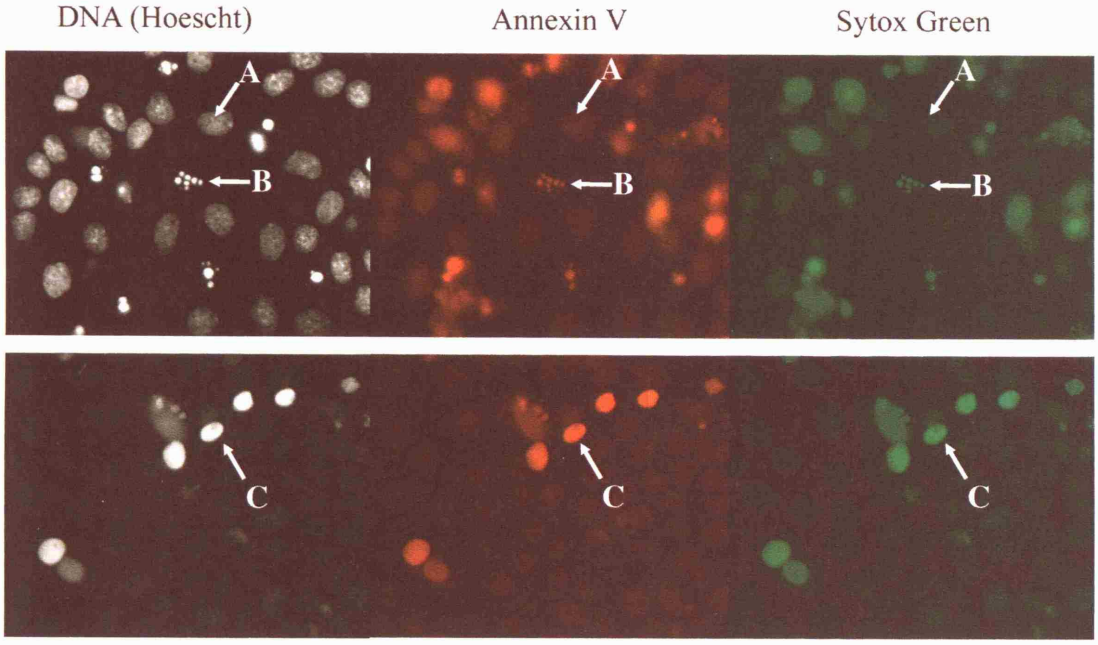

Figure 7.2: UVA irradiated HaCaT cells with **S3** in the presence of Annexin V and Sytox Green. All of the nuclei present are seen in the DNA micrographs (black and white). Micrographs of (A) Interphase or normal nuclei seen in the DNA do not stain for Annexin V (red) or Sytox Green (green) (B) normal apoptotic (late stage) and (C) hypercondensed nuclei staining positively for Annexin V and Sytox Green. This is strong evidence that the hypercondensed cells are apoptotic and they have compromised outer membranes.

7.1.3 Antibody Specific Caspase-3 Detection

7.1.3.1 Introduction

Activation of caspases is one of the most widely known features of apoptosis. Caspases (*c*ysteine-dependent, *asp*artate-specific prote*ases*) are enzymes that cleave specific proteins at aspartic residues. The caspases are broadly divided into two groups, the initiator caspases which are responsible for propagating death signals by activating the second group, the effector/executioner caspases which in turn cleave cellular substrates[178]. The overall mechanism of how caspases work is still not fully elucidated but it is known that caspase-3 is one of the effector caspases that is

important for the occurrence of certain apoptotic features such as membrane blebbing, DNA degradation and nuclear fragmentation[179]. The cells were stained for capase-3. If a positive staining is acquired with the hyper-condensed nuclei then this nuclear phenotype is most likely apoptotic.

7.1.3.2 Antibody Specific Caspase-3 Detection Results and Discussion

In this experiment, all of the mid to late apoptotic cells were stained green and the early stage apoptotic cells were only faintly labelled. The antibody labelled the hyper-condensed nuclei very slightly and unsystematically and was very close to the background staining of the interphase cells. This means either that the caspase-3 enzyme is not activated in the hyper-condensed nuclei's apoptotic pathway or that the nuclei are so compact that the antibody was not able to penetrate and bind to the active site.

If caspases are not part of the death sequence, then the hyper-condensed nuclei may be necrotic as necrosis is caspase-independent cell death. However, necrotic cells are characterized by initial swelling of the cell nucleus and organelles. This was not observed with the shrunken hyper-condensed nuclei. The Annexin V test also confirmed that these nuclei were late stage apoptotic. In UVA induced apoptosis, caspase-8 is one of the most important primary initiators that later activates caspase-3 which in turn, triggers the appearance of apoptotic morphology particularly DNA and nuclear fragmentation[180]. Markers of apoptosis such as caspase activity may be expressed only transiently and the exact time of expression may also be difficult to detect. This is perhaps a reason why not all of the hyper-condensed nuclei were stained. Recent studies [181] have shown that cells still die in an apoptosis-like fashion

in the absence of caspase-3 or 9. Therefore in this assay, it maybe that caspases other than caspase 3 is/are involved in the cell death leading to the hyper-condensed nuclear phenotype. Alternatively, the cells could have been stained at a time when caspase-3 had not yet been activated.

Cell death is a vast and important field in biology yet it is still poorly understood. There are new evidences found on a regular basis, which that do not adhere to the original descriptions of apoptosis and necrosis. There are cell deaths that have been described as 'apoptotic-like' and even 'apoptotic necrosis'[182]. Internucleosomal DNA fragmentation is considered to be one of the hallmarks of apoptosis, however several studies[183,184] have shown apoptosis to occur without this feature. In this study the exact cell death molecular mechanism induced by UVA is not yet known for these types of nuclei. However, the cells that die displaying hyper-condensed nuclei are removed from the monolayer within 12-24 hours, which is within the same time frame as that of 'normal' apoptotic cells.

7.1.4 Caspase Inhibitor – Z-VAD-FMK

7.1.4.1 Introduction

Caspases exist as latent precursors, which, when activated, initiate the death program by destroying key components of the cellular infrastructure and activating factors that mediate damage to the cells[178]. Z-vad-fmk (benzyloxycarbonyl-valyl-ananyl-aspartic acid (O-methyl)-fluoro-methylketone) is a broad-spectrum caspase inhibitor[185]. The caspase inhibitors are synthetic peptides that irreversibly bind the activated caspases. Therefore, the cells which are going through a caspase cell death mechanism will not die in the presence of a caspase inhibitor such as Zvad-fmk.

Their development provided important tools in the understanding of the caspase family and apoptosis in general. For example, these peptide-based inhibitors have been reported to be effective in animal models of stroke, myocardial ischemia injury, liver disease, and traumatic brain injury[186]. Unfortunately, little information has been available on the selectivity of these inhibitors for caspase family members. These large biological molecules can have a fluorescent chemical group attached by a chemical reaction, and the fluorescence of the attached tag enables very sensitive detection of the molecule. In this case, the caspase inhibitor Zvad is coupled to a fluoromethylketone (FMK). The inhibitors contain a methyl ester amino acid (O-Me) to enhance membrane permeability.

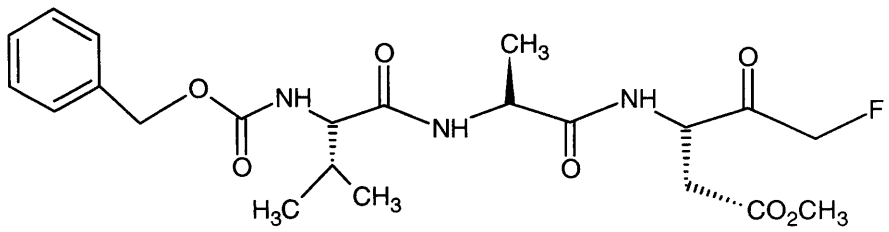

Figure 7.3: Chemical structure of Zvad-fmk[185].

7.1.4.2 Caspase Inhibitor Results and Discussion

The results for the caspase inhibitor experiment are shown qualitatively in Figure 7.4 and quantitatively in Figure 7.5. In the presence of Zvad-fmk, there was more than a 50% reduction in the number of hyper-condensed nuclei in both the control consisting of UV only and the irradiated Degussa P25 treated cells. This shows that the hyper-condensed morphology is indicative of a cell going through a caspase-dependent apoptotic pathway. The result exhibits a reduction of the number of

hyper-condensed nuclei in the presence of the caspase inhibitor, Zvad-fmk, and is therefore confirmation that this nuclear phenotype is apoptotic.

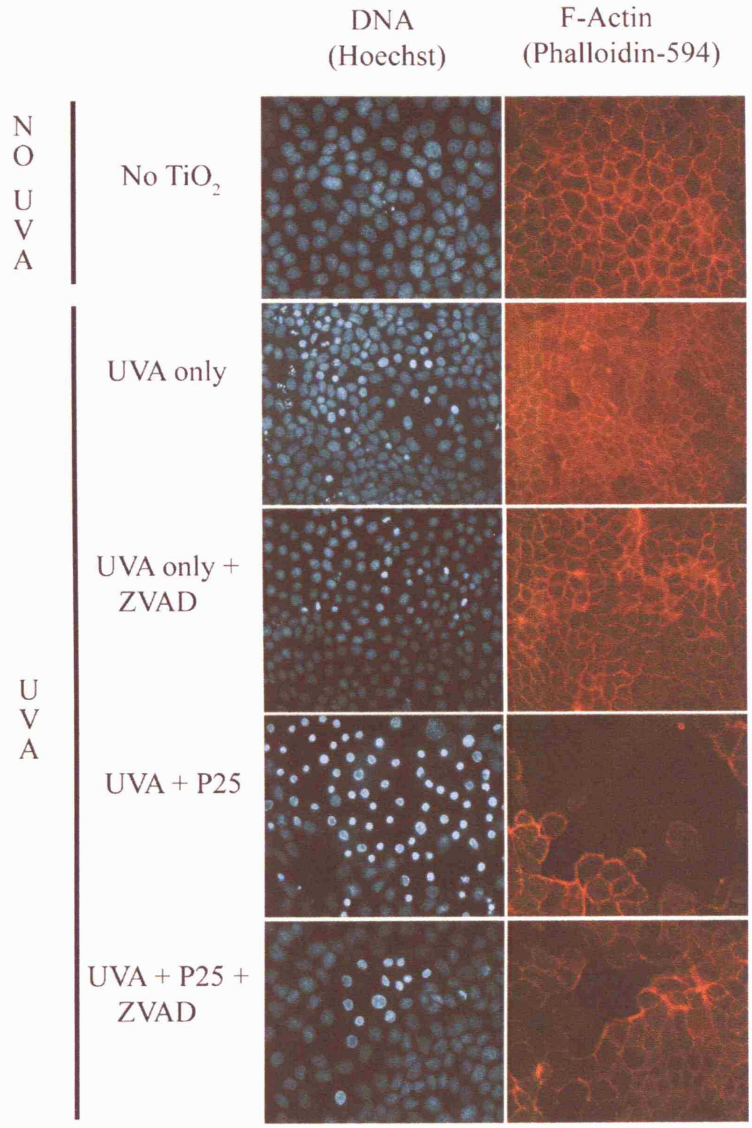

Figure 7.4: Zvad-fmk (8 μM) reduces the number of hyper-condensed, apoptotic nuclei as seen here in the DNA and corresponding F-Actin fluorescent micrographs of the UVA treated cells in the presence of Degussa P25 (**S1**) ± Zvad-fmk. UVA illumination (35 W/m^2; 365 nm)

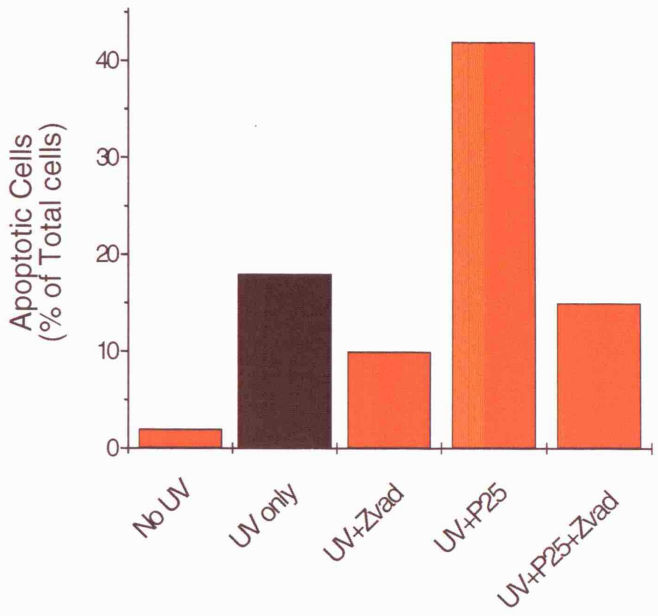

Figure 7.5: Quantification of caspase inhibitor, Zvad-fmk in the presence of Degussa P25 and UVA illumination (35 W/m^2; 365 nm). A 50% reduction in the number of apoptotic nuclei in the presence of zvad-fmk.

The micrograph in Figure 7.4, (F-actin: UV+P25) showed the corresponding F-actin distribution for the hyper-condensed nuclei displaying a reduced F-actin staining which resemble dark areas in the F-actin monolayer. This is an easier way of showing that these nuclei are apoptotic. Actin depolymerisation is another consequence of apoptotic cell death[182]. A higher concentration of 16 μM of Zvad-fmk was used in order to completely reduce the number of apoptotic cells by 100%, however the cells were abnormally affected by this increase in concentration with their nuclei becoming small and distorted. This could be due to the fact that inhibitors such as Zvad-fmk can be toxic and have been found to induce a necrotic type death in mouse fibroblasts and human cells[179].

Inhibitors of caspases may not completely prevent the structural morphologies characteristic of apoptosis from occurring in a dying cell. Instead, it may retard or modify the morphology depending upon the cell type and/or the stimuli [187]. This effect was observed in the Zvad-fmk treated cells (Figure 7.4, UVA+Zvad; UVA+P25+Zvad). Many of the apoptotic cells remaining were at an early stage where their chromatin had only just begun to visibly condense (early stage apoptotic nuclei in Figure 7.1 B).

As Zvad-fmk is a broad range caspase inhibitor, it is not able to differentiate amongst the 14 (or more as they have not all yet been identified) caspases. Instead, it is used to provide an indication of the involvement of caspases and apoptosis in general rather than singling out a specific caspase. Research has shown Zvad-fmk to be a competitive and irreversible indicator of 10 caspases[186] however it is a potent inhibitor of caspase-8, which is activated by UVA irradiation as previously mentioned[188]. Therefore, in this study, it can be speculated that caspase-8 was targeted by Zvad-fmk in order to prevent the apoptotic pathway that leads to the formation of hyper-condensed nuclei.

From Figure 7.4, a large number of dying cells were observed when irradiated in the presence of uncoated titanium dioxide, Degussa P25 (formed 42% apoptotic nuclei) as compared to the control of UVA only (formed 18% apoptotic nuclei). The coatings on titanium dioxide particles should prevent such cellular damage and decrease the number of apoptotic nuclei during UV irradiation. The biological analysis of the modified titanium dioxide particles is examined in the next section.

7.2 UVA IRRADIATION OF CELLS IN THE PRESENCE OF MODIFIED TITANIUM DIOXIDE

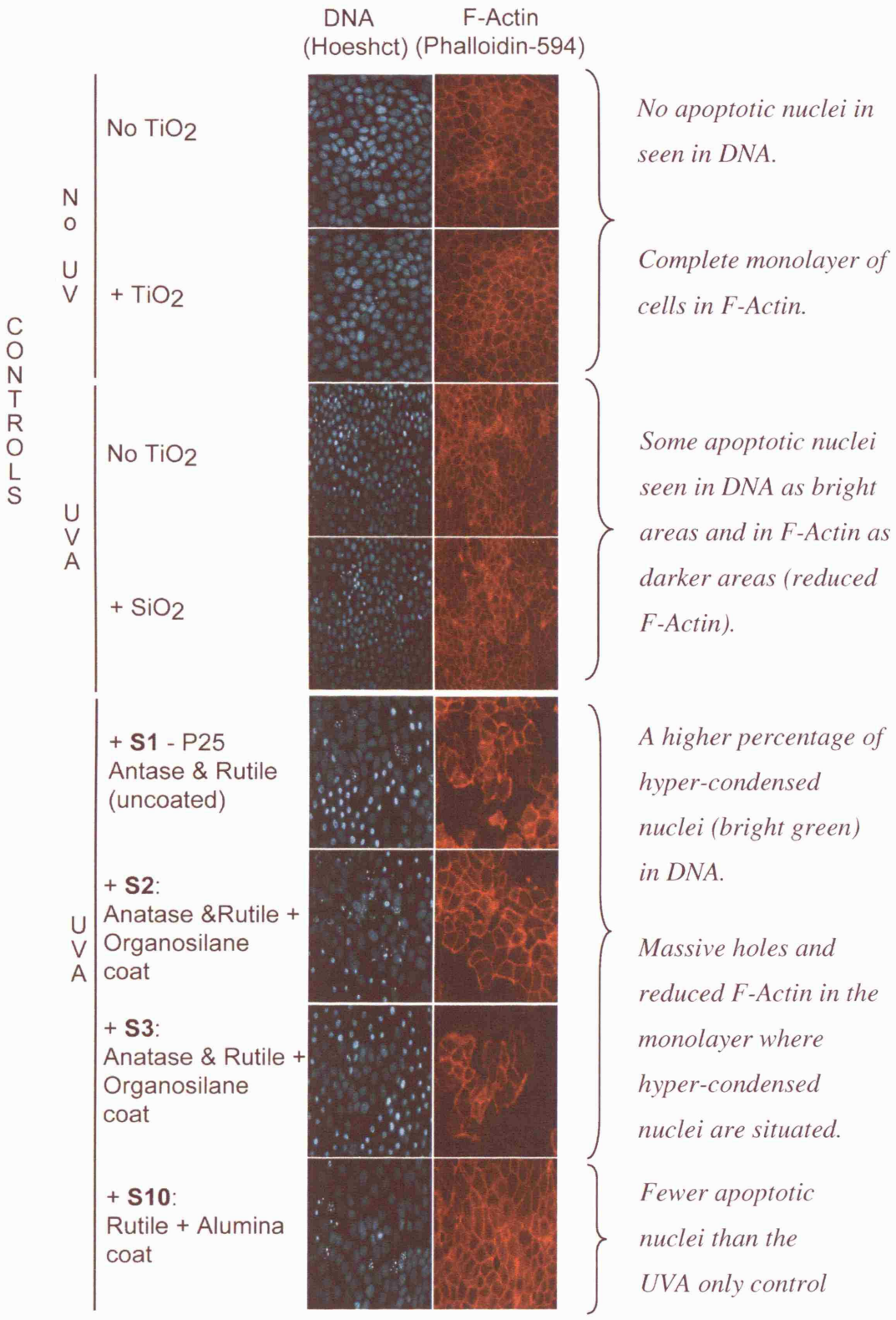

Figure 7.6: Irradiation of MDCK cells with modified forms of titanium dioxide (**S2**, **S3**, **S10**) and compared to uncoated P25. UVA (3.5 mW/cm^2; 365 nm); TiO_2 (0.4 mg/cm^2).

7.2.1 UVA Irradiation of MDCK-1 (0.4 mg/cm^2 Titanium Dioxide)

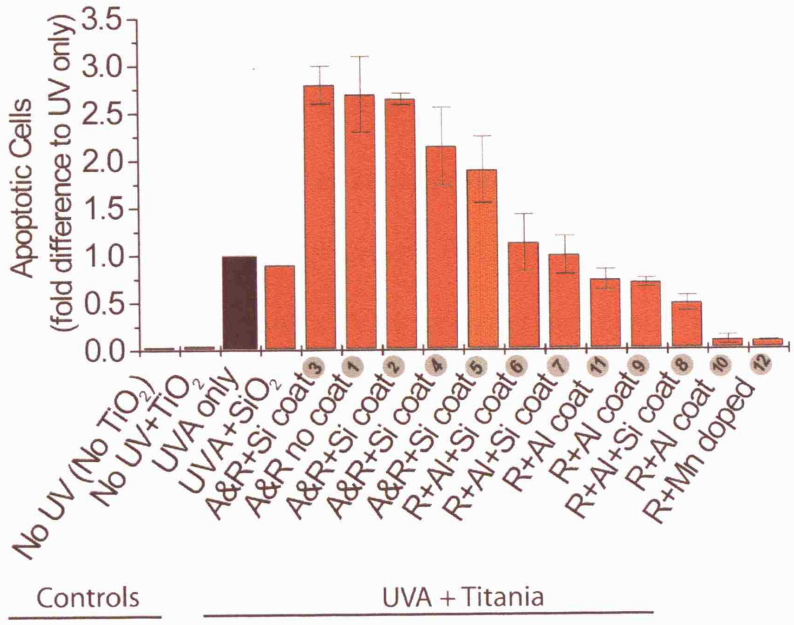

Figure 7.7: Quantification of MDCK-1 cells and 0.4 mg/cm^2 titanium dioxide irradiated with 35W/m^2 of 365 nm light for 2 hours, incubated at 37 °C/5% CO_2 for 3 hrs. Error bars are standard error of the mean. Numbers in shaded circle are the sample numbers e.g. ❶ is **S1**. A=Anatase; R=Rutile. The control, No UV+TiO_2 is an average of all the samples **S1** to **S12**. Experiment repeated three times with a total of 1000 cells counted per coverslip.

The titanium dioxide loadings used in these experiments are 0.1 and 0.4 mg/cm^2 which is less than the maximum recommended amount of 0.5 mg/cm^2. In the presence of UVA only, the number of apoptotic nuclei varied between 15-30% out of the total number of cells. In these experiments silica, SiO_2, was used as a control as it as an inert powder with similar physical characteristics to titanium dioxide but without the photocatalytic ability. Using this powder resulted in a slight decrease in the number of apoptotic cells compared to that induced by UVA only. This is most likely due to physical blocking and scattering of the ultraviolet radiation. Degussa P25 was used as an internal standard for all of these experiments. As P25 is uncoated and one of the most powerful photocatalytic agents on the market today, its

cytotoxic effects should be more apparent as it would be expected to exhibit the greatest killing effect. This was not the case as shown in Figure 7.6, which demonstrates the effects of modified titanium dioxide from sunscreens on MDCK-1 cells. Four (**S2**, **S3**, **S4**, **S5**) out of the eleven powders tested, both pure and extracted, had a deleterious effect on the cells, incurring up to three times the number of apoptotic nuclei as the UVA only control. All of these four powders had an anatase and rutile mix crystal form with an organosilane coat. The sunscreen **S2** showed the highest photocatalytic activity, producing a 2.6 (± 0.2) fold increase in the quantity of apoptotic nuclei compared to the UVA only control. The photocatalytic activity of UV irradiated titanium dioxide is known to generate this toxic effect on **S3** cells because the 'No UVA + TiO_2' control showed no increase in apoptotic nuclei compared to the untreated (no UVA, no TiO_2) control. The effects of Degussa P25 were comparable to that of the extracted sunscreen with a 2.4 (± 0.4) fold increase. The pure powder **S3** also had a similar fold increase, 2.4 (± 0.06) in apoptotic nuclei. Taking into consideration the error in the results of one of the extracted sunscreens, **S6**, it can be said that it had an inert effect on the MDCK-I cells. It was neither protective nor destructive. Four samples, **S9**, **S8**, **S10** and **S12** had a protective effect on the MDCK cells. All of these have a rutile crystal form with alumina coats except for **S12**, which contains rutile and is manganese doped. With 0.4 mg/cm^2 titanium dioxide, **S10** and **S12** produced a considerable decrease in apoptosis with a ten-fold reduction compared to the UVA only control.

7.2.2 UVA Irradiation of MDCK-1 (0.1 mg/cm^2 Titanium Dioxide)

As a detrimental effect was seen with 0.4 mg/cm^2 titanium dioxide, the amount of titania was then decreased by a quarter to 0.1 mg/cm^2, in order to study whether there would be an appreciable drop in the number of dying cells. Only the most destructive (**S1**, **S2**, **S3**) and protective powders (**S10**, **S12**) were tested with this lower concentration.

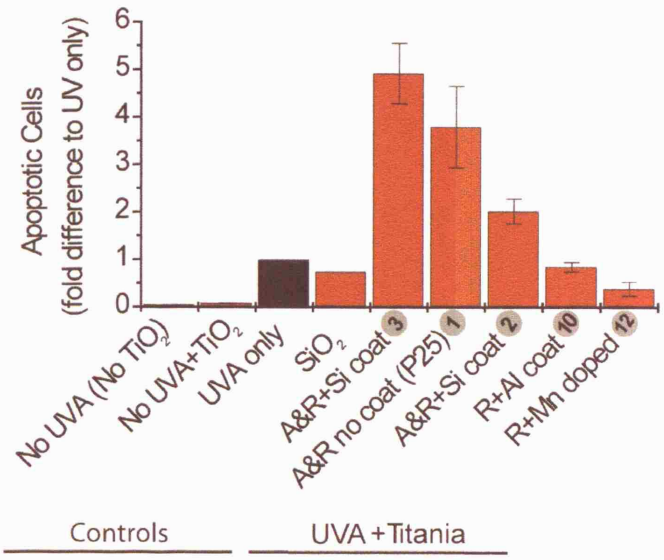

Figure7.8: Quantification of MDCK-1 cells and 0.1 mg/cm^2 titanium dioxide irradiated with 35W/m^2 of 365 nm light for 2 hours, incubated at 37 °C/10% CO_2 for 3 hrs. Numbers in shaded circle are the sample numbers e.g. ❶ is **S1**. A=Anatase; R=Rutile. The control, No UV+TiO_2 is an average of all the samples without UVA irradiation. Experiment repeated three times with a total of 1000 cells counted per coverslip.

The pure powder **S3** showed the highest photocatalytic activity, producing a five-fold increase in the number of apoptosed cells compared to the UVA only control. In comparison, Degussa P25 produced a 3.75% increase. The sunscreen **S2** also showed a considerable amount of apoptosis, with a two-fold increase in apoptotic cells. Given that the amount of titanium dioxide used in these experiments was one

third less, there was a substantial increase in the number of dying cells compared to the previous experiment. With 0.4 mg/cm^2 TiO_2, many holes, both large and small, were noticed in the cell monolayers (Figure 7.9). These holes were due to the excessive number of dying cells going through the apoptotic pathway and being removed from the monolayer. This would give an underestimation of the number of dying cells considering that the 0.1 mg/cm^2 TiO_2 experiment had confluent monolayers containing both healthy and dying cells.

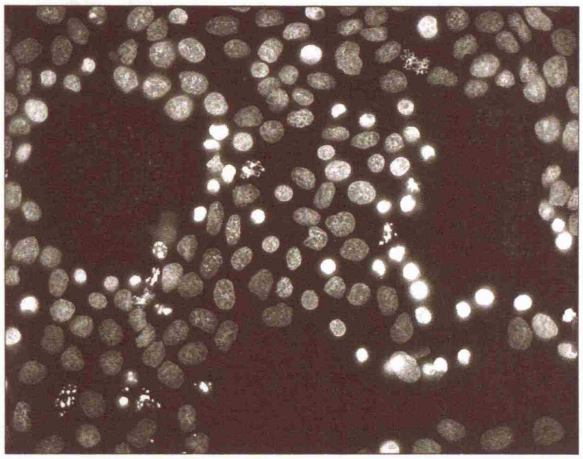

Figure 7.9: DNA fluorescent micrograph of MDCK-1 cells with 0.4 mg/cm^2 titanium dioxide showing holes in the cell monolayer due to excessive cell loss.

This effect however of excessive cell loss, is not seen for both of the rutile samples, one with an alumina coat, **S10** and the other, manganese doped, **S12**, which showed protective effects on the cells. The manganese doped rutile powder induced a 50% decrease in the amount of apoptotic nuclei when tested at 0.4 mg/cm^2 compared to 10% in the 0.1 mg/cm^2 TiO_2 experiment. This lesser protection of the cells can be attributed to the lower concentration of **S12** used. As these particles are unlikely to be producing any free radicals, adding a larger mass to the cells would act more as a physical barrier or scattering agent against the penetrating UVA photons rather than as a photocatalyst.

7.2.3 UVA Irradiation of PtK2 (0.1 mg/cm^2 Titanium Dioxide)

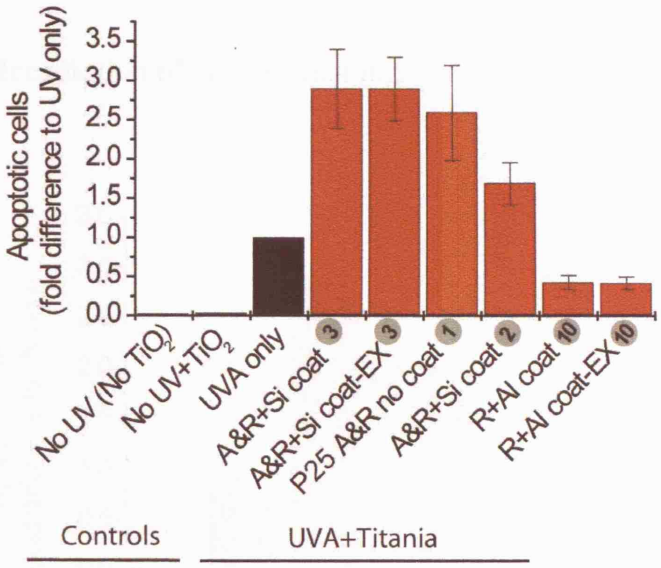

Figure 7.10: Quantification of PtK2 cells and 0.1 mg/cm^2 titanium dioxide irradiated with 35W/m^2 of 365 nm light for 2 hours, incubated at 37 °C/5% CO_2 for 3 hrs. Error bars indicate the standard deviation. Numbers in shaded circle are the sample numbers e.g. ❶ is **S1**. A=Anatase; R=Rutile. The control, No UV+TiO_2 is an average of all the samples. Experiment repeated three times with a total of 1000 cells counted per coverslip.

Another animal epithelial cell line, PtK2, was also used to test the effects of coated titanium dioxide powders. As seen with the MDCK-1 cells, the UVA-only (no TiO_2) control with the PtK2 cells varied from 15-30%. Only the most photocatalytically active and inactive were examined on this cell line. The sequence of the most active samples was also the same as 0.1 mg/cm^2 MDCK-1 with the mixed anatase and rutile + organosilane coated powders (**S2**, **S3**) being the most reactive. **S3** exhibited the highest kill rate, with a 2.9 fold increase in apoptotic cells, followed by uncoated P25 (**S1**) with a 2.6 fold increase and then the extracted powder, **S2** with a 1.7 fold increase in the dying cells. **S10**, the rutile + alumina coated particles again showed a

positive effect on this different cell line, protecting more than half of the cells from going through apoptosis via UVA irradiation.

7.2.4 UVA Irradiation of HaCaT (0.4 mg/cm^2 Titanium Dioxide)

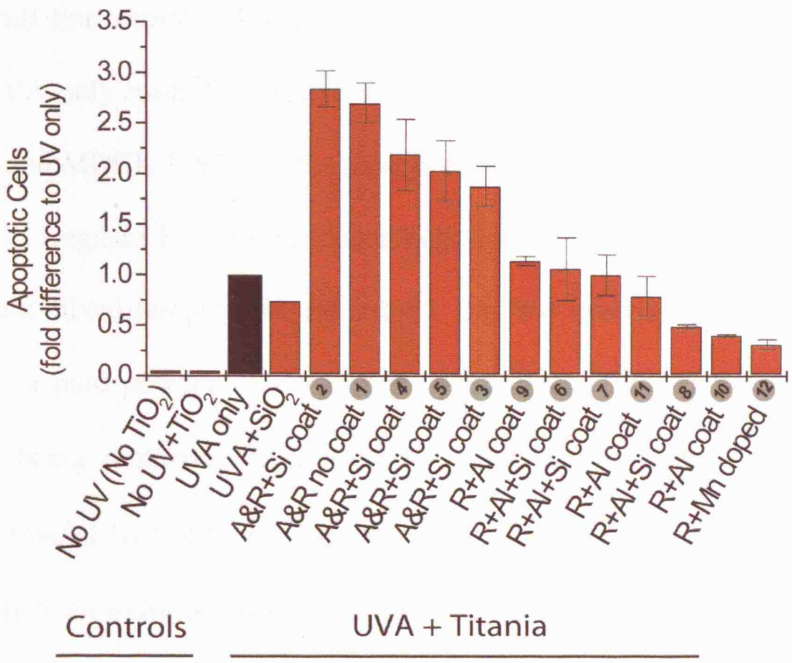

Figure 7.11: Quantification of HaCaT cells and 0.4 mg/cm^2 titanium dioxide irradiated with 35W/m^2 of 365 nm light for 2 hours, incubated at 37 °C/10% CO_2 for 3 hrs. Error bars indicate the standard deviation. Numbers in shaded circle are the sample numbers e.g. ❶ is **S1**. A=Anatase; R=Rutile. The control, No UV+TiO_2 is an average of all the samples **S1** to **S12**. Experiment repeated three times with a total of 1000 cells counted per coverslip.

The keratinocyte cell line HaCaT was used instead of primary keratinocytes because this cell line provides an almost unlimited supply of identical cells which would mean that the experiments would be highly reproducible. The materials needed for primary keratinocyte cultures are limited and variable unlike that for HaCaT cell cultures. Previous studies have compared the effect of treatments between HaCat and primary keratinocytes cultures, and HaCat cells and human keratinocytes *in*

vivo[189,190]. It was found that the results were comparable and there was a good correlation between the two. Therefore, HaCaT cell cultures are probably the best cell line to get a realistic determination of the UVA and titanium dioxide induced damage to human keratinocytes.

The human cell line showed similar results to the two animal cells lines (Figure 7.11). The UVA-only control varied from 15-30% apoptotic cells. As seen with 0.4 mg/cm^2 TiO_2 and MDCK-I, **S2** was the most potent, producing a 2.8 fold increase in apoptotic cells. Degussa P25 also produced high death figures as did the other three anatase & rutile mixed samples, **S5**, **S4** and **S3**, the first two being from sunscreens and the latter, a pure powder. Two extracted sunscreens **S7** and **S6** were on the borderline of being protective or destructive. **S6** incurred a 1.06 (± 0.31) fold difference compared to UVA-only and **S7** a 1.0 (±0.32) fold difference. Three samples, the first an extracted sunscreen **S8**, and two pure powders, **S10** and **S12** definitely had protective effects on HaCaT cells. **S8** reduced the number of apoptotic cells by a factor of 0.49, **S9** by 0.4 and **S10** by 0.31. **S8**, **S9** and **S10** are powders, which have a pure rutile crystal form and are coated with aluminium oxide.

7.2.5 Cell Protection

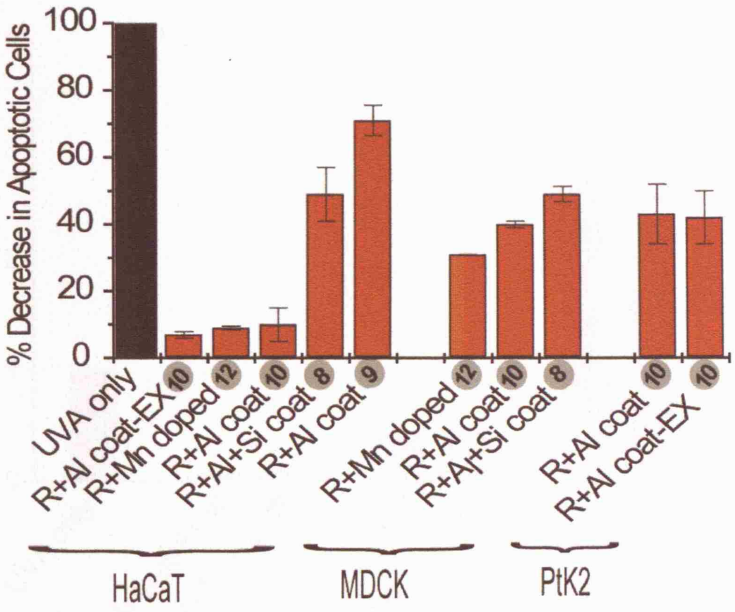

Figure 7.12: Protection effect of some modified titanium dioxide particles against UVA only, with all three cell lines. Error bars indicate the standard deviation. Numbers in shaded circle are the sample numbers e.g. ❶ is **S1**. A=Anatase; R=Rutile.

The UV only column in Figure 7.12 is at a value of 1 and has the same scale as the other graphs but this figure shows the percentage of cells which are prevented from UVA oxidative damage by the various modified titanium dioxide particles. Even though there is a disparity in the actual number of apoptotic cells, the same powders that caused the least cell damage in the animal cell lines had similar activity in the human cell line. **S8**, **S10** and **S12** consistently showed a protective effect over the animal and human cells. These powders reduced the number of apoptotic nuclei to below the quantity obtained when the cells were irradiated with UVA only. These three powders, **S10** and **S12** being pure and **S8** being an extracted sunscreen are all rutile crystal forms however, their modifications are all different. **S10** has an alumina coat, **S12** is manganese doped and **S8** has a double coat of aluminium oxide and silica.

7.2.6 Control for Solvent Extraction Procedure

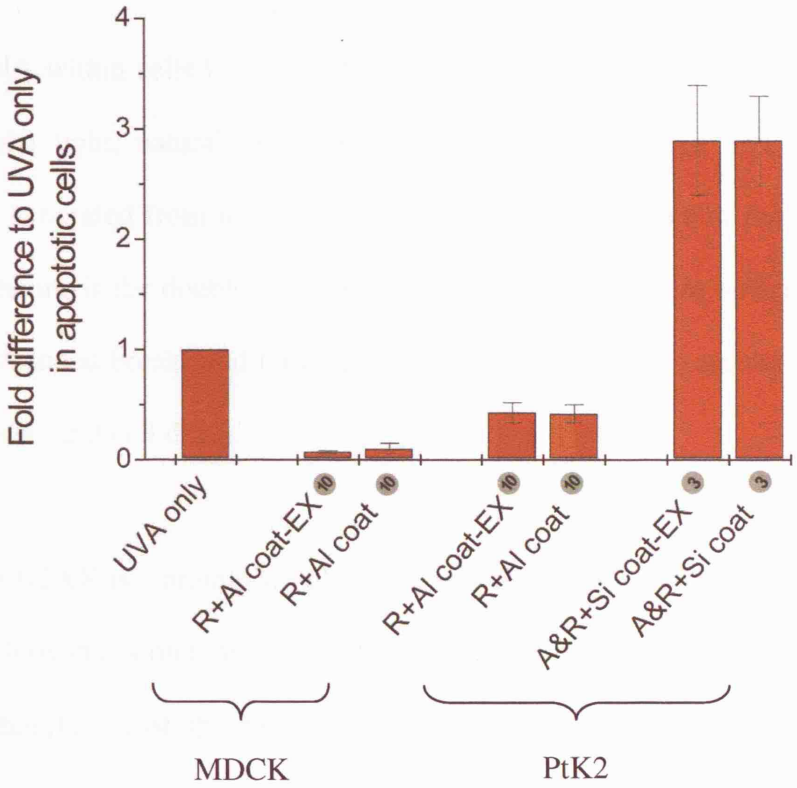

Figure 7.13: Control for solvent extraction process with **S3** and **S10**. EX=extracted

A small amount of the pure powders, **S3** and **S10** were put through the solvent extraction process that the sunscreens were subjected to and tested biologically with MDCK-1 and PtK2 cells. The washed samples were then compared to the unwashed samples. As seen from Figure 7.13, the extracted powders, **S10**-EX and **S3**-EX had similar reactivities to the original powders, **S10** and **S3**, indicating that the wash process apparently did not adversely affect the different types of coatings present. **S10** has an alumina coat and **S3** has an organosilane coat. Similar results were found for all cell types. These different chemical compounds were resilient enough to withstand the solvents used in the extraction step.

7.3 DNA DAMAGE ASSAY

7.3.1 Introduction

The DNA within cells is constantly being bombarded with damaging agents such as ultraviolet light, natural and synthetic mutagenic chemicals and reactive oxygen species generated from internal or external reactions[191]. One of the most dangerous DNA lesions is the double-stranded break (DSB) as it is more difficult to repair than single stranded breaks and base damage. Its misrepair often results in chromosomal aberrations and cell death.

Histone H2AX is a protein which is a member of the H2A histone family and part of the nucleosome structure. One of the first processes initiated by DSBs is major phosophorylation of the histone variant H2AX to form the protein known as γ-H2AX. This protein is thought to facilitate the retention of repair proteins in the vicinity of the DSB thereby enhancing the efficiency of their function[192]. The phosphorylation occurs within 1 – 3 minutes of the DNA chromosomal damage[193]. Phosphorylation is the addition of a phosphate group PO_4, to a protein or small molecule. Many enzymes and receptors are switched on or off by phosphorylation or dephosphorylation. By using an antibody specific for the γ-H2AX modification, it is therefore possible to detect H2AX phosphorylation and assay for DNA damage.

7.3.2 Results and Discussion

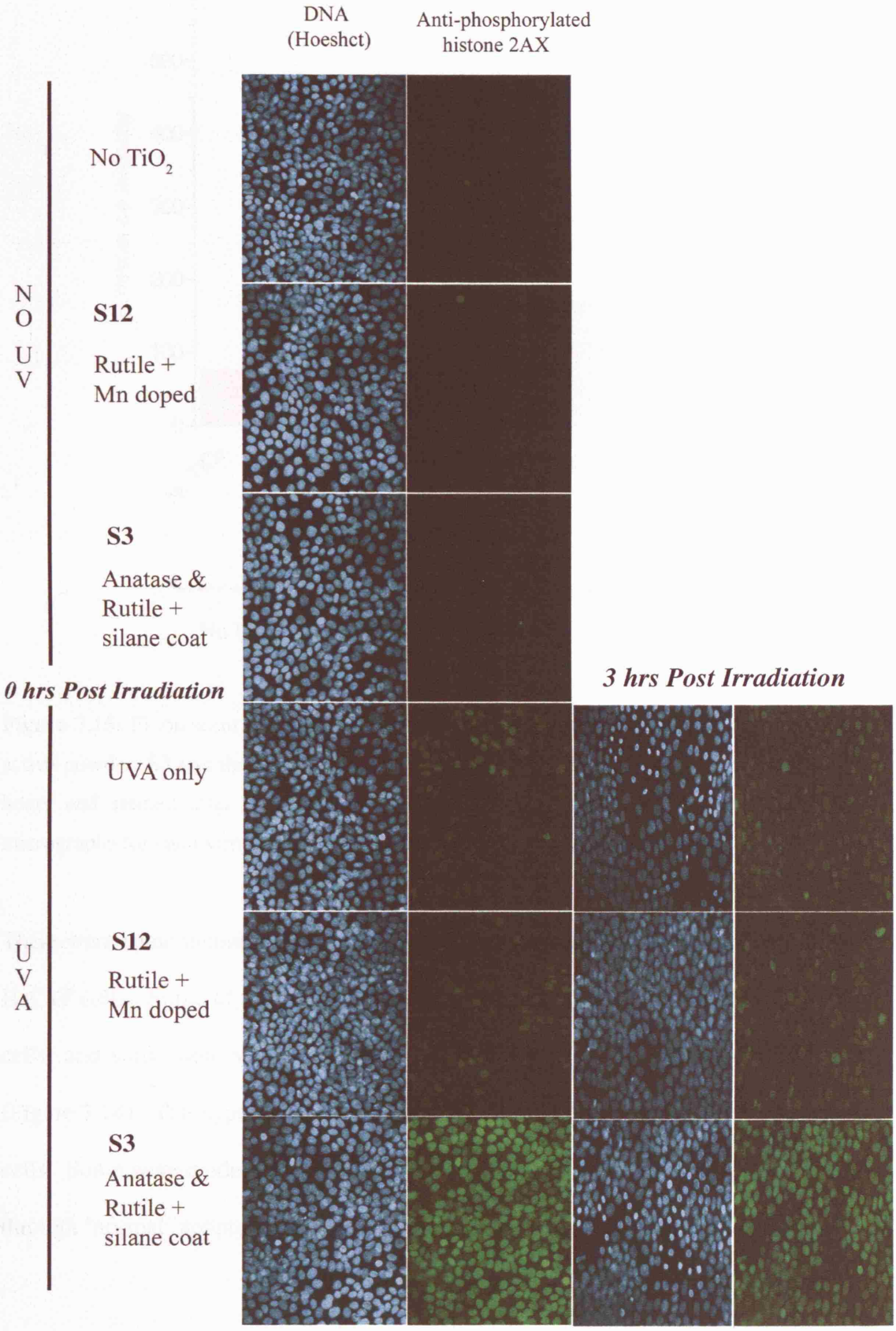

Figure 7.14: UVA irradiation of HaCaT cells with **S3** and **S12**. Anti-phosphorylated histone showing double stranded breaks with green fluorescence.

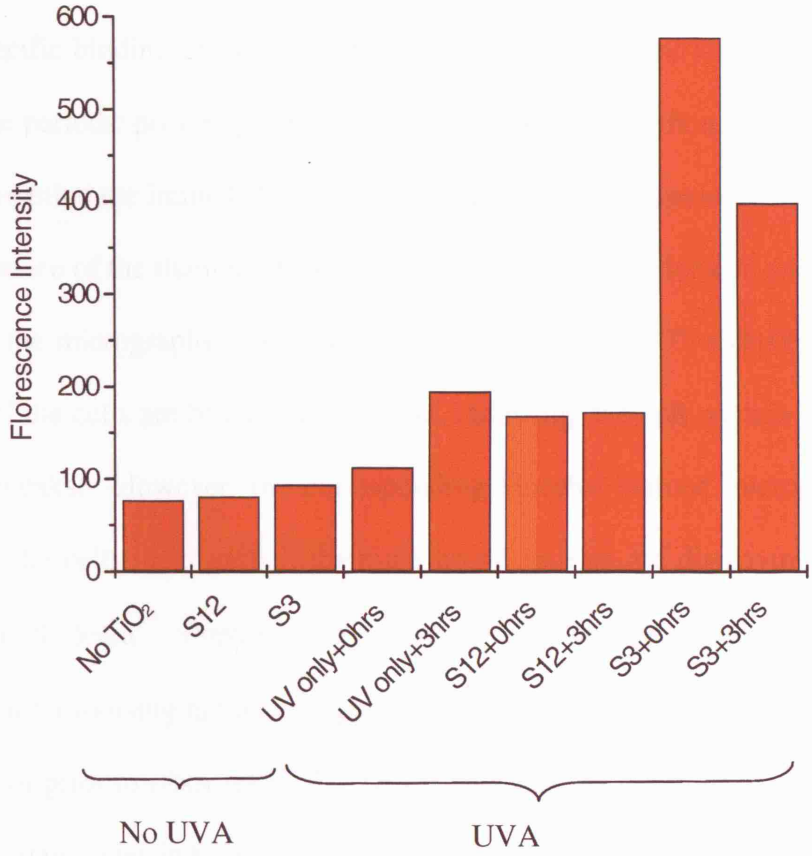

Figure 7.15: Fluorescent quantification for anti-phosphorylated histone 2AX with the most active powder, **S3** and the least active, **S12** irradiated with 365 nm light, 3.5 mW/cm^3 for 2 hours and stained after 0hrs and 3hrs incubation. Average intensity taken out of 10 micrographs for each sample.

There were some inconsistencies with the phosphorylated anti-histone staining of the HaCaT cells. Some of the nuclei were stained brightly (mostly the normal apoptotic cells) and some were very faintly labelled, similar to the background fluorescence (Figure 7.14). The hyper-condensed nuclei varied in brightness just as the interphase cells. Some were moderately bright compared to cells with fragmented nuclei (going through 'normal' apoptosis) but they were generally brighter than the control cells.

An average of the fluctuating fluorescence was determined for 10 stained micrographs of each sample and the results shown in Figure 7.15. There was a small

amount of fluorescence from the non-irradiated samples, which was most likely due to non-specific binding of the antibody to the interphase cells. The cells were tested at two time periods: post irradiation after zero hours and three hours incubation. This was to determine the immediate and subsequent effects of ultraviolet A light on cells in the presence of the titanium dioxide powders. The most noticeable and remarkable feature in the micrographs of Figure 7.14 in the staining of UV+**S3**+0hrs is that the majority of the cells are brightly fluorescent, indicating they all contain DNA double stranded breaks. However, the corresponding Hoechst stained micrographs show that all of the cells look normal; there are no nuclei that are displaying any visible signs of cell death. Previous studies have suggested that the rapid λ-H2AX formation after ionising radiation exposure is related to DNA damage response at the beginning or prior to DNA repair[194]. This results show that **S3**, the anatase and rutile mix with silane coat induces major DNA damage to the cells after 2 hours UVA irradiation. Only if the nuclei were unable to be repaired do they go through the process of cell death and subsequently display the corresponding morphological features.

After 3 hours incubation, there was substantial anti-histone staining. In two of the cases, UVA only and UVA+**S12**, there was an increase in the fluorescence of the nuclei after the later time interval of 3 hours. The only exception was UVA+**S3**+3hrs, which showed a drop in the number of cells with DNA damage. There could be a number of reasons for this observation. Usually after 3 hours incubation, **S3** induces a large number of hyper-condensed apoptotic nuclei. As this type of nuclei does not stain with the anti-histone H2AX antibody very well (Figure 7.16), a decrease in the fluorescence of UVA+**S3**+3hrs would be expected as the majority of cells are of this type. This decrease could also mean that the DNA DSBs

of the cells were being repaired during the 3 hours incubation. Lastly, a confounding factor is that λ-H2AX is de-phosphorylated with a half-life of ~ 2 hours[195]. So the reduced staining after 3 hours incubation for UVA+**S3**+3hrs could also be due to the de-phosphorylation of the protein λ-H2AX. The UVA only control usually has a mixture of normal apoptotic and hyper-condensed nuclei with a greater majority of the first, so as these are stained more brightly, an increase in fluorescence intensity is seen. **S12** induced similar DNA damage after zero and three hours.

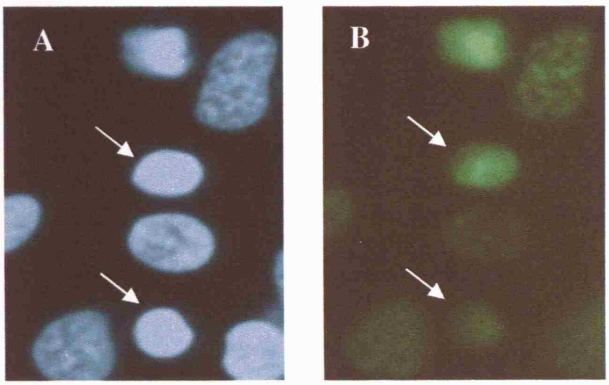

Figure 7.16: Variability of phosphorylated anti-histone staining with hyper-condensed nuclei. The arrows show two hyper-condensed nuclei with different λ-H2AX staining. (A) DNA stained with Hoechst dye (B) Corresponding anti-histone micrograph.

Caspase-3 is responsible for the final execution of the disassembly of the cell and it cleaves a number of cell structure proteins. It is also dependable for the generation of DNA strand breaks[178] . As shown previously, caspase-3 was not present or was not yet activated in the hyper-condensed nuclei, which would explain the irregular staining if this enzyme had to be present in order for λ-H2AX labelling to occur. Another reason for the inconsistent labelling is that not all of the nuclei would be synchronous in suffering DNA strand breaks. This would result in some nuclei being more brightly stained at one time point compared to others which were going through the same process but with a delayed or accelerated time scale.

In summary, **S3**, the mixed anatase and rutile crystal form with organosilane coat, upon UVA irradiation produced substantial DNA double stranded breaks in the human keratinocyte cell line. The most interesting finding was that the nuclei which had DSBs, seen by the green fluorescence, had no other visible morphological features to distinguish them from the normal nuclei.

7.4 SUMMARY

- All of the pure and sunscreen extracted titanium dioxide powders which possess an anatase/rutile mix crystal phase and a silicon-containing coat (Organosilane and Dimethicone) increased UVA induced death in animal and human cells.

Cell Type	**Amount of Titanium Dioxide (mg/cm^2)**	**Fold Increase in Cell Death**
MDCK-1	0.4	2-3
MDCK-1	0.1	2-5
PtK2	0.1	2-3
HaCaT	0.4	2-3

- Two pure powders had a protective effect against UVA irradiation (365 nm) on all of the cell lines. The titanium dioxide powder with rutile only crystal phase and alumina coat and the manganese doped rutile only phase both protected against UVA induced apoptosis.

- A new cell death pathway may have been discovered. UVA irradiation in the presence of the inorganic powder titanium dioxide formed hyper-condensed nuclei, which follow the caspase-dependent pathway of apoptotic cell death as determined by a positive outcome with the caspase inhibitor, zvad-fmk. These nuclei also gave reduced F-actin staining which is a characteristic of apoptotic cells and tested positively for Annexin V which shows membrane

damage in late phase apoptotic nuclei. The exact mechanism of its cell death is unknown, however, caspase-8 may be one of the initiator caspases present in these UVA irradiated cells.

- Increasing the concentration of the most phocatalytically active titanium dioxide particles increased cell death. However, the presence of holes in the monolayer indicated that many of the cells had died and lifted off from the coverslip giving a false and underestimated reading of the total number of dying cells.

- The most potent organosilane coated titanium dioxide powder **S3**, showed that it can cause extensive DNA double stranded breaks via phosphorylation of histone H2AX as compared to the manganese doped rutile powder.

7.5 CONCLUSION

UVA radiation mediates its genotoxicity via oxidative DNA damage. Oxidative stress occurs when the production of reactive oxygen species (ROS) exceeds the body's natural antioxidant defence mechanisms, causing damage to biomolecules such as lipids, proteins and DNA. If left unrepaired, the damaged DNA can lead to dire circumstances such as mutations, cell death and transformations to malignant cells. The epidermis contains antioxidant defences including enzymes such as superoxide dismutase and also free radical scavengers such as Vitamin C and E, which reduce the damaging effects of ROS. Moderate amounts of ROS are essential for the cell to survive. They take part in cell regulation; act as mediators and signal transduction molecules[196]. However, excessive production of ROS due to UV

exposure can deplete these antioxidants, leaving the skin vulnerable to attack from more ROS[197]. These ROS include the superoxide anion, singlet oxygen, hydroxyl radical and hydrogen peroxide. Superoxide anion and singlet oxygen are moderately reactive compared to the hydroxyl radical, which is highly reactive and can account for the major DNA oxidative damage such as DSBs. However, it has been shown that the superoxide anion and singlet oxygen generated by UVA1 (340-400 nm) can damage mitochondria and can induce apoptosis in cell culture[198].

When titanium dioxide becomes photo-activated, many types of ROS are formed including the superoxide anion, singlet oxygen and the hydroxyl radical. These are the perfect candidates for causing oxidative stress in biological organisms. Once these radicals are produced, a cascade of reactions can then ensue. Superoxide anions can be transformed into dangerous hydroxyl radicals in the cell via certain chromophores such as quinones and enzymes such as superoxide dismutase (Figure 7.17).

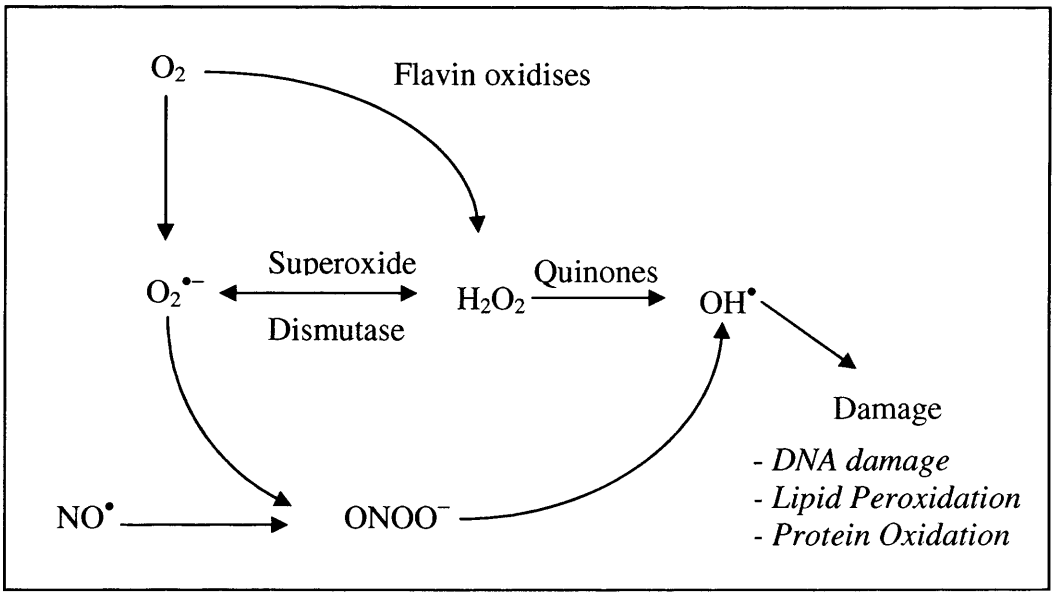

Figure 7.17: Reactive Oxygen Species relating to biological damage. Adapted from [199]

The EPR experiments proved that the superoxide anion was being generated from these irradiated coated titanium dioxide powders used in sunscreens.

Peroxynitrite ($ONOO^-$) is toxic and is able to directly nitrate and hydroxylate the aromatic rings of amino acids and to react with lipids, thiols, proteins and DNA. The amount of titanium dioxide used in these experiments were at only 5% and 20% concentration which is at a range that is used in sunscreens (0-25%). However, the ROS that the titanium dioxide powders such as **S3** and **S2** generated during the UVA irradiation period were potent enough and in a high enough concentration to cause a large number of cells to initiate apoptosis.

It is still unknown whether titanium dioxide particles can diffuse into the living layers of the skin due to different experimental outcomes by various researchers. If the titania particles were able to reach that part of the skin and produce the quantities of free radicals shown here to kill cells, there is a strong risk of mutation possibly leading to skin cancer. However, besides showing that the anatase/rutile powders killed human cells, these biological experiments have revealed that in some cases, such vast numbers of nuclei were affected that when they left the monolayer, large holes were produced. As the skin is a dynamic organ which is constantly renewing itself, there is close control of cell proliferation and cell death. Excessive cell loss from the skin via ultraviolet light and ROS can disturb this delicate equilibrium of tissue homeostasis in the skin. This in turn can leave the body open to disease, as the skin is the body's primary barrier against infection from viruses, bacteria and chemicals. Oxidative stress from ROS has been associated with contact dermatitis, which is the inflammatory skin reaction to chemical exposure[196]. Antioxidant imbalance and ROS generation has been linked to pathological skin diseases such as

psoriasis which has been associated with the superoxide anion, one of the main ROS produced by UV irradiated titanium dioxide[196].

This work was a necessity that had to be undertaken in order to determine whether the modified titanium dioxide particles used in sunscreens posed a threat to human health. In toxicology studies, *in vitro* experiments are initially undertaken such as in these experiments. Since a positive correlation has been found regarding the mixed anatase/rutile crystal form of titanium dioxide and the organosilane modification type being harmful to cultured epithelia, further animal studies can be carried out in the future.

Chapter 8 - Comparison of Chemical and Biological Experimentation

The purpose of this research was to determine whether the inorganic compounds namely titanium dioxide and zinc oxide, used in sunscreen lotions were capable of producing reactive oxygen species and if so, whether the quantities generated were able to cause substantial photocatalytic damage. This was tested by directly measuring the reactive oxygen species produced when the powders were UV irradiated via the EPR technique. This technique has never been used before to analyse modified titanium dioxide particles used in sunscreens. It was also indirectly tested by photodegradation of methylene blue dye, a common organic compound used to measure photocatalysis rates. After determining whether the photocatalysts were reactive enough to oxidise the dye, they were irradiated in contact with cultured animal and human cells, with similar UVA light to that of a summer day in the U.K. Fluorescence microscopy and the apoptosis assay with titanium dioxide powders has not been researched previously.

The inorganic powders have been modified for several reasons. Firstly, for aesthetic reasons, they are made within the nanometer range of 20-50 nm as determined by SEM, TEM and XRD measurements. Powders within this size range are optically blue shifted towards higher energies therefore being able to scatter visible light less and appear transparent. Secondly, to increase dispersion within certain sunscreen matrices and lastly, to prevent the photocatalytic redox reactions for occurring in these systems. The powders tested were either coated with an organosilane, dimethicone or alumina or they were doped with manganese ions. Doping of titanium dioxide to prevent photocatalysis

from occurring is a new area for cosmetics. However, in the chemical industry, titanium dioxide is doped with metals and other compounds in order to increase its photocatalytic activity as one of its assets is the ability to destroy almost any material in its vicinity, after being activated by UV light. These coats and dopants were characterised by a number of different techniques, each contributing a part to the overall picture of the structure of the coating materials. Using XPS, a surface sensitive technique, and with the aid of sputter depth profiling, the different chemical elements on the surface of the titanium dioxide core were determined. XPS gave a quantitative analysis of the concentrations of the different coating materials. The surface coatings ranged from 1.0% silicon in **S2** to 5.8% aluminium in **S10** indicating that they form a very thin layer (< 2.5 nm) around the titanium core.

The methylene blue tests showed that the most photocatalytically active titanium dioxide powders were **S2**, **S3**, **S4** and **S5**. These powders were capable of degrading the dye within minutes and produced half-lives i.e. the time that it takes to degrade the methylene blue to 50% of its original concentration, comparable to that of **S1** (Degussa P25). **S2**, **S3**, **S4** and **S5** all contain a mixture of anatase and rutile crystal forms as determined by XRD and Raman Spectroscopy, however they consist of different percentages of each type. **S2** contains 90% anatase and 10% rutile (90:10); **S3** (85:15); **S4** (85:15) and **S5** (75:25). Moderately active powders were **S6**, **S7** and relatively inactive powders were **S8**, **S9**, **S10**, **S11** and **S12**. These all contain 100% rutile and no anatase. From these results, the higher the percentage of the anatase crystal form present in the powders, the greater the photocatalytic activity. However there must be another factor to take into consideration, as not all of the rutile powders are completely inactive. **S6** and **S7** produce moderate photodegradation of the methylene blue dye

despite containing 100% rutile. Another factor to take into consideration is the outer coating on the titanium dioxide particle.

XPS and SSNMR were used to determine the elemental composition and structure of the coatings on the titanium dioxide surfaces. **S2**, **S3** and **S5** contained organosilane coatings of trimethoxycaprylylsilane and **S4** consisted of a dimethicone polymer coat. The most photocatalytically active powders **S2-S5** all comprised of a silicon coating with an organic part. The EPR measurements showed that reactive oxygen species are produced on these surfaces especially the superoxide anion radical and the hydroperoxy radical, which can be produced from the very reactive hydroxyl radical. **S2** and **S3** showed that the photogenerated holes were being trapped on the surface of the particles and not in the sub-lattice regions. This means that the oxygen can diffuse to the surface of these particles and it is not being blocked by a coating material. The photogenerated charge carriers can then migrate to the surface and produce ROS, which can react with most adsorbed species. The electrons and holes can also attack the organosilane or dimethicone coating, causing photodegradation of the coating material. The length of time that it would take to degrade the coating is unknown, however any photogenerated charge carrier which reaches the surface, can weaken the bond between the coating and the titanium dioxide lattice. The ability of **S2** and **S3** to create the greatest concentration of charge carriers and for surface oxygen centred species to be formed signifies that oxygen is able to access the surface. This indicates that the coating maybe patchy and not uniform. A coating that is patchy would have an effect on the photocatalysis reactions possibly increasing its ability to produce reactive oxygen species because more of the titanium dioxide surface is in contact with oxygen in the atmosphere. The organosilanes would be more susceptible to degradation by the photogenerated

electrons and holes compared to the alumina coatings as they are carbon based compounds that can easily be mineralised to water, carbon dioxide and acids.

For different catalysts, the photocatalytic activity of titanium dioxide depends upon characteristics such as absorption ability, specific surface area, particle size and crystalline form. Particles which are porous and of small size means a large surface area, which leads to the possibility of a greater absorption amount and high photocatalytic reaction area. However, in the photocatalytic reactions, only a proportion of the photocatalyst particles can absorb incident photons, and the remainder does not take part in the reaction. The samples tested showed differing specific surface areas with one of the most active in the methylene blue tests, **S5** having the lowest surface area value of 12.6 m^2/g and one of the least active, **S9** also having a comparably low S.A. of 13.8 m^2/g. A moderately active powder, **S6** had a S.A. of 77.9 m^2/g which was higher than the most active powder, P25 which has a S.A. of 45 m^2/g. There is a variation in the specific surface areas of the powders, both pure and extracted. No trend can be seen whereby the greater the surface area the greater the photocatalytic activity of the powder. **S5** has the lowest surface area and yet, it is one of the most active powders. **S6** is a borderline photocatalytic material, tending towards inactive however it possesses the highest surface area of all tested powders.

This signifies that in the case of coated and doped titanium dioxide particles, the specific surface area measured does not have a direct relationship to its photocatalytic activity. The number of surface active sites i.e. sites on the surface of the particles that can take part in a photocatalytic reaction, is different in each sample possibly due to the various coating material attached to the titanium dioxide core. If all of the particles

were uncoated, a trend in the specific surface area with the photocatalytic activity would probably be expected. However, with modified titanium dioxide particles used in sunscreens, there are other factors besides surface area that affect their photocatalytic strength. One such factor is adsorption ability.

The adsorption ability of the powders depended wholly on the chemical composition of the coating material. From the methylene blue experiments, the silicon-containing coatings adsorbed a greater amount of the dye compared to the aluminium-containing coatings. This correlates with the results that the organosilane and dimethicone coated titania were the most photocatalytically active. These powders (**S2**, **S3**, **S4**, **S5**) also had a mixed anatase and rutile crystal phase which was the second major contributor to their high photocatalytic strength. As methylene blue dye was degraded at the surface of the titanium dioxide particle, a coating such as trimethoxycaprylylsilane would adsorb more of the organic compound, and the powders, which consist of anatase naturally produces more charge carriers thereby increasing the rate of degradation.

UVA light was used in all of the experiments and is known to be a carcinogen and a possible cause of the highly lethal malignant melanoma. However, in contrast to UVB and UVC, the mechanisms that cause mutations and cancer from UVA light are not well known. In the apoptosis assay conducted in this body of work, a new type of cell death pathway may have been discovered. Upon UVA irradiation in the presence of titanium dioxide particles, the nuclei of cells became extremely condensed and were extruded from the monolayer of cells before exhibiting the usual morphologies of normal apoptotic nuclei. Such structural changes include fragmentation of shrunken nuclei into small, round apoptotic bodies. This new nuclear phenotype was termed 'hyper-

condensed' and was resolved to proceed through a caspase dependent apoptotic pathway as determined by a positive outcome with the caspase inhibitor, Zvad-fmk. These nuclei also gave reduced F-actin staining which is a characteristic of apoptotic cells and tested positively for Annexin V which shows membrane damage in late phase apoptotic nuclei. The exact mechanism of its cell death is unknown, however, caspase-8 may be one of the initiator caspases present in these UVA irradiated cells.

In the methylene blue photodegradation experiments, the most photoactive powders were the mixed anatase and rutile crystal forms with organosilane coating. A similar trend is observed with the cellular degradation experiments. **S2**, **S3**, **S4** and **S5** all increased UVA induced cell death in animal and human cells. Only two powders had a consistent protective effect against the UVA light. These were **S10** and **S12**, both of rutile composition but **S10** is alumina coated and **S12** is manganese doped. These compounds also showed a low activity in the photocatalysis reactions.

Increasing the concentration of the most photocatalytically active titanium dioxide particles increased cell death. However, the presence of holes in the monolayer indicated that many of the cells had died and lifted off from the coverslip giving a false reading of the total number of dying cells. Excessive cell loss such as that seen in these experiments with a high amount of titanium dioxide (0.4 mg/cm^2) can cause its own implications such as leaving the body open to disease, as the skin is the body's primary barrier against infection from viruses, bacteria and chemicals.

From the EPR experiments, one of the main and most long-lived free radical detected was the superoxide anion. Superoxide anions can be transformed into dangerous

hydroxyl radicals in the cell via certain chromophores such as quinones and enzymes such as superoxide dismutase. The hydroxyl radical is highly reactive and can account for the major DNA oxidative damage such as Double Stranded Breaks.

A DNA damage assay was carried out on the most potent organosilane coated titanium dioxide powder **S3** and the least potent, **S12** manganese doped rutile powder. The results showed that **S3** could cause extensive DNA Double Stranded Breaks via phosphorylation of histone H2AX as compared to **S12**. If these Double Stranded Breaks are not repaired properly, possibly due to the high volume created at a single time, there is a chance that the cell could become mutated.

Overall, the graph in Figure 8.1 shows that there is a good correlation between the chemical photocatalytic tests and the biological experiments.

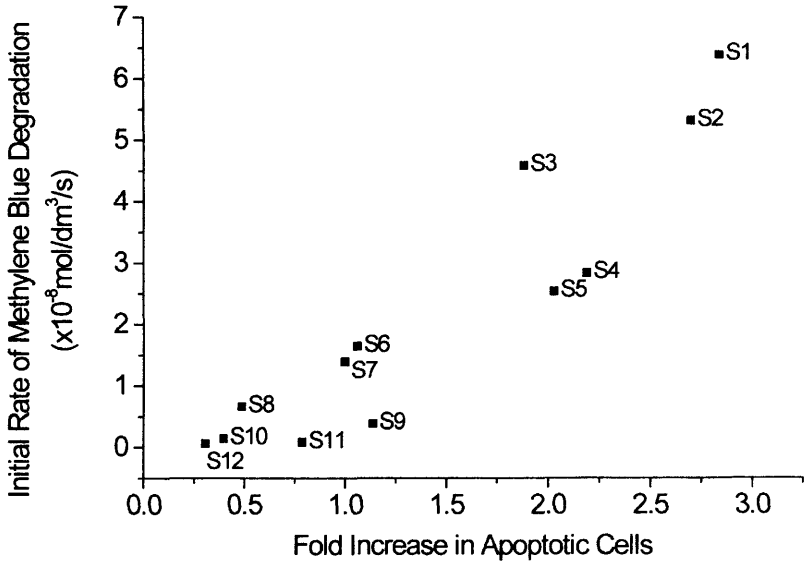

Figure 8.1: Correlation of photocatalytic and cellular degradation studies. Initial rate of degradation of methylene blue vs. Fold increase in apoptotic nuclei for HaCat cells.

The samples which were slightly inactive in the methylene blue photodegradation tests did not affect cell death. In fact, some samples (**S9**, **S10**) protected the cells from the UVA light so there were less apoptotic nuclei. In contrast, the samples which were active in degrading methylene blue dye and had a high initial rate of reaction, were as potent in killing cells, producing a high fold increase in apoptotic nuclei.

The most damaging powders were the anatase and rutile mixed crystal types with an organosilane or dimethicone coating. On average, these nanoparticles, which were tested at a lower amount than that used in sunscreens, more than doubled the number of dying cells in the presence of UVA light. However, this number is underestimated due to a large number of dying cells leaving the cellular monolayer during the incubation period. The research in this thesis does not prove that there is a link between skin cancer and the titanium dioxide nanoparticles used in sunscreens. Nonetheless, it does show that not all titanium dioxide powders used in sunscreens are protective towards human keratinocytes and in fact, causes more UVA induced damage to cells. The DNA damage assay showed that DNA Double Stranded Breaks were apparent in cells which had not yet started the apoptotic pathway. Due to the increased rate of DNA damage of cells in contact with some modified titanium dioxide, it is possible that a small percentage of cells would not go through the cell death mechanism but will still possess Double Stranded Breaks. After clonal expansion of these mutated cells, tumours (basal cell carcinomas, squamous cell carcinomas and melanomas) may ultimately form. This work also shows that there are some titania nanoparticles (manganese doped and alumina coated rutile) which have a consistently protective effect on human keratinocytes and should perhaps be the titanium dioxide type used in sunscreen formulations.

This research uses cultured cells to test toxicity effects and is essential as the foundation to consider chemicals such as titanium dioxide, which is already in the market and has not been adequately assessed for its safety. In accordance with UK government guidelines[200], cultured cell experimentation is absolutely necessary before justifying animal testing. Future work leading from these experiments can include using live animals or engineered skin whereby the entire cream is applied to the skin cells. A 3-5 year sunscreen study would have to be undertaken to observe the development of malignant tumours. However, for a shorter study, specific cancer markers can be identified, as the induction of malignant lesions is a lengthy process.

Bibliography

(1) Kyprianou, M. Commission Directive amending Directive 95/45/EC as regards to titanium dioxide (E 171). In *The Commission of the European Communities*, 2006.

(2) Serpone, N. *Photocatalysis, Fundamentals and Applications*; Wiley: New York, 1989.

(3) Hoffman, M. R.; Martin, S. T.; Choi, W.; Bahnemann, D. W. *Chem. Rev.* **1995**, *95*, 69.

(4) Mills, A.; Elliott, N.; Parkin, I. P.; O'Neill, S. A.; Clark, R. J. *J. Photochem. Photobiol., A* **2002**, *151*, 171.

(5) Cancer Statistics: Malignant Melanoma. Cancer Research UK, 2005; Vol. 2005.

(6) Quinn, M.; Babb, P.; Brock, A.; Kirby, E. A.; Jones, J. *Cancer Trends in England and Wales 1950-1999*; The Stationary Office: London, 2001; Vol. 66.

(7) Knowland, J.; Mckenzie, E.; P.J., M.; Cridland , N. A. *FEBS Lett.* **1993**, *324*, 309.

(8) Inbaraj, J. J.; Bilski, P.; Chignell, C. *Photochem. Photobiol.* **2002**, *75*, 107.

(9) Deflandre, A.; Lang, G. *Int. J. Cos. Sci.* **1988**, *10*, 53.

(10) Gonzalez, H. G.; Farbrot, A.; Larko, O. *Expt. Dermatol.* **2002**, *27*, 691.

(11) Lowe, N. J.; Shaath, N. A.; Pathak, M. A. *Sunscreens, development, evaluation and regulatory aspects*; Marcel Dekker: New York, 1997.

(12) Dunford, R.; Salinaro, A.; Cai, L.; Serpone, N. *FEBS Lett.* **1997**, *418*, 87.

(13) Wingo, P. A.; Ries, L. A.; Rosenberg, H. M.; Miller, D. S.; Edwards, B. K. *Cancer* **1998**, *82*, 1197.

(14) *eMedicine Dermatology (http:/www.emedicine.com/derm/topic401.htm)*; Ramsey, M., Ed. St. Petersburg, 2001; Vol. 2.

(15) Madronich, S.; McKenzie, R. L.; Bjorn, L. O.; Caldwell, M. M. *Journal of Photochemistry and Photobiology B: Biology* **1998**, *46*, 5.

(16) Armstrong, B. K.; Kricker, A. *Journal of Photochemistry and Photobiology B* **2001**, *63*, 8.

(17) Setlow, R. B.; Grist, E.; Thompson, K.; Woodhead, A. D. *Proc. Natl. Acad. Sci. U. S. A.* **1993**, *90*, 6666.

(18) Stevenborg, H. J. C. M.; Van der Leun, J. C. *Photochem. Photobiol.* **1990**, *51*, 325.

(19) Tyrrell, R. M. *Biochem. Soc. Symp.* **1995**, *61*, 47.

(20) De Fabo, E. C.; Noonan, F. P.; Fears, T.; Merlino, G. *Cancer Res* **2004**, *64*, 6372.

(21) Madronich, S.; McKenzie, R. L.; Bjorn, L. O.; Caldwell, M. M. *J. Photochem. Photobiol. B* **1998**, *46*, 5.

(22) Sunglasses and Protection from Solar Ultraviolet Radiation. Australian Radiation Protection and Nuclear Safety Agency http:\\www.arpansa.gov.au/images/nir/spectrum.gif: Australia, 2003.

(23) Avre, A. Structure of the Skin; http://www.avro.co.za/misc/about_skincare/about_skin.html, 2002.

(24) Ward, D. Looking at Skin Cancer in a Different Light. A Chronicle of Cancer Programs at the Ohio State University; http://www.acs.ohio-state/units/cancer/aut98front/light.htm.

(25) Young, A. R.; Walker, S. L. *Rad. Protect. Dos.* **2000**, *91*, 265.

(26) Alberts, B.; Johnson, A.; Lewis, J.; Raff, M.; Roberts, K.; Walter, P. *Molecular Biology of the Cell*; Garland Science, 2002.

(27) Melnikova, V. O.; Ananthaswamy, H. N. *Mutat. Res.* **2005**, *571*, 91.

(28) *Basal Cell Carcinoma*; Thackery, E.; Gale, T., Eds.; eNotes.com, 2002.

(29) *Squamous Cell Carcinoma of the Skin*; Thackery, E.; Gale, T., Eds.; eNotes.com, 2002.

(30) *Malignant Melanoma*; Longe.J.L., Ed.; eNotes.com, 2002.

(31) Holman, C. A. J.; Armstrong, B. K.; Heenan, P. J. *JNCI* **1986**, *76*, 403.

(32) Hertzfeld, P. M.; Fitzgerald, E. F.; Hwang, S. A.; Stark, A. *Cancer Detect. Prev.* **1993**, *17*, 601.

(33) Naldi, L.; Gallus, S.; Imberti, G. L.; Cainelli, T.; Negri, E.; La Vecchia, C. *Int. J. Cancer* **2000**, *86*, 879.

(34) Autier, P.; Dore, J.; Schifflers, E. *Int. J. Cancer* **1995**, *61*, 1.

(35) Westerdahl, J.; Olsson, H.; Masback, A. *Mel.Res.* **1995**, *5*, 59.

(36) Westerdahl, J.; Indvar, C.; Masback, A.; Olsson, H. *Int. J. Cancer* **2000**, *87*, 145.

(37) Autier, P.; Pedeaux, R.; Dore, J. *J. Natl. Cancer. Inst.* **1999**, *91*, 1304.

(38) Autier, P.; Dore, J.; Cattaruzza, M. S. *J. Natl. Cancer Inst.* **1998**, *90*, 1873.

(39) Gallagher, R. P.; Rivers, J. K.; Lee, T. K.; Bajdik, C. D.; Mclean, D. I.; A.J, C. *JAMA* **2000**, *283*, 2955.

(40) Vainio, H.; Bianchini, F. "IARC Handbooks of Cancer Prevention Vol.5 - Sunscreen," World Health Organisation (International Agency for Research), 2001.

(41) Green, A. *The Lancet* **1999**, *354*, 723.

(42) De Gruijl, F. R.; Sterenborg, H. J. C. M.; Forbes, P. D. *Cancer Res.* **1993**, *53*, 53.

(43) De Gruijl, F. R.; Van der Leun, J. C. *Health Phys.* **1994**, *67*.

(44) Lavker, R. M.; BGerberick, G. F.; Veres, D.; Irwin, C. J.; Kaidbey, K. H. *J. Am. Acad. Dermatol.* **1995**, *32*, 53.

(45) Setlow, R. B.; Woodhead, A. D. *Mutat. Res.* **1994**, *307*, 365.

(46) Naylor, M.; Farmer, K. C. Sunscreens. In *The Electronic Textbook of Dermatology*; Drugge, R., Ed., 1999.

(47) Sterling, G. B. *Cutis* **1992**, *50*, 221.

(48) lnbaraj, J. J.; Bilski, P.; Chignell, C. *Photochem. Photobiol.* **2002**, *75*, 102.

(49) Maibach, H. "Percutaneous Penetration," FDA COntract, 1978.

(50) Maira, A. J.; Yeung, K. L.; Lee, C. Y.; Yue, P. L.; Chan, C. K. *J. Catal.* **2000**, *192*, 185.

(51) Ditchburn, R. W. *Light*; Blackie & Sons: London, 1963.

(52) Wakefield, G.; Lipscomb, S.; Holland, E.; Knowland, J. *Photochem. Photobiol. Sci.* **2004**, *3*, 648.

(53) Stott, J. "Sunscreens with enhanced UVA protective capabilities. The application of doped nanoparticles.," Oxonica Ltd., 2005.

(54) Fujishima, A.; Rao, D. A.; Tryk, D. *J. Photochem. Photobiol. C: Rev.* **2000**, *1*, 1.

(55) Mills, A.; Le Hunte, S. *J. Photochem. Photobiol., A* **1997**, *108*, 1.

(56) Peral, J.; Domenech, X.; Ollis, D. F. *J. Chem. Technol. Biotechnol.* **1997**, *70*, 117.

(57) Picatonotto, T.; Vione, D.; Calotti, M. E. *J. Disp. Sci. Tech.* **2002**, *23*, 845.

(58) Hager, S.; Bauer, R.; Kudielka, G. *Chemosphere* **2000**, *41*, 1219.

(59) Topalov, A.; Molnar-Gabor, D.; Kosanic, B.; Abramovic, B. *Wat. Res.* **2000**, *34*, 1473.

(60) Maness, P. C.; Smolinski, S.; Blake, D. M.; Huang, Z.; Wolfrum, E. J.; Jacoby, W. A. *Appl. Environ. Microbiol.* **2001**, *65*, 4094.

(61) Huang, Z.; Maness, P. C.; Blake, D. M.; Wolf, E. J. *J. Photochem. Photobiol., A* **2000**, *130*, 163.

(62) Ireland, W. A.; Klostermann, P.; Rice, E. W.; Clark, R. M. *Appl. Environ. Microbiol.* **1993**, *59*, 1168.

(63) Jacoby, W. A.; Maness, P. C.; Blake, D. M.; Wolfrum, E. J. *Environ. Sci. Technol.* **1998**, *32*, 2650.

(64) Tan, B. J.; Klabunde, K. J.; Sherwood, P. M. A. *J. Am.Chem.Soc.* **1991**, *113*, 855.

(65) Hadgraft, J. *Int. J. Pharmaceutics* **2001**, *224*, 1.

(66) Schulze, J.; Hohenberg, H. *Ad. Drug Del. Revs.* **2002**, *54*, S157.

(67) Desset, S.; Spalla, O.; Lixon, P.; Cabane, B. *Colloids Surf., A* **2002**, *196*, 1.

(68) Lademann, J.; Weigmann, H.-J.; Schafer, H.; Muller, G.; Sterry, W. *Skin Pharmacol. Appl. Skin Physiol.* **2000**, *13*, 258.

(69) van der Molen, R. G.; Hurks, H. M. H.; Out-Luiting, C.; Spies, F.; van't M.; Koerten, H. K.; Mommaas, A. M. *J. Photochem. Photobiol B* **1998**, *44*, 143.

(70) Menzel, F.; Reinert, T.; Vogt, J.; Butz, T. *Nucl. Instrum. Methods Phys. Res., Sect. B* **2004**, *219-220*, 82.

(71) Van Dyk, A. C.; Heyns, A. M. *J. Coll. Inter. Sci.* **1998**, *206*, 381.

(72) Kim, S. J. *J. Sol-Gel Sci. Technol.* **2001**, *22*, 63.

(73) Ohno, T.; Sarukawa, K.; Matsumura, M. *New J. Chem.* **2002**, *26*, 1167.

(74) Tanaka, K.; Capule, M. F. V.; Hisanaga, T. *Chem. Phys. Letts.* **1991**, *187*, 73.

(75) Anpo, M.; Shima, T.; Kubokawa, Y. *Chemistry Letters* **1985**.

(76) Cai, R. X.; Kubata, Y.; Shuin, T.; Sakai, H.; Hashimoto, K.; Fujishima, A. *Cancer Res.* **1992**, *52*, 2346.

(77) Jaeger, C. D.; Bard, A. J. *J. Phys. Chem.* **1979**, *83*, 3146.

(78) Yamamoto, Y.; Imai, N.; Masima, R.; Konaka, R.; Inoue, M.; Dunlap, W. C. *Methods Enzymol.* **2000**, *319*, 29.

(79) Konaka, R.; Kasahara, E.; Dunlap, W. C.; Yamamoto, Y. *Free Radical Biol. Med.* **1999**, *27*, 294.

(80) Wamer, W. G.; Yin, J.-J.; Wei, R. R. *Free Radical Biol. Med.* **1997**, *23*, 851.

(81) Toby, B. The Portable CMPR and LOGIC programs; National Institute of Standards and Technology, 2004.

(82) Li, D.; Haneda, H. *Chemosphere* **2003**, *51*, 129.

(83) Humin, C.; Ma, J.; Zhenguo, Z.; Limin, Q. *Chem. Mater.* **1995**, *7*, 663.

(84) Yin, S.; Hasegawa, H.; Maeda, D.; Ishitsuka, M.; Sato, T. *J. Photochem. Photobiol., A* **2004**, *163*, 1.

(85) Meng, L.-J.; dos Santos, M. P. *Thin Solid Films* **1993**, *226*, 22.

(86) Spurr, R. A.; Myers, H. *Anal. Chem* **1957**, *29*, 760.

(87) Sanchez, E. L., T.;Gomez, R.;Bokhimi, X.;Morales, A.;Novaro, O. *J. Solid State Chem.* **1996**, *122*, 309.

(88) Restori, R. S., D.;Schneider, J.R. *Acta Crystallogr., Sect. B: Struct. Sci* **1987**, *43*, 251.

(89) Post, J. E. *Proc.Natl.Acad.Sci.USA* **1999**, *96*, 3447.

(90) Toby, B. The Portable CMPR and LOGIC programs; National Institute of Standards and Technology, 2004.

(91) Gesenhues, U.; Rentschler, T. *J. Solid State Chem.* **1999**, *143*, 210.

(92) Balachandran, D.; Morgan, D.; Ceder, G. *J. Solid State Chem.* **2002**, *166*, 91.

(93) Sanjines, R.; Tang, H.; Berger, H.; Gozzo, F.; Margaritondo, G.; Levy, F. *J. Appl. Phys.* **1994**, *75*, 2945.

(94) Diebold, U. *Surf. Sci. Rep.* **2003**, *48*.

(95) Gray, R. C.; Carver, J. C.; Hercules, D. M. *J. Electron. Spectrosc. Relat. Phenom.* **1976**, *8*, 343.

(96) Borgmann, D.; Hums, E.; Hopfengartner, G.; Wedler, G.; Spitznagel, G. W.; Rademacher, I. *J. Electron. Spectrosc. Relat. Phenom.* **1993**, *63*, 91.

(97) Wagner, C. D.; Riggs, W., M; Davis, L. E.; Moulder, J. F.; Muilenberg, G. E. *Handbook of X-Ray Photoelectron Spectroscopy*; Perkin-Elmer Corporation, Physical Electronics Division, 1979.

(98) Yu, D.-G.; An, J. H. *Colloids Surf., A* **2004**, *237*, 87.

(99) Barr, T. L. *Modern ESCA: The Principles and Practice of X-Ray Photoelectron Spectroscopy*; CRC Press, 1994.

(100) De Angelis, B. A.; Rizzo, C.; Contarini, S.; Howlett, S. P. *Appl. Surf. Sci.* **1991**, *51*, 177.

(101) Campbell, D. S.; Leary, H. J.; Slattery, J. S.; Sargent, R. J. "ECSA surface analysis of plasma exposed silicon nitride and photoresist polymer films.," IBM General Technology Division, 1999.

(102) Hollinger, G.; Marest, G.; Jaffrezic, H.; Tousset, J.; Moncoffre, N. *Nucl. Instrum. Methods Phys. Res., Sect. A* **1985**, *7*, 177.

(103) Laoharojanapand, P.; Lin, T. J.; Stoffer, J. O. *J. Appl. Polymer Sci.* **1990**, *40*, 369.

(104) Sherwood, P. M. A.; Thomas, S. *Anal. Chem* **1992**, *64*, 2488.

(105) Beamson, G.; Briggs, D. High Resolution XPS of Organic Polymers Scienta 300 ESCA Database, 1992.

(106) Rats, D.; Sevely, J.; Vandenbulcke, L.; Benoit, R.; Erre, R.; Herbin, R.; Serin, V. *Thin Solid Films* **1995**, *270*, 177.

(107) Sanjines, R.; Tang, H.; Berger, H.; Gozzo, F.; Margaritondo, G.; Levy, F. *J. Appl. Phys.* **1994**, *75*, 2945.

(108) Tan, B. J.; Klabunde, K. J.; Sherwood, P. M. A. *J. Am.Chem.Soc.* **1991**, *113*, 855.

(109) Li, F.; Zhang, L.; Evans, D. G.; Duan, X. *Colloids and Surfaces A: Physicochemical and Engineering Aspects* **2004**, *244*, 169.

(110) Oku, M.; Hirokawa, K. *J. Electron Spectrosc. Relat. Phenom.* **1976**, *8*, 475.

(111) Ibach, H. *Electron spectroscopy for surface analysis*; Springer: Berlin, 1977.

(112) Jablonski, A. *Surf. Sci.* **1987**, *188*, 164.

(113) NIST XPS Database. http://srdata.nist.gov/xps.

(114) Porto, S. P. S.; Fleury, P. A.; Damen, T. C. *Phys. Rev.* **1967**, *522*, 154.

(115) Ma, W.; Lu, Z.; Zhang, M. *Appl. Phys. A.* **1998**, *66*, 621.

(116) Ohsaka, T. *J. Phys. Soc. Jpn.* **1980**, *48*, 1661.

(117) Misra, A.; Bist, H. D.; Navati, M. S.; Thareja, R. K.; Narayan, J. *Materials Science and Engineering B* **2001**, *79*, 49.

(118) Kostov-Kytin, V.; Mihailova, B.; Kalvachev, Y.; Tarassov, M. *Microporous and Mesoporous Materials* **2005**, *86*, 223.

(119) Kniepp, K.; Kniepp, H.; Itzkan, I.; Dasari, R. R.; Field, M. S. *Chem. Rev.* **1999**, *99*, 2957.

(120) Ruan, H. D.; Frost, R. L.; Kloprogge, J. T. *J. Raman Spec.* **2001**, *32*, 745.

(121) Engelhardt, G.; Michel, D. *High resolution solid-state NMR of silicates and zeolites*; Wiley: New York, 1987.

(122) Duer, M. *Introduction to Solid State NMR Spectroscopy*; Blackwell, 2004.

(123) Fyfe, C. A. *Solid State NMR for Chemists*; C.F.C. Press: Ontario, Canada, 1983.

(124) Bauer, F.; Glasel, H.-J.; Decker, U.; Ernst, H.; Freyer, A.; Hartmann, E.; Sauerland, V.; Mehnert, R. *Progress in Organic Coatings* **2003**, *47*, 147.

(125) Waithe Solid State NMR Facility. http://www.waite.adelaide.edu.au/NMR/nmrlist.html.

(126) Stebbins, J. F.; Farnan, I. *J. Am. Ceram. Soc.* **1989**, *72*, 2198.

(127) Magnenet, C.; Massiot, D.; Klur, I.; Coutures, J.-P. *J. Chim. Phys.* **1998**, *95*, 310.

(128) Gervais, C.; Julian, B.; Cordoncillo, E.; Escribano, P.; Smith, M. E.; Babonneau, F.; Sanchez, C. *Mater. Res. Soc. Symp. Proc.* **2005**, *847*.

(129) Smith, M. E. *Applied Magnetic Resonance* **1993**, *4*, 1.

(130) Ashbrook, S. E.; MacKenzie, K. J. D.; Wimperis, S. *Solid State Nuclear Magnetic Resonance* **2001**, *20*, 87.

(131) Mackenzie, K. J. D.; Smith, M. E. *Multinuclear Solid-State NMR of Inorganic Materials*; Pergamon, 2002; Vol. 6.

(132) Brunauer, S.; Emmet, P. H.; Teller, E. *J. Am. Chem. Soc.* **1938**, *60*, 309.

(133) SINTEF. Materials and Chemistry. http://www.sintef.com.

(134) Howe, R. F.; Gratzel, M. *J. Phys. Chem.* **1985**, *89*.

(135) Davies, M. J. Recent developments in spin trapping. In *Electron Paramagnetic Resonance*; Gilbert, B. C., Davies, M. J., Murphy, D. M., Eds.; Royal Society of Chemistry: Cambridge, 2002; Vol. 18; pp 47.

(136) Attwood, A. L.; Murphy, D. M.; Edwards, J. L.; Egerton, T. A.; Harrison, R. W. *Res. Chem. Intermed.* **2003**, *29*, 449.

(137) Segal, B. G.; Kaplan, M.; Fraenkel, G. K. *J. Chem. Phys.* **1965**, *43*, 4191.

(138) Jaeger, C. D.; Bard, A. J. *J. Phys. Chem.* **1979**, *83*, 3146.

(139) Krzystek, J.; Sienkiewicz, A.; Pardi, L.; Brunel, L. C. *Journal of Magnetic Resonance* **1997**, *125*, 207.

(140) Hurum, D. C.; Agrios, A. G.; Gray, K. A. *J. Phys. Chem. B* **2003**, *107*, 4545.

(141) Coronado, J. M.; Maira, A. J.; Conesa, J. C.; Yeung, K. L.; Augugliaro, V.; Soria, J. *Langmuir* **2001**, *17*, 5368.

(142) Micic, O. I.; Zhang, Y.; Cromack, K. R.; Trifunac, A. D.; Thurnauer, M. C. *J. Phys. Chem.* **1993**, *97*, 7277.

(143) Nakaoka, Y.; Nosaka, Y. *J. Photochem. Photobiol., A* **1997**, *110*, 299.

(144) Amorelli, A.; Evans, J. C.; Rowlands, C. C. *J. Chem. Soc., Faraday Trans. 1* **1989**, *85*, 4031.

(145) Cordischi, D.; Valigi, M.; Gazzoli, D.; Indovina, V. *J. Solid State Chem.* **1975**, *15*, 82.

(146) Kemp, T. J.; McIntyre, R. A. *Polymer Degradation and Stability* **2006**, *91*, 165.

(147) Anpo, M.; Shima, T.; Kubokawa, Y. *Chemistry Letters* **1985**.

(148) Howe, R. F.; Gratzel, M. *J. Phys. Chem.* **1987**, *91*, 3906.

(149) Yamamoto, Y.; Imai, N.; Masima, R.; Konaka, R.; Inoue, M.; Dunlap, W. C. *Methods Enzymol.* **2000**, *319*, 29.

(150) Zhang, T.; Oyama, T.; Horikoshi, S.; Hidaka, H.; Zhao, J.; N, S. *Sol. Energy Mater. Sol. Cells* **2002**, *73*, 287.

(151) Zhang, F.; Zhao, J.; Shen, T.; Hidaka, H.; Pelizzetti, E.; Serpone, N. *Appl. Catal. B: Environ.* **1998**, *15*, 147.

(152) Ditchburn, R. W. *Light*; Blackie & Sons: London, 1963.

(153) Konstantinou, I.; Albanis, T. *Appl. Catal. B* **2004**, *49*, 1.

(154) Lakshmi, S.; Renganathan, R.; Fujita, S. *J. Photochem. Photobiol., A* **1995**, *88*, 163.

(155) Pearson, A. J.; Driscoll, C.; Hunter, N.; Campbell, J. I.; Dean, S. F.; Clark, I. E. "Solar Radiation Measurements at a Network of Seven Sites in the UK, January-December 2003," National Radiation Protection Board, 2003.

(156) Solar UV Index. http://www.metoffice.gov.uk.

(157) Li, D.; Haneda, H. *Chemosphere* **2003**, *51*, 129.

(158) Serpone, N. *Photocatalysis, Fundamentals and Applications*; Wiley: New York, 1989.

(159) Noh, J. S.; Schwarz, J. A. *J. Coll. Inter. Sci.* **1989**, *130*, 157.

(160) Allen, S. J.; Koumanova, B. *J. Univ. Chem. Tech. Metall.* **2005**, *40*, 175.

(161) Quinton, J. S.; Dastoor, P. C. *Surf. Inter. Anal.* **1999**, *28*, 12.

(162) Giles, C. H.; Easton, I. A.; McKay, R. B.; Patel, C. C.; Shah, N. B.; Smith, D. *J. Bacteriol.* **1965**, *89*, 390.

(162) Murphy, G.; Young, A. R.; Wulf, H. C.; Kulms, D.; Schwarz, T. *Exp. Dermatol.* **2001**, *10*, 155.

(163) Hengartner, M. O. *Nature* **2000**, *407*, 770.

(164) Alberts, B.; Johnson, A.; Lewis, J.; Raff, M.; Roberts, K.; Walter, P. *Molecular Biology of the Cell*; Garland Science, 2002.

(165) Antibodies (Biotech). http://www.accessexcellence.org/RC/VL/GG/images, 2004.

(166) Invitrogen. Structure for Hoechst; http://probes.invitrogen.com, 2006.

(167) Arndt-Jovin, D. J.; Jovin, T. M. *Methods Cell Biol.* **1989**, *30*, 417.

(168) Lowe, N. J.; Shaath, N. A.; Pathak, M. A. *Sunscreens, development, evaluation and regulatory aspects*; Marcel Dekker: New York, 1997.

(169) Pearson, A. J.; Driscoll, C.; Hunter, N.; Campbell, J. I.; Dean, S. F.; Clark, I. E. "Solar Radiation Measurements at a Network of Seven Sites in the UK, January-December 2003," National Radiation Protection Board, 2003.

(170) Fink, S. L.; Cookson, B. T. *Infect. Immun.* **2005**, *73*, 1907.

(171) Rosenblatt, J.; Raff, M. C.; Cramer, L. P. *Curr. Biol.* **2001**, *11*, 1847.

(172) Assefa, Z.; Van Laethem, A.; Garmyn, M.; Agostinis, P. *Biochim. Biophys. Acta, Rev. Cancer* **2005**, *1755*, 90.

(173) Rudel, T.; Bockoch, G. M. *Science* **1997**, *276*, 1571.

(174) Alberts, B.; Johnson, A.; Lewis, J.; Raff, M.; Roberts, K.; Walter, P. *Molecular Biology of the Cell*; Garland Science, 2002.

(175) Koopman, G.; Reutelingsperger, C.; Kuijten, G.; Keehnen, R.; Pals, S.; van Oers, M. *Blood* **1994**, *84*, 1415.

(176) Annexin V. BD Biosciences http://www.bdbiosciences.com.

(177) Biovision (Sytox Green) http://www.biovision.com/pdf/K203.

(178) Earnshaw, W. C.; Martins, L. M.; Kaufmann, S. H. *Annu. Rev. Biochem.* **1999**, *68*, 383.

(179) Degterev, A.; Boyce, M.; Yuan, J. *Oncogene* **2003**, *22*, 8543.

(180) Zhuang, S.; Kochevar, I. E. *Photochem. Photobiol.* **2003**, *78*, 61.

(181) Danial, N. N.; Korsmeyer, S. J. *Cell* **2004**, *116*, 205.

(182) Darzynkiewicz, Z.; Juan, G.; Li, X.; Gorcyca, W.; Murakami, T.; Traganos, F. *Cytometry* **1997**, *27*, 1.

(183) Schulze-Osthoff, K.; Walczak, H.; Droge, W.; Krammer, P. H. *J. Cell Biol.* **1994**, *127*, 15.

(184) Sun, D.; Jiang, S.; Zheng, L.; Ojcius, D.; Young, J. *J. Exp. Med.* **1994**, *179*, 559.

(185) Caspase Inhibitor - Z-VAD (Ome)-FMK. Merck http://www.merckbiosciences.co.uk.

(186) Garcia-Calvo, M.; Peterson, E. P.; Leiting, B.; Ruel, R.; Nicholson, D. W.; Thornberry, N. A. *J. Biol. Chem.* **1998**, *273*, 32608.

(187) Zamzami, N.; Kroemer, G. *Nature* **1999**, *401*, 127.

(188) Yu, L.; Alva, A.; Su, H.; Dutt, P.; Freundt, E.; Welsh, S.; Baehrecke, E. H.; Lenardo, M. J. *Science* **2004**, *304*, 1500.

(189) Grabbe, J.; Welker, P.; Rosenbach, T.; Nurnberg, W.; Kruger-Krasagakes, S.; Artuc, M.; Fiebiger, E.; Henz, B. M. *J. Invest. Dermatol.* **1996**, *107*, 219.

(190) Wilhelm, K.-P.; Bottjer, B.; Siegers, C.-P. *Br. J. Dermatol.* **2001**, *145*, 709.

(191) Jackson, P. *Carcinogenesis* **2002**, *23*, 687.

(192) Fernandez-Capetillo, O.; Celeste, A.; Nussenzweig, A. *Cell Cycle* **2003**, *2*, 426.

(193) Rogakou, E. P.; Nieves-Neira, W.; Boon, C.; Pommier, Y.; Bonner, W. M. *J. Biol. Chem.* **2000**, *275*, 9390.

(194) Rogakou, E. P.; Pilch, D. R.; Orr, A. H.; Ivanova, V. S.; Bonner, W. M. *J. Biol. Chem.* **1998**, *10*, 5858.

(195) Redon, C.; Pilch, D. R.; Rogakou, E. P.; Sedelnikova, O.; Newrock, K.; Bonner, W. M. *Curr. Opin. Genet. Dev.* **2002**, *12*, 162.

(196) Briganti, S.; Picardo, M. *J. Eur. Acad. Dermatol. Ven.* **2003**, *17*, 663.

(197) Podda, M.; Traber, M. G.; Weber, C.; Yan, L.-J.; Packer, L. *Free Radical Biol. Med.* **1998**, *24*, 55.

(198) Kochevar, I. E.; Lynch, M. C.; Zhuang, S.; Lambert, C. R. *Photochem. Photobiol.* **2000**, *72*, 548.

(199) Halliwell, B.; Gutteridge, J. M. *Methods Enzymol.* **1990**, *186*, 1.

(200) Invitrogen. Structure for Hoechst; http://probes.invitrogen.com, 2006.

Appendix A – X-Ray Diffraction

S2

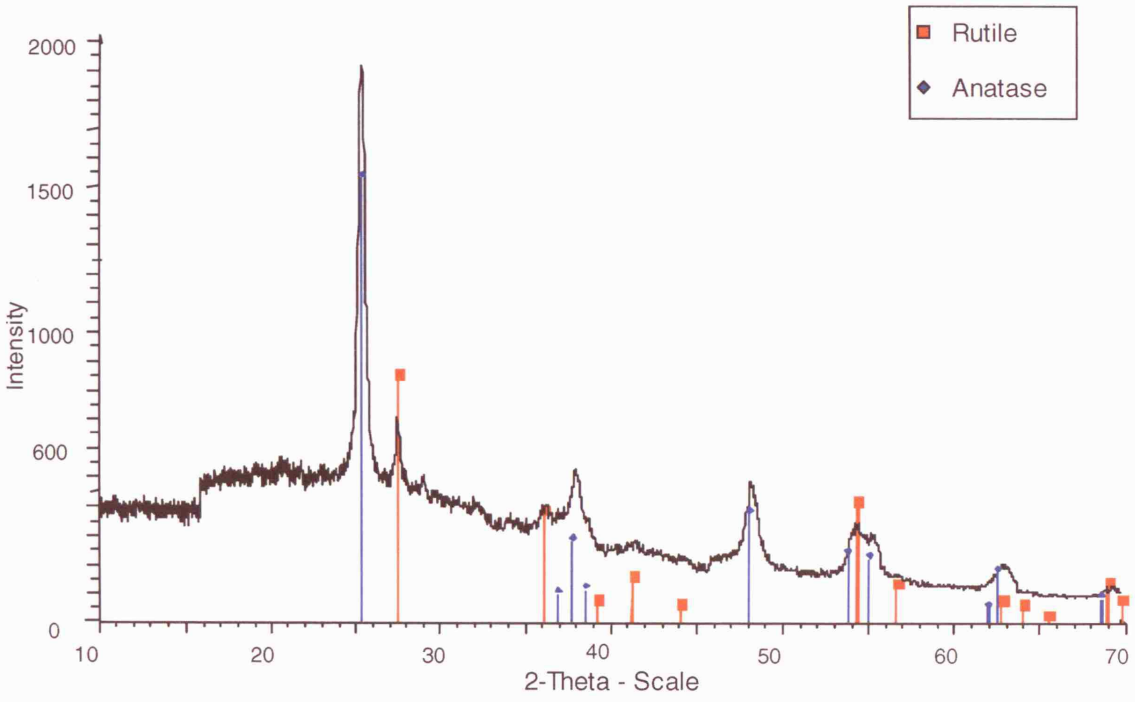

Figure A1: X-Ray Diffraction pattern of **S2** showing a mixture of anatase and rutile.

S4

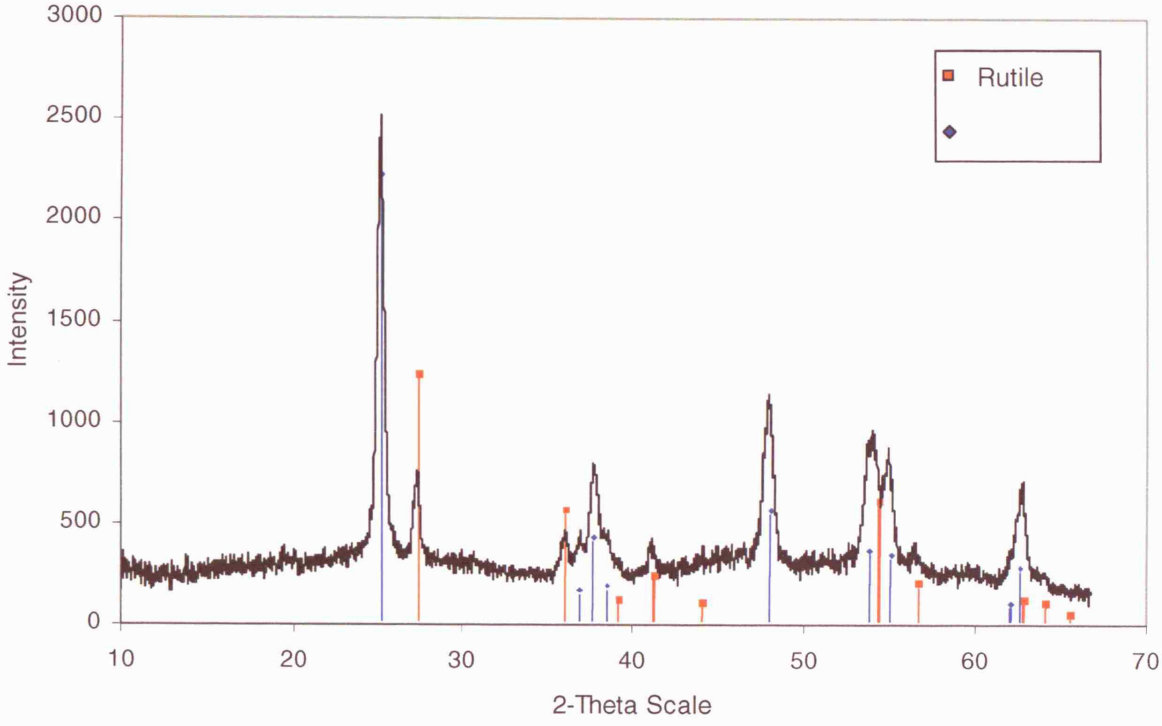

Figure A2: X-Ray Diffraction Pattern of **S4** showing both anatase and rutile crystal forms.

S6

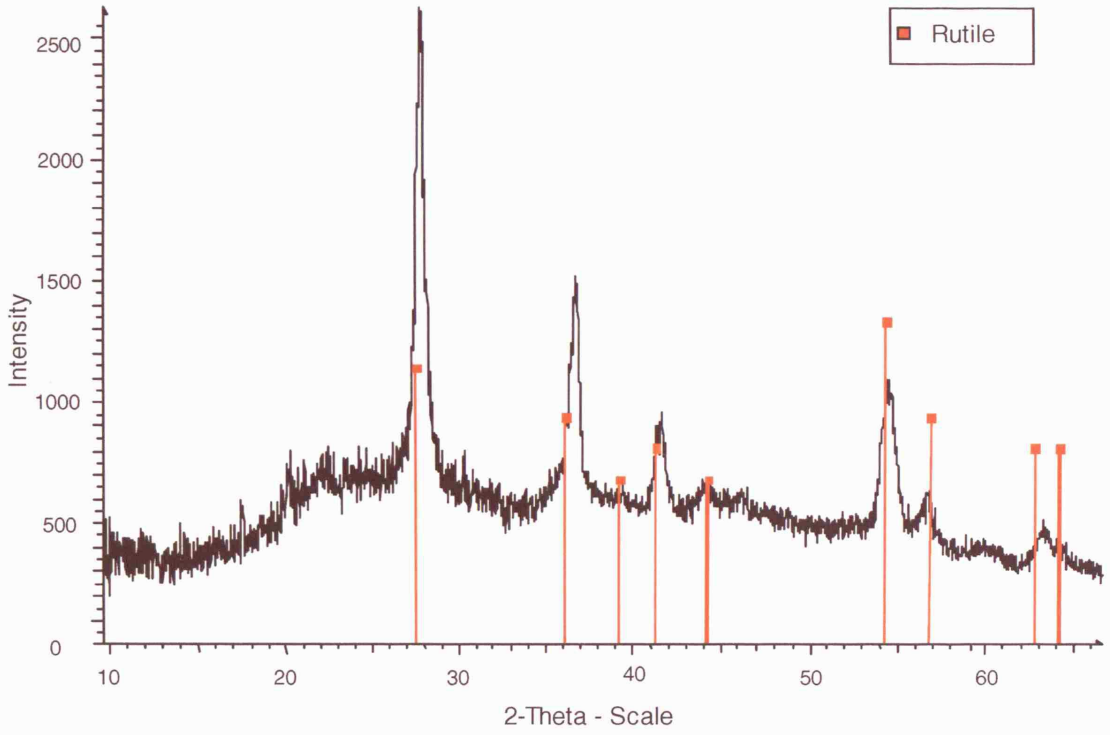

Figure A3: X-Ray Diffraction pattern of **S6** showing a pure rutile crystal structure.

S7

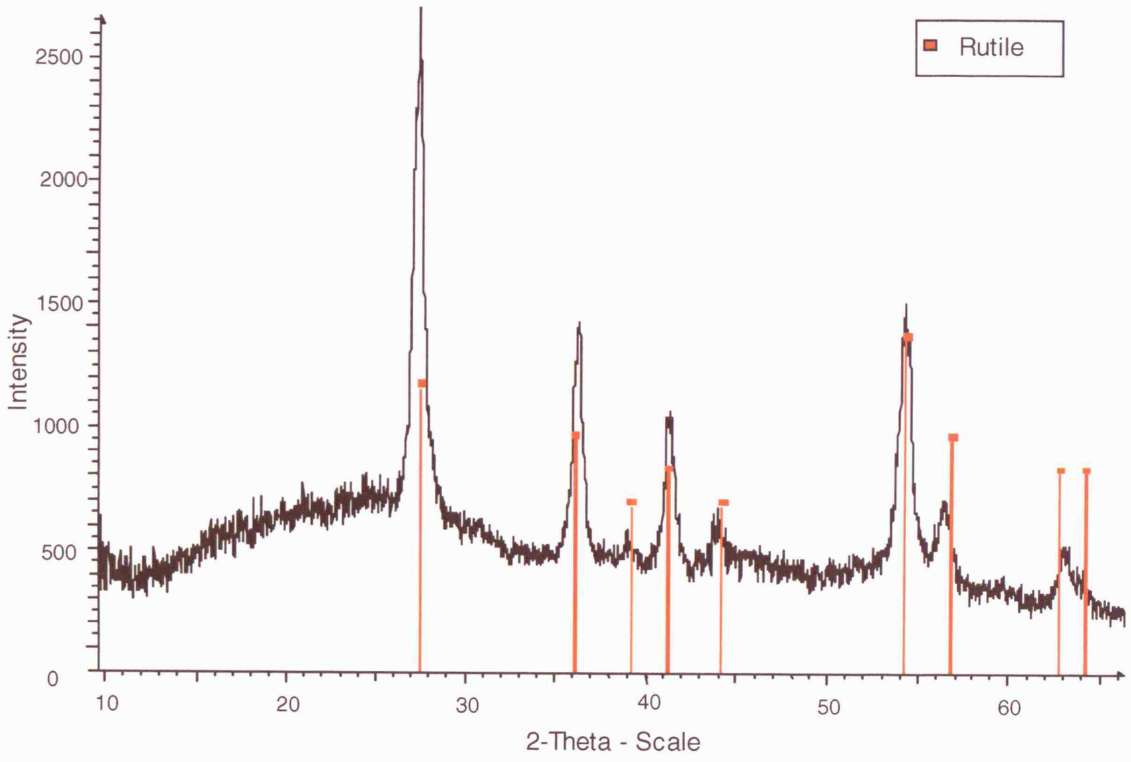

Figure A4: X-Ray Diffraction pattern of **S7** showing a rutile crystal form.

S8

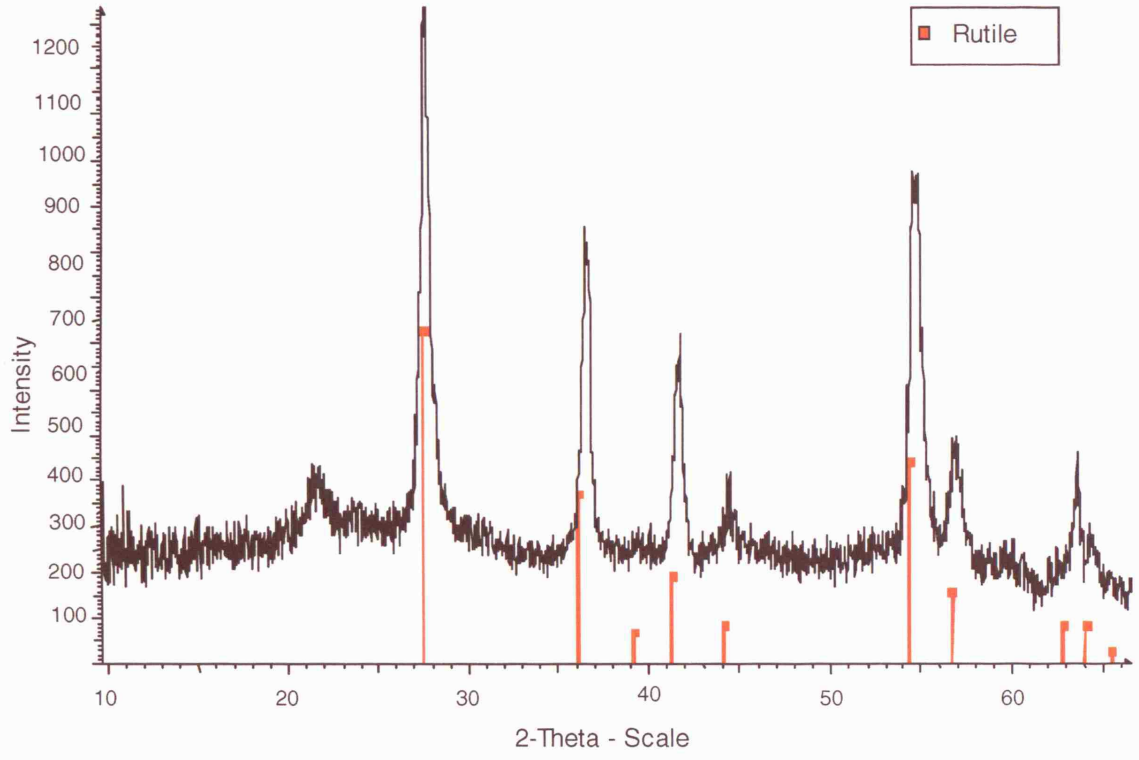

Figure A5: X-Ray Diffraction pattern of **S8** showing a pure rutile crystal structure.

S9

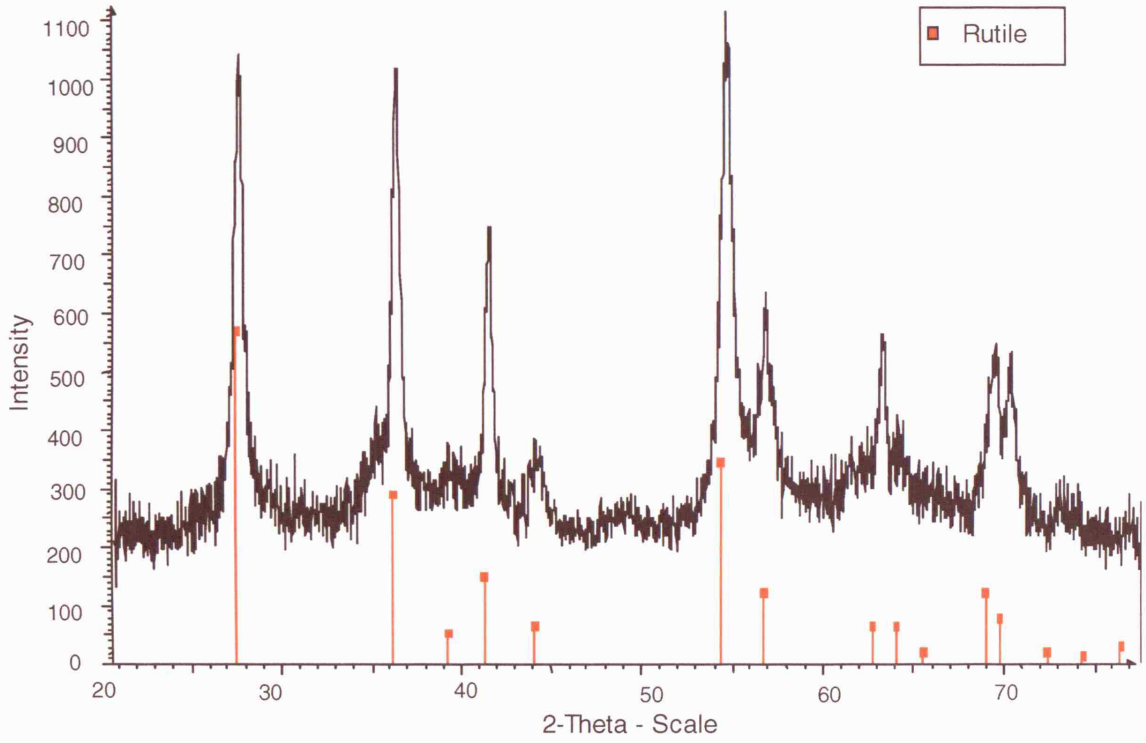

Figure A6: X-Ray Diffraction pattern of **S9** showing a pure rutile crystal structure.

Appendix B

X-Ray Photoelectron Spectroscopy

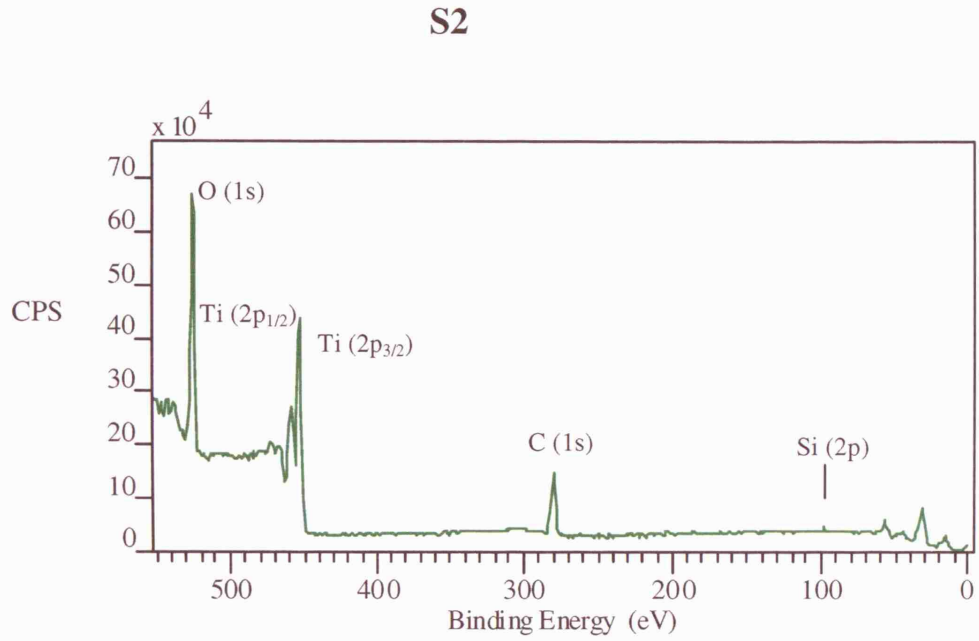

Figure B1: X-Ray Photoelectron Spectroscopy survey of **S2**, anatase and rutile mixed crystal form with an organosilane coating, extracted sunscreen.

Table B1: X-Ray Photoelectron Spectroscopy binding energies of **S2** components.

Binding Energy/eV	**Species**
531.0	O (1s)
464.4	Ti^{4+} ($2p_{1/2}$)
458.9	Ti^{4+} ($2p_{3/2}$)
285.0	C (1s)
153.1	Si (2s)
102.1	Si (2p)
62.9	Ti (3s)
37.5	Ti (3p)

S4

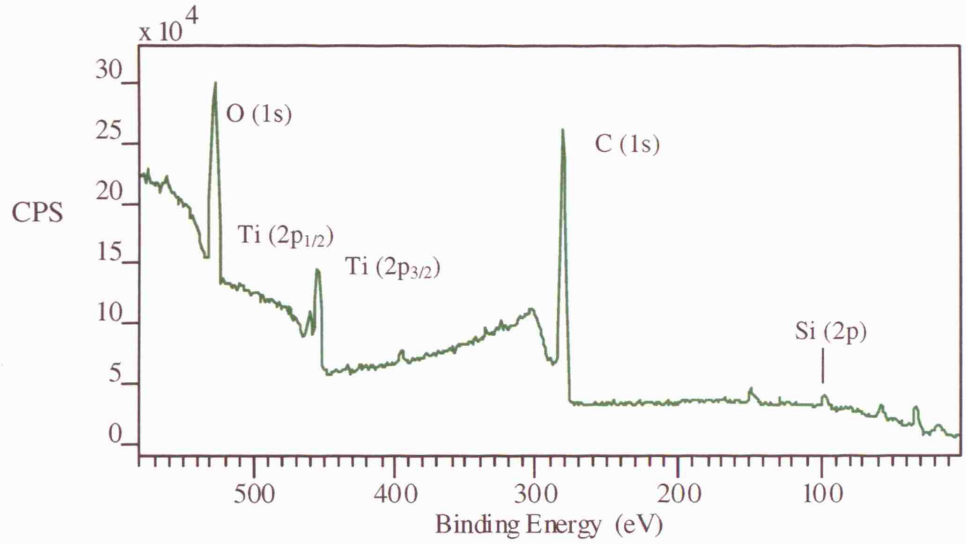

Figure B2: X-Ray Photoelectron Spectroscopy survey for **S4**, anatase and rutile mixed rutile crystal form with dimethicone coating.

Table B2: X-Ray Photoelectron Spectroscopy binding energies of **S4** components.

Binding Energy/eV	**Species**
531.0	O (1s)
464.4	Ti^{4+} ($2p_{1/2}$)
458.9	Ti^{4+} ($2p_{3/2}$)
285.0	C (1s)
153.1	Si (2s)
102.1	Si (2p)
62.9	Ti (3s)
37.5	Ti (3p)

S5

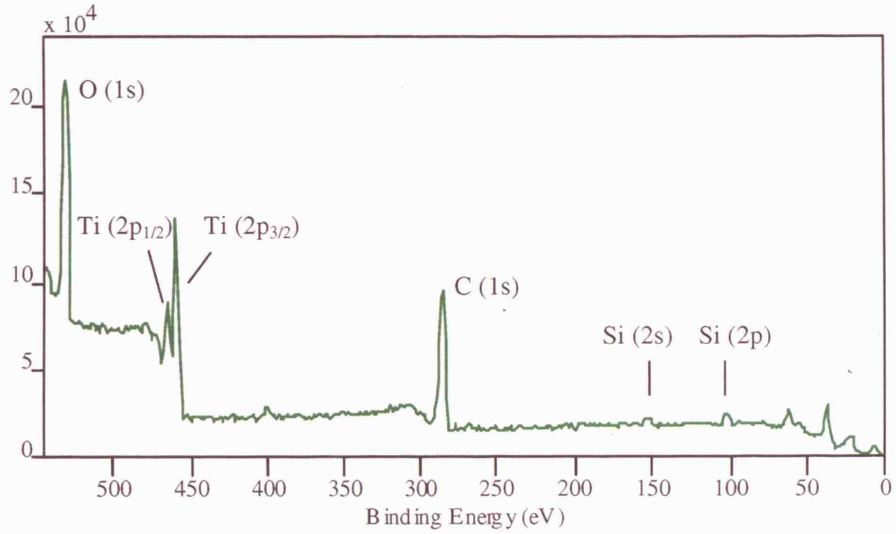

Figure B3: X-Ray Photoelectron Spectroscopy survey of **S5**.

Table B3: X-Ray Photoelectron Spectroscopy binding energies for **S5** components.

Binding Energy/ eV	Species
531	O (1s)
464.7	Ti^{4+} ($2p_{1/2}$)
459	Ti^{4+} ($2p_{3/2}$)
400	N (1s)
285.2	C (1s)
153	Si (2s)
102.7	Si ($2p_{3/2}$)
62.07	Ti (3s)
37.2	Ti (3p)

S9

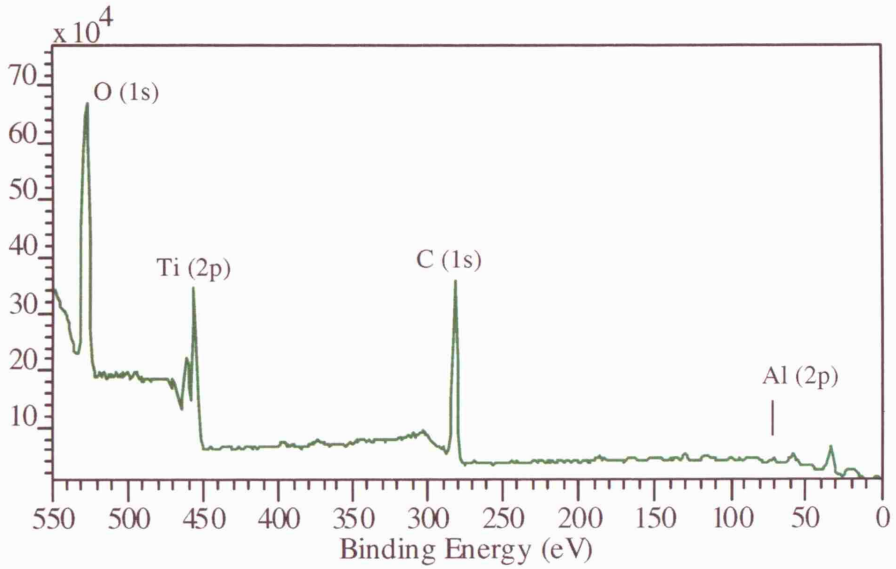

Figure B4: X-Ray Photoelectron Spectroscopy survey of **S9**.

Table B4: X-Ray Photoelectron Spectroscopy binding energies of **S9** components.

Binding Energy/ eV	Species
533, 531, 530	O (1s)
458.8	Ti^{4+} ($2p_{1/2}$)
464.8	Ti^{4+} (2p3/2)
400.2	N (1s)
285	C (1s)
153.1	Si (2s)
119.6	Al (2s)
102.5	Si (2p)
76.4; 74.6	Al ($2p_{3/2}$)
62.3	Ti (3s)
36.9	Ti (3p)

S11

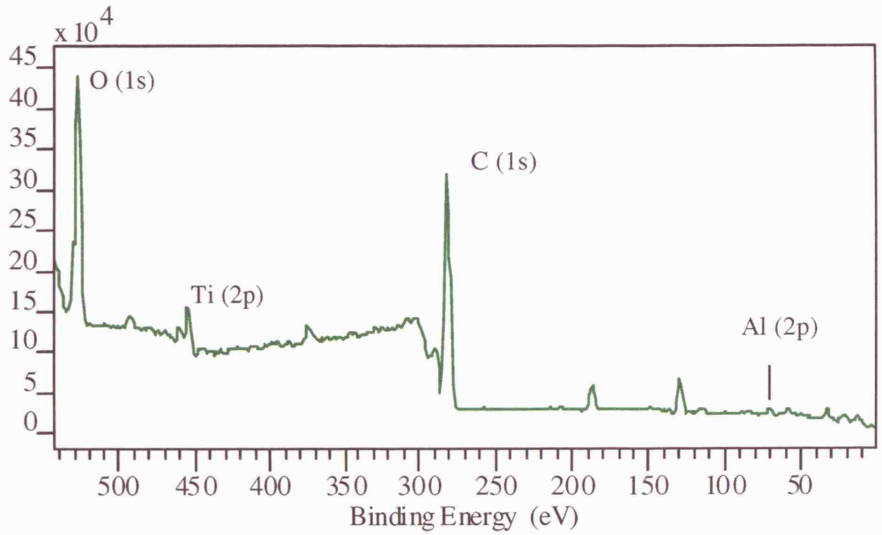

Figure B5: X-Ray Photoelectron Spectroscopy survey of **S11**.

Table B5: X-Ray Photoelectron Spectroscopy binding energies of **S11** components.

Binding Energy	**Species**
532.8	O (1s)
464	Ti^{4+} ($2p_{1/2}$)
459	Ti^{4+} ($2p_{3/2}$)
378	K (2s)
285	C (2p)
192	P (2s)
134	P ($2p_{3/2}$)
119	Al (2s)
75	Al (2p)
62	Ti (3s)
37	Ti (3p)